The Dissertation Committee for Yao-Lun Yang certifies that this is the approved version of the following dissertation:

The Three-dimensional Structure and Kinematics of Protostellar Envelopes

Committee:

Stella S. R. Offner, Supervisor

Neal J. Evans II, Co-Supervisor

Joel D. Green

Jeong-Eun Lee

Daniel T. Jaffe

John H. Lacy

Volker Bromm

The Three-dimensional Structure and Kinematics of Protostellar Envelopes

by

Yao-Lun Yang

Dissertation
Presented to the Faculty of the Graduate School of
The University of Texas at Austin
in Partial Fulfillment
of the Requirements
for the degree of
Doctor of Philosophy

The University of Texas at Austin
May, 2019

Dedicated to my wife 珮綺, my family, and Taiwan.

Acknowledgements

I am extremely fortunate to have help from many others on this journey. Needless to say, this dissertation would not be possible without them. As a Taiwanese studying in the United States, it is only appropriate to divide this acknowledgement in two languages to express my gratitude to them.

First, I want to thank my advisor, Prof. Neal Evans, for your guidance and patience in the past six years, allowing me to explore my interests and keep me anchored on the important questions. I also want to thank Dr. Joel Green for many discussions and actively including me to a larger network, and Prof. Jeong-Eun Lee for the supports via scientific discussions and encouragement. This journey would not start without the mentoring from Dr. Ciska Kemper, who took me in when I knew nothing about astronomy. Moreover, I want to thank my collaborators, mentors, and committee members. Also, I want to thank my fellow graduate students and postdocs for motivating me to step outside of my comfort zone and every bit of your support on this journey.

The city of Austin plays an important role in my graduate journey. I could not think of any other place I would go to finish my graduate study. Thank you Austin for awesome Austinites, for the accessible nature environment, and most importantly for many local coffee shops. In particular, thanks Epoch, where I did my homework and write my papers, for the great environment to pull an all-nighter and many interesting people I have met there.

珮綺，感謝妳在這六年來陪伴著我，努力著縮短台灣與美國的距離，也感謝妳一路上支持我從一開始帶領我體會我們身處的宇宙，到六年來的遠距離，以及我們未知的未來。感謝爸媽，從小讓我能夠自由的追尋夢想。另外還有六年來一起在Austin生活的朋友們，Patrick、王董、奕寬、Andy、Benny、Wei-Jin、Johnny還有許多的你們，讓六年異鄉生活充滿了回憶。

The Three-dimensional Structure and Kinematics of Protostellar Envelopes

by

Yao-Lun Yang, Ph.D.
The University of Texas at Austin, 2019

SUPERVISORS: Neal J. Evans II and Stella S. R. Offner

Star formation is one of the key process that drives the evolution of galaxies and planetary systems. Understanding the formation and evolution of protostellar systems that would eventually form Sun-like stars not only provides insights on the origin of our solar system, but also constrains the properties of planetary systems similar to our solar system. The observations at far-infrared and submillimeter wavelengths using *Herschel* and ALMA, best characterize the youngest protostars, where disks are still small or not yet formed. Together with 3D radiative transfer calculations, we have begun to constrain the complex structure and kinematics of the protostellar envelopes, and eventually probe the initial conditions of disk formation.

In this dissertation, I present a spectroscopy archive of young protostars observed by *Herschel*, the CDF archive, to characterize the observational signatures of embedded protostars, the stage soon after the formation of the protostars. The full spectra of protostars from 50–670 μm reveal a forest of molecular and atomic lines, probing the warm protostellar envelope heated by the central protostars and outflows. I characterize the spectral energy distributions of 27 embedded protostars, and analyze the correlations of the molecular and atomic emission. Moreover, I focus on the CO rotational emission from $J_{\rm up} = 4$ to 43 to constrain the origins of CO emission. A statistical analysis shows that the fitted CO rotational temperatures form two distinct populations around 100 K and 350 K, consistent with the proposed origins of CO from entrained outflows and shocked gas. To quantitatively analyze the outflow morphology seen from the CO emission, I developed a method of using normalized azimuthal flux profile to quantify the bipolarity of the CO emission, indicating that

the bipolarity extent decreases in higher-J CO transitions.

With a well-calibrated dataset, I focus on the structure of the envelope surrounding the embedded protostars and the mass transfer occurred in the envelope. I use BHR 71 as the test-bed for modeling the structure of envelope and the infall kinematics constrained by the continuum spectral energy distribution consist of *Herschel* and *Spitzer* spectra and the recently-acquired ALMA observations, respectively. I successfully modeled the continuum SED of BHR 71 with a slowly rotating infalling envelope which shows an "inside-out" collapse. I simulate the synthetic observations with a 3D continuum radiative transfer pipeline using the publicly-available package, HYPERION. The model includes not only the envelope but also bipolar cavities and a disk defined by the centrifugal radius of the envelope. I demonstrate a method for finding the best-fitting model by comparing with the SED as well as the photometric images from *Herschel* and *Spitzer*. The best-fitting model suggests an upper limit of 36000 years for the age since the collapse began and an inclination angle of 50°.

Understanding the evolution of infall requires direct measurements of infall. Thus, I use ALMA to observe optically-thick molecular emission to exclusively probe the line-of-sight velocity structure toward protostars, minimizing the unrelated kinematics. The colder opaque gas infalling in front of a bright continuum source results in a red-shifted absorption against the continuum, which is an unambiguous signature of infall. The ALMA observation of BHR 71 shows a clear infall signature from the emission of HCO^+ $J = 4 \rightarrow 3$ and HCN $J = 4 \rightarrow 3$ lines. I also observe CS $J = 7 \rightarrow 6$ and $H^{13}CN$ $J = 4 \rightarrow 3$ lines, which show red-shifted self-absorption along with a double-peaked profile. I calculated the synthetic infall profile of the HCO^+ line using the previously constrained envelope model to unveil the infall kinematics. I extend the 3D radiative transfer pipeline for molecular emission and the absorption against the continuum using another publicly available package, LIME, and a customized ray-tracing package, LIME-AID. I construct a parameterized abundance profile for modeling the observations of HCO^+, HCN, CS, and $H^{13}CN$. Together with the infall kinematics from the envelope model, I iterate the abundance profiles and ages to find the best-fitting models for each lines, which suggests a younger envelope at 15000 years.

While the optically-thick transitions constrain the infall, the rich spectra of BHR 71 reveal a complex chemistry at the central ∼100 AU of BHR 71. I identified 12 species of complex organic molecules (COMs) from the same observation that probes infall,

suggesting that BHR 71 is a "hot corino." The emission of $^{13}CH_3OH$ and CH_3OCHO show significant velocity gradients along the midplane of the envelope. A rotating infall ring conserving in angular momentum agrees with the morphology of the position-velocity diagrams, suggesting a specific angular momentum of 10^{20} cm^2 s^{-1} and a centrifugal barrier of 14 au.

Contents

List of Tables

List of Figures

Chapter One: Introduction

The formation and evolution of stars drive the evolution of galaxies. The mass distribution of newly formed stars, also known as the initial mass function (IMF), affects how we understand the galactic structure and evolution as well as the production of heavy elements (Offner et al., 2014). The star formation process also drives feedback to the environment via radiation (Bate, 2009; Offner et al., 2009; Urban et al., 2010), outflows/jets (Wang et al., 2010), and supernovae (Li & Nakamura, 2006), affecting future generations of stars (Offner & Chaban, 2017). Star formation converts mass from parsec scales down to stellar scale, increasing the density by 21 orders of magnitude (Evans, 1999b). Once the mass concentrates, protostars form along with the development of protoplanetary disks, followed by the formation of planets. The mass assembly of protostars determines the properties of their disks and the initial condition of planet formation (Li et al., 2014). Eventually, planetary systems like our solar system may form. Therefore, constraining the physical processes that govern the course of star formation is crucial to understanding the origins of our solar system as well as astronomical sources ranging from planets to galaxies.

Beginning with giant molecular clouds, gravity overcomes the turbulence of gas at small scale, gradually accumulating mass into compact regions, called dense cores, with a typical density of 10^4–10^5 cm^{-3} (Ward-Thompson et al., 2007; André et al., 2014). However, not all dense cores eventually form stars. Only when gravity dominates over other sources of pressure support, the collapse of dense cores begins, resulting in the formation of Sun-like stars.

Research about star formation has been one of the most important fields of astrophysics. However, the mass transfers from clouds to cores and from cores to protostars occur in low temperature environments that are often highly obscured at optical wavelengths by dust. Therefore, the study of star formation began with the late stages of star formation, which are visible at optical wavelengths. In the past few decades, the advance of infrared and radio astronomy has enabled the research that probes earlier stages of star formation. Observations have been surveying the properties of nearby molecular clouds that host numerous sites of star formation (e.g. Evans et al., 2009a; Dunham et al., 2015), and begin to constrain the occurrence rate

of protoplanetary disks and their properties (Tobin et al., 2016; Segura-Cox et al., 2018). Still, the sources in the stage right after the initial collapse of dense cores emit mostly at far-infrared wavelengths (15 μm to 1 mm) and peak at $\sim$100 μm at which only few observation had been done before the launch of the *Herschel Space Observatory* (Pilbratt et al., 2010). Moreover, the sensitivity and spatial resolution of observations at submillimeter wavelengths are greatly improved since the operation of Acatama Large Millimeter/submillimeter Array (ALMA). In this dissertation, I present studies on the sources in the early stage of star formation using far-infrared and submillimeter observations from *Herschel* and ALMA.

1.1 The Early Stage of Star Formation: The *Herschel* View

The evolution from dense cores to protostars is a hydrodynamical process involving gravity, shocks, turbulence, rotation, magnetic field, and outflows. While many theoretical models have attempted to characterize the formation and evolution of dense cores, a definitive answer has not yet converged and been confirmed by observations. The properties of protostars largely depend on the processes at the early stage of star formation before the surrounding envelope dissipates (Gong & Ostriker, 2009). Because the surrounding envelope embeds the forming protostar, the protostellar systems at its early stage is referred to as embedded protostars. The mass transfer occurs most actively during this embedded phase as the collapse of envelopes transports mass from $\sim$0.1 pc scale to $\sim$100 au scale. After the dissipation of the envelope, the protoplanetary disk becomes the only mass reservoir for the growth of protostars; however, the typical mass of the disk is only 1–10% of $M_\star$ after the embedded phase (Li et al., 2014), making the growth of protostar at the late stage insignificant. Thus, understanding the processes that regulate the early evolution of star formation is essential to determine the outcome of star formation.

Embedded protostars emit mostly at far-infrared wavelengths because of the low temperature of their surrounding envelopes. Prior to the launch of *Herschel*, the observations of embedded protostars were limited to a few bands of photometry from the satellites in space and ground-based submillimeter observations of the molecules emission from low energy rotational transitions with single-dish antennas (e.g. Shirley

et al., 2002; Enoch et al., 2006; Evans et al., 2009a). First previewed by the *Infrared Space Observatory*, the launch of *Spitzer Space Telescope* provides a nearly complete identification of protostars in the nearby clouds; however, the structures around those protostars remains largely unknown due to the low temperature. Therefore, the observational signatures of the structures around the embedded protostars were far from complete at the peak of their emission. *Herschel* enabled, for the first time, complete spectral scans at far-infrared wavelengths, probing the dense material that actively feeds the growth of protostars.

Mass loss also occurs at the embedded phase of star formation. Outflows are a ubiquitous signature of embedded protostars. Even without any systematic initial rotation, gas particles carry trace amount of angular momentum. If the angular momentum is conserved throughout the collapse of envelopes, the rotational velocity would increase by orders of magnitude, preventing any further infall. Thus, the processes of star formation must involve ways to remove angular momentum from protostellar systems. Outflows are the main mechanism to remove angular momentum by ejecting high angular momentum material along the rotation axis. Outflows not only regulate the final mass of protostars but also interact with the embedding envelope, modifying the geometry of the envelope and depositing thermal and mechanical energy into the envelope. While observations at radio wavelengths (λ >1 mm) best identify the swept-up material in outflows, only far-infrared observations can probe the outflowing material that is currently interacting with the envelope due to its elevated temperature. The shocks arisen from the interaction between outflows and envelopes produce a rich spectra of highly excited rotational molecular emission as well as atomic lines at far-infrared wavelengths.

Given these points, *Herschel* observations are the best dataset to characterize the embedded protostars. *Herschel* has instruments for both spectroscopy and photometry, providing a complete spectrum at far-infrared wavelengths as well as deep images. As part of this dissertation, I present *Herschel* observations of a sample of embedded protostars to address the following questions.

- How can we best identify and classify embedded protostars from their spectral energy distributions?
- How do the outflows feedback the protostellar envelopes probed by the emission lines in far-infrared wavelengths.

- Where do the outflows most actively interact with the envelopes seen at far-infrared wavelengths?

1.2 The Structure of Infalling Envelopes

The dynamical evolution of the collapsing envelope governs the course of star formation. The balance between gravity and pressure supports from thermal motion, turbulence, and magnetic field determines the dynamical evolution of dense cores. Theoretical models show two types of infall in dense cores, the Larson-Penston (hereafter LP) "outside-in" collapse (Larson, 1969a; Penston, 1969) and the "inside-out" collapse (Shu, 1977a; Cassen & Moosman, 1981; Terebey et al., 1984a). While the transition from one type of collapse to the other has not been confirmed by observations, several simulations show the LP collapse typically occurs for the formation of dense cores, and then the collapse becomes "inside-out." Gong & Ostriker (2009) present an 1D model of protostar formation, which suggests that the early phase of star formation proceeds in four stages, core building, the "outside-in" collapse, the "inside-out" collapse, and fully free-fall. Initially, high-density gas arises from the collisions within a supersonic turbulent medium, which will undergo a slow gravitational contraction process as the high-density gas remains gravitationally subcritical. The dense core will become gravitationally supercritical when it becomes more massive, and starts to collapse. Such collapse starts at the edge of the core, where the dense region exceeds the critical radius that can be supported by pressures. Thus, the outermost layer begins to collapse and the wave of collapse extends inward, similar to the LP collapse. Subsequently, the density profile becomes centrally concentrated, approaching the density profile predicted by hydrostatic Bonner-Ebert spheres (Ebert, 1955; Bonnor, 1956). The central condensation of mass eventually becomes a singularity when the density increases to infinity, indicating the formation of the protostar. Then, the collapse becomes free-fall starting from the immediate region near the protostar, removing the pressure support for the adjacent outer layer of gas to propagate the wave of collapse outward. Therefore, an "inside-out" collapse begins, similar to the calculation by Shu (1977a), which starts to collapse from an isothermal sphere. Finally, the entire envelope becomes free-fall. Characterizing and confirming these evolutionary stages is the key for understanding the evolution from dense cores to

protostars and determines the observational properties of the embedding envelopes.

Embedded protostars emit primarily at far-infrared wavelengths, making the *Herschel* observations the best dataset to constrain the properties of the embedding envelope and further probe the collapse of the envelope. The spectral energy distribution (SED) is a simple but powerful observable to characterize the protostellar envelope. The continuum spectrum represents the density and temperature profiles of the envelope. In Chapter 2, I present a well-calibrated *Herschel* dataset of embedded protostars. This dataset has the first continuous spectral coverage at far-infrared wavelengths for embedded protostars, making it the ideal data to constrain the properties of the collapsing envelope.

The density profile of the embedding envelope evolves as a function of time since the collapse began. In the simplified case where only gravity is considered, gas would free-fall toward the central protostar once the pressure support disappears as the gas closer to the center collapses. Because the infall proceeds "inside-out," the outer envelope remains close to stable until the wave of infall arrives. Thus, there are two relevant regions in the embedding envelope, the infalling envelope and the quasi-static envelope. The free-falling gas leads to a density profile $\rho(r) \propto r^{-3/2}$ in the regions that are fully free-fall and reach dynamical equilibrium. The simplest quasi-static envelope is an isothermal envelope, whose density profile $\rho(r)$ is proportional to r^{-2}. The boundary between these two regions in the infalling envelope represents the progress of infall. In reality, rotation and magnetic field modify the simple picture of the infall process (e.g. Li et al., 2014; Zhao et al., 2018). The centrifugal force from the rotation prevents gas infalling onto the central protostar, but instead it falls to a certain radius, which eventually forms the protoplanetary disk. The infall also pinches the magnetic field lines toward the central protostar, while the rotation winds the field lines. The magnetic field that mis-aligns with the gas motion exerts torques to the infalling gas, reducing the rotation speed. Many magnetohydrodynamics (MHD) simulations have attempted to quantify the infall process by considering all dominant physics (e.g. Gong & Ostriker, 2009; Li et al., 2014; Offner & Chaban, 2017); however, the model of the infalling envelope has not been conclusively constrained by observations.

While gas dynamics determine the density profile of the infalling envelope, dust distribution couples with the gas, making dust a tracer of gas. If the dust emission is optically thin, which is typically a valid assumption except for the inner envelope, the brightness distribution of the continuum probes the density profile of the infalling

envelope. Observations with single-dish data (e.g. James Clerk Maxwell Telescope, IRAM 30m Telescope, and Caltech Submillimeter Observatory) have successfully constrained the density profiles of the envelope at a resolution of 3000–6000 au (Shirley et al., 2002; Young & Evans, 2005). However, such resolution is insufficient to distinguish the boundary between the infalling envelope and the quasi-static envelope for the embedded protostars within 0.1 Myr of their initial collapse. Therefore, characterizing the embedding envelope requires high resolution observations at far-infrared and submillimeter wavelengths, which *Herschel* provides.

In this dissertation, I will present a research project in Chapter 3 that aims to characterize the structure of the infalling envelope using the recently available *Herschel* spectroscopy and photometry. This project focuses on an embedded protostar, BHR 71, selected from the *Herschel* survey of embedded protostars presented in Chapter 2. With 3D continuum radiative transfer calculations, I present how the *Herschel* continuum observation revises our understanding of the infalling envelope, and further explore the limitation of using dust emission to characterize the envelope. In reality, the outflow cavities significantly modify the structure of the envelopes, which is not only determined by infall but also rotation. The 3D radiative transfer calculations enable the characterization of the effects of outflow cavities and rotation to the observational signatures of embedded protostars. With both the SED and images, the observations constrain the envelope model in three dimensions, incorporating the effect of outflow cavities and the source orientation. I will address the following questions in this research.

- How do we use dust emission to constrain the structures of the infalling envelope?
- What is the structure of envelope for BHR 71?
- How does the outflow cavities affect the observed continuum spectrum?

1.3 The Kinematics of Infalling Envelopes

Gas kinematics determines the density structure of the infalling envelope. As previously mentioned, a broken power-law density profile can describe a simplified infalling envelope. The dust continuum infers the infall kinematics by constraining the

density distribution as the effects of the infall, but the assumption of the infall motion remains untested. Rotation and magnetic field become substantial at the high-density inner region, modifying the structure of the envelope. Therefore, understanding the infall process and its role in the transformation from dense cores to protostars requires direct measurements of the gas kinematics.

Molecular emission is the best tracer of gas kinematics for embedded protostars. Molecular species dominate the infalling envelope because of the low temperature and high density. The high collision rate makes the rotational transitions of those molecules easy to observe in far-infrared and submillimeter wavelengths. If the molecular emission is optically thin, the observed spectrum traces the gas kinematics along the entire line of sight. Different components of kinematics may contribute to the same velocity, which are indistinguishable from molecular spectra. Not only rotation and magnetic field disrupt the kinematics, which is what we want to measure, but also outflows as well as inclination effects can produce similar line profiles as that of the infall, confusing the interpretation. To isolate the signature of the infalling gas, one would either observe with higher spatial resolution to exclude the outflows from the telescope beam or target the spectral features that only trace the infall. Even with sufficiently high spatial resolution, the observations would inevitably capture the outflowing gas for any source with outflows that do not lie perfectly on the plane of sky. On the other hand, optically thick transitions and the emission of rare molecules that only exist at the warm inner envelope can provide unambiguous measurements of kinematics.

Cold gas absorbs the radiation from the background hot gas. For embedded protostars, hot gas comes from the inner envelope that has a higher infall velocity, while cold gas resides in the outer envelope, which has a slower infall. For a given molecular line, the cold gas only absorbs the emission at low velocity and the high velocity emission from the hot gas still reaches our telescopes. Thus, the kinematic signature of the absorption directly probes the kinematics of the cold gas. The choice of the molecular line (e.g. HCO^+ $J = 4 \rightarrow 3$) can further narrow the region traced by the absorption, which only occurs for the molecules at the lower state of the selected molecular transition (i.e. HCO^+ $J = 3$). By choosing a transition from a higher energy state, only the gas in a certain range of excitation temperatures will contribute to the absorption. Therefore, the observations of optically thick lines can distinctively probe the kinematics of a cold layer of gas in the line of sight.

In Chapter 4, I present the study of the infalling envelope of BHR 71 probed by the absorption features from the molecular lines that trace high density gas. In this study, I acquired ALMA observations of BHR 71 to measure the redshifted absorption from the infalling gas in the foreground of the central protostar. ALMA has the unprecedented spatial resolution that eliminates most of the contamination from outflows. Furthermore, the small beam can measure the continuum from the compact protostar and the absorption against the continuum due to the cold infalling gas. A line profile with a redshifted absorption that goes below the continuum directly probes the infalling gas in the envelope, which is an unambiguous signature of infall. In this project, I successfully detect the infall signatures in the envelope of BHR 71, and model the underlying kinematics to constrain the models of infall. This study addresses the following questions.

- How fast is the protostar growing, and where does the mass come from?
- What are the dominant processes that govern the collapse of the envelope, and what are the relevant spatial scales for those processes?

1.4 The Chemistry of Infalling Envelopes

The infall process not only governs the envelope structure but also controls the chemical evolution of the envelope. Being centrally heated by the protostar and the associated accretion, the temperature of the infalling envelope increases as the radius decreases, determined by absorption and emission of the dust. The infall process determines the thermal history of gas as it travels from the outer cold region to the inner warm region. Temperature controls the rate of chemical reactions, leading to the formation or destruction of certain molecular species. Simple molecules, such as H_2, CO, CH_4, start to form at low temperature, preferentially frozen onto the dust grains. While simple molecules form at low temperature via ion-molecule reactions, the formation of larger complex molecules remains inefficient. As the temperature increases to 20–40 K, larger radicals become mobilized on the dust grains to react with each other to form complex organic molecules (COMs). At the similar temperature, CO becomes abundant in the gas-phase due to thermal desorption, and further triggers the formation of other molecules, such as H_2O, HCO^+, HCN, and

CS. The grain-surface chemistry dominates the chemical evolution at low temperature. At ∼100 K, COMs start to be released from the dust grains, and the gas-phase chemistry becomes the dominant process. The time which gas spends at different temperature regimes controls the chemical evolution of the infall envelope. Since the infall process governs the thermal history of gas, the dynamical and chemical evolutions are therefore coupled.

Chemistry is a critical factor for interpreting molecular spectra. Beside the gas kinematics, the abundance profiles of the targeted molecules can significantly change the observed line profiles. Freeze-out is the most common feature in the molecular abundance. CO freeze-out limits the carbon in the gas-phase, reducing the abundances of other carbon-based molecules, such as HCN and HCO^+. Those freeze-out regions become invisible to our observations. Therefore, molecular abundance needs to be considered for modeling the gas kinematics with molecular spectra.

Life is a series of chemical reactions that consume organic molecules and generate energy. Those chemical reactions occur all the way throughout the formation of planetary systems before the earth formed. First discovered in massive star-forming regions, such as Sgr B2, COMs appear at different stages of star formation from prestellar cores to protoplanetary disks. The relation between the COMs at each stage remains unclear due to the small sample of unbiased line surveys. Whether the COMs observed in star-forming regions eventually reside in planetary systems is far from understood. Regulated by the dynamical evolution of the infalling envelope, the emission of COMs provides an independent probe to the evolution in the past. Moreover, COMs evaporate from the dust grains at a temperature $\gtrsim$100 K, which corresponds to ∼100 au for embedded protostars; therefore, the emission of the gas-phase COMs exclusively traces the kinematics at the inner 100 au, where the disk is forming or formed. In Chapter 4, I model the chemical abundance of the species that trace infall and identify the emission of COMs to address the following questions.

- What are the chemical abundance of the molecules that trace gas kinematics in the collapsing envelope?
- Do complex organic molecules exist in BHR 71?
- What are the gas kinematics at the inner 100 au of BHR 71?

This dissertation contains three studies (Chapter 2–4), starting from a survey of embedded protostars to characterize their envelope and outflows to the models of the infalling envelope of BHR 71 and the infall kinematics traced by molecular emission. I also present the first detection of COMs at BHR 71 in Chapter 4 as well as the implication to the infall kinematics at the disk-forming region. In Chapter 5, I summarize the properties of the infalling envelope and outflows learned from the observations by *Herschel* and ALMA together with 3D radiative transfer calculations, and discuss potential future works.

Chapter Two: CO in Protostars (COPS): *Herschel*-SPIRE Spectroscopy of Embedded Protostars[1]

2.1 Introduction

Large samples of protostars in relatively nearby ($d \leq 300$ pc) clouds have been developed through recent surveys with the *Spitzer* Space Telescope (e.g. Evans et al., 2009b; Dunham et al., 2015) as well as the *Herschel* Space Observatory (e.g. André et al., 2010; van Dishoeck et al., 2011; Kirk et al., 2013; Green et al., 2013a; Manoj et al., 2016; Mottram et al., 2017), along with ground-based surveys (e.g. Jørgensen et al., 2009). Over recent decades, infrared and submillimeter studies of such samples have allowed significant advances in our understanding of the properties, structure and evolution of such protostars.

ISO/LWS spanned the 20–200 μm spectral region and was well-suited to study the warm (T $>$ 100 K) region of protostellar envelopes, distinguishable from the ambient cloud typically probed in ground-based millimeter studies. ISO-LWS detected gas phase H_2O, high-J CO rotational transitions, and fine structure emission lines toward protostars and related structures (e.g., Lorenzetti et al., 1999; Giannini et al., 1999; Ceccarelli et al., 1999; Lorenzetti et al., 2000; Giannini et al., 2001; Nisini et al., 2002). These lines were considered to originate from the outflows (Giannini et al., 1999, 2001; Nisini et al., 2002), or the inner envelope (Ceccarelli et al., 1999); however, recent observations of *Herschel* Space Observatory clearly show that these lines are dominated by outflow activity (Kristensen et al., 2010, 2012b; Mottram et al., 2014b).

Herschel was an European Space Agency (ESA) space-based far-infrared/submillimeter telescope with a 3.5-meter primary mirror (Pilbratt et al., 2010). For the first time, *Herschel*-SPIRE (Spectral and Photometric Imaging REceiver, 194–670 μm; Griffin et al., 2010) enabled low resolution spectroscopy of the entire submillimeter domain.

[1]This chapter has been published on The Astrophysical Journal 860, 174. The author is the lead author of this published article, contributing to the data reduction, data analyses, and the preparation of the manuscript.

These wavelengths are sensitive to dust continuum, and provide access to the full suite of mid-J CO, HCO^+, ^{13}CO and several H_2O emission lines.

In the previous analysis with data from the Dust, Gas, and Ice In Time *Herschel* Key Program (DIGIT), we used the PACS spectrograph (50–200 μm, Poglitsch et al. 2010) to characterize a sample of well-studied protostars, selected from the c2d sample, including both Class 0 and Class I objects (Green et al., 2013a). Similar studies also used PACS data to characterize the properties of protostars in different regions with data from the Water in Star-forming Regions with Herschel (WISH) Key Program (Karska et al., 2013a) and the Herschel Orion Protostar Survey (HOPS) Key Program (Manoj et al., 2013, 2016). The analysis of the combined PACS and SPIRE spectra was also presented for specific sources (e.g. Serpens SMM1, Goicoechea et al. 2012).

The full *Herschel* bands contain numerous pure rotational transitions of CO, as well as lines of H_2O, OH, HCO^+, and atomic lines ([C I], [C II], [N II], and [O I]), all potential tracers of gas content and properties. *Herschel* enabled access to the CO ladder toward higher energy levels (J_{up}=4–48), providing an opportunity to constrain the origin of CO emission entirely. At least two rotational temperatures are typically found with the PACS spectra toward embedded protostars (e.g. Green et al., 2013a; Manoj et al., 2013; Karska et al., 2013a). The SPIRE spectra reveal the colder CO component, which has a different physical origin than the one for the higher-J CO lines, suggested from velocity-resolved observations (see Kristensen et al. 2017b). Visser et al. (2012a) argued that C-type shocks dominate the high-J CO lines at embedded sources with the the velocity-unresolved PACS data, while Yıldız et al. (2012) found the signature of shocked gas in the broad line profiles in the CO $J = 6 \rightarrow 5$ line, suggesting a different origin for the higher-J CO lines compared to the CO lines that are typically accessed from the ground ($J_{up} \leq 3$). Kristensen et al. (2017b), who have a similar source list, showed that the CO $J = 16 \rightarrow 15$ line contains a broad component at the source velocity and a narrow component offsetting from the source velocity.

The emission of water has a similar line profile to the broad component found in CO $J = 3 \rightarrow 2$ and $J = 10 \rightarrow 9$ lines (Kristensen et al., 2012b; Mottram et al., 2014b, 2017). Both the line profiles and spatial extent of water emission suggest its close relation to outflows (Santangelo et al., 2012a; Vasta et al., 2012a; Kristensen et al., 2012b; Mottram et al., 2014b, 2017). Detailed modelings of water emission indicate

a similar shock origin to the high-J CO lines (Karska et al. 2014a; Manoj et al. 2013, Karska et al. to be accepted) Thus, these lines make excellent diagnostics of opacity, density, temperature, and shock velocities (e.g., Kaufman & Neufeld, 1996; Flower & Pineau Des Forêts, 2010; Neufeld, 2012) of the gas surrounding these systems (Kristensen et al., 2013; Mottram et al., 2014b).

In this work, we present *Herschel*-SPIRE observations from the "CO in Protostars-SPIRE" (COPS-SPIRE) survey (PI: J. Green), of 27 protostars taken from the "DIGIT" and "WISH" samples. In Section 2, we describe the sample, and provide an archive of 1–1000 μm spectral energy distributions (SEDs), combining the *Spitzer*-IRS, PACS, and SPIRE spectra, along with the description of the data processing pipeline. In Section 3, we present the SEDs and the line fitting results, as well as the effect of emission lines on photometry. We characterize the molecular and atomic lines with a customized line fitting pipeline previously optimized for *Herschel* spectra, and provide the detection statistics and limits. In Section 4, we derive the optical depth of CO and discuss the uncertainties. We perform rotational diagram analysis of CO and HCO^+. Furthermore, we characterize the correlations of each pair of lines detected in our sample, and discuss the origin of CO gas. In Section 5, we consider the classification system in the context of the origin of the CO emission. We also compare our analyses to those of FU Orionis objects, T Tauri stars, and Herbig Ae/Be stars (Green et al., 2013b; Fedele et al., 2013a). We summarize our conclusions in Section 6.

2.2 Observations

2.2.1 The Sample

Our sample of 27 "COPS" protostars contains 20 sources overlapping with the DIGIT (PI: N. Evans; Green et al. 2013a; Fedele et al. 2013a; Meeus et al. 2013; Lee et al. 2014) and 17 overlapping with the WISH (PI: E. van Dischoek; van Dishoeck et al. 2011; see also Nisini et al. 2010; Kristensen et al. 2012b; Wampfler et al. 2013; Karska et al. 2013a; San José-García et al. 2013; Yıldız et al. 2013) *Herschel* Key programs. The sources were originally chosen to be well-studied (e.g. Jørgensen et al., 2002a, 2004a, 2007), nearby (within 450 pc), and spanning a range of luminosities. The Class 0 protostars were originally chosen from the sample of Andre

et al. (2000). The selected protostars have a wide range of bolometric temperatures (33.2 K–592.0 K) and bolometric luminosities (0.33 $L_\odot$–70.4 $L_\odot$). Additionally, the sources were carefully chosen to have well-studied *Spitzer* data to complement our observations (Evans et al., 2009b; Dunham et al., 2015), and drawn from both larger clouds and isolated environments (see Column 2 in Table 2.1). The data for all sources were reprocessed with identical techniques detailed in the next section. The full list of sources appears by region in Table 2.1, and by observation date in Table 2.2. We have updated the distances of several sources based on the recent studies (see the references in Table 2.1). In particular, we update the distance of L1551 IRS5 to 147 pc due to its proximity to T Tau and XZ Tau, for which the distance is measured by Galli et al. (in prep.). The characteristics of the SEDs (e.g. bolometric luminosity and temperature) are updated with the *Herschel* data presented in this study (Table 2.3). A nearly identical sample was observed in CO $J = 16 \rightarrow 15$ with HIFI (PI: L. Kristensen) summarized in Kristensen et al. (2017b).

Table 2.1: Source List

Source	Cloud	Dist. (pc)	RA (J2000)	Dec (J2000)	Program	Ref.	Dist. Ref.
IRAS 03245+3002	Per	235	03h27m39.1s	+30d13m03.1s	D	c2d	1
L1455 IRS3	Per	250	03h28m00.4s	+30d08m01.3s	D	c2d	2,3,4,5
IRAS 03301+3111	Per	250	03h33m12.8s	+31d21m24.2s	D	c2d	2,3,4,5
B1-a	Per	250	03h33m16.7s	+31d07m55.2s	D	c2d	2,3,4,5
B1-c	Per	250	03h33m17.9s	+31d09m31.9s	D	c2d	2,3,4,5
L1551 IRS5	Tau	147	04h31m34.1s	+18d08m04.9s	D/W	2MASS	6
TMR 1	Tau	140	04h39m13.9s	+25d53m20.6s	D/W	H	7
TMC 1A	Tau	140	04h39m35.0s	+25d41m45.5s	D/W	H	7
TMC 1	Tau	140	04h41m12.7s	+25d46m35.9s	D/W	A	7
HH 46	Core	450	08h25m43.9s	–51d00m36.0s	W	vD	8,9,10
Ced110 IRS4	ChaI	150	11h06m47.0s	–77d22m32.4s	W	vD	11,12,13
BHR 71	Core	200	12h01m36.3s	–65d08m53.0s	D/W	c2d	14,15
DK Cha	ChaII	178	12h53m17.2s	–77d07m10.7s	D/W	c2d	11
IRAS 15398−3359	Core	130	15h43m01.3s	–34d09m15.0s	W	vD	16,17
GSS 30 IRS1	Oph	137	16h26m21.4s	–24d23m04.3s	D/W	c2d	18
VLA 1623−243	Oph	137	16h26m26.4s	–24d24m30.0s	D	c2d	18
WL 12	Oph	137	16h26m44.2s	–24d34m48.4s	D	c2d	18
RNO 91	Oph	130	16h34m29.3s	–15d47m01.4s	W	vD	19
L483	Aqu	200	18h17m29.9s	–04d39m39.5s	W	vD	20
RCrA IRS5A	CrA	130	19h01m48.1s	–36d57m22.7s	D/W	N	21,22,23
HH 100	CrA	130	19h01m49.1s	–36d58m16.0s	W	vD	21,22,23
RCrA IRS7C	CrA	130	19h01m55.3s	–36d57m17.0s	D	L	21,22,23
RCrA IRS7B	CrA	130	19h01m56.4s	–36d57m28.3s	D	L	21,22,23
L723 MM	Core	300	19h17m53.7s	+19d12m20.0s	W	vD	24
B335	Core	106	19h37m00.9s	+07d34m09.7s	D/W	PROSAC	25
L1157	Core	325	20h39m06.3s	+68d02m16.0s	D/W	PROSAC	26
L1014	Core	200	21h24m07.5s	+49d59m09.0s	D	Y	27,28

List of protostellar sources discussed in this work by region, sorted by RA. Coordinate reference code: D = Dunham et al. (2006); Y = Young et al. (2004a); L = Lindberg et al. (2011); N = Nisini et al. (2005); H = Haisch et al. (2004); A = Apai et al. (2005); B = Brinch et al. (2007); c2d = Evans et al. (2009b); PROSAC = Jørgensen et al. (2009); vD = van Dishoeck et al. (2011).

List of references for distance: 1 = Hirota et al. (2011); 2 = Černis (1993); 3 = Belikov et al. (2002); 4 = Černis & Straižys (2003); 5 = Enoch et al. (2006); 6 = Galli et al. (in prep.); 7 = Kenyon et al. (1994); 8 = Brandt et al. (1971); 9 = Reynolds (1976); 10 = Eggen (1980); 11 = Whittet et al. (1997); 12 = Bertout et al. (1999); 13 = Luhman (2008); 14 = Seidensticker & Schmidt-Kaler (1989a); 15 = Straizys et al. (1994); 16 = Knude & Hog (1998a); 17 = van Dishoeck et al. (2011); 18 = Ortiz-León et al. (2017); 19 = de Geus et al. (1990) 20 = Dame & Thaddeus (1985); 21 = Casey et al. (1998); 22 = de Zeeuw et al. (1999); 23 = Neuhäuser & Forbrich (2008); 24 = Goldsmith et al. (1984); 25 = Olofsson et al. (2009); 26 = Straižys et al. (1992); 27 = Young et al. (2004a); 28 = Maheswar et al. (2004).

Table 2.2: Observing Log

Source	Other Name	OBSID	Date Obs.	PACS 1D aperture[1]	Notes
IRAS 03245+3002	L1455 IRS1	1342249053	04 Aug 2012	31.8	
L1455 IRS3		1342249474	13 Aug 2012	A	
IRAS 03301+3111	Perseus Bolo76	1342249477	13 Aug 2012	A	
B1-a		1342249475	13 Aug 2012	A	
B1-c		1342249476	13 Aug 2012	36.8	
L1551 IRS5		1342249470	12 Aug 2012	24.8	
TMR 1	IRAS 04361+2547	1342250509	02 Sep 2012	51.8	
TMC 1A	IRAS 04362+2535	1342250510	02 Sep 2012	41.8	
TMC 1	IRAS 04381+2540	1342250512	02 Sep 2012	A	
HH 46		1342245084	28 Apr 2012	N/A	linescan
Ced110 IRS4		1342248246	17 Jul 2012	N/A	linescan
BHR 71		1342248249	17 Jul 2012	29.8	
DK Cha	IRAS 12496–7650	1342254037	28 Oct 2012	31.8	linescan
IRAS 15398–3359	B228	1342250515	02 Sep 2012	N/A	
GSS 30 IRS1		1342251286	23 Sep 2012	A	
VLA 1623−243		1342251287	23 Sep 2012	41.8	
WL 12		1342251290	23 Sep 2012	A	
RNO 91		1342251285	23 Sep 2012	N/A	linescan
L483	IRAS 18140–0440	1342253649	19 Oct 2012	N/A	linescan
RCrA IRS5A		1342253646	19 Oct 2012	A	
HH 100		1342252897	07 Oct 2012	N/A	mis-pointed
RCrA IRS7C		1342242621	11 Mar 2012	41.8	mult. sources
RCrA IRS7B		1342242620	11 Mar 2012	41.8	mult. sources
L723 MM		1342245094	28 Apr 2012	N/A	linescan
B335		1342253652	19 Oct 2012	24.8	
L1157		1342247625	02 Jul 2012	21.8	
L1014		1342245857	16 May 2012	A	

Observations log for protostellar sources discussed in this work. The "mode" indicates the spatial coverage of the observation.
[1]The unit is arcsec. If all 25 PACS spaxels are used for extracting 1D spectrum, it will be denoted as "A," and "N/A" indicates that no PACS 1D spectrum is extracted.

2.2.2 Data Processing Pipeline

The data processing pipeline is based on the method described in (Green et al., 2016a, hereafter the CDF archive) with the modifications presented in Yang et al. (2017b). The major differences between the data presented here and the CDF archive are the PACS 1D spectra and the version of Herschel Interactive Processing Environment (HIPE, Ott 2010). The PACS 1D spectra were extracted from the central 3×3 spaxels for the CDF archive, whereas we sum over the emission within a circular aperture determined from the flux agreement with the SPIRE 1D spectra to extract the PACS 1D spectra. We also adopt the same method shown in Yang et al. (2017b) to choose the apertures for measuring photometry that is consistent with the spectroscopy. The detailed procedures of the reduction are described in the following sections.

2.2.2.1 SPIRE

The SPIRE-FTS (Fourier Transform Spectrometer) data were taken in a single pointing with sparse image sampling in 1 hr of integration time per source. The spectra were taken with the high resolution (HR) mode and are divided into two orders covering the spectral ranges of 194 – 325 μm ("SSW"; Spectrograph Short Wavelengths) and 320 – 690 μm ("SLW"; Spectrograph Long Wavelengths), with a spectral resolution element $\Delta\nu$ of 2.16 GHz after the apodization ($\lambda/\Delta\lambda \sim$ 200–670, or $\Delta v \sim$ 400–1500 km s^{-1}, Griffin et al. 2010). The SPIRE-FTS has a field-of-view of 180″×180″, with spatial pixel (spaxel) separations of 33″ and 51″ for SSW and SLW, respectively. The SPIRE beam size ranges from 17″–40″, equivalent to physical sizes of ∼3200–7600 AU at the mean distance of the COPS sources (189 pc), comparable to the size of a typical core (Ward-Thompson et al., 2007) but smaller than the typical length of an outflow (Arce et al., 2007; Yıldız et al., 2015). The SPIRE beam size increases with wavelength. But the beam size also jumps at 300 μm (Makiwa et al., 2013) due to the complex modes of waveguide at the short wavelength end of the SLW module. SPIRE used an onboard calibration source for flux calibration, resulting in $< 6\%$ calibration uncertainty updated in Swinyard et al. (2014).

Each module was reduced separately within HIPE version 14.0.3446 with the SPIRE calibration dataset `spire_cal_14_3`. We applied an apodization of 1.5, which reduces the resolution by a factor of 1.5 to 2.16 GHz but suppresses baseline variation.

The SPIRE data were extracted using the "extended source" calibration pipeline, as this produced a smoother continuum between modules, better S/N, and fewer spectral artifacts than the "point source" pipeline. The extracted SPIRE data contain the spectra of each spaxel from two modules, which is used for analyzing the spatial distribution of spectral lines in this study. We further extracted the 1D spectrum of each source with the SemiExtendedSourceCorrector (SECT) script from HIPE version 14.0.3446, using SPIRE calibration dataset `spire_cal_14_3`. Most of the COPS sources are partially resolved, therefore neither a standard point source extraction nor an extended source extraction is suitable to extract a single spectrum of each source, which would result in a mismatch between the spectra of the SLW and SSW modules. This script fits a "source size" that produces a smooth spectrum, and then normalizes the 1D spectrum with a given aperture (Wu et al., 2013). We adopted the prescription developed by Makiwa et al. (2016a) to extract the 1D spectrum of the entire source. The SECT script failed to produce the 1D spectrum for HH 100, which is mis-pointed and contaminated by nearby RCrA IRS7C. No background subtraction was performed (unlike, for example in van der Wiel et al. 2014, who examined point-like disk sources and subtracted non-central pixels from the center pixel), whereas, for PACS, a spectrum was taken at off-source position for the background subtraction. Thus, possible contribution from extended background emission should be considered when interpreting the spectra. We note cases where extended emission was seen in Section 2.3.5.

The methodology of the SECT script provides the calibrated spectrum that best describes the emission from entire source. When comparing the photometry with the SECT-corrected spectra, we find a good agreement when we use the convolution of the fitted source size and the beam sizes of SPIRE as the apertures. The convolved aperture is larger at long wavelengths due to the beam profile of SPIRE. Therefore, the SECT-corrected spectrum has more emission in the longer wavelengths compared to the spectrum extracted with a single aperture, resulting in shallower slopes at long wavelengths.

The observed source size is a strong function of wavelength for embedded protostars arises from cooler dust that is farther from the source. To characterize the entire source, it is necessary to use larger apertures at longer wavelengths. Therefore, we argue that using the SPIRE spectra with semi-extended source correction to calibrate the extraction of PACS 1D spectra best represents the emission from entire

protostars, which yielding realistic estimates of $L_{\rm bol}$ and $T_{\rm bol}$.

2.2.2.2 PACS

We also collect and reduce PACS spectroscopy and photometry data from the CDF archive for comparison. Of the 27 COPS sources, 21 sources have PACS rangescan spectroscopy from the DIGIT program, 16 sources have PACS linescan spectroscopy from the WISH program, and all have photometry available from the Herschel Science Archive (HSA) except for HH 46. The PACS reduction was updated with HIPE version 14.0.3446 (calibration version 72), using the Telescope Background Correction algorithm, including a PSF correction and a correction for telescope jitter (changes in pointing offset during the observation), when possible, to produce the best flux calibration. The jitter correction was only applicable to rangescans (linescans are too narrow to properly determine the source centroid), and thus for the 6 sources where only linescan data is available, we use the reductions from Karska et al. (2013a). We only consider the linescan data for calculating the properties of the SED. Note that HH 100 was not observed with PACS spectroscopy.

The PACS 1D spectra are extracted using the method described in Yang et al. (2017b), which is different from the one used in the CDF archive. This method calculates the total flux density within a circular aperture. Using the same aperture size for all sources results in flux mismatches between PACS and SPIRE for several sources. To provide useful PACS products for comparison, we modify the aperture size used for the PACS data of each source until the PACS and SPIRE spectra agree within 5% of the flux density at the conjunction of PACS and SPIRE, where we take the median flux from 185–190 μm, and 195–200 μm, respectively. However, five sources have PACS and SPIRE spectra that disagree by more than 5% even if all PACS spaxels are included (see Section 2.3.5). A direct comparison in the overlapping wavelengths is prohibited due to the increase of noise toward the end of band. The fitted aperture sizes are listed in Table 2.2.

2.3 Results

2.3.1 Source Confusion in the RCrA region

Our data processing pipeline successfully reduced all sources, except for HH 100, where the reduction of the SPIRE 1D spectrum failed due to the contamination from RCrA IRS7C. We found that HH 100 was mis-pointed by about 30″ toward the contaminating source, confusing the emission from HH 100; therefore, we exclude HH 100 from our analysis. Furthermore, our SPIRE observation does not completely resolve some sources in the RCrA region, such as RCrA IRS7B and RCrA IRS7C. The separation between two sources is only 17″. Thus, we adopt the bolometric temperature and luminosity from Lindberg et al. (2014) for RCrA IRS7B and RCrA IRS7C, where the PACS data are carefully deconvolved. We exclude these two sources from most of the analyses, and in few cases, we use the spectrum of RCrA IRS7C as the combined spectrum of both sources, noted as RCrA IRS7B/C. In the end, we present the data of 25 protostars including RCrA IRS7B/C.

2.3.2 Comparing Spectra with Photometry

Our data processing pipeline produces flux-calibrated spectra, which typically match photometric observations, as well as line-free continua for SEDs. As a cross-check on the flux calibration of our method, we collected archival PACS and SPIRE imaging from the Herschel Science Archive. We list the OBSIDs used for the photometry in Appendix A.1. The photometry was then extracted with HIPE version 14.0.3446 using DAOPHOT (Stetson, 1987), from a top-hat circular aperture. For SPIRE, the apertures were chosen to be the convolved size of the source size fitted by SECT and the beam sizes at 250, 350, and 500 μm (18.4″, 25.2″, and 36.7″). For PACS, we adopted the aperture used for extracting the 1D spectra (see Section 2.2.2.2). We apply color corrections to SPIRE photometry with the power law index fitted from spectra. The color correction at PACS 160 μm is 3–4% without any systematic increase or decrease. Due to the increasing contribution of hot dust at shorter wavelengths and the gap of spectra at 100 μm, we add an uncertainty of 3% to PACS photometry instead of applying color correction directly.

The photometry, both PACS and SPIRE, was typically observed in two or more OBSIDs, which we averaged together and used the standard deviation of the obser-

vations as its uncertainty (typically 1–3%). We choose a sky annulus between 100″ and 150″ in radius to avoid any extended emission from sources but include the emission from the surrounding filamentary structure. Using this technique to minimize contamination, the sky emission is less than 10% of the source flux at any given wavelength, except for a few cases where the background is as high as 20–30%.

In addition to PACS and SPIRE photometry and spectroscopy, we collected 2MASS JHK, WISE Bands 3.4, 4.6, 12, and 22 μm, *Spitzer*-IRAC 3.6, 4.5, 5.8, and 8 μm, MIPS 24 μm and 70 μm photometry, and archival photometry for all sources where available. It became apparent upon comparison to the PACS 70 μm, that the MIPS 70 μm photometry was saturated in most sources, and thus we discard the MIPS 70 μm photometry in those cases. Additionally, we collected millimeter data where available. The detailed reference for the photometry used in this study is shown in the Appendix (Table A.3).

2.3.3 The SEDs before and after *Herschel*

The bolometric luminosities, which include both spectroscopic and photometric measurements, and the bolometric temperatures calculated with the prescription proposed by Myers & Ladd (1993) and Chen et al. (1995a) are shown in Table 2.3. We compute $L_{\rm bol}$ following the trapezoidal summation method used in Dunham et al. (2010b). In summary, we integrate over the finitely sampled SED by treating each datapoint as a trapezoid covering half of the wavelength range to its nearest neighbor, at the given value. We then add the areas of trapezoids together. Similarly, we compute $T_{\rm bol}$ as the blackbody that peaks at the flux-weighted average wavelength of the SED (using the trapezoidal summation method), and translate into a temperature via the Planck blackbody law. The difference is then the values of $L_{\rm bol}$ and $T_{\rm bol}$ computed with this method, with and without the *Herschel* data. Photometry is treated as a single flux density at its representing wavelength, and inserted into the spectra. A single photometry only contributes to the area within its trapezoid (i.e. its width is smaller than the wavelength channel of spectra) Thus the values of $L_{\rm bol}$ and $T_{\rm bol}$ are dominated by spectra, rather than photometric points. Thus, the spectral data dominate the uncertainties in cases of overlapping wavelength coverage.

The excellent sampling from *Herschel* spectroscopy has decreased the uncertainties of $L_{\rm bol}$ and $T_{\rm bol}$ substantially. Models of star formation predict the bolometric

luminosity of protostars. However, the bolometric luminosity can be underestimated by 35–40% if a significant portion of data between 70 μm and 850 μm is missing (Dunham et al., 2013). *Herschel* fills this gap perfectly. To compare the change of bolometric luminosity resulted from the addition of *Herschel* data, we collected the bolometric luminosities measured primarily with *Spitzer* (Furlan et al., 2008; Dunham et al., 2015) for 15 COPS sources where bolometric luminosities were calculated, and compare with the bolometric luminosities measured from our PACS and SPIRE data. We found a mean increase of 50% with the *Herschel* data, where 12 of 15 protostars have their luminosities increased.

The addition of *Herschel* observations affect the bolometric temperatures as well. With the same sample (Furlan et al., 2008; Dunham et al., 2015), we found the bolometric temperature decreases by 10% on average after including the *Herschel* spectroscopy, suggesting that the protostars would be systematically less evolved with *Herschel* under the classification of $T_{\rm bol}$.

Some sources have photometry that deviate significantly from spectroscopy (see the discussion in Section 2.3.5). Although the spectroscopy dominates the values of $L_{\rm bol}$ and $T_{\rm bol}$, the mismatch between photometry and spectroscopy may suggest potential calibration problems, introducing systematic uncertainties. If we simply calibrate the spectroscopy to photometry, the $L_{\rm bol}$ and $T_{\rm bol}$ can vary by as much as +90%/-60% and +65%/-15% respectively, but no systematic offset is found as the average differences for $L_{\rm bol}$ and $T_{\rm bol}$ among the COPS sources are 2% and 4% respectively. Among the 16 sources that we have photometry to scale the spectroscopy, only three (one) sources have $L_{\rm bol}$ ($T_{\rm bol}$) varies more than $\pm$20%. However, the calibration between spectroscopy and photometry is not likely to be the problem since the systematic uncertainties of PACS and SPIRE are only 1% and 3%, and our extracted spectra agree with photometry at long wavelengths. If we further calibrate the SPIRE spectra to the PACS spectra, assuming that the PACS spectra are less confused by extended emission, $L_{\rm bol}$ becomes smaller while $T_{\rm bol}$ becomes larger, since the SPIRE spectra are always greater than the PACS spectra when there is a mismatch. On average, $L_{\rm bol}$ decreases by 5%, while $T_{\rm bol}$ increases by 5%. L1455 IRS3 is the most extreme case, whose $L_{\rm bol}$ and $T_{\rm bol}$ vary by -30% and +40%. Rebull et al. (2015) found that the mid-infrared fluxes of Class 0 sources are highly variable by 10–15% across 6–7 years baseline. Thus, the mismatches between photometry and spectroscopy may be due to the intrinsic variability of the sources.

For the sources whose SPIRE spectrum disagrees with their PACS spectrum (see the discussion in Section 2.3.5), their $L_{\rm bol}$ and $T_{\rm bol}$ can differ up to -25% and +25%, respectively, if we manually scale the SPIRE spectra to match the PACS spectra.

Table 2.3: Evolutionary Indicators

Source	$L_{\rm bol}$ ($L_\odot$)	$L_{\rm smm}$ ($L_\odot$)	$L_{\rm CO}$ ($L_\odot$)	$T_{\rm bol}$ (K)	$\alpha_{\rm NIR}$	Class$_{\alpha_{\rm NIR}}$	Class$_{L_{\rm smm}}$	Class$_{T_{\rm bol}}$	Ref.
IRAS 03245+3002	6.06	0.05	0.012	48.2	2.54±0.79	0+I	0	0	D
L1455 IRS3	0.55	0.05	0.0012	128.0	1.18±0.29	0+I	0	I	D
IRAS 03301+3111	3.91	0.05	0.0083	354.0	0.37±0.06	0+I	0	I/flat[1]	D
B1-a	2.47	0.09	0.048	79.9	1.87±0.45	0+I	0	I	D
B1-c	4.41	0.11	0.021	55.9	3.01±1.47	0+I	0	0	D
L1551 IRS5	25.9	0.09	0.0087	110.0	1.43±0.17	0+I	0	I	G
TMR 1	2.0	0.015	0.0064	125.0	1.02±0.33	0+I	0	I	R
TMC 1A	2.62	0.015	0.0023	159.0	-0.15±0.84	flat	0	I	R
TMC 1	0.79	0.015	0.0042	149.0	0.55±0.04	0+I	0	I	R
HH46	23.2	0.18	0.079	111.0	0.71±0.03	0+I	0	I	G
Ced110 IRS4	1.28	0.03	0.0064	53.6	1.99±0.54	0+I	0	0	G
BHR 71	13.5	0.16	0.039	51.1	1.95±0.33	0+I	0	0	G
DK Cha	35.1	0.025	0.017	592.0	-0.05±0.34	flat	I	flat	D
IRAS 15398−3359	1.49	0.032	0.0097	43.2	1.32±0.15	0+I	0	0	G
GSS 30 IRS1	19.7	0.07	0.064	129.0	1.58±0.30	0+I	I	I	D
VLA 1623−243	5.36	0.15	0.034	33.2	2.34±0.07	0+I	0	0	c2d
WL 12	2.23	0.039	0.010	210.0	2.93±0.60	0+I	0	I	D
RNO 91	2.53	0.016	0.0030	349.0	0.48±0.16	0+I	0	I/flat[1]	c2d
L483	8.78	0.11	0.015	49.3	2.05±1.12	0+I	0	0	G
RCrA IRS5A[2]	1.7	0.013	0.039	209.0	0.40±0.30	0+I	0	0	P, L
RCrA IRS7C[2]	9.1	0.092	0.18	79.0	2.65±0.71	0+I	I	0	P, L
RCrA IRS7B[2]	4.6	0.096	0.13	89	2.68±1.19	0+I	0	0	P, L
L723 MM	3.3	0.065	0.016	66.8	1.50±0.32	0+I	0	0	G
B335	0.57	0.012	0.0032	45.5	0.74±0.18	0+I	0	0	A
L1157	5.26	0.11	0.031	40.1	0.87±0.38	0+I	0	0	D
L1014	0.33	0.024	... [3]	63.4	0.75±0.24	0+I	0	0	Y

$L_{\rm bol}$ and $T_{\rm bol}$ measured from the SEDs presented herein. $L_{\rm smm}$is defined as the bolometric luminosity of the spectrum $> 350\ \mu$m. The $\alpha_{\rm NIR}$ is re-calculated with photometric fluxes collected from literatures. If the photometric fluxes are not found, we use the spectrophotometric fluxes extracted from the *Spitzer*-IRS spectra.

Reference code: c2d = Evans et al. (2009b), D = Dunham et al. (2015), L = Lindberg et al. (2014), P = Peterson et al. (2011), R = Rebull et al. (2010), A = Stutz et al. (2008), Y = Young et al. (2004a), G = Green et al. (2013a).

[1] The sources have $T_{\rm bol}$ close to the criteria dividing between Class I and flat spectrum.

[2] The $L_{\rm bol}$, $T_{\rm bol}$, and $L_{\rm smm}$ are collected from Lindberg et al. (2014). Other quantities are calculated from the SEDs with the COPS spectra and data from the CDF archive, which have obvious source contaminations.

[3] No CO line is detected toward L1014.

2.3.4 Detection Limits

We measured the continuum RMS in the line-free spectrum, where the noise is dominated by the correlated baseline variation due to the nature of the FTS spectrograph and the apodization. The continuum RMS scales roughly with the continuum flux when the continuum flux is greater than 50 Jy (Figure 2.1). We found a mean RMS between 0.01 Jy to 0.1 Jy for the sources with their mean continuum fluxes lower than 50 Jy, whose RMS noise does not scale with the continuum flux. The RMS noise significantly increases toward the edges of spectra. We detect line fluxes down to 6.9×10^{-18} W m^{-2} (equivalent to a peak flux of 0.28 Jy for unresolved lines) and 3.0×10^{-17} W m^{-2} (equivalent to a peak flux of 1.6 Jy for unresolved lines), in PACS and SPIRE, respectively, for typical DIGIT/COPS integration times.

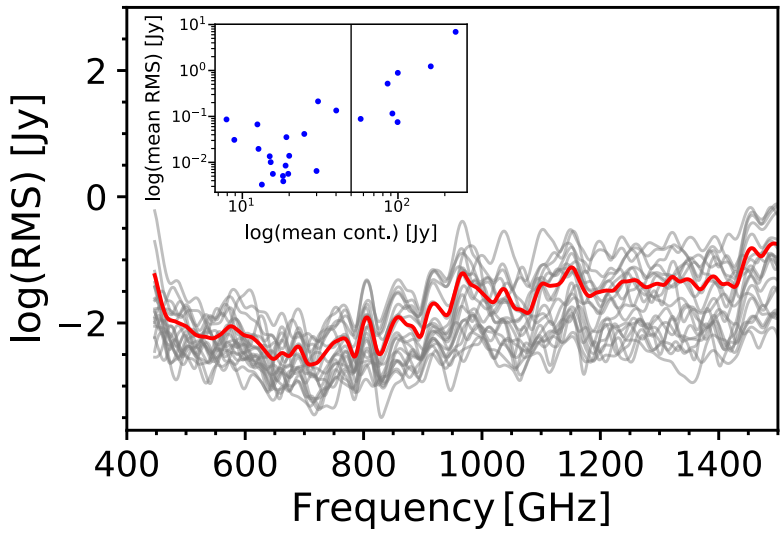

Figure 2.1: The RMS noises of the sources with their mean continuum fluxes lower than 50 Jy are shown in gray lines, while the mean RMS noise of those sources is shown in red line. The RMS noise is convolved with a Gaussian that has a width of 20 wavelength channels for better visualization. The inset figure shows the relation between the continuum flux and the RMS noise averaging over frequencies for the COPS sources. The relation suggests a positive correlation when the mean continuum flux is greater than 50 Jy, and no specific trend is found when the mean continuum flux is lower than 50 Jy.

2.3.5 Spectral Energy Distributions

The full 1–1000 μm SEDs of 26 protostars, excluding HH 100, observed in the COPS program are shown in Figure 2.2, along with the *Herschel* PACS spectra observed in the DIGIT program (Green et al., 2013a), archival *Spitzer*-IRS spectra, and archival photometry. We show the SEDs of both RCrA IRS7B and RCrA IRS7C for their difference at shorter wavelength, although only RCrA IRS7C (noted as RCrA IRS7B/C) is considered in some of the analyses. The agreement between the PACS and SPIRE spectra are improved with our extraction of the PACS 1D spectra. In five sources (TMC 1, WL 12, L1014, L1455 IRS3, and IRAS 03301+3111), the total flux at 200 μm derived from all 25 PACS spaxels is significantly less than the flux measured from the SPIRE data at the same wavelength. We found that the SPIRE emission in all five sources is extended, and therefore the observed SPIRE flux is derived from an even greater spatial extent than the entire PACS footprint. However, we do not see such large-scale extended emission in either PACS spectroscopy or imaging, suggesting that the SPIRE flux may be contaminated by unrelated emission. Note that the SPIRE-FTS calibrated the background emission with an on-board instrumental feed instead of chopping between source and background, which was used in PACS background calibration. However, our data are insufficient to determine the origin of the extended emission; therefore, we do not correct for the extended emission.

The SPIRE images are available for 24 protostars, for which we performed aperture photometry to extract their photometric fluxes to compare with their 1D spectra. The SPIRE spectroscopic and photometric flux, when extracted in the same size aperture for each band, match to within 15% for 21 of 24 protostars at 250 μm (TMC 1, BHR 71, and DK Cha have 17%, 16%, and 17% agreements, respectively) and 23 of 24 protostars at 350 μm (IRAS 03301+3111 has a 19% agreement), and they match to within 35% for all 24 protostars at 500 μm. The median percentage differences between SPIRE photometry and SPIRE spectroscopy are 8%, 3%, and 24% for 250 μm, 350 μm, and 500 μm, respectively. All sources show higher photometric fluxes at 500 μm than the spectroscopic fluxes at the same wavelength, suggesting the presence of extended emission that is not considered by the SECT correction. As a comparison, the PACS spectra presented in this study, which were originally published in Green et al. (2016a), have median percentage differences between pho-

tometry and spectroscopy of 16%, 8%, and 10% at 70 μm, 100 μm, and 160 μm, respectively.

2.3.6 Lines: Atomic and Molecular Emission

With the improved reduction, we performed an automatic line fitting, which was developed for the CDF archive (Green et al., 2016a), on the spectra of each spaxel and the 1D spectra. The line fluxes were updated from the CDF archive based on the updated reduction. Here we briefly describe the concept of this automatic line fitting routine.

The routine utilizes a pre-defined line list (see Table 2–6 in Green et al., 2016a), including the emission of molecules and atoms, such as CO, ^{13}CO, H_2O, HCO^+, [C I], and [O I], to fit the local baselines around all potential lines. After subtracting the baseline, we fit a Gaussian profile around the theoretical line centroid with limited flexibility on the exact wavelength of line centroids. The full width at half maximum (FWHM) is fixed at the instrumental resolution for PACS spectra, while the FWHM is allowed to vary within $\pm$30% of the instrumental resolution to better fit the apodized SPIRE spectra. In some cases where two lines are blended together, we fit two Gaussian profiles simultaneously when the signal-to-noise ratio (SNR) is sufficiently large. Then, we re-evaluate the uncertainties of the fitted parameters by re-fitting the baselines on the original spectra with the fitted line profiles subtracted. Finally, the line fitting is performed for the third time to include the updated uncertainties, improving the fitting results. Most of the lines are unresolved except for [O I] $^3P_1 \rightarrow ^3P_2$ at 63 μm, which can be as wide as 1.5$\times$FWHM, a limit set by the line fitting pipeline. The line fitting pipeline allows us to separate the continuum from the spectrum. We present the line-free continua in the SEDs (Figure 2.2), while showing the continuum-free spectra in Appendix A.2 (Figure A.1).

Our fitting pipeline produces more than just the 1D spectra with the line taken out; it further smoothes the line-free continuum by 20 wavelength channels, resulting in continuum spectra with $\lambda/\Delta\lambda$=16–50. The smoothing process has little effect on the mean photometry across the whole sample, only a 0.04% decrease in SPIRE 500 μm band. However, the difference of the photometry ranges from $-$0.6% to 0.4%.

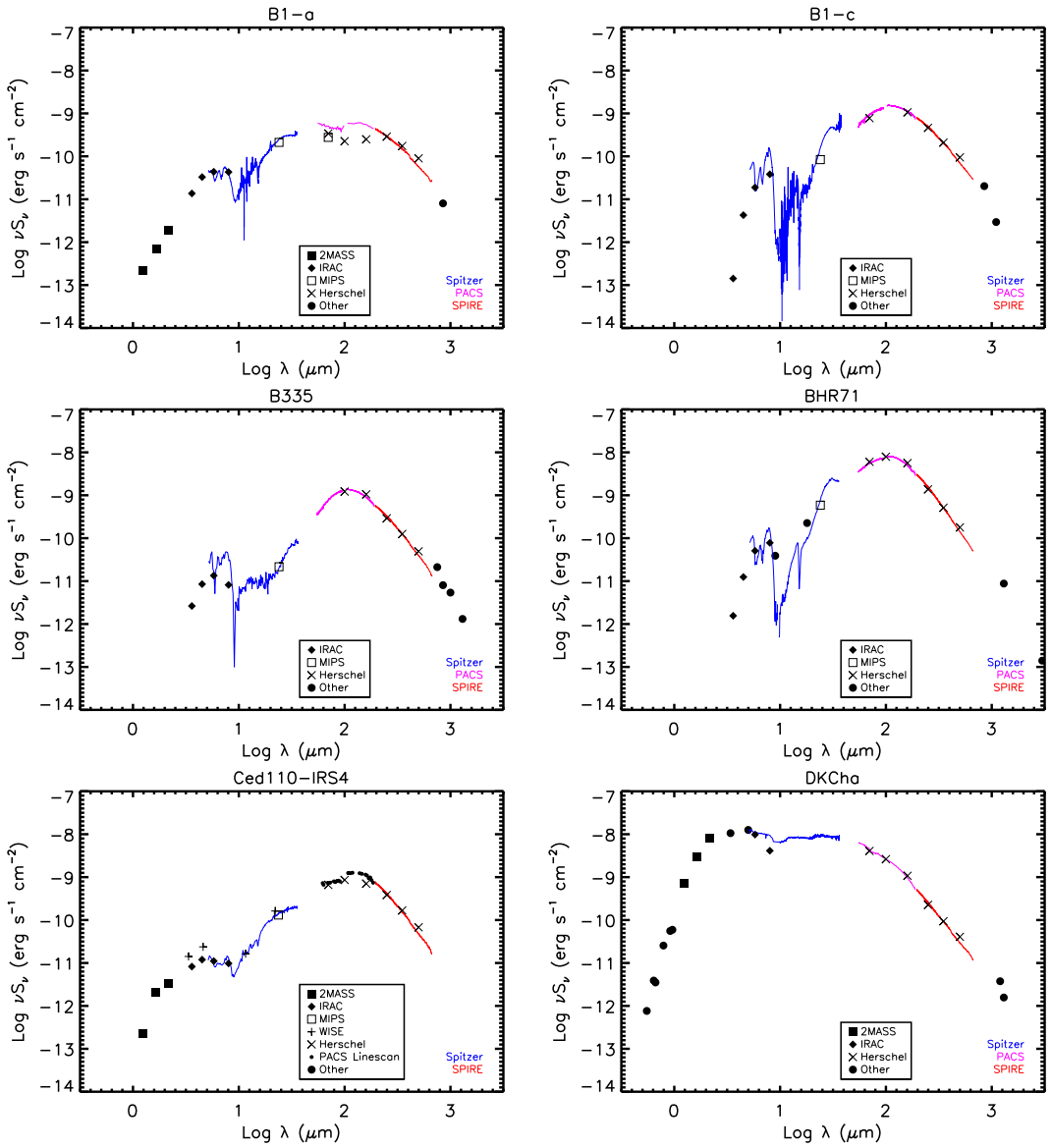

Figure 2.2: The SEDs of the COPS sources. The spectra of *Spitzer*-IRS, PACS, and SPIRE are shown in blue, magenta, and red, respectively. We only show the line-free continuum for PACS and SPIRE, while the continuum-free SPIRE spectra are shown in the Appendix. The black filled circles illustrate the linescan data where the ranges-can PACS data is unavailable. The sources of the photometry are shown in the legend. For a better visualization, the PACS spectra of B1-a, DK Cha, IRAS 03301+3002, and TMC1 are rebinned to R=100, while the PACS spectra of L1014 and L1455 IRS3 are rebinned to R=50.

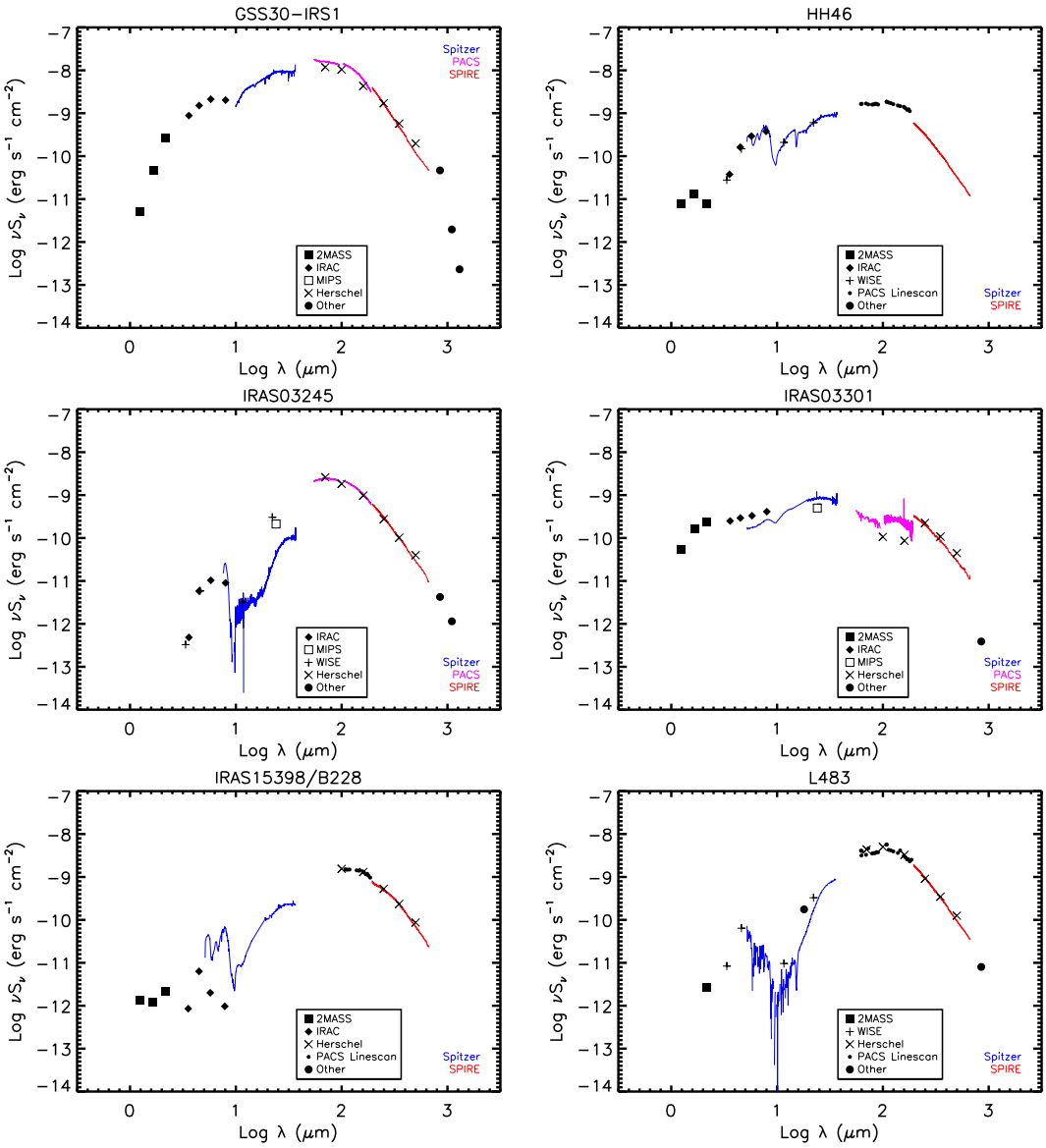
GSS30−IRS1
HH46
IRAS03245
IRAS03301
IRAS15398/B228
L483
Log νS_ν (erg s^−1 cm^−2)
Log λ (μm)
2MASS
IRAC
MIPS
WISE
Herschel
PACS Linescan
Other
Spitzer
PACS
SPIRE

Figure 2.2

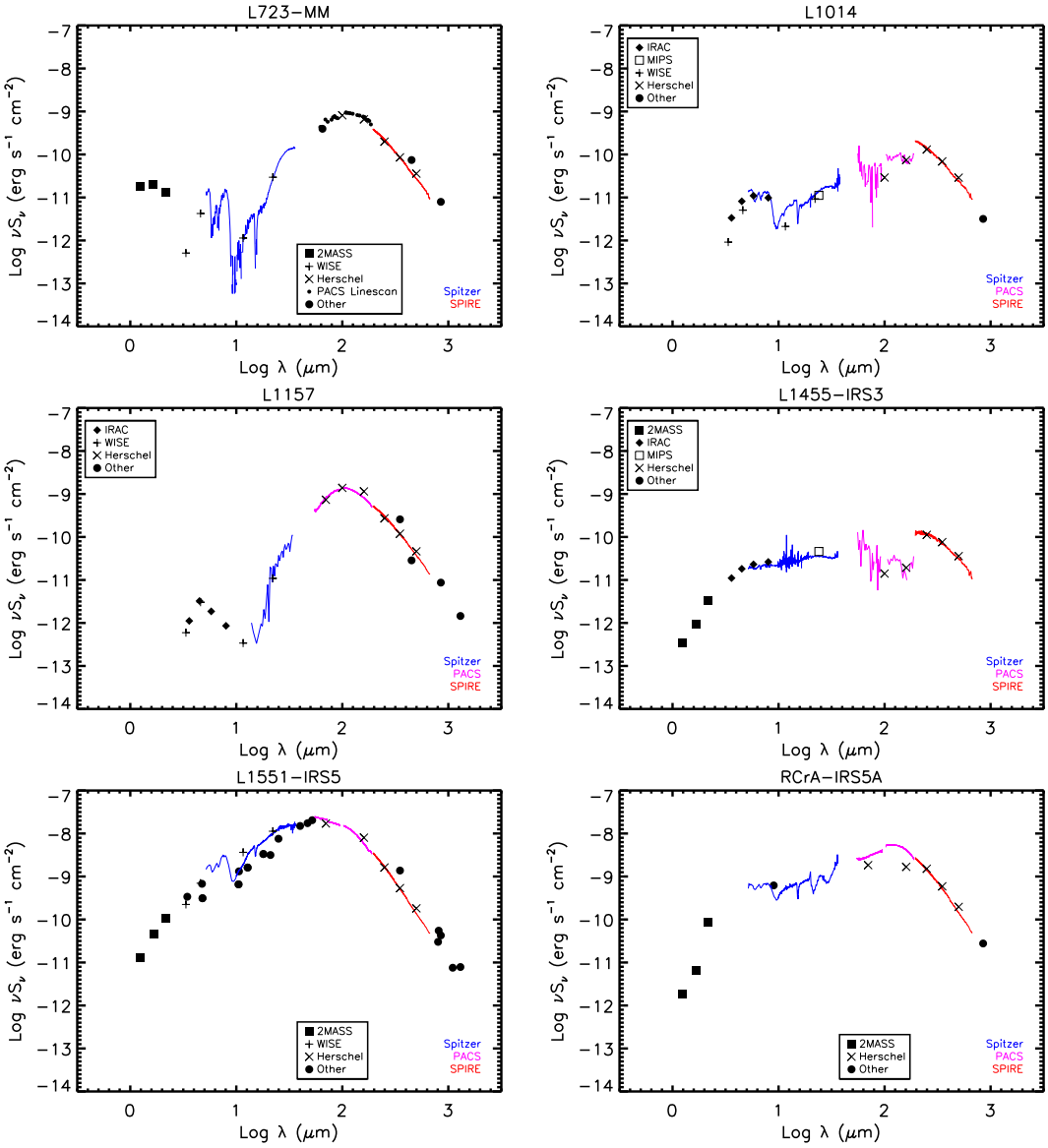
L723−MM
L1014
L1157
L1455−IRS3
L1551−IRS5
RCrA−IRS5A
Log νS_ν (erg s^−1 cm^−2)
Log λ (μm)
2MASS
IRAC
MIPS
WISE
Herschel
PACS Linescan
Other
Spitzer
PACS
SPIRE

Figure 2.2

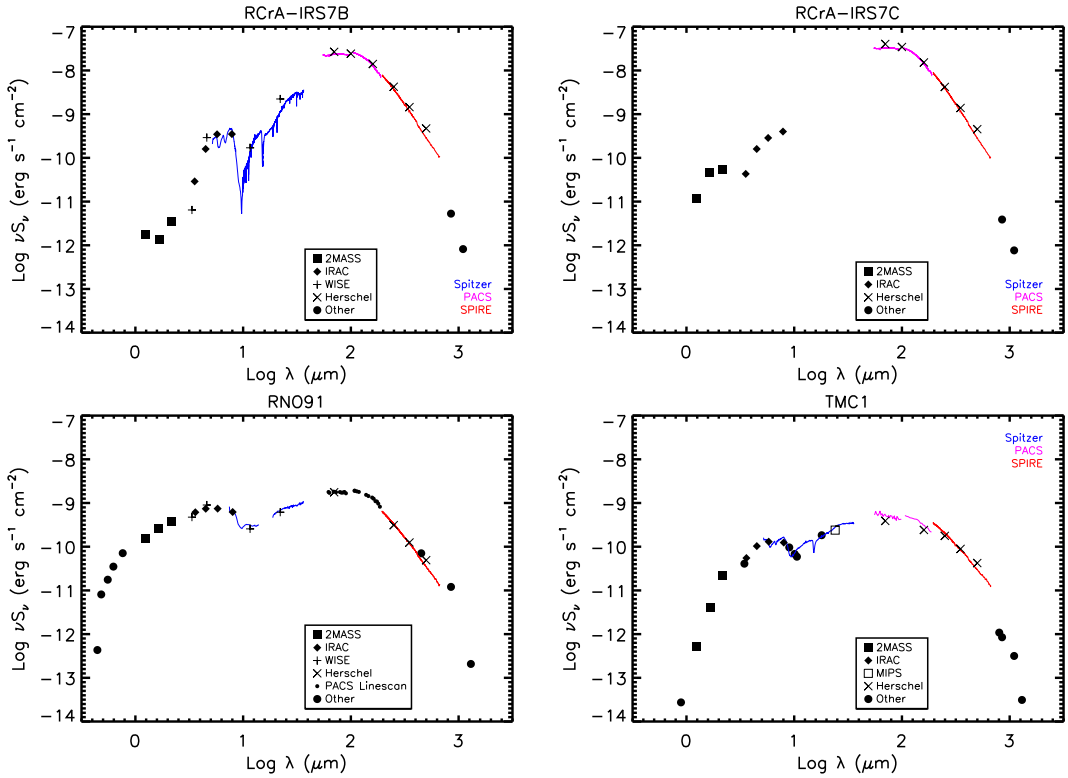

Figure 2.2

2.3.6.1 Detection Statistics for the SPIRE Spectra

Quasi-periodic baseline variations at scales between 0.3–1 μm are found in the SPIRE spectra because of the nature of the Fourier Transform Spectrograph (FTS) even if the side-lobes of the sinc function have been suppressed by the apodization, which convolves the spectra with a taper function. We ran the same fitting pipeline with the line centroids shifted to supposedly line-free regions to quantify the false-positive rate of detections as a function of the SNR threshold. We found that SNR thresholds of 3, 4, and 5 yield false-positive rates of 1.3%, 0.98%, and 0.84%, respectively. The false-positive rate with an SNR threshold of 3 is greater than the rate assuming Gaussian noise, which predicts a false-positive rate of 0.3%, indicating that the apodization on the FTS spectra indeed introduces non-Gaussian noise. To obtain a robust analysis, we choose a threshold of 1% for the false-positive rate, corresponding to a SNR threshold of 4 for the SPIRE spectra, while we consider lines as detections with SNRs greater than 3 for the PACS spectra. We summarize the

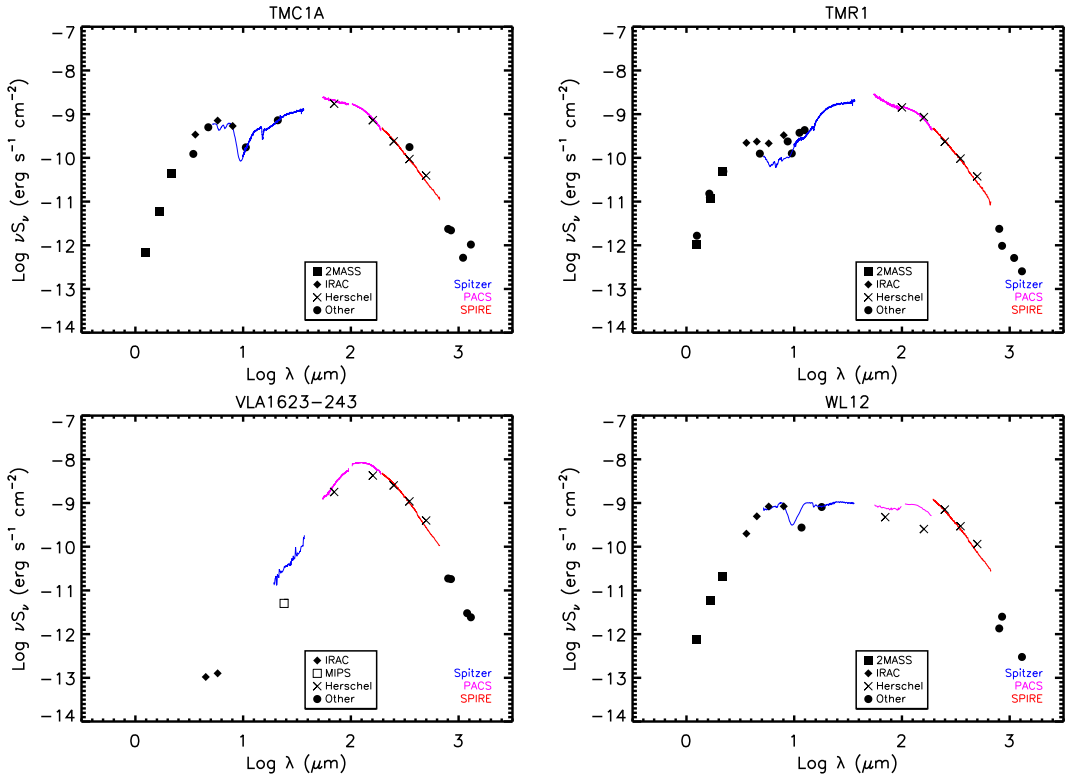

Figure 2.2

detections of lines in Table 2.9. We attempted to fit 28 lines of interest (see the full list in Green et al. 2016a) for each source.

The lowest excitation line of water, o-H_2O $1_{10} \rightarrow 1_{01}$ at 557 GHz (538 μm; $E_{\rm up}/k =$ 61 K) was surveyed with HIFI for the DIGIT/WISH sources, which include all of the COPS sources (Kristensen et al., 2012b; Green et al., 2013a; Mottram et al., 2014b). The line was detected by HIFI in 24 sources, while we detected the line toward 8 sources in the SPIRE spectra. The main reason for this difference in detection rates is the difference of sensitivities of two instruments/programs. The SPIRE-FTS spectral resolution ($\Delta\nu$ =2.16 GHz after apodization, corresponding to Δv = 1162 km s^{-1} at 557 GHz) is much greater than the linewidth measured with HIFI ($<$ 180 km s^{-1}); thus, the water lines remain unresolved and therefore spectrally diluted. Mottram et al. (2014b) found an RMS noise of $\sim$20 mK for the same line, while our data show an RMS noise of $\sim$0.7 K, which is about 35 times larger. Overall, we detect up to six transitions of H_2O in the SPIRE bands, with at least one detection in 17 protostars, while H_2O in PACS bands is detected in almost all COPS protostars (24 sources)

with PACS.

2.3.6.2 Line Fitting Results

The line fitting results are written to an ASCII file for further analyses. Table 2.4 shows an example of the line fitting results used in this study. The full table can be accessed online as a machine readable table. Each column follows the same terminology described in Green et al. (2016a), which will be outlined briefly in the following. Table 2.5 lists all of the column names along with their descriptions. Special numbers, `-998` and `-999`, can be found under `Sig_Cen(um)`, `Sig_str(W/cm2)`, and `Sig_FWHM(um)` columns. The `-998` indicates that the fitted parameter can be used, but the uncertainty must be extrapolated from other nearby fitted lines. The `-999` indicates that the fitted parameter is not well-constrained. The `Pixel_No.` shows the spaxel name of the fitted spectrum. In the case of our extracted 1D spectrum, it will list as `c`. The blending flag highlights if there is any possible line in our line list within one resolution to the fitted line centroid. Note that whether the nearby line is detected is not considered in reporting the blending flag. We further selected several pairs of nearby lines to perform double Gaussian fittings, which are reported as `DoubleGaussian` in the blending flag. Finally, the validity flag suggests whether the fitting result should be used. If `-999` flag is found in any column of the fitting result, the validity will be flagged as `0`, indicating the line is not well-constrained; otherwise, the validity flag is `1`.

Table 2.4: A portion of the line fitting results.

Object	Line	LabWL(um)	ObsWL(um)	Sig_Cen(um)	Str(W/cm2)	Sig_str(W/cm2)
B1-a	o-H2O8_27-7_16	55.13238	55.09925	-999.00000	5.136442e-21	1.588567e-21
B1-a	o-H2O4_41-4_32	94.70758	94.68837	0.00613	-1.408871e-21	4.175396e-22
B1-a	p-H2O6_42-6_33	103.91892	103.93085	-999.00000	-2.282466e-22	3.550550e-22
B1-a	p-H2O6_15-6_06	103.94278	104.01953	-999.00000	-5.827662e-22	3.471036e-22
B1-a	o-H2O6_34-6_25	104.09629	104.04658	0.03396	-6.743942e-22	3.439754e-22
L1157	p-H2O6_42-5_51	636.66803	636.52551	0.64353	-5.939747e-25	1.666154e-25
L1157	CO4-3	650.26788	650.03816	0.49030	1.179826e-24	4.539972e-25
L1157	CI3P2-3P1	370.42438	370.42438	-998.00000	0.000000e+00	-9.980000e+02
B335	o-H2O4_23-4_14	132.41173	132.36006	0.03324	7.017522e-22	3.188232e-22
L723-MM	HCO+7-6	480.28812	480.43103	0.28217	2.894226e-22	1.482337e-22

FWHM(um)	Sig_FWHM(um)	Base(W/cm2/um)	Noise(W/cm2/um)	SNR	E_u(K)	A(s-1)
0.03899	-998.00000	-5.290667e-20	7.962727e-20	1.554990	1274.2000	1.89700e+00
0.03444	-998.00000	2.251379e-20	2.661830e-20	1.444368	702.3000	1.52800e-01
0.11076	-998.00000	4.141600e-21	6.019659e-21	0.321756	1090.3000	2.27200e-01
0.11077	-998.00000	3.302900e-21	5.905709e-21	0.837283	781.1000	1.36000e-01
0.11084	-998.00000	3.093281e-21	5.437168e-21	1.051746	933.7000	2.18100e-01
3.81872	-999.00000	-5.091552e-26	1.091546e-25	1.339266	1090.3000	3.18300e-05
3.96728	1.15402	-9.832410e-26	1.527495e-25	1.829799	55.3200	6.12600e-06
0.99437	-998.00000	8.266724e-25	1.427042e-25	0.000000	62.4620	2.65000e-07
0.12178	-998.00000	9.048764e-19	4.785423e-21	1.131773	432.2000	8.08400e-02
1.71562	0.66422	6.333804e-21	1.026068e-22	1.545234	119.8400	2.04020e-02

g	RA(deg)	Dec(deg)	Pixel_No.	Blend	Validity
51	53.3244040	31.1379872	1	x	0
27	53.3244638	31.1379599	1	x	1
13	53.3243090	31.1380844	1	Red	0
13	53.3243077	31.1380844	1	Red/Blue	0
39	53.3243048	31.1380791	1	Red/Blue	0
13	309.7550000	68.0161000	SLWA2	Red/Blue	0
9	309.7550000	68.0161000	SLWA2	x	1
5	309.7550000	68.0161000	SLWA2	DoubleGaussian	1
27	294.2535754	7.5692374	c	x	1
15	289.4740000	19.2062000	c	x	1

The table in the ASCII file have the same columns and style except that the rows are chopped into three parts here for better display. Also this table has selected lines from different parts of the original results to demonstrate different flags. As mentioned in Section 2.3.6.2 , any column with `-999` indicates a fitting result that is not well-constrained. Therefore, the `Validity` flag is set to be 0. The `Pixel_No.` column lists `c` for the 1-D spectrum measurements, and the specific pixel number/name for individual spaxels. This table (all line measurements for all sources) is published in its entirety online as a machine readable table.

Table 2.5: The definitions of columns in the line fitting result

Column name	Description
Object	object name
Line	line name
LabWL(um)	theoretical line centroid
ObsWL(um)	fitted line centroid
Sig_Cen(um)	uncertainty on the fitted line centroid
Str(W/cm2)	fitted line strength
Sig_str(W/cm2)	uncertainty on the fitted line strength
FWHM(um)	fitted full width at half-maximum
Sig_FWHM(um)	uncertainty on the fitted FWHM
Base(W/cm2/um)	fitted baseline intensity
Noise(W/cm2/um)	residual intensity
SNR	the signal-to-noise ratio
E_u(K)	the upper energy level from LAMDA[1]
A(s-1)	the Einstein-A value from LAMDA[1]
g	the multiplicity of the upper energy from LAMDA[1]
RA(deg)	right ascension
Dec(deg)	declination
Pixel_No.	the pixel label
Blend	the blending flag which highlight any other line within one resolution element to the fitted line centroid
Validity	the validity flag which determines the overall certainty of the fitting for a given line

[1]Leiden Atomic and Molecular Database (Schöier et al., 2005a).

2.3.6.3 The Effect of Lines on Photometry

The line fitting pipeline provides us a chance to investigate the impact of the emission lines on the broad band photometry, which inevitably includes lines. We calculated the spectrophotometry at SPIRE 250, 350, and 500 μm bands with the corresponding filters for the spectra with and without lines. After the removal of lines, the photometry decreases by 0.8%, 1.0%, and 0.7% on average, respectively, while the maximum decrease of photometry is 2–3%. At longer wavelength, Drabek et al. (2012) found the emission of CO $J = 3 \rightarrow 2$ typically contributes to less then

20 % of the 850 μm continuum, but the contamination can be as high as 79% in the regions dominated by outflows. They also suggest the contribution of CO to the continuum would be small at shorter wavelengths (e.g. 450 μm), because the continuum is brighter.

2.4 Analysis

2.4.1 CO Optical Depth

The ^{13}CO line is usually taken to be optically thin for the transitions detected with SPIRE, while ^{12}CO is typically optically thick at low-J before becoming optically thin at high-J (e.g. Goldsmith et al., 1984). For the COPS sources with ^{13}CO detections, we tested this assumption. Figure 2.3 (left) shows the ratios of integrated fluxes of ^{12}CO and ^{13}CO as a function of J-level. If both ^{12}CO and ^{13}CO are optically thin at a certain J-level, we should find the ratio of two lines approaching the intrinsic isotope ratio of 62 (Langer & Penzias, 1993); however, the ratio reaches only 10–20 for the transitions where ^{13}CO was detected. We can further derive the optical depth from the following expression:

$$\tau_{12} = R\frac{J_\nu(T_{\mathrm{rot},^{12}\mathrm{CO}})}{J_\nu(T_{\mathrm{rot},^{13}\mathrm{CO}})}\frac{F_{13}}{F_{12}}, \tag{2.1}$$

where R is the abundance ratio of ^{12}CO to ^{13}CO, $J_\nu(T)$ is the Planck function, T_{rot} is the rotational temperature, and F_{12} and F_{13} are the integrated line fluxes of ^{12}CO and ^{13}CO lines. We also assume that both ^{12}CO and ^{13}CO have the same excitation temperature and the same line profile. We average the measurements of ^{12}CO/^{13}CO shown in Figure 2.3 (left) to better constrain the relation. We also collect other measurements of ^{12}CO/^{13}CO from literatures to better constrain the optical depth of the entire CO ladder. We calculated the averaged ^{12}CO/^{13}CO at $J = 10 \rightarrow 9$ measured by San José-García et al. (2013), which includes 11 COPS sources. Figure 2.3 (right) shows the distribution of the averaged optical depth of ^{12}CO versus the upper energy levels, derived from Equation 2.1, assuming R=62.

From a simple two-level atom assumption, the relation between the optical depth and upper energy can be approximated as $\tau_{12} \propto E_{\mathrm{u}}^{-a}$, a relationship supported by the data (Figure 2.3, right). The optical depth has a larger scatter between J_{up}=7–9

due to the low detection rates of ^{13}CO among the COPS sources. Figure 2.3 (right) also shows the optical depth of CO $J = 16 \rightarrow 15$ of Serpens SMM1 (black), a massive low-mass embedded protostar, derived from the ^{12}CO/^{13}CO measured by Goicoechea et al. (2012). We included all data other than the data of Serpens SMM1 for the fitting of the relation of optical depth as a function of the upper energy (Figure 2.3, right), and found the relation can be described as

$$log(\tau_{12}) = -(2.6 \pm 0.6) \times 10^{-3} \times E_{\rm u} + (1.4 \pm 0.1). \quad (2.2)$$

We further extrapolated the fitted relation to find out that τ_{12} approaches to 1 as $E_{\rm u}$ reaches 522.3 K, which makes $J_{\rm up}$=13 the highest $J_{\rm up}$ level requiring correction. The uncertainty of the extrapolation for $\tau_{12} = 1$ is -55.6 K/+86.8 K. Before we adopt this result, some other uncertainties need to be considered.

The optical depth of resolved CO lines for low to mid-J is known to be high at the peak of the line profile, and the lines become optically thin in the line wing (e.g. Arce & Goodman, 2001; Dunham et al., 2014a). Both ^{12}CO and ^{13}CO lines are spectrally unresolved with SPIRE, which we have to consider when adopting our derived relation of optical depth. Yıldız et al. (2012, 2013) presented the optical depth of CO as a function of velocity and the integrated fluxes of ^{12}CO and ^{13}CO toward NGC1333 IRAS4A and 4B. Using our method to calculate the optical depth with the integrated fluxes of NGC1333 IRAS4A and 4B, we found the derived optical depths are equal to or greater than the highest optical depth found with the resolved line profiles by up to a factor of 4. The overestimation of the optical depth is likely because the self-absorption of ^{12}CO lines cannot be excluded from our analysis with the unresolved lines. Self-absorption is rarely seen in ^{13}CO lines due to the lower optical depth (Yıldız et al., 2012; San José-García et al., 2013); therefore, the derived optical depth is higher due to the self-absorption at the center of ^{12}CO lines. On the other hand, the broad components are rarely seen in the observed line profiles of ^{13}CO (San José-García et al., 2013), possibly due to their low sensitivity, and thus signal-to-noise ratio. However, the optical depth derived from unresolved lines is less affected by the undetected line wings compared to the studies using resolved lines, because all components of line profiles contributing to the measured line flux.

Despite the uncertainties of the optical depth, our fitted relation is consistent with the results of Goicoechea et al. (2012), which suggests an optical depth of 0.88 for the CO $J = 16 \rightarrow 15$ line. Our relation suggests an optical depth of $0.25^{+1.0}_{-0.1}$ for the

CO $J = 16 \rightarrow 15$ line. In the following analysis, we adopt the fitted relation of the optical depth as a function the upper energy, suggesting that CO lines with $J_{\rm up}$ lower or equal to 13 need to be corrected for optical depth. The correction is applied to all COPS sources regardless of whether ^{13}CO was detected.

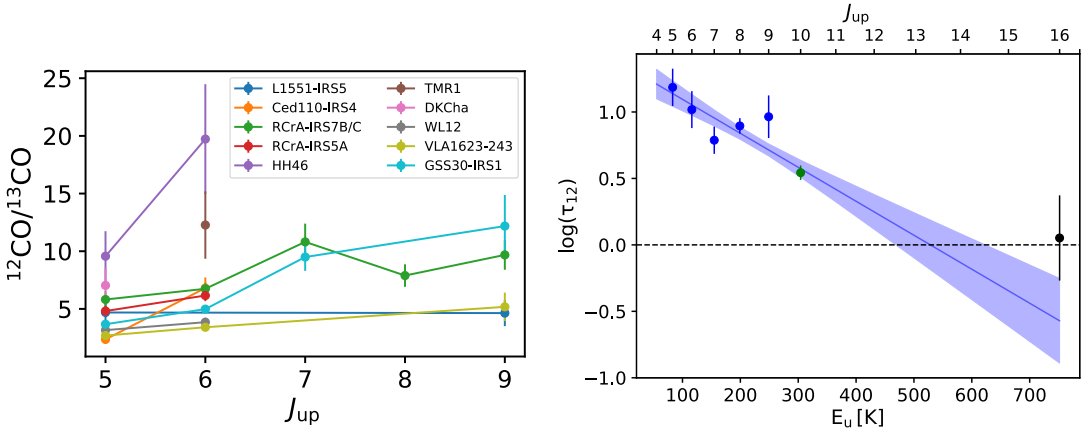

Figure 2.3: **Left:** The flux ratios of ^{12}CO and ^{13}CO originating from the same $J_{\rm up}$-level. **Right:** The derived optical depth of ^{12}CO with the corresponding upper energy. The green point indicates the optical depth derived from the averaged ^{12}CO/^{13}CO measured by San José-García et al. (2013), while the black point shows the optical depth derived from the ^{12}CO/^{13}CO of Serpens SMM1 measured by Goicoechea et al. (2012). The blue line indicates the fitting result, while the shaded region indicates the 1-σ uncertainty of the fit.

2.4.2 CO Rotational Diagrams

One useful tool in analyzing molecular emission is the rotational diagram; a detailed review can be found in Goldsmith & Langer (1999); brief reviews in the context of *Herschel* spectroscopy are in Green et al. (2013a); Manoj et al. (2013); Karska et al. (2013a). Here we focus only on the rotational diagram analysis for CO. Other molecular species, such as OH, and H_2O, also probe the molecular budget of embedded protostars but require detailed analyses with extensive radiative transfer modeling (e.g. Goicoechea et al., 2012; Herczeg et al., 2012; Karska et al., 2013a; Wampfler et al., 2013; Kristensen et al., 2013; Mottram et al., 2014b; Karska et al., 2014a), which is beyond the scope of this study.

As noted in many previous studies (e.g. van Kempen et al., 2010; Manoj et al., 2013; Goicoechea et al., 2012; Dionatos et al., 2013; Karska et al., 2013a; Green et al., 2013a; Yıldız et al., 2013; Karska et al., 2014a; Matuszak et al., 2015), the CO transitions from $J = 14 \rightarrow 13$ to $J = 40 \rightarrow 39$ can be approximated with two components: a "warm" component ($T_{\rm rot} \sim 300$ K) and a "hot" component ($T_{\rm rot} \sim 600$–800 K); when detected, the hot component is approximately an order of magnitude less abundant, independent of the source luminosity (Green et al., 2013a). Karska et al. (to be accepted) further constrained the median temperatures of the two components as 324 K and 719 K, using the largest sample of sources studies to date, with a broader range of temperature, 600–1100 K, for the "hot" component. The higher-J CO lines, up to the highest detected in these sources ($J = 48 \rightarrow 47$), have been fitted with an even hotter component (Goicoechea et al., 2012; Manoj et al., 2013; Karska et al., 2014a).

If we use only the two components inferred from the PACS data, the "warm" component alone under-predicts the intensity of the CO lines from $J_{\rm up} \leq 10$. The addition of the "low-J" CO ($J_{\rm up}$=4–13) from SPIRE requires additional one ("cool") or two ("cold" and "cool") component(s), noted in a few previous studies derived from *Herschel*-HIFI, SPIRE, and ground-based observations (e.g. van Kempen et al., 2009a; Goicoechea et al., 2012; Yıldız et al., 2013; Yang et al., 2017b).

The rotational diagrams of the COPS sources all show positive curvature, which is always seen in the CO lines observed with *Herschel* toward protostars (e.g. van Kempen et al. 2010; Goicoechea et al. 2012; Herczeg et al. 2012; Green et al. 2013a; Karska et al. to be accepted). The positive curvature suggests that the CO gas has multiple rotational temperatures increasing with the energy levels, or that the transitions were sub-thermally excited in certain conditions. Neufeld (2012) demonstrated that a low density ($n < 10^{4.8}$ cm^{-3}) and high temperature ($\sim$2000 K) isothermal medium or a power-law distribution of the kinetic temperature produces positive curvature in the CO rotational diagram. The isothermal medium is unlikely to fully describe the CO gas as many studies have shown heterogeneous environments toward protostars (e.g. Dunham et al., 2014a), and the velocity-resolved line profiles show multiple velocity components (e.g. San José-García et al., 2013; Kristensen et al., 2017b). While the rotational temperatures need not equal the kinetic temperatures, we follow most other work in assuming that they do (LTE). In this case, the changing $T_{\rm rot}$ correspond to changes in gas temperature. While the power-law distribution of temperature can

also explain the rotational diagrams (Manoj et al., 2013), we focus here on multiple discrete temperature components.

As we have learned from Section 2.4.1, CO lines remain optically thick up to $J_{\rm up}$=13. The observed fluxes increase in proportion to the optical depth after the correction of optical depth; therefore, the temperatures decrease with increases of the number of molecules. Thus, we need to correct for the effect of optical depth before fitting the rotational diagrams. We use the fitted optical depth as a function of the upper energy to determine the optical depth at each J-level (see Equation 2.2). Finally, we add the systematic uncertainties derived from the differences between the spectroscopy and photometry (3%–16%, see Section 2.2.2).

The previous analyses of rotational temperatures adopted fixed break points to break the CO ladder into pre-determined regions for fitting the temperatures (Green et al., 2013a; Karska et al., 2013a; Manoj et al., 2013). We adopt the fixed break points from Green et al. (2013a) with additional break points at the gap of PACS and SPIRE and the boundary between the two SPIRE modules. The fixed break points separate the CO ladder into $J_{\rm up}$=4–8, $J_{\rm up}$=9–13, $J_{\rm up}$=14–25, and $J_{\rm up}$=28–48. We adopt the choice of breakpoints that has been widely used in many *Herschel* studies (Manoj et al., 2013; Green et al., 2013a; Karska et al., 2013a, e.g.) so that the fitted rotational temperatures can be consistently compared with other studies. There are only three detections of CO lines at wavelengths shorter than 70 μm (B2A module); therefore, we combine the B2A module with the B2B module (70–100 μm). We recover the same division of the rotational temperatures that have been found previously (Figure 2.5, left). Here we label the temperature components by their $J_{\rm up}$-levels, corresponding to the four regions separated by the fixed break points.

However, fixing the break points may restrict the range of the temperatures over which each component can vary. We take this opportunity to investigate the change if the break points remain flexible with a CO ladder with a maximum of 45 lines when combining the CO lines detected in both SPIRE and PACS spectra. We attempt to fit up to four temperature components as well as the break points only if the χ^2 is further minimized by increasing the number of temperature components. The number of free parameters scales with the number of components we fit. We start with a single component fitting, which has two free parameters; by adding one more component, we add three free parameters, one for the break point and two for the line. Thus, the fitting can have a maximum of 11 free parameters. We also require

at least three data points for each component. Each temperature component is fitted separately and simultaneously after determining the break points that separate those components. Finally, the goodness-of-fit is estimated by the reduced χ^2 by considering all fits and the total degrees of freedom from all components.

We include the systematic uncertainties based on the differences between spectroscopy and photometry at given photometry bands when we fit for the rotational temperatures. Systematic uncertainties are applied independently. There is no additional calibration performed for the fitting of rotational temperatures.

With flexible break points, we found that distributions of the four components overlap more with each other (Figure 2.5, right), indicating that the fixed break points indeed restricts the range of fitted temperatures. Two populations are seen from the distribution of $T_{\rm rot}$, a primary population at $\sim$100 K, and a secondary population at $\sim$350 K. Here we do not label the temperature components because there is no restriction on the range of $T_{\rm rot}$ at certain $J_{\rm up}$-level. Many sources have a component around 100 K contributed by the entrained gas in outflows. Yıldız et al. (2013) found similar components labelled as "cold" and "cool" (41–68 K and 109–229 K) with CO data from $J = 2 \rightarrow 1$ to $J = 10 \rightarrow 9$, and our primary population has a similar range of temperature. For the case of flexible break points, the "warm" and "hot" components, which were seen in the $T_{\rm rot}$ distribution with fixed break points, merge together to form the secondary population at $\sim$350 K (centered on 356 K with a 1-σ width of 126 K when fitted with a Gaussian distribution between 200 K and 700 K), where the number of the "very hot" ($\sim$1000 K) components reduces from 3 to 1 compared to the distribution with fixed break points. The secondary population is likely to represent the "warm" component that is ubiquitously found toward embedded protostars (e.g. Green et al. 2013a; Karska et al. 2013a, to be accepted; Kristensen et al. 2017b); Kristensen et al. (2017b) suggested that the universal "warm" component results from CO being the dominant coolant when H_2 cooling becomes insufficient around 300 K because of its widely-spaced energy levels ($E_{\rm u}$=510 K for the $J = 2 \rightarrow 0$ transition).

Although fitting more temperature components to rotational diagrams may further reduce the χ^2 value, we do not expect to find more components in the distribution of rotational temperatures. The exercise of flexible breakpoints was intended to test whether a specific number of components was consistently indicated across the source sample. Figure 2.5 (right) shows the distributions of rotational temperatures from fitting of a maximum of three and four temperature components. We find that the

distribution is well-characterized not by an increasing number of fixed breakpoint components, but more simply by two primary components with flexible breakpoints. This is a simpler solution than the larger number of fixed breakpoint components.

Table 2.6 shows the fitted rotational temperatures with both fixed and flexible break points as well as the corresponding number of molecules in each temperature component. We label the temperature components by the number of components found in each source. Figure 2.4 shows two examples of the rotational diagrams used for this study. High rotational temperatures characterize the high-J CO emission, which has high critical density, $\sim 10^7 cm^{-3}$ at $J_{\rm up}$=30–40. The high-J CO emission comes from recently shocked gas which has been compressed to even higher density. Alternatively, the high-J emission may NOT be in LTE.

We calculate the effect of optical depth on rotational diagram analysis. The correction mostly affects the two coldest components, where the correction of optical depth is directly applied. For the coldest component, the temperature decreases by 14 K on average after the correction, while the temperature drops by 7 K on average after the correction for the second coldest component. The opacity correction also increases the total molecules found in each component. The mean number of the CO molecules in the coldest component increases by a factor of about 15.3 from 1.8×10^{50} to 2.8×10^{51}, and the number of the CO molecules in the second coldest component increases by a factor of about 8 from 7.4×10^{49} to 5.9×10^{50}.

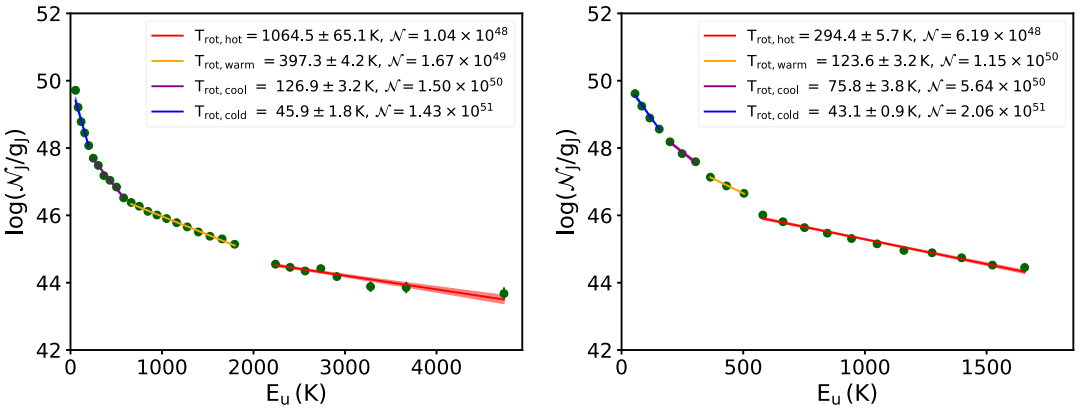

Figure 2.4: The CO rotational diagrams of BHR 71 (left) and VLA 1623−243 (right). The solid lines indicate the fitted component of rotational temperature, while the shaded areas illustrate the corresponding uncertainties.

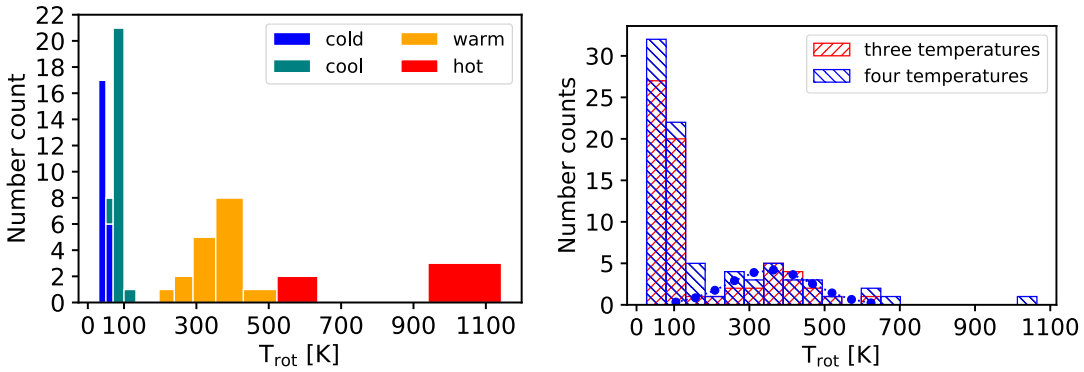

Figure 2.5: The distribution of the fitted rotational temperatures from all sources with fixed break points (left) and flexible break points (right). The blue histogram shows the results of using a maximum of four temperature components, while the red histogram shows the results of using up to three temperature components. The dotted blue line indicates the secondary population fitted with a Gaussian distribution from $T_{\rm rot}$=200–700 K, which centers at 356 K with a 1-σ width of 112 K.

Table 2.6: Rotational Temperatures

Source	T_4 (K)	T_3 (K)	T_2 (K)	T_1 (K)	$\mathcal{N}_4$	$\mathcal{N}_3$	$\mathcal{N}_2$	$\mathcal{N}_1$
B1-a	···	266.5±12.1	83.3±3.3	45.3±0.7	···	$6.3(48)^{+2.4(48)}_{-1.8(48)}$	$5.5(50)^{+2.9(50)}_{-1.9(50)}$	$2.6(51)^{+2.5(51)}_{-3.2(50)}$
	266.5±12.1	113.2±6.3	71.6±1.9	40.8±0.5	$6.3(48)^{+2.4(48)}_{-1.8(48)}$	$1.8(50)^{+1.2(50)}_{-7.1(49)}$	$8.5(50)^{+1.8(50)}_{-1.5(50)}$	$3.4(51)^{+3.0(51)}_{-3.6(50)}$
	14–48	11–13	8–10	4–7	···	···	···	···
B1-c	···	234.4±4.1	90.4±3.2	47.7±1.2	···	$1.1(49)^{+1.8(48)}_{-1.6(48)}$	$1.6(50)^{+6.3(49)}_{-4.5(49)}$	$1.1(51)^{+1.2(51)}_{-2.0(50)}$
	238.5±5.4	138.7±4.1	73.2±0.3	47.7±1.2	$1.1(49)^{+2.4(48)}_{-2.0(48)}$	$4.0(49)^{+1.1(49)}_{-8.6(48)}$	$2.8(50)^{+9.7(48)}_{-9.4(48)}$	$1.1(51)^{+1.0(51)}_{-2.0(50)}$
	15–48	12–14	9–11	4–8	···	···	···	···
B335	···	322.5±5.5	97.9±2.9	47.2±1.3	···	$1.2(48)^{+1.6(47)}_{-1.4(47)}$	$2.5(49)^{+7.5(48)}_{-5.8(48)}$	$1.3(50)^{+1.4(50)}_{-2.8(49)}$
	371.7±8.2	125.1±3.1	80.4±1.4	40.0±1.2	$8.6(47)^{+1.5(47)}_{-1.3(47)}$	$1.2(49)^{+2.9(48)}_{-2.3(48)}$	$4.1(49)^{+4.8(48)}_{-4.3(48)}$	$2.0(50)^{+2.1(50)}_{-4.6(49)}$
	16–48	11–15	8–10	4–7	···	···	···	···
BHR 71	1064.5±65.1	387.0±4.4	128.3±5.0	45.9±1.8	$1.0(48)^{+4.5(47)}_{-3.2(47)}$	$1.8(49)^{+1.5(48)}_{-1.4(48)}$	$1.5(50)^{+4.4(49)}_{-3.4(49)}$	$1.4(51)^{+1.9(51)}_{-4.1(50)}$
	1064.5±65.1	397.3±4.2	126.9±3.2	45.9±1.8	$1.0(48)^{+4.5(47)}_{-3.2(47)}$	$1.7(49)^{+1.3(48)}_{-1.2(48)}$	$1.5(50)^{+3.1(49)}_{-2.6(49)}$	$1.4(51)^{+1.9(51)}_{-4.1(50)}$
	26–48	15–25	9–14	4–8	···	···	···	···
Ced110 IRS4	···	···	68.0±3.0	47.4±0.8	···	···	$1.3(50)^{+7.8(49)}_{-4.8(49)}$	$4.0(50)^{+3.3(50)}_{-5.3(49)}$
	···	···	68.0±3.0	47.4±0.8	···	···	$1.3(50)^{+7.8(49)}_{-4.8(49)}$	$4.0(50)^{+6.2(49)}_{-5.3(49)}$
	···	···	9–48	4–8	···	···	···	···
DK Cha	993.4±109.4	431.1±4.8	117.7±4.6	48.6±1.0	$8.3(47)^{+9.7(47)}_{-4.5(47)}$	$6.9(48)^{+5.0(47)}_{-4.7(47)}$	$8.0(49)^{+2.7(49)}_{-2.0(49)}$	$5.1(50)^{+5.4(50)}_{-8.5(49)}$
	637.2±63.2	428.2±4.4	115.4±3.2	48.6±1.0	$3.8(48)^{+8.4(48)}_{-2.6(48)}$	$7.0(48)^{+5.1(47)}_{-4.7(47)}$	$8.3(49)^{+2.1(49)}_{-1.7(49)}$	$5.1(50)^{+5.3(50)}_{-8.5(49)}$
	31–48	15–30	9–14	4–8	···	···	···	···
GSS 30 IRS1	1061.7±49.6	322.7±6.3	106.1±1.8	52.6±1.1	$6.8(47)^{+2.0(47)}_{-1.6(47)}$	$1.2(49)^{+2.1(48)}_{-1.8(48)}$	$4.7(50)^{+6.9(49)}_{-6.0(49)}$	$2.4(51)^{+2.3(51)}_{-3.5(50)}$
	533.7±18.4	246.3±5.4	106.1±1.8	52.6±1.1	$3.5(48)^{+9.7(47)}_{-7.6(47)}$	$2.0(49)^{+3.6(48)}_{-3.0(48)}$	$4.7(50)^{+6.9(49)}_{-6.0(49)}$	$2.4(51)^{+2.3(51)}_{-3.5(50)}$
	20–48	14–19	9–13	4–8	···	···	···	···
HH 46	···	···	75.9±2.7	44.6±1.1	···	···	$7.7(50)^{+3.6(50)}_{-2.4(50)}$	$4.9(51)^{+5.4(51)}_{-1.0(51)}$
	···	···	83.5±4.0	45.1±0.8	···	···	$5.1(50)^{+3.4(50)}_{-2.1(50)}$	$4.8(51)^{+8.6(50)}_{-7.3(50)}$
	···	···	10–48	4–9	···	···	···	···
IRAS 03245+3002	···	388.8±19.1	88.4±3.1	41.7±1.7	···	$2.2(48)^{+7.5(47)}_{-5.6(47)}$	$8.9(49)^{+3.6(49)}_{-2.6(49)}$	$7.4(50)^{+1.0(51)}_{-2.4(50)}$
	448.1±27.9	113.4±2.2	65.7±0.7	33.5±1.4	$1.7(48)^{+7.1(47)}_{-5.0(47)}$	$3.7(49)^{+8.0(48)}_{-6.5(48)}$	$2.1(50)^{+1.9(49)}_{-1.8(49)}$	$1.4(51)^{+2.0(51)}_{-5.0(50)}$
	16–48	12–15	8–11	4–7	···	···	···	···
IRAS 03301+3111	···	···	111.5±5.1	29.5±1.2	···	···	$6.3(49)^{+2.8(49)}_{-2.0(49)}$	$1.2(51)^{+1.8(51)}_{-4.2(50)}$
	···	···	105.9±3.8	29.5±1.2	···	···	$7.1(49)^{+2.7(49)}_{-1.9(49)}$	$1.2(51)^{+6.4(50)}_{-4.2(50)}$
	···	···	8–48	4–7	···	···	···	···

Table 2.6 (continued)

Source	T_4 (K)	T_3 (K)	T_2 (K)	T_1 (K)	$\mathcal{N}_4$	$\mathcal{N}_3$	$\mathcal{N}_2$	$\mathcal{N}_1$
IRAS 15398−3359	···	···	115.1±3.8	60.5±2.8	···	···	$1.1(50)^{+3.2(49)}_{-2.5(49)}$	$2.0(50)^{+1.6(50)}_{-5.1(49)}$
	···	···	115.1±3.8	60.5±2.8	···	···	$1.1(50)^{+3.2(49)}_{-2.5(49)}$	$2.0(50)^{+6.8(49)}_{-5.1(49)}$
	···	···	9–48	4–8	···	···	···	···
L1157	−2439.8±413.3	367.4±5.1	105.8±3.6	44.1±1.3	···	$1.0(49)^{+1.0(48)}_{-9.3(47)}$	$1.5(50)^{+5.0(49)}_{-3.8(49)}$	$1.5(51)^{+1.8(51)}_{-3.6(50)}$
	680.7±46.1	357.2±5.5	116.6±2.2	47.0±1.3	$2.5(48)^{+1.3(48)}_{-8.6(47)}$	$1.0(49)^{+1.1(48)}_{-9.9(47)}$	$1.1(50)^{+1.9(49)}_{-1.7(49)}$	$1.3(51)^{+1.5(51)}_{-2.8(50)}$
	23–48	15–22	10–14	4–9	···	···	···	···
L1455 IRS3	···	···	···	···	···	···	···	···
	···	···	···	113.2±10.4	···	···	···	$5.1(49)^{+4.0(49)}_{-2.2(49)}$
	···	···	···	4–48	···	···	···	···
L1551 IRS5	···	378.7±9.1	98.3±5.0	46.2±2.1	···	$2.6(48)^{+4.3(47)}_{-3.7(47)}$	$6.4(49)^{+3.3(49)}_{-2.2(49)}$	$3.8(50)^{+4.9(50)}_{-1.2(50)}$
	479.5±10.3	127.8±4.7	78.9±4.4	38.1±1.4	$1.7(48)^{+2.4(47)}_{-2.1(47)}$	$2.7(49)^{+1.1(49)}_{-7.8(48)}$	$1.1(50)^{+5.5(49)}_{-3.7(49)}$	$5.9(50)^{+7.1(50)}_{-1.7(50)}$
	16–48	11–15	8–10	4–7	···	···	···	···
L483	···	···	99.1±6.1	45.0±0.9	···	···	$1.1(50)^{+7.4(49)}_{-4.5(49)}$	$9.1(50)^{+9.6(50)}_{-1.4(50)}$
	···	···	99.1±6.1	45.0±0.9	···	···	$1.1(50)^{+7.4(49)}_{-4.5(49)}$	$9.1(50)^{+1.7(50)}_{-1.4(50)}$
	···	···	9–48	4–8	···	···	···	···
L723 MM	···	···	100.2±4.6	44.8±1.7	···	···	$1.0(50)^{+4.9(49)}_{-3.3(49)}$	$8.9(50)^{+1.1(51)}_{-2.6(50)}$
	···	···	114.3±6.7	47.8±1.5	···	···	$6.7(49)^{+4.1(49)}_{-2.5(49)}$	$7.6(50)^{+2.4(50)}_{-1.8(50)}$
	···	···	10–48	4–9	···	···	···	···
RCrA IRS5A	···	273.4±5.2	88.2±3.2	51.8±1.9	···	$5.4(48)^{+9.1(47)}_{-7.8(47)}$	$4.1(50)^{+1.7(50)}_{-1.2(50)}$	$1.6(51)^{+1.7(51)}_{-3.9(50)}$
	273.4±5.2	119.2±2.0	68.9±1.3	40.7±1.0	$5.4(48)^{+9.1(47)}_{-7.8(47)}$	$1.5(50)^{+2.2(49)}_{-1.9(49)}$	$8.3(50)^{+1.3(50)}_{-1.1(50)}$	$2.7(51)^{+2.5(51)}_{-5.1(50)}$
	14–48	11–13	8–10	4–7	···	···	···	···
RCrA IRS7B/C	598.5±16.4	303.0±4.7	103.7±2.5	61.8±2.3	$4.5(48)^{+1.4(48)}_{-1.1(48)}$	$5.3(49)^{+8.3(48)}_{-7.2(48)}$	$1.3(51)^{+3.0(50)}_{-2.4(50)}$	$4.1(51)^{+3.9(51)}_{-9.0(50)}$
	598.5±16.4	323.7±4.7	101.6±2.2	62.8±1.7	$4.5(48)^{+1.4(48)}_{-1.1(48)}$	$4.2(49)^{+6.1(48)}_{-5.3(48)}$	$1.3(51)^{+3.5(50)}_{-2.8(50)}$	$4.0(51)^{+3.4(51)}_{-6.5(50)}$
	26–48	16–25	10–15	4–9	···	···	···	···
RNO 91	···	···	79.7±4.2	40.5±1.0	···	···	$3.5(49)^{+2.3(49)}_{-1.4(49)}$	$2.2(50)^{+2.4(50)}_{-4.4(49)}$
	···	···	75.9±2.4	37.6±1.4	···	···	$4.2(49)^{+1.3(49)}_{-1.0(49)}$	$2.7(50)^{+1.1(50)}_{-7.8(49)}$
	···	···	8–48	4–7	···	···	···	···
TMC 1	···	359.6±19.9	107.2±3.6	45.9±0.3	···	$1.3(48)^{+5.3(47)}_{-3.8(47)}$	$3.8(49)^{+1.2(49)}_{-9.0(48)}$	$1.7(50)^{+1.4(50)}_{-9.6(48)}$
	359.6±19.9	138.2±5.8	133.4±9.9	44.5±0.4	$1.3(48)^{+5.3(47)}_{-3.8(47)}$	$1.9(49)^{+6.9(48)}_{-5.1(48)}$	$3.0(49)^{+1.1(49)}_{-8.1(48)}$	$1.8(50)^{+1.6(50)}_{-1.1(49)}$
	14–48	11–13	8–10	4–7	···	···	···	···

Table 2.6 (continued)

Source	T_4 (K)	T_3 (K)	T_2 (K)	T_1 (K)	$\mathcal{N}_4$	$\mathcal{N}_3$	$\mathcal{N}_2$	$\mathcal{N}_1$
TMC 1A	···	374.4±13.3	96.4±6.1	38.8±1.0	···	$8.2(47)^{+1.9(47)}_{-1.6(47)}$	$1.8(49)^{+1.2(49)}_{-7.3(48)}$	$1.5(50)^{+1.8(50)}_{-3.4(49)}$
	374.4±13.3	191.3±0.9	99.6±2.7	36.0±1.4	$8.2(47)^{+1.9(47)}_{-1.6(47)}$	$3.5(48)^{+8.6(46)}_{-8.4(46)}$	$1.8(49)^{+3.1(48)}_{-2.6(48)}$	$1.8(50)^{+2.4(50)}_{-5.5(49)}$
	14–48	11–13	8–10	4–7	···	···	···	···
TMR 1	···	392.9±8.7	112.4±3.7	51.6±1.1	···	$2.0(48)^{+3.0(47)}_{-2.6(47)}$	$4.8(49)^{+1.4(49)}_{-1.1(49)}$	$2.3(50)^{+2.2(50)}_{-3.3(49)}$
	392.9±8.7	146.1±2.9	90.1±0.6	57.3±2.7	$2.0(48)^{+3.0(47)}_{-2.6(47)}$	$2.4(49)^{+3.6(48)}_{-3.2(48)}$	$7.4(49)^{+3.1(48)}_{-3.0(48)}$	$1.9(50)^{+1.8(50)}_{-4.7(49)}$
	14–48	11–13	8–10	4–7	···	···	···	···
VLA 1623−243	···	294.4±5.7	86.7±3.8	47.4±1.0	···	$6.2(48)^{+1.0(48)}_{-9.0(47)}$	$3.7(50)^{+1.8(50)}_{-1.2(50)}$	$1.7(51)^{+1.6(51)}_{-2.6(50)}$
	294.4±5.7	123.6±3.2	75.8±3.8	43.1±0.9	$6.2(48)^{+1.0(48)}_{-9.0(47)}$	$1.2(50)^{+2.5(49)}_{-2.1(49)}$	$5.6(50)^{+2.5(50)}_{-1.7(50)}$	$2.1(51)^{+1.9(51)}_{-3.3(50)}$
	14–48	11–13	8–10	4–7	···	···	···	···
WL 12	···	371.6±10.0	113.3±5.1	47.9±3.7	···	$1.5(48)^{+2.7(47)}_{-2.3(47)}$	$6.8(49)^{+2.7(49)}_{-1.9(49)}$	$3.9(50)^{+6.5(50)}_{-1.8(50)}$
	371.6±10.0	165.9±0.0	75.7±1.4	26.8±1.0	$1.5(48)^{+2.7(47)}_{-2.3(47)}$	$2.8(49)^{+2.4(46)}_{-2.4(46)}$	$1.6(50)^{+2.0(49)}_{-1.8(49)}$	$1.2(51)^{+1.5(51)}_{-3.0(50)}$
	14–48	11–13	7–10	4–6	···	···	···	···

There are two sets of rotational temperatures and the numbers of molecules associated with each source. The top row shows the temperatures and the number of molecule fitted from data with *fixed break points*, and the second row shows the temperatures and the number of molecules fitted from data with *flexible break points*. The third row indicates the ranges of J levels where the temperature and number density are fitted. L1014 does not have enough detections of CO for rotational temperature analysis and is not shown in this table. The negative temperature in L1157 are fitted from four CO lines appearing nearly flat in the rotational diagram.

2.4.3 HCO^+

HCO^+ has a higher critical density, $n_{\rm crit}$ =(3.3–9.9) $\times$ 10^7 cm^{-3} for the lines relevant here (Schöier et al., 2005a), which is often used for probing dense molecular gas around protostars. Its effective density can be 1–2 orders of magnitudes lower than the critical density (Evans, 1999b; Shirley, 2015). We found GSS 30 IRS1 and the combined RCrA IRS7B/C have significant detections of HCO^+. RCrA IRS7B/C shows the emission of HCO^+ $J = 6 \rightarrow 5$, $J = 7 \rightarrow 6$, and $J = 8 \rightarrow 7$, while GSS 30 IRS1 shows only the emission of HCO^+ $J = 7 \rightarrow 6$. RCrA IRS7B/C has sufficient amount of HCO^+ detections for rotational temperature analysis. Benz et al. (2016) detected HCO^+ toward 12 YSOs including both low-mass and high-mass sources, suggesting that our low detection rate of HCO^+ $J = 6 \rightarrow 5$ may be due to the lack of spectral resolution, similar to the problem we have on the emission of o-H_2O $1_{10} \rightarrow 1_{01}$. Figure 2.6 shows the constructed rotational diagram along with the fitted rotational temperature of 42.0±2.7 K, which is slightly lower than the "cold" component (51.5±2.5 K) fitted from the CO rotational diagram, hinting that the HCO^+ may be sub-thermally excited or it is simply colder than CO.

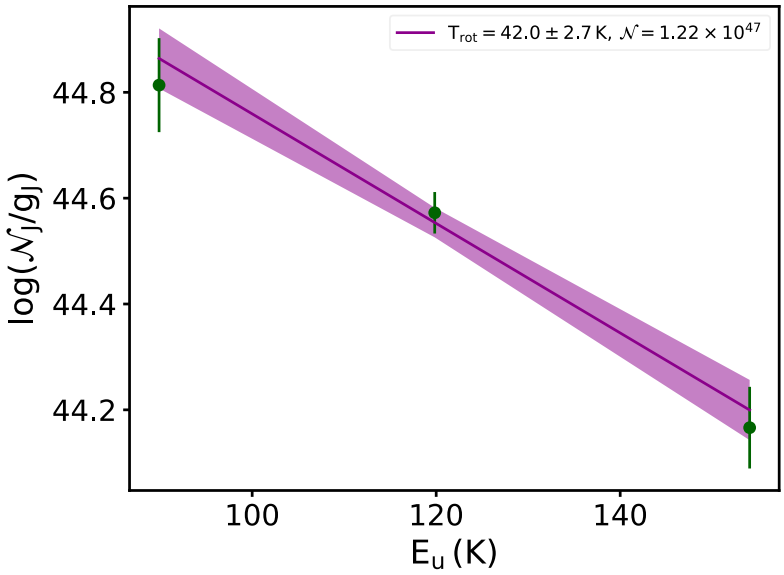

Figure 2.6: The rotational diagram of HCO^+ detected toward RCrA IRS7B/C. The solid line indicates the fitted temperature, and the filled area shows the uncertainty.

2.4.4 Beam Filling Factor

The optical depth and the rotational temperature provide constraints on the beam filling factor of CO emission. We explore the filling factors derived from unresolved CO lines and compare with the maps of low-J CO lines resolved both spectrally and spatially (e.g. Yıldız et al., 2015). To reduce uncertainty, we only calculate the filling factors for the transitions where both ^{12}CO and ^{13}CO emissions are detected.

The brightness temperature of CO emission can be related to the filling factor, rotational temperature, and the optical depth with Equation 2.3.

$$I_\nu = B_\nu(T_\mathrm{B}) = f B_\nu(T_\mathrm{rot})(1 - e^{-\tau}), \tag{2.3}$$

where $\mathrm{B}_\nu(T)$ is the Planck function for a given temperature, and f is the beam filling factor. The T_rot and τ are derived from our analyses above (see Section 2.4.1 and 2.4.2). The rotational temperature is selected from the rotational diagram based on the component of temperature which dominates the transition. The remaining variable is T_B, which can be derived from the integrated fluxes if we know the line width, which is much smaller than the spectral resolution of SPIRE. Yıldız et al. (2013) presented the observations of CO $J = 6 \rightarrow 5$ toward 26 Class 0+I protostars, 14 of which are included in the COPS sample. We calculated an average FWHM of 4.3±1.4 km s^{-1} for the CO $J = 6 \rightarrow 5$ line from T_peak and the integrated fluxes presented in the Appendix of Yıldız et al. (2013), assuming Gaussian profiles. We take the 1-σ value of 5.7 km s^{-1} as the line width for the calculation of the filling factor since the CO line often become broader at higher J-levels (Yıldız et al., 2013, 2015; Kristensen et al., 2017b).

Table 2.7 shows the filling factors calculated with Equation 2.3. The filling factors are all smaller than 0.53, ranging from 0.035 to 0.53. We compared our result with the maps shown in Yıldız et al. (2015), where 6 COPS sources (L1551 IRS5, Ced110 IRS4, GSS 30 IRS1, HH 46, DK Cha, and TMR 1) were observed in either CO $J = 3 \rightarrow 2$ or CO $J = 6 \rightarrow 5$ lines. In general, the relative values of our filling factors are consistent with the maps, showing that GSS30 IRS1 and HH 46 have the densest emission at the central $\sim$30$''$ regions. However, the maps of TMR 1 and DK Cha show the emission extending in the central $\sim$20$''$ regions, suggesting a higher filling factor than 0.074 (or 0.035). Thus, we are likely to underestimate the filling factor, perhaps because we took a conservative estimate of the line width. The uncertainty on the line width

leads to a factor of two difference in the filling factor. Another source of uncertainty comes from the correction of optical depth. We overestimate the optical depth by using the unresolved SPIRE spectra (see Section 2.4.1). A lower optical depth results in a lower $(1-e^{-\tau})$ in Equation 2.3 but a higher $T_{\rm rot}$ at the low-J CO lines. However, we found that if we artificially decrease the optical depth by 50%, $T_{\rm rot}$ only increases 1% on average. Thus, an overestimation of optical depth makes us underestimate the derived filling factor. Outflows often show clumpy morphology (Arce et al., 2013; Lee et al., 2015a), which may remain unresolved in the observations presented by Yıldız et al. (2013). Thus, the filling factor is prone to be underestimated.

The beam filling factor decline as the J-level increases. As we learned from Kristensen et al. (2017b), the CO $J = 16 \rightarrow 15$ is dominated by broad components coming from the cavity shocks at the inner regions of outflow/envelope. If the CO emission from the cavity shocks becomes more significant as the J-level increases, one should expect a decrease of the spatial extent of CO emission, closer to the small values found for water by Mottram et al. (2014b). Thus, the filling factors extracted from the 1D spectra, which cover apertures $>20''$, naturally decrease with the increase of J-level due to the unresolved spatial distribution.

Table 2.7: Beam filling factor of CO lines

Line	*L1551 IRS5*	*Ced110 IRS4*	*GSS 30 IRS1*	*VLA 1623−243*	*WL 12*	*RCrA IRS5A*	*RCrA IRS7B/C*	*HH 46*	*DK Cha*	*TMR 1*
CO $J = 5 \rightarrow 4$	0.14	0.043	0.41	0.30	0.061	0.42	0.75	0.16	0.088	···
CO $J = 6 \rightarrow 5$	···	0.061	0.39	0.29	0.043	0.39	0.73	0.15	···	0.044
CO $J = 7 \rightarrow 6$	···	···	0.30	···	···	···	0.60	···	···	···
CO $J = 8 \rightarrow 7$	···	···	···	···	···	···	0.48	···	···	···
CO $J = 9 \rightarrow 8$	0.054	···	0.11	0.088	···	···	0.71	···	···	···

2.4.5 The Correlations of Line Emission

Line emission from different molecules and atoms in the embedding envelope carries information of the physical properties of the gas. However, a complete modeling of the line emission is complicated by the complexity of source-to-source difference and the combination of emission from different components (envelope, outflow, and shocks). Thus, we took a different approach to investigate the line-to-line correlations from all of the lines detected from the 1D spectra. We use the generalized Spearman's rank correlation to estimate the correlations of all line pairs detected toward all COPS sources, using `ASURV` Rev. 1.2 (Isobe & Feigelson, 1990; Lavalley et al., 1992), which implements the methods presented in Isobe et al. (1986). The Spearman's rank correlation estimates how well the fluxes from two transitions can be described by a monotonic function. We further compute the significance of the Spearman's correlation coefficient (r) using the Fisher transformation (Equation 2.4)

$$z = \sqrt{\frac{n-3}{1.06}}\frac{1}{2} ln\left(\frac{1+r}{1-r}\right), \tag{2.4}$$

where z is the significance, $n = 20$ is the sample size, and r is the Spearman's rank correlation coefficient. `ASURV` allows us to consider both the detections and the upper limits, so that the correlations remain unbiased when only a few detections are found for high energy emission lines. We restricted our analysis to 20 sources, where both SPIRE and PACS spectra are available, to have the same number of sources for all lines.

2.4.5.1 Correlation: CO

We found that the correlation strengths of all CO line pairs show systematic behaviors within three square regions (Figure 2.8). Those regions coincide with the wavelength ranges covered by SPIRE-SLW, SPIRE-SSW, and PACS R1 modules, suggesting an instrumental effect. The regions covered by the PACS B2A and B2B modules show less obvious systematic effect due to fewer detections of high-J CO lines. Therefore, we only focus the correlations *within* the instrumental boundaries in the following discussion. We discuss the characteristics of the distribution of correlations of different species in the following sections. We first discuss the correlations of CO shown in Figure 2.8; then we describe the correlations of other species, shown in Figure 2.9.

Within each module, the correlation strength smoothly decreases as the difference between the $J_{\rm up}$-levels of two lines increases. No CO lines show significant offset of correlation strength other than the smooth decrease over J-levels. For each CO line, the correlation strength gradually decreases when comparing either with a higher-J CO line or a lower-J CO line, showing no clear asymmetry on the distribution of correlations. The smooth variation of the correlation strength together with the discrete origin of CO emission evident in the velocity-resolved profiles (Kristensen et al., 2017b) suggests that each component of the CO emission contributes to a wide range on energy levels, and the contributing ranges of J-levels overlap well with each other, so that there is no distinct discontinuity seen in the distribution of correlations.

2.4.5.2 Correlation: ^{13}CO

The ^{13}CO lines correlate with each other, but show much more variation from pair to pair than the distribution of correlations for CO lines (Figure 2.9), reflecting the lower detection rate of ^{13}CO lines compared to CO lines. Weaker but significant correlations are also found with low-J ^{13}CO lines. The ^{13}CO $J = 7 \rightarrow 6$ line shows relatively low strengths of correlation with other ^{13}CO lines, mainly due to the fact that it is only detected toward GSS 30 IRS1 and RCrA IRS7B/C (see more discussion of ^{13}CO emission in Section 2.4.1).

2.4.5.3 Correlation: H_2O

Figure 2.9 presents the distribution of correlation strength of selected H_2O lines, which have multiple detections among the entire sample. All H_2O lines best correlate with other water lines. Two selected H_2O lines are observed by SPIRE, including p-H_2O $1_{11} \rightarrow 0_{00}$ (269 μm) and p-H_2O $2_{02} \rightarrow 1_{11}$ (303 μm). The o-H_2O $1_{10} \rightarrow 1_{01}$ line at 557 GHz (538 μm; $E_{\rm up}/k = 61$ K), predominantly observed with HIFI, is not detected toward most of COPS sources with SPIRE (see the discussion in Section 2.3.6.1). Three H_2O lines are selected from the PACS spectra, including p-H_2O $3_{13} \rightarrow 2_{02}$ (139 μm), o-H_2O $3_{03} \rightarrow 2_{12}$ (174 μm), and o-H_2O $2_{12} \rightarrow 1_{01}$ (179 μm). Figure 2.7 shows the correlations of the selected water lines with the CO lines. All water lines show better correlations with the CO lines in the middle of the range between $J_{\rm up}$=4–25. The instrumental effect causes the discontinuity in the distribution of correlations. The water lines observed with PACS typically have a higher correlation with the CO

lines compared to the water lines observed with SPIRE, however, they all have a similar behavior for the correlations with CO lines.

Other studies have shown that the low-J CO lines have weaker correlations with water. Kristensen et al. (2012b) found a weak correlation between o-H_2O $1_{10} \rightarrow 1_{01}$ line and CO $J = 3 \rightarrow 2$ from 29 protostars, eight of which are included in this analysis. Kristensen et al. (2017b) presented a similar analysis for a larger sample. The water line also show inconsistent spatial extent with CO $J = 3 \rightarrow 2$ line (Santangelo et al., 2012a, 2014), whereas the high-J CO emission spatially coincides with the water emission. The higher correlation of water lines with CO ranging from $J_{\rm up}$=10–15 suggests hidden components associated with both species, possibly the cavity shocks in the outflow due to the similar line profile between the emission of CO $J = 16 \rightarrow 15$ and water (Kristensen et al., 2012b, 2017b).

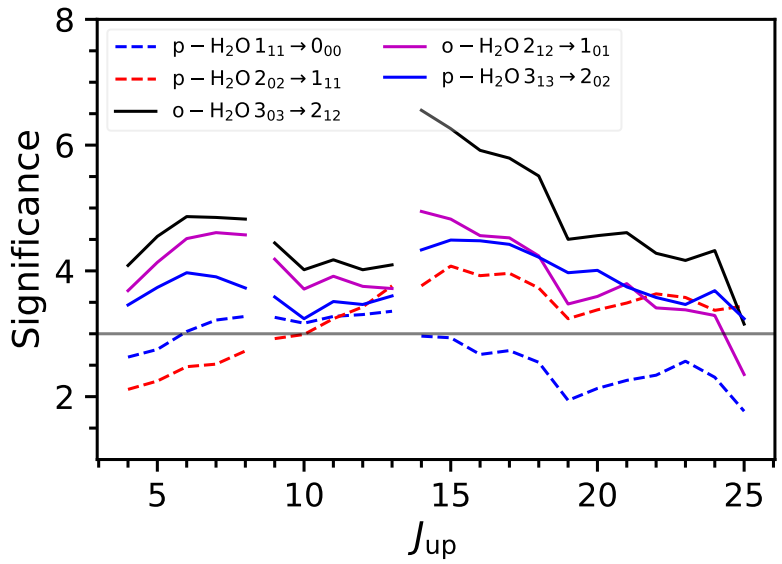

Figure 2.7: The 1D distributions of the significance of correlation with the CO lines for five water lines observed with PACS (p-H_2O $3_{13} \rightarrow 2_{02}$, o-$H_2O$ $3_{03} \rightarrow 2_{12}$, and o-$H_2O$ $2_{12} \rightarrow 1_{01}$) and SPIRE (p-$H_2O$ $1_{11} \rightarrow 0_{00}$ and p-H_2O $2_{02} \rightarrow 1_{11}$).

2.4.5.4 Correlation: OH

We select the strongest OH doublet lines around 119 μm to investigate the correlation of OH lines with other species. The OH lines correlate with CO lines ($J_{\rm up} \leq 24$) and H_2O lines. The correlations between OH and high-J CO lines ($J_{\rm up} > 24$) are

relatively weak despite the fact that high-J CO lines are detected toward one-third of the entire sample. Wampfler et al. (2013) found that the OH from a sample of Class 0+I sources, where four of them are included in this study, and intermediate-mass protostars shows correlations with water and [O I]. An outflow origin was suggested by the broad component found in the line profiles of both high-mass and low-mass protostars, W3 IRS5 (Wampfler et al., 2011) and Serpens SMM1 (Kristensen et al., 2013). The broad component contributes significantly to the high-J CO lines, such as CO $J = 16 \rightarrow 15$ (Kristensen et al., 2017b). Thus, it is reasonable to have significant correlations between OH and high-J CO lines given their similar origins. While our result suggests that OH correlates with water, the COPS sources show only 2.6σ and 2.4σ correlations between OH and [O I].

Since the water emission mostly traces the outflows (Kristensen et al., 2012b; Santangelo et al., 2014), the correlation between OH and water suggests that H_2O and OH may co-exist in the outflow (Mottram et al. 2014b; Kristensen et al. 2017b, Kristensen & Wampfler in prep.). Karska et al. (2013a) and Karska et al. (to be accepted) suggest the presence of OH from the irradiated shocks that best describe the emission of water and high-J CO lines.

2.4.5.5 Correlation: Atomic Species

The [C I] lines at 370 μm and 609 μm are widely detected toward our sample. The two lines show correlations with low-J ^{13}CO lines, whereas some correlation is found with the low-J ^{12}CO lines and the [C I] line at 370 μm. The ^{13}CO lines (e.g. ^{13}CO $J = 6 \rightarrow 5$) are found to trace the UV-heated outflow cavity wall as well as the quiescent envelope (Yıldız et al., 2012, 2015), and the same origins were suggested for the [C I] 370 μm line (van Kempen et al., 2009c).

The forbidden transition of atomic oxygen, which is predominantly detected at 63 μm, shows correlations with CO lines, and correlates better with the CO lines ranging from $J_{\rm up}$=10 to 24. [O I] is thought to be a tracer of outflow (Hollenbach, 1985a; Dionatos & Güdel, 2017), at least for the short term activity of outflows (Mottram et al., 2017). The emission of outflows contributes significantly to the high-J CO line, so greater strengths of correlation are to be expected between the [O I] line and high energy CO lines. Toward NGC1333 IRAS4A, Kristensen et al. (2017a) found that part of the [O I] line at 63 μm exhibits the same line profile as

the CO $J = 16 \rightarrow 15$ line and few water lines at the same velocity channels.

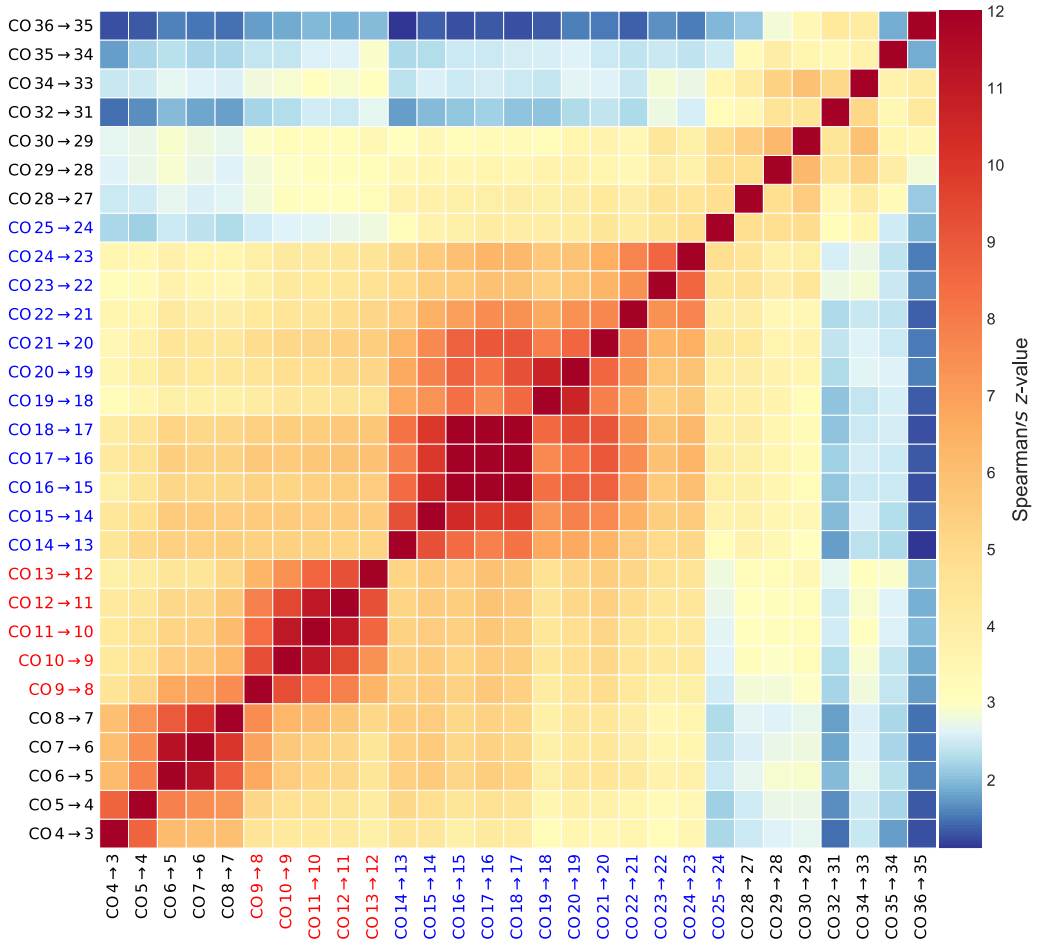

Figure 2.8: The Spearman's z-value for all CO line pairs. The colors of labels indicate the lines covered by the same module/instrument.

2.4.6 Spatial Extent of Line and Continuum Emission

In the previous analyses, we focused on the 1D spectra for simplicity. In fact, the SLW and SSW modules in SPIRE have 19 and 35 spaxels in a hexagonal layout with separations of 19″ and 33″ (see the "plus" markers in Figure 2.10), respectively, providing information on the spatial morphology of emission lines. Figure 2.10 shows two contours of CO $J = 4 \rightarrow 3$ and CO $J = 10 \rightarrow 9$ detected toward VLA 1623−243 as examples. The CO emission is detected, not only at the central position but also in the outer spaxels, and the morphology also varies from line to line. Although it

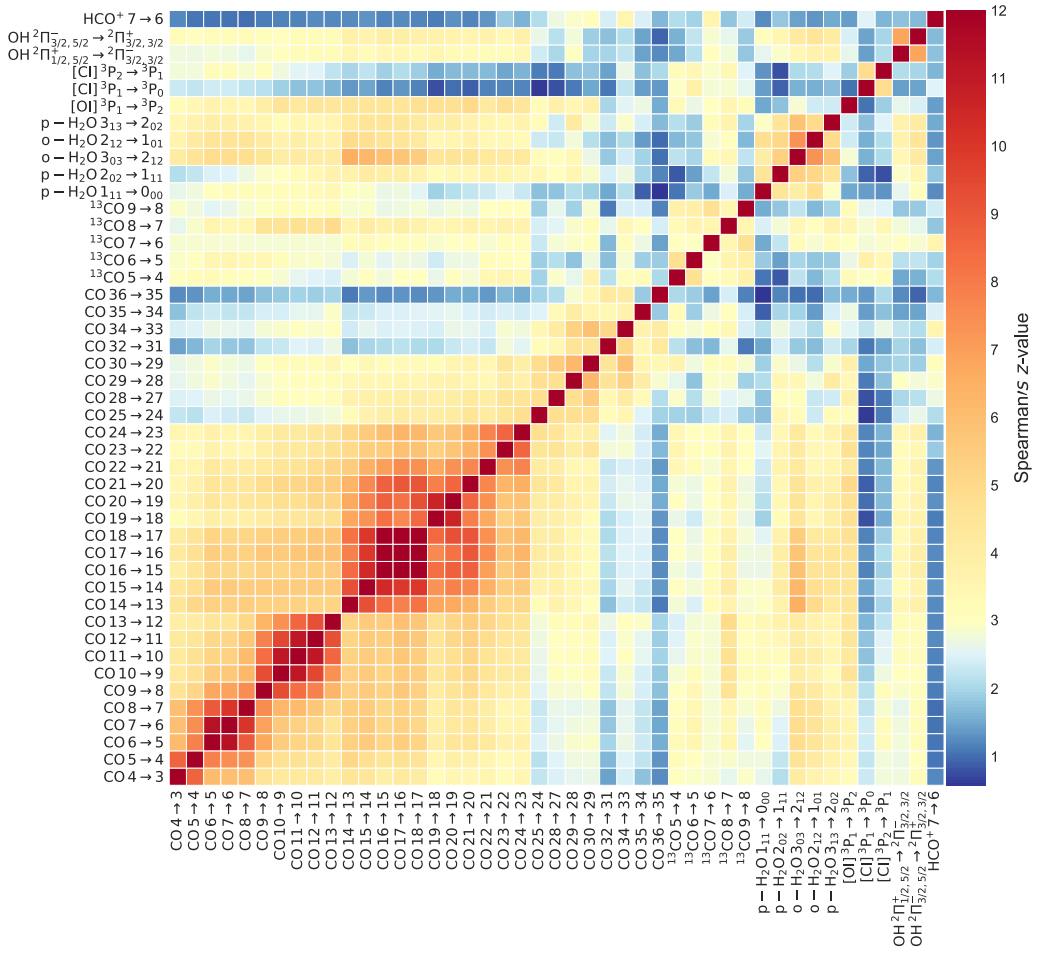

Figure 2.9: The Spearman's z-value for all line pairs.

is easier to show the morphology of emission lines as contours, the information on spatial extent needs to be simplified when we investigate the morphology of each line toward all sources at once.

2.4.6.1 1D profiles of Morphology

We take advantage of the hexagonal spaxel layout to project the 2D morphology into a 1D profile as a function of azimuthal angle. For each non-central spaxel, we first calculate its distance to the central spaxel and the azimuthal angle with respect to north. Then we take the ratio of the flux at the non-central spaxel to the flux at the central spaxel to construct a 1D profile of the flux ratios as a function of the azimuthal angle. We restrict our analysis to the outer spaxels within a radius of 75″

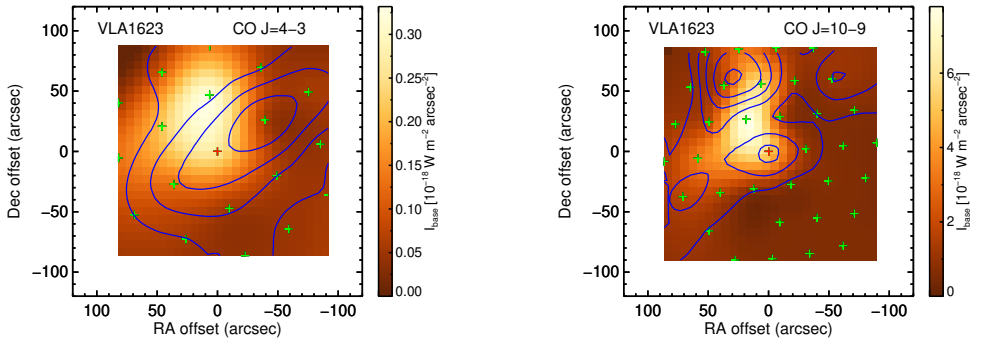

Figure 2.10: The smoothed contours of CO $J = 4 \rightarrow 3$ and CO $J = 10 \rightarrow 9$ emission detected toward VLA 1623−243. The blue contours indicate the line fluxes down to 20% of the peak flux, and the flux level increases by 20% between contours. The "plus" signs mark the location of spaxels in green for detections. The central position is plotted in red "plus." The background image is the smoothed distribution of continuum at the line centroid.

from the central spaxel to exclude the low SNR outermost spaxels. The 75″ radius allows us to include the nearest hexagon in the SLW module (6 spaxels), and the two nearest hexagons in the SSW module (16 spaxels). As the distance to the central spaxel increases, the detected line flux generally decreases as well; however, in some cases, including B1-c, BHR 71, L1157, L1551 IRS5, VLA 1623−243, and WL 12, the strongest CO emission is found at off-center positions. We reduce the radius to 50″ for RCrA IRS5A to avoid source confusion.

We apply a Gaussian smoothing kernel to the profile of flux ratios to produce a smooth profile for investigating the large scale morphology. The Gaussian kernel has a 1-σ width of 30 degree for a 60 degree spacing between two adjacent spaxels in the inner ring.

With the 1D profiles of all CO emission lines derived for each source, we investigate the variation of morphology of CO emission from line to line in two ways, the smoothed 1D profile and the difference of the maximum and minimum ratios of the 1D profile.

2.4.6.2 Morphology with the 1D Profiles

Figure 2.11 shows the smoothed profiles of CO emission lines. Six sources are excluded due to the low detection rate at the outer spaxels; therefore, not enough

data are available for constructing the 1D profile. In principle, if the emission centers at the central spaxel and decreases outward in all directions uniformly, the 1D profile will appear to be a flat line (e.g. WL 12). If the distribution of the emission is concentrated but offset from the center, the 1D profile will show a single peak at the angle toward the offset spaxel (e.g. HH 46). If the distribution shows a bipolar feature, the 1D profile will have two peaks at two azimuthal angles separated by the angle between two lobes (e.g. BHR 71). All three cases are seen in Figure 2.11.

We found that all bipolar features seen in the 1D profiles correspond to the observed outflows in the spatially-resolved maps. The single peak profiles also agree with the maps, suggesting a single outflow. We discuss the detailed comparison in Appendix A.3. For the sources with two peaks, we noted that the flux ratio decreases as the $J_{\rm up}$-level increases. In addition to the variation of the flux ratios, we sometimes found the positions of the peaks also vary with the $J_{\rm up}$-level (B1-c, BHR 71, and L1157); however, this variation may result from the difference of spaxel layout of the SLW and SSW modules, which changes between $J_{\rm up}$=8 and 9. Also, in the cases of L483, the lower-J CO lines show two-peak profiles, but only a dominant peak exists in the profiles of the higher-J CO lines due to the lack of detections at the higher-J CO lines, making one of the lobes disappear from the observed morphology.

2.4.6.3 Variations of Bipolarity

Beside the visual inspection of the 1D profiles, we explore the difference between the maximum and the minimum values (hereafter the peak-to-valley difference) of each profile as a probe of morphology. A flat profile will result in a difference close to zero, while a strong double-peak profile leads to a significant difference. However, a double-peak profile produces the same difference as a equally strong single-peak profile. Thus, we only compare the peak-to-valley difference for the sources with bipolar features.

Figure 2.12 shows the distribution of the peak-to-valley difference derived from the sources with more than three detections in the outer spaxels. The sources include B1-c, L483, L1157, HH 46, IRAS03245+3002, BHR 71, GSS 30 IRS1, and VLA 1623−243, where B1-c, L483, L1157, HH 46, and IRAS 03245+3002 are only considered for the SLW module. Selecting those sources reduces the effect of sensitivity (see Appendix A.3). The values of each source were normalized by the SSW and

SLW modules before we averaged the peak-to-valley differences of all COPS sources. The peak-to-valley difference shows a shallow decrease at $J_{\rm up}$=4–8, and exhibits a steady decrease at $J_{\rm up}$=9–13, suggesting that the bipolar feature is diminishing as the J-level increases at higher-J regime.

The change of beam size between the two SPIRE modules hinders a direct comparison of the peak-to-valley differences from the SLW and SSW modules. We should cautiously conclude that the diminishment of the bipolar feature is seen in each module.

To summarize, the flux ratios (outer to center) as a function of azimuthal angles simplifies the 2D morphology to the 1D profiles. Among the 17 sources, 6 sources show bipolar distributions of CO emission lines, while single lobes and irregular profiles are seen in the 1D smoothed profiles of a further 11 sources. The morphology identified from the 1D profiles is consistent with the velocity-resolved observations, suggesting that the extended CO emission seen in the SPIRE data can be related to outflows. The CO emission exhibits bipolarity between $J_{\rm up}$=4–13. We use the peak-to-valley difference derived from the smoothed 1D profiles to quantify the strength of bipolarity, and find that the bipolarity decreases as the J-level increases.

2.5 Discussion

2.5.1 SED Classification

Several methods of classification have been established in the past few decades, such as the spectral index at near-infrared wavelengths (Adams et al., 1987), bolometric temperature (Myers & Ladd, 1993; Chen et al., 1995a), and the ratio of bolometric luminosity to the submillimeter luminosity (Andre et al., 2000). Evans et al. (2009b) summarized the history of classification methods. SED classes were assigned for sources in the combined c2d and Gould Belt *Spitzer* Legacy programs by Dunham et al. (2015), who demonstrated that the main limitation was the lack of well-sampled data through the far-infrared to submillimeter. Those data are now available, albeit for only a small sample, so we focus in this section on whether the previous conclusions are changed by such data.

Table 2.3 shows the $\alpha_{\rm NIR}$, $T_{\rm bol}$, $L_{\rm bol}$, $L_{\rm smm}$, and the corresponding classifications based on each method for all sources. Our sources are all Class 0 or I with 23

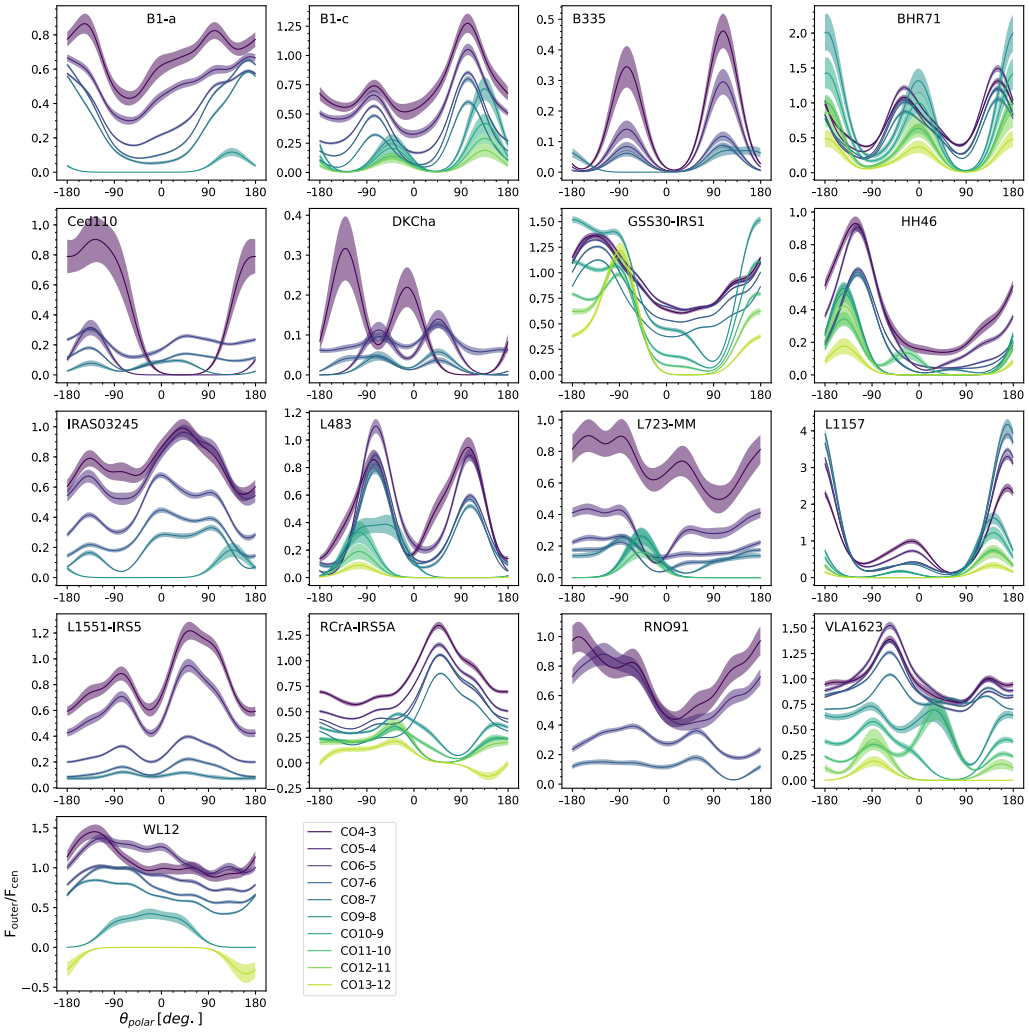

Figure 2.11: The distribution of flux ratios with the flux at the central spaxel as a function of the azimuthal angle. The colors of the lines indicate the different $J_{\rm up}$-levels of the CO lines, and the shaded area represents the uncertainty of the smooth profile. We only consider the outer spaxels within 75″ from the central spaxel, yielding 6 and 16 outer spaxels for the SLW and SSW modules, which have spaxels in hexagonal layout with separations of 19″ and 33″, respectively. The 75″ radius is reduced to 50″ for RCrA IRS5A to avoid source confusion.

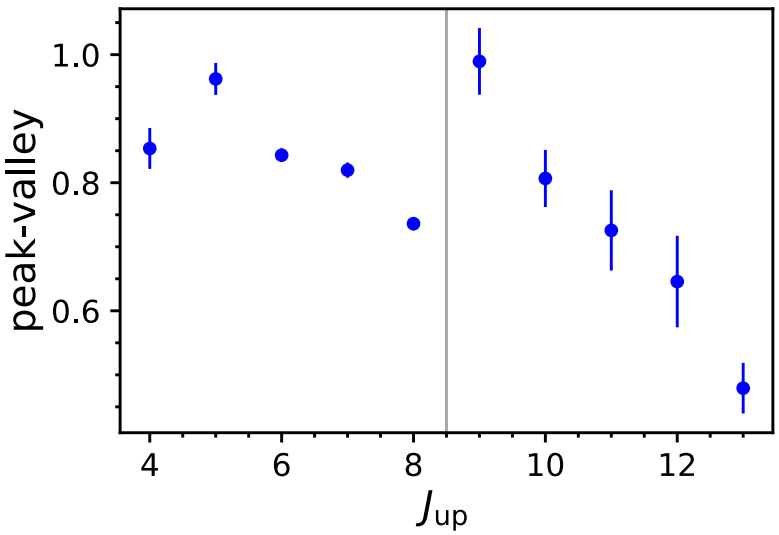

Figure 2.12: The averaged peak-to-valley differences from the 1D profiles of the sources with more than three detections at the outer spaxels. The peak-to-valley differences of each source were normalized separately for the SLW and SSW modules before we took the average of all sources. The vertical line separates the SLW and SSW modules.

of 26 protostars classified as Class 0 by the $L_{\rm bol}/L_{\rm smm}$ criterion. In the following paragraphs, we follow the original definition (Andre et al., 1993a) of the Class 0 protostars, $L_{\rm bol}/L_{\rm smm} > 200$, and ask if other classification methods agree with that classification. This parameter was found to be the best indicator of age for very young systems in models that followed the SED evolution through the infall phase (Young & Evans, 2005; Dunham et al., 2010b, 2014b).

The original definition of SED classes was based on the slope of the relation between $\log(\lambda F_\lambda)$ and $\log(\lambda)$ between 2 and 25 μm (Adams et al., 1987; Andre et al., 1993a; Greene et al., 1994), the spectral index α (denoted as $\alpha_{\rm NIR}$ in this paper). While useful for distinguishing Classes II and III from earlier classes, many papers have shown that it cannot separate Class 0 from Class I sources (e.g., Dunham et al. 2015) and this conclusion is borne out in Figure 2.13. The combined Class, 0+I, defined by Dunham et al. (2015), is separated from Class II by $\alpha_{\rm NIR}$, with only three exceptions: IRAS 03301+3111 and TMC 1A, and DK Cha, which are classified as flat spectrum sources.

The bolometric temperature, $T_{\rm bol}$, is also commonly used to separate Class 0

from Class I. In this framework, Class 0 sources have $T_{\rm bol}$ less than 70 K. However, $T_{\rm bol}$ is quite sensitive to the near-IR flux due to inclination effects. With inclination correction, protostars with measured $T_{\rm bol} < 70$ K are relatively rare, making up 3% of the distribution of protostars in Orion (Fischer et al., 2013). Figure 2.13 shows that our well-sampled data confirm previous results (e.g. Figure 2 of Dunham et al. 2014b) showing that many Class 0 sources (using $L_{\rm bol}/L_{\rm smm}$) fall into Class I according to $T_{\rm bol}$. In particular, 10 of 26 protostars are classified as Class I (or flat) sources by $T_{\rm bol}$, but as Class 0 sources by $L_{\rm bol}/L_{\rm smm}$. No simple adjustment of the boundaries can bring the two tracers into substantially better agreement.

The original idea for defining SED classes and variables like $T_{\rm bol}$ was that they would reflect physical stages. In particular, a Class 0 source would ideally correspond to a Stage 0 source, with more mass in the envelope than in the star. While there is general agreement between classes and stages in simulations (Robitaille et al., 2006a), variations in original core mass (affects $L_{\rm smm}$), orientation relative to the observer (affects $T_{\rm bol}$), and evolutionary path (e.g., episodic accretion) make this connection between class and stage difficult (Dunham et al., 2010b; Fischer et al., 2017). Harsono et al. (2014) found three Taurus sources in the COPS sample, TMC 1, TMC 1A, and TMR 1, have more than 70% of the total mass in the central protostars, suggesting Stage I sources; however, all three sources are classified as Class 0 sources by $L_{\rm bol}/L_{\rm smm}$.

Without even a decent estimate of the stellar mass in deeply embedded stages, only indirect proxies are available. Mottram et al. (2017) found that the force in the entrained CO gas in the outflows ($F_{\rm CO}$ derived from CO $J = 3 \rightarrow 2$ maps) correlates weakly with $L_{\rm bol}$ (p=3.5σ), whereas $F_{\rm CO}$ are systematically different for Class 0 and I sources classified by $T_{\rm bol}$.

We explore the correlation of the total CO luminosity ($L_{\rm CO}$) with different classification indicators. We sum up the luminosities of all CO lines with the optical depth correction for calculating $L_{\rm CO}$. Figure 2.14 shows the relation of $L_{\rm CO}$ versus $L_{\rm bol}/L_{\rm smm}$, $L_{\rm bol}$, and $T_{\rm bol}$, where $L_{\rm CO}$ is the total CO luminosity from the CO lines observed with PACS and SPIRE. We found a strong linear relation between $L_{\rm CO}$ and $L_{\rm bol}$, which can be expressed as

$$log(L_{\rm CO}) = (0.62 \pm 0.14) log(L_{\rm bol}) - 2.10 \pm 0.13, \tag{2.5}$$

but no systematic offset of $L_{\rm CO}$ distinguished by the $T_{\rm bol}$ of the sources. The same

scenario is also found for the HOPS and DIGIT programs (Manoj et al., 2013, 2016).

We found that the classification of embedded protostars still remains uncertain with the addition of *Herschel*-SPIRE spectra. The two main classification methods, $L_{\rm bol}/L_{\rm smm}$ and $T_{\rm bol}$, only agrees for 15 of 26 COPS sources. Studies that modeled the infall process of embedded protostars found the $L_{\rm bol}/L_{\rm smm}$ better described the evolution of protostars (e.g. Young & Evans, 2005; Dunham et al., 2010b, 2014b), whereas some studies found that the classification based on $T_{\rm bol}$ is more consistent with the evolution of outflows (e.g. Mottram et al., 2017). Direct investigation on the properties of central protostars will provide an accurate estimate on the evolutionary of embedded protostars.

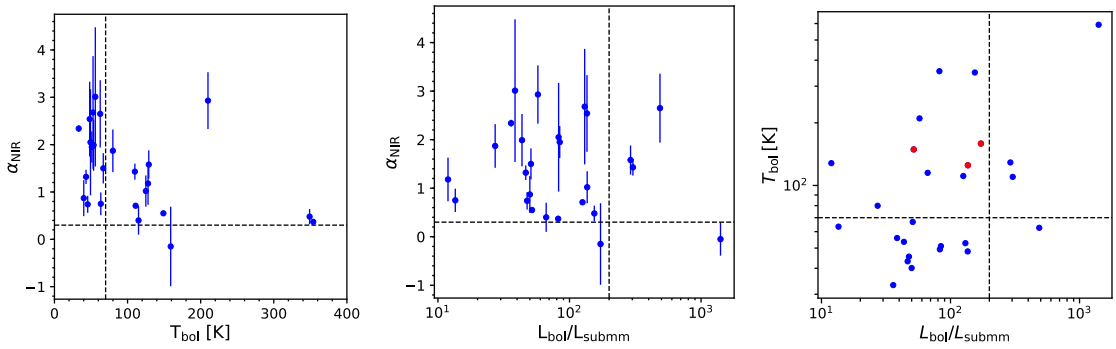

Figure 2.13: **Left:** The relation between $\alpha_{\rm NIR}$ and $T_{\rm bol}$. **Middle:** The relation between $\alpha_{\rm NIR}$ and the ratio of $L_{\rm bol}$ to $L_{\rm smm}$ for all sources in logarithm scale. **Right:** The relation between $T_{\rm bol}$ and the ratio of $L_{\rm bol}$ to $L_{\rm smm}$ for all sources in logarithm scale. The three Taurus sources (TMR 1, TMC 1, and TMC 1A) that are suggested as Stage I sources (Harsono et al., 2014) are shown in red.

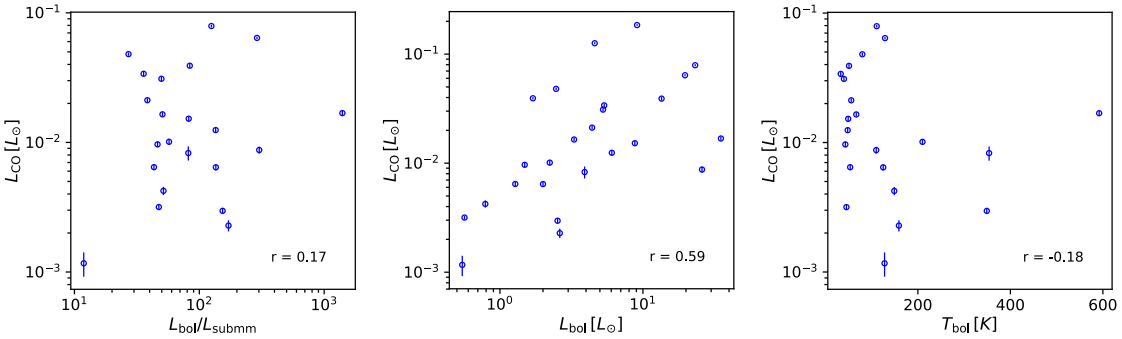

Figure 2.14: The relation of $L_{\rm CO}$ verses $L_{\rm bol}/L_{\rm smm}$, $L_{\rm bol}$, and $T_{\rm bol}$ from left to right. The Pearson's correlation coefficient is shown in the bottom right for each relation.

2.5.2 The Origin of CO Emission

It has been proposed by both observational and theoretical studies that different structure, such as UV-irradiated cavity walls, shocks, and the molecular envelope, may be responsible for CO emission over different ranges of J-levels. (e.g. van Kempen et al., 2010; Visser et al., 2012a; Manoj et al., 2013; Mottram et al., 2014b; Lee et al., 2015b; Kristensen et al., 2017b). Combined with the PACS data, the COPS program covers a wide range of CO lines and the spatial distribution of CO emission, providing us a unique opportunity to review this issue with a more comprehensive view. We discuss the origin of CO emission in the context of spatial extent, the comparison with kinematic studies, the rotational diagrams, and the distribution of correlations.

In Section 2.4.6, we have concluded that the extended CO emission observed toward the COPS sample has an outflow-related origin. Santangelo et al. (2014) found that the morphology of CO $J = 6 \rightarrow 5$ line is much more consistent with the spatial extent of water emission, which traces the shocked gas, than the morphology of CO $J = 3 \rightarrow 2$ line. This comparison shows that the higher-J CO line traces the shocked gas, while the lower-J CO line traces the gas entrained by outflows. Velocity-resolved studies with HIFI also show a similar line profile between water and CO lines (Kristensen et al., 2012b; Yıldız et al., 2013; Mottram et al., 2014b). Yıldız et al. (2013) showed that the CO $J = 10 \rightarrow 9$ line is broader than the CO $J = 3 \rightarrow 2$ line, where the water emission has a broad line width. For higher-J CO lines, Kristensen et al. (2017b) found two components in the line profile of CO $J = 16 \rightarrow 15$ emission, a narrow offset component and a broad centered component. They suggested that the narrow offset component originates from the spot shocks, while the broad centered component comes from cavity shocks or disk wind. The profile of CO emission seems to change from centered narrow+broad components from the quiescent envelope and outflowing material at low-J ($J = 3 \rightarrow 2$) to a broader component along with a narrow offset component dominated by cavity shocks (or disk wind) and spot shocks, respectively. It is clear that there are multiple origins contributing to the CO emission, likely dominating in different ranges of energy levels of CO.

We also see multiple origins of CO emission from our analysis of the rotational temperatures. Figure 2.5 (right) shows the distribution of the rotational temperatures fitted with flexible break points, suggesting a primary population around 100 K (cold), and a secondary population around 400 K (warm). The cold population represents

the entrained gas in the outflows; the warm population corresponds to the cavity shocks (or disk wind), which contributes to the broad component seen in the line profiles of CO $J = 16 \rightarrow 15$ (Kristensen et al., 2017b). Our spectrally unresolved data are insensitive for identifying spot shocks. However, we do not find the proposed rotational temperature ($\sim$700 K) for spot shocks in the distribution of rotational temperatures, unless we use fixed break points. We detect CO lines at $J_{\rm up}$=24–38, excluding $J_{\rm up}$=25 and 26, which are in the gap between two PACS modules, toward 5 sources on average. Thus, we conservatively argue that spot shocks are missing from our analysis of rotational temperatures of CO, but detection limits for high-J CO lines may prevent the discovery of spot shocks.

The distribution of correlation strength identifies any offset of correlations from any group of lines. The correlations of all CO lines show no systematic offset of correlations from any group of CO lines, other than the instrumental effects, despite the fact that the distribution of the rotational temperatures clearly shows two distinct populations, suggesting that multiple origins contribute to the entire CO ladder. If some CO lines are dominated by a certain origin, the correlations among those lines would be much higher than others, appearing to be a regional clustering in the distribution of correlation strength. On the other hand, if the ranges of J-level contributed by different origins overlap with each other significantly, such regional clustering effect may not be seen.

Figure 2.8 shows a rather smooth variation of correlations instead of clustering for the CO lines observed in each module. The smooth variation suggests that each origin contributes to a wide range of CO lines, and the range of J-levels contributed by each origin significant overlaps with each other. To summarize, both the distribution of rotational temperatures and the observations of resolved CO lines show multiple components of CO gas; however, the discrete origin of CO gas produces a rather smooth distribution of correlation strengths, suggesting that each origin contributes to a wide range of J-levels, and the dominance of each origin is smoothly varying across the CO ladder. This illustrates the importance of spectrally resolved data to find the "hidden" components.

2.5.2.1 A Single CO Line as a Probe of the Total CO Luminosity

We explore the potential to infer $L_{\rm CO}$ with a single low-J CO line. We only focus on CO $J = 6 \rightarrow 5$ and $J = 4 \rightarrow 3$ lines for their accessibility from ground-based observations. The optical depth correction applies to the luminosities of CO $J = 6 \rightarrow 5$ and CO $J = 4 \rightarrow 3$ as well. Both lines show strong correlation with $L_{\rm CO}$, with Spearman's ρ of 0.878 and 0.926 for CO $J = 4 \rightarrow 3$ and $J = 6 \rightarrow 5$, respectively. The data are more scattered for CO $J = 4 \rightarrow 3$ at the lower $L_{\rm CO}$ regime, probably due to increased contribution from the envelope. The different spatial extent of CO $J = 3 \rightarrow 2$ and $J = 6 \rightarrow 5$ lines (Santangelo et al., 2014) also suggests different combinations of origins for the CO $J = 4 \rightarrow 3$ and $J = 6 \rightarrow 5$ emission. We fit a power-law for the relations between the $L_{\rm CO}$ and both the luminosity of CO $J = 4 \rightarrow 3$ and CO $J = 6 \rightarrow 5$, with the orthogonal distance regression offered in `SciPy` (Figure 2.15). The fitted relation can be described as

$$log(L_{\rm CO}\,[L_\odot]) = a \times \log(L_{\rm CO}\,[L_\odot]) + b. \tag{2.6}$$

For CO $J = 6 \rightarrow 5$, a = 0.93±0.04 and b = 0.66±0.09; for CO $J = 4 \rightarrow 3$, a = 1.00±0.07 and b = 0.91±0.19. The tight relation between the $L_{\rm CO}$ and the luminosity of CO $J = 6 \rightarrow 5$ provides a pathway to assess the total CO luminosity from the ground-based observations.

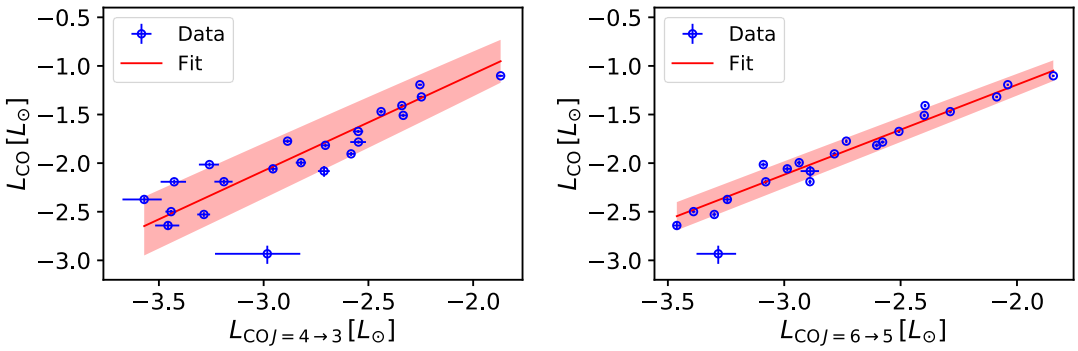

Figure 2.15: The correlation between the total CO luminosity and the luminosity of CO $J = 4 \rightarrow 3$ (left) and CO $J = 6 \rightarrow 5$ (right) with a fitted linear relation. The fitted lines can be described as $\log(L_{{\rm CO}\ J=4\rightarrow3\,[L_\odot]}) = {\rm a}\times\log(L_{\rm CO}\,[L_\odot])+{\rm b}$, where a = 1.00±0.07 and b = 0.91±0.19; and $\log(L_{{\rm CO}\ J=6\rightarrow5\,[L_\odot]}) = {\rm a}\times\log(L_{\rm CO}\,[L_\odot])+{\rm b}$, where a = 0.93±0.04 and b = 0.66±0.09.

2.5.2.2 Comparison with FU Orionis Objects, T Tauri stars, and Herbig Ae/Be stars

In principle, the molecular gas eventually infalls onto the protostars or dissipates into the environment, suggesting that the amount of CO should be lower for T Tauri stars and Herbig Ae/Be stars compared to embedded protostars, such as the COPS sources. The FU Orionis objects (FUors) are often considered as the protostars which have undergone a sudden rise in accretion rate (Herbig, 1977), resulting in a rapid increase in source bolometric luminosity followed by a slow decay over 10–100 years (e.g. Bell & Lin, 1994; Green et al., 2016b). See Audard et al. (2014) for a recent review. If the FUors just experienced an outburst of energy, their molecular gas may have been heated up, leading to an increase of the 400–500 K component in the CO rotational diagram. We utilize the PACS spectra from the CDF archive to examine if the differences of Herbig Ae/Be stars, T Tauri stars, and FUors appeared in the rotational diagrams of CO. Table 2.8 shows the lists of sources.

Table 2.8: List of Herbig Ae/Be stars, FUors, and T Tauri stars

Herbig Ae/Be	AB Aur, AS 205, HD 100453, HD 100546, HD 104237, HD 135344B HD 139614, HD 141569, HD 142527, HD 142666, HD 144432 HD 144668, HD 150193, HD 163296, HD 169142, HD 179218 HD 203024, HD 245906, HD 35187, HD 36112, HD 38120 HD 50138, HD 97048, HD 98922
FUors	HBC 722, V1735 Cyg, V1057 Cyg, V1331 Cyg, V1515 Cyg, FU Ori
T Tauri	S CrA, HT Lup, RU Lup, RY Lup, SR 21

Figure 2.16 shows the CO rotational diagram of different types of sources as rotational diagrams. The data for Class 0 and I sources are averaged separately. The CO rotational diagrams of Class 0 and I sources have similar characteristics. There are few detections of CO for FUors except for V1057 Cyg. We found that the CO rotational diagram of V1057 Cyg is indistinguishable from the COPS sources, although there is a hint that the data of V1057 Cyg lie at the higher-end of the region populated by the embedded sources, especially at the high upper energy regime. The CO line profiles of FUors are in fact similar to the line profiles found toward embedded protostars (Green et al., 2013b), which supports the similarity of the rotational diagrams between V1057 Cyg and embedded protostars.

The CO rotational diagrams of the Herbig Ae/Be stars are consistently lower than the data of the COPS sources by about 1 in $\log(\mathcal{N}_J/\mathrm{g}_J)$, and they show a much more irregular decrease with E_u/k compared to the COPS protostars. However, the detailed study of two Herbig Ae/Be stars shows a much smoother decrease similar to the protostars (Jiménez-Donaire et al., 2017). Double-peaked line profiles were observed in CO $J = 10 \rightarrow 9$ and CO $J = 16 \rightarrow 15$ for disk sources (Fedele et al., 2013a), which are quite different from the line profiles seen by Kristensen et al. (2017b), confirming a disk origin for the CO emission. However, how the different origins contribute to the shape of rotational diagrams is unclear without further investigation, but it certainly makes the difference of rotational diagram expected. There are only a few detections of CO toward the T Tauri stars, which lie at the bottom-end of the diagram among the lower-end of the data from the Herbig Ae/Be stars. In summary, V1057 Cyg has similar CO rotational diagrams as the embedded protostars, whereas the Herbig Ae/Be stars and T Tauri stars have lower values in $(N_J)/g_J$ but similar shapes to the diagrams of embedded sources. The similarity between embedded protostars and FUors and difference between embedded protostars and Herbig Ae/Be stars and T Tauri stars are also seen in their line profiles.

2.6 Conclusions

We have presented a statistical analysis of the full sample of 26 Class 0+I protostars from the COPS-SPIRE Open Time Program using *Herschel*-SPIRE 200–670 μm spectroscopy, utilizing improvements in calibration and sensitivity from the data pipeline over the mission lifetime.

- We present 1–1000 μm SEDs of 26 COPS sources with excellent spectral coverage in submillimeter wavelengths. We update the reduction method used in the CDF archive (Green et al., 2016a) to extract the 1D PACS spectra that are consistent with the SPIRE 1D spectra, which have less than 5% difference of flux at the conjunction between the spectra of PACS and SPIRE for all sources, except for TMC 1, WL 12, L1014, and IRAS 03301+3111 due to excessive background emission in SPIRE. We further investigated the change of L_bol, T_bol, and L_smm because of the addition of the SPIRE spectra. With *Herschel* data, the

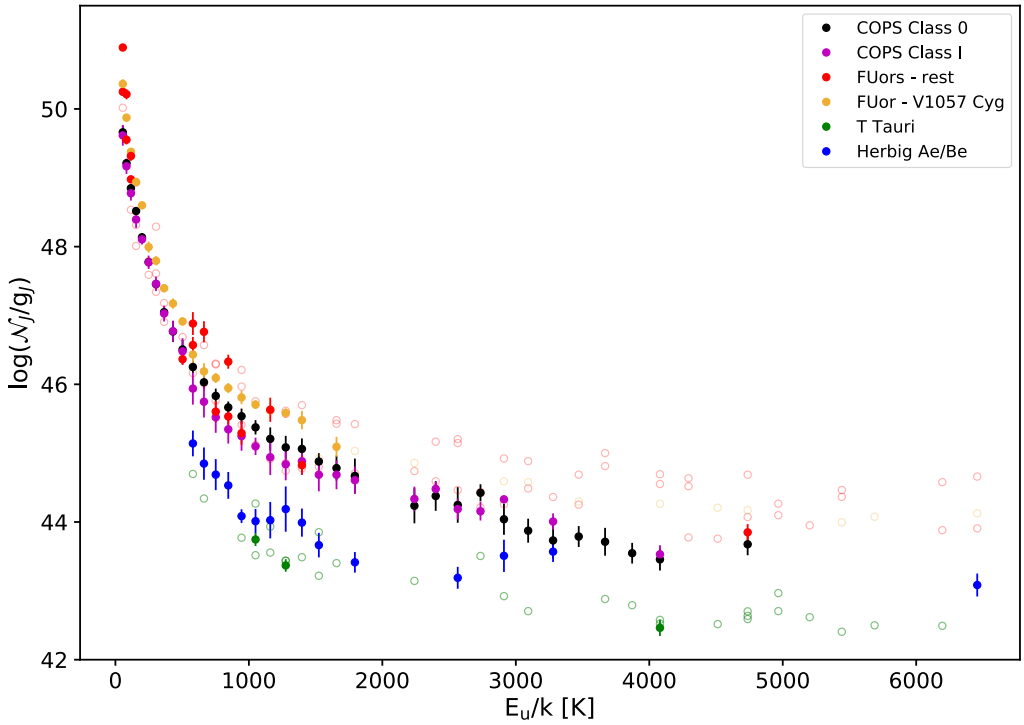

Figure 2.16: The CO rotational diagram of the COPS sources (black and magenta for the Class 0 and the Class I sources classified by $T_{\rm bol}$) and other types of sources from the CDF archive (Green et al., 2016a), including FUors (orange and red for V1057 Cyg and other FUors, respectively), T Tauri stars (green), and Herbig Ae/Be stars (blue). The data of the COPS sources and the Herbig Ae/Be stars are shown as averaged by their upper energy, while the data are all shown for the other sources. The upper limits are shown as open circles.

$L_{\rm bol}$ increases by 50% on average compared to the pre-*Herschel* observations, while the $T_{\rm bol}$ decreases by 10% on average. (Section 2.3.3 and 2.3.5)

- All spectra were processed with an automatic line fitting pipeline to extract emission lines, producing the line-free continuum (Figure 2.2) and continuum-free spectra (Figure A.1). The line fitting result is provided as a machine readable table (Table 2.4). We found that the SPIRE photometric flux densities decrease by only ∼1% after removing the emission lines. (Section 2.3.6.2 and 2.3.6.3)

- The ^{12}CO lines typically have high optical depth at low-J, which affects the total CO luminosity as well as the comparison with the emission of other species.

With the emission of ^{13}CO detected in a few sources, we characterize the optical depth of ^{12}CO and discuss the uncertainties due to the lack of spectral resolution and sensitivity. We fitted the optical depth as a function of the upper energy levels (Equation 2.2), and found that the ^{12}CO lines remain optically thick until $J_{\rm up} > 13$. (Section 2.4.1)

- We fitted multiple rotational temperatures for each source with the correction of optical depth. We adopted the conventional break points to separate the CO ladder, and produce four components of rotational temperature, <100 K, ∼100 K, ∼200–300 K, and $\gtrsim$500 K, which is similar to the scenario concluded by many studies (e.g. Yıldız et al., 2013; Green et al., 2013a; Manoj et al., 2013; Karska et al., 2014a; Matuszak et al., 2015). However, the separation between components becomes indistinct when the break points remain flexible during the fitting of rotational temperature. The distribution of rotational temperatures (Figure 2.5) shows two populations, the dominant cold components (50–120 K) and a secondary population centered at ∼400 K, which trace the entrained gas in the outflows and possibly the cavity shocks/disk wind, respectively. (Section 2.4.2)

- We calculate the beam filling factor for the sources where we detect ^{13}CO emission, which constrains the optical depth directly. The beam filling factors range from 0.035 to 0.53, which are lower limit of the filling factor due to the uncertainties on the line width and optical depth. A clumpy nature of the CO gas at embedded protostars learned from ground-based observations with higher spatial resolution (9″ beam) (Arce et al., 2013; Lee et al., 2015a; Yıldız et al., 2015), suggesting a smaller beam filling factor, which is consistent with our result. (Section 2.4.4)

- We constrain the correlations of all pairs of lines drawn from the line fitting results with the generalized Spearman's rank correlation. The distribution of correlation strength (Figure 2.9) show systematic offsets of correlation strength from several groups of lines, where the lines of each group are observed with the same module/instrument, suggesting that the bias is due to the instrumental effect. Therefore, any comparison of the lines observed in different modules needs to be done with caution. (Section 2.4.5)

- Within each module, the correlations between each CO line pair are smoothly decreasing as the difference between J-level between two lines increases. The emission of ^{13}CO is found to have weak correlations with ^{12}CO, and stronger correlations with [C I] $^3P_2 \rightarrow ^3 P_1$. Both ^{13}CO and [C I] were associated with the UV-heated outflow cavity wall, which explains the correlation. The H_2O lines show significant correlations with CO and OH. The water lines correlate better with the CO lines ranging from $J_{\rm up}$=10–15 in the middle of the range of J-levels shown in Figure 2.7. The [O I] $^3P_1 \rightarrow ^3 P_2$ at 63 μm has weak correlations with low-J CO lines observed with SPIRE, and shows no correlation with [C I]. (Section 2.4.5.1 to 2.4.5.5)

- The spatial distribution of CO emission shows an extended feature in low-J CO lines. We develop a method to project the 2D distribution into an 1D profile as a function of the azimuthal angles from the center of the sources. The 1D profile shows the ratios of the flux at outer spaxels to the flux at the central spaxel. The 1D profiles show consistent morphology with the spatially resolved map. The bipolar CO distribution indeed has an outflow-related origin. The bipolar distribution of CO emission is more significant for lower-J CO lines, and typically show a separation of 180 degree between the two peaks.

  We use the difference of the maximum and the minimum values of the extracted 1D profiles as a probe of the extent of bipolar feature. The averaged peak-to-valley differences show a general decline as the J-level increases, suggesting a less predominant bipolar feature at higher-$J_{\rm up}$ CO lines. (Section 2.4.6)

- The classifications using $L_{\rm bol}/L_{\rm smm}$, $T_{\rm bol}$, and the spectral index at near-infrared ($\alpha_{\rm NIR}$) as the indicators all conclude that our sample consists of Class 0+I protostars. The classifications using $T_{\rm bol}$ and $L_{\rm bol}/L_{\rm smm}$ are not very consistent in separating 0 from I: 10 of 26 sources have different classifications under these two methods. (Section 2.5.1)

- The origin of the CO emission can be constrained with its spatial extent, rotational temperature, and correlations with other CO lines. We show that the extended CO emission traces the outflows. Also, two populations of the CO rotational temperatures are found in the distribution of rotational temperatures, which is consistent with multiple origins of CO emission inferred from

the velocity-resolved line profiles (Kristensen et al., 2012b; Yıldız et al., 2013; San José-García et al., 2013; Kristensen et al., 2017b). The cold population ($\lesssim$100 K) indicates the entrained gas in the outflows. While the origin of the broad component of the resolved CO line profiles is consistent with the warm population ($\sim$400 K), we do not find the hot component ($\sim$700 K) in the distribution of rotational temperatures. The distributions of correlation strength do not exhibit multiple distinct patterns, suggesting that either the CO emission comes from numerous components, or the few mechanisms of CO excitation contribute to a wide range of CO ladder and well-overlap with each other. The kinematics of the resolved line profiles rule out the former scenario (Kristensen et al., 2017b). Thus, the discrete origins of CO emission contribute to a wide range of CO ladder, and their contributions significantly overlap with each other on the CO ladder. (Section 2.5.2)

- The comparison of the CO rotational diagrams of different types of sources, such as embedded protostars, FUors, T Tauri stars, and Herbig Ae/Be stars, collected from the CDF archive (Green et al., 2016a), shows that the rotational diagrams of one FUor (V1057 Cyg) is indistinguishable from that of an emvedded protostar, except for the higher $\mathcal{N}_J/g_J$ at high upper energy transitions(Figure 2.16). The other FUors exhibit few CO detections. The data from the embedded sources form a coherent pattern in the rotational diagram, where the data of the Herbig Ae/Be stars lie at the lower end of $\log(\mathcal{N}_J/g_J)$ compared to the embedded sources. Only a few detections are found toward the T Tauri stars, which have weaker emission than the Herbig Ae/Be stars. (Section 2.5.2.2)

Table 2.9: Line Detection Summary

Source	^{13}CO $J = 5 \rightarrow 4$	^{13}CO $J = 6 \rightarrow 5$	^{13}CO $J = 7 \rightarrow 6$	^{13}CO $J = 8 \rightarrow 7$	^{13}CO $J = 9 \rightarrow 8$	CO $J = 4 \rightarrow 3$	CO $J = 5 \rightarrow 4$	CO $J = 6 \rightarrow 5$	CO $J = 7 \rightarrow 6$	CO $J = 8 \rightarrow 7$	CO $J = 9 \rightarrow 8$	CO $J = 10 \rightarrow 9$	CO $J = 11 \rightarrow 10$	CO $J = 12 \rightarrow 11$	CO $J = 13 \rightarrow 12$	[C I] $^3P_1 \rightarrow ^3P_0$	[C I] $^3P_2 \rightarrow ^3P_1$	HCO$^+$ $J = 6 \rightarrow 5$	HCO$^+$ $J = 7 \rightarrow 6$	HCO$^+$ $J = 8 \rightarrow 7$	o-H_2O $1_{10} \rightarrow 1_{01}$	o-H_2O $3_{12} \rightarrow 2_{21}$	o-H_2O $3_{12} \rightarrow 3_{03}$	o-H_2O $3_{21} \rightarrow 3_{12}$	p-H_2O $1_{11} \rightarrow 0_{00}$	p-H_2O $2_{02} \rightarrow 1_{11}$	p-H_2O $2_{11} \rightarrow 2_{02}$
B1-a	...	...	...	...	...	Y	Y	Y	Y	Y	Y	Y	Y	Y	Y	Y	Y	...	...	...	...	Y	...	...	Y	...	...
B1-c	...	...	...	...	...	Y	Y	Y	Y	Y	Y	Y	Y	Y	Y	Y	Y	...	...	...	Y	Y	Y	Y	Y	Y	Y
B335	...	...	...	...	...	Y	Y	Y	Y	Y	Y	Y	Y	Y	Y	...	...	...	...	...	...	...	...	...	Y	Y	...
BHR 71	...	...	...	...	...	Y	Y	Y	Y	Y	Y	Y	Y	Y	Y	...	...	...	...	...	Y	Y	...	...	Y	Y	Y
Ced110 IRS4	Y	Y	...	...	...	Y	Y	Y	Y	Y	Y	Y	Y	Y	Y	Y	Y	...	...	...	...	...	...	...	...	...	...
DK Cha	Y	...	...	...	...	Y	Y	Y	Y	Y	Y	Y	Y	Y	Y	...	...	...	...	...	...	Y	...	...	...	Y	...
GSS 30 IRS1	Y	Y	Y	...	Y	Y	Y	Y	Y	Y	Y	Y	Y	Y	Y	Y	Y	...	Y	...	...	Y	...	...	Y	Y	...
HH 46	Y	Y	...	...	...	Y	Y	Y	Y	Y	Y	Y	Y	Y	Y	Y	Y	...	...	...	...	...	...	...	...	...	...
IRAS 03245+3002	...	...	...	...	...	Y	Y	Y	Y	Y	Y	Y	Y	Y	Y	Y	Y	...	...	...	...	Y	...	...	...	...	...
IRAS 03301+3111	...	...	...	...	...	Y	Y	Y	Y	...	Y	Y	Y	Y	Y	Y	Y	...	...	...	...	...	...	...	...	...	...
IRAS 15398−3359	...	...	...	...	...	Y	Y	Y	Y	Y	Y	Y	Y	Y	Y	...	...	...	...	...	...	...	...	...	...	Y	...
L1014	...	...	...	...	...	...	...	...	...	...	...	...	...	...	...	Y	...	...	...	...	...	...	...	...	...	...	...
L1157	...	...	...	...	...	Y	Y	Y	Y	Y	Y	Y	Y	Y	Y	...	...	...	...	...	...	Y	Y	...	Y	Y	Y
L1455 IRS3	...	...	...	...	...	...	...	Y	Y	...	...	...	...	...	Y	...	...	...	...	...	...	...	...	...	...	...	...
L1551 IRS5	Y	...	...	...	Y	Y	Y	Y	Y	Y	Y	Y	Y	Y	Y	Y	...	...	...	...	...	...	...	...	...	...	...
L483	...	...	...	...	...	Y	Y	Y	Y	Y	Y	Y	Y	Y	Y	Y	...	...	...	...	...	Y	...	...	Y	Y	...
L723 MM	...	...	...	...	...	Y	Y	Y	Y	Y	Y	Y	Y	Y	Y	Y	...	...	...	...	...	...	...	...	...	Y	...
RCrA IRS5A	Y	Y	...	...	...	Y	Y	Y	Y	Y	Y	Y	Y	Y	Y	Y	Y	...	...	...	...	...	...	...	Y	...	...
RCrA IRS7B	Y	Y	Y	Y	Y	Y	Y	Y	Y	Y	Y	Y	Y	Y	Y	Y	Y	Y	Y	Y	...	Y	...	...	...	Y	...
RCrA IRS7C	Y	Y	Y	Y	Y	Y	Y	Y	Y	Y	Y	Y	Y	Y	Y	Y	Y	Y	Y	Y	...	...	...	...	Y	Y	...
RNO 91	...	...	...	...	...	Y	Y	Y	Y	Y	Y	Y	Y	Y	Y	Y	Y	...	...	...	...	...	...	...	...	...	...
TMC 1	...	...	...	...	...	Y	Y	Y	Y	Y	Y	Y	Y	Y	Y	...	...	...	...	...	...	...	...	...	...	...	...
TMC 1A	...	...	...	...	...	Y	Y	Y	Y	Y	Y	Y	Y	Y	Y	...	Y	...	...	...	...	...	...	...	...	...	...
TMR 1	...	Y	...	...	...	Y	Y	Y	Y	Y	Y	Y	Y	Y	Y	Y	Y	...	...	...	...	Y	...	...	Y	Y	...
VLA 1623−243	Y	Y	...	...	Y	Y	Y	Y	Y	Y	Y	Y	Y	Y	Y	Y	Y	...	...	...	...	...	...	...	...	...	...
WL 12	Y	Y	...	...	...	Y	Y	Y	Y	Y	Y	Y	Y	Y	Y	Y	Y	...	...	...	...	...	...	...	...	...	...

Chapter Three: The Class 0 Protostar BHR71: *Herschel* Observations and Dust Continuum Models[1]

3.1 Introduction

3.1.1 Background

Embedded protostars are the youngest protostars, emitting most of their light at far-infrared wavelengths. After collapse begins, the protostar forms and accretes mass from the envelope, and a wind and/or jet is formed, which sweeps up material into a molecular outflow. The radiation from the protostar encounters a thick and dense envelope on its way out from the center. Therefore, embedded protostars can only be observed at infrared and submillimeter wavelengths unless they are seen face-on. Observationally, protostars are classified by their radiation at infrared wavelengths. Lada (1987) introduced the α-index, classifying protostars into Class I, II, and III based on the shape of the spectral energy distribution (SED) in the near-infrared to mid-infrared. Observations at submillimeter wavelengths suggested that a subset of Class I protostars were especially embedded, based on the ratio of the submillimeter luminosity (λ >350μm) to the bolometric luminosity, $L_{\rm submm}/L_{\rm bol}$. Andre et al. (1993b) defined Class 0 protostars as sources that have $L_{\rm submm}/L_{\rm bol} > 0.5\%$. Chen et al. (1995b) classified protostars by their bolometric temperatures: $T_{\rm bol}$ below 70 K for Class 0; 70-650 K for Class I; 651-2880 K for Class II; and above 2880 K for Class III. The different methods of classification generally agree, but some sources receive different classifications from different methods.

The distinction between SED classes and physical stages was emphasized by Robitaille et al. (2006b). The detailed relation between the Classes defined by SEDs and the theoretical stages of protostellar evolution is still unclear (van Kempen et al.,

[1]This chapter has been published on The Astrophysical Journal 835, 259. The author is the lead author of this published article, contributing to the data reduction, data analyses, modelings, and the preparation of the manuscript.

2009b), but recent studies have shown a generally good, though imperfect, correlation between Class I sources and Stage I sources (Heiderman & Evans, 2015; Carney et al., 2016).

The general path of star formation starts from the collapse of a dense core due to gravitational instability, forming a protostar at the center of the core. Shu (1977b) showed that the collapse of a singular isothermal core follows a similarity solution. This model begins with an isothermal core near hydrostatic equilibrium. The collapse starts at the center; once the central region begins collapsing, the shell adjacent to the collapsing region loses pressure support and starts to fall in. A wave of infall propagates outward through the envelope at the sound speed. (We use the term "envelope" to describe the surrounding gas and dust that is not in the star, the disk, or the outflow.) The original model (Shu, 1977b) simplified the collapse process by neglecting rotation, turbulence, and magnetic fields. Rotational motion has been widely observed in young stellar objects. The conservation of angular momentum implies a small but non-zero rotational speed for the pre-collapse core. Terebey et al. (1984b) (hereafter TSC) generalized the Shu model by including the effect of rotational motion, making the inner part of envelope flatten toward the equatorial plane. The angular momentum of a dense core is much larger than that of a main-sequence star, suggesting that angular momentum must be removed from the core by some mechanism, most likely involving magnetic fields. A large magnetic field can suppress the fragmentation of the envelope (Padoan & Nordlund, 2011; Körtgen & Banerjee, 2015) or slow the rotation (Li et al., 2014). While these effects may be important, the TSC model used here does not consider the magnetic field. Incorporating a magnetic field and turbulence is beyond the scope of this study.

When material falls inward, the centrifugal barrier becomes important at the centrifugal radius, where the centrifugal force is comparable to the gravitational force. Bipolar outflows, which are widely observed around objects that have accretion activities, remove angular momentum from the system by ejecting material along the rotational axis at high velocity. The outflow process involves a highly collimated atomic or molecular jet or wind ($v \sim 300$ km s^{-1}) and a less collimated molecular outflow ($v \sim$1-30 km s^{-1}) consisting of shells of gas swept up by the high velocity jet (Hollenbach, 1985b). The molecular outflow in Class 0 protostars sweeps up the envelope and carves out an outflow cavity. The low density in the outflow cavity makes the cavity wall more exposed to the ultraviolet radiation from the central protostar,

producing numerous molecular and atomic fine-structure lines observed by *Herschel* Space Observatory (Vasta et al., 2012b; Santangelo et al., 2012b; Nisini et al., 2013; Lee et al., 2013). Modeling the energetics of the CO and water lines shows that different types of shocks contribute to most of the emission, but a general consensus has not been reached on the detailed structure of shocks among different Class 0 objects (Visser et al., 2012b; Karska et al., 2013b, 2014b).

Synthetic SEDs of protostars calculated with 3-D radiative transfer simulations provide a direct comparison with observations to test the models of star formation (Young & Evans, 2005; Dunham et al., 2010a; Robitaille et al., 2006b; Offner et al., 2009, 2012). Robitaille et al. (2006b) modeled protostars with a fully collapsing envelope, a flared disk, an outflow cavity with a constant dust density, and a central luminosity source, and they simulated a grid of SEDs of the protostars with a wide variety of parameters. This grid of SEDs serves as a tool to understand the structure of individual protostars before an in-depth modeling (Je et al., 2015; Chiang et al., 2015). Young & Evans (2005) developed 1-D evolutionary models assuming steady accretion and an inside-out collapse. Dunham et al. (2010a) used a more complicated 2-D model setup that included episodic accretion and a rotating, collapsing envelope to obtain better agreement of the evolution of low-mass protostars throughout different stages with the observed population of protostars in different Classes. Radiative transfer calculations also play an important role in hydrodynamic simulations of star formation to realize the synthetic images and SEDs to compare with measured properties in simulations or observations (Offner et al., 2012).

3.1.2 BHR71

BHR71 is a Bok globule, apparently associated with the Southern Coalsack. The distance of the Coalsack is generally taken to be 200 pc (Seidensticker & Schmidt-Kaler, 1989b; Straizys et al., 1994), but some recent studies suggest a closer distance of 150 pc (Corradi et al., 1997; Knude & Hog, 1998b; Nyman, 2008). We adopt 200 pc as the distance of BHR71 for better comparison with other studies of this source. NH_3 emission was found in BHR71 by Bourke et al. (1995a). Bourke et al. (1997) (hereafter B97) discovered a strong bipolar molecular outflow, estimated an outflow dynamical age of 10000 years, and concluded that the outflow was almost in the plane of sky, with an inclination angle of 84°.

Observations in the *Herschel* Key Program, *Dust, Ice, and Gas In Time* (DIGIT; PI: N. Evans), show substantial emission at far-infrared wavelengths, and suggest that BHR71 is a Class 0 protostar with an estimated bolometric temperature of 47 K (Green et al., 2013c). Using a 1-D dust radiative transfer model, Kristensen et al. (2012a) estimated an infall radius of 3500 AU with the mass accretion rate of 3×10^{-5} $M_\odot$ yr^{-1}. Shock activity has been observed in the SiO and H_2 knots along the outflow direction suggesting the presence of non-stationary shocks (CJ-type) (Gusdorf et al., 2011, 2015). Mass loss rates of 2-4 $\times 10^{-7}$ $M_\odot$ yr^{-1} are estimated from the [O I] 63 μm line (Nisini et al., 2015).

We use spectroscopy data from DIGIT and archival *Spitzer* as our primary data in this paper. We discuss the observations and reduction in Section 3.2, the results of spectra analyses in Section 3.3, the continuum modeling in Section 3.4, the discussion of the best fit model in Section 3.5, and finally we summarize our conclusions in Section 3.6. A parameter study for the continuum modeling is described in the Appendix.

3.2 Observations and Reduction

BHR71 was observed by the PACS and SPIRE instruments on *Herschel*. The PACS spectra come from the DIGIT *Herschel* Key Program, while the SPIRE spectra come from the *Herschel* Open Time Program, CO in Protostars (COPS, PI: J. Green). The PACS instrument is a 5×5 array of 9.4″×9.4″ spatial pixels (hereafter "spaxels") covering wavelengths from 50 to 210 μm with $\lambda/\Delta\lambda \sim$ 1000-3000. The spatial resolution of PACS ranges from $\sim 9''$ at 50 μm to $\sim 18''$ at 210 μm, corresponding to 1800-3600 AU at the distance of BHR71. The regions observed with PACS and SPIRE are indicated in Figure 3.1.

The SPIRE instrument is a Fourier-Transform Spectrometer (FTS). There are two bands on SPIRE covering $194-313$ μm (SSW; Spectrograph Short Wavelengths) and 303-671 μm (SLW; Spectrograph Long Wavelengths) with $\lambda/\Delta\lambda \sim 300-800$. The spatial resolution of SPIRE ranges from 17″-40″, corresponding to 3400-8000 AU at the distance of BHR71. The on-source exposure times for PACS and SPIRE spectra are 7268 seconds and 3168 seconds respectively, achieving line flux RMS values of $17 \times 10^{-18} - 66 \times 10^{-18}$ W m^{-2} and $3.8 \times 10^{-18} - 36 \times 10^{-18}$ W m^{-2} respectively.

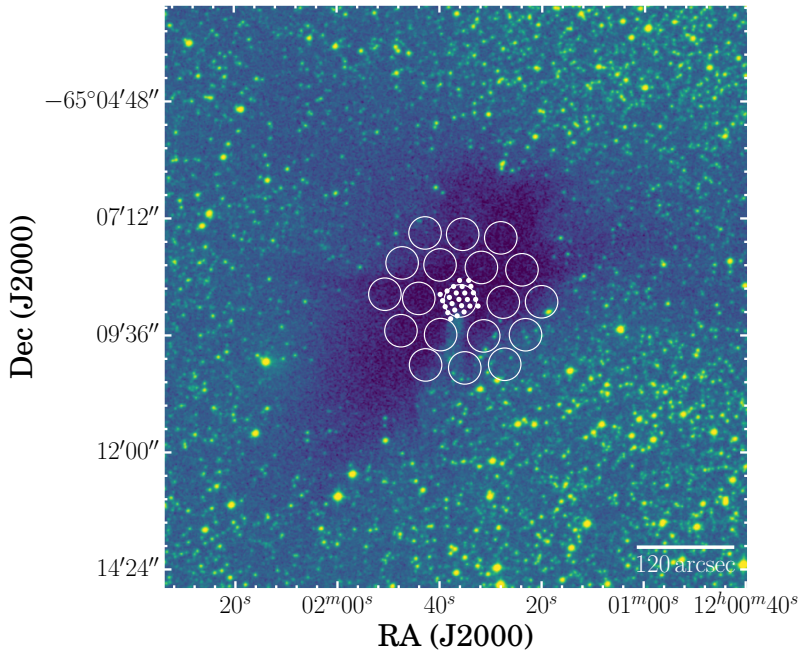

Figure 3.1: The footprint of PACS and SPIRE (SLW) spaxels overlaid with the optical image of BHR71 collected from the STScI Digitized Sky Survey. The optical image is observed in AAO-SES/SERC-ER survey with IIIaF+OG590 filter centered around 6600Å. The circles show the SPIRE spaxels, while the dots show the PACS spaxels.

3.2.1 Data Reduction

There are two types of data products used in this study: the datacube product is used for comparing the spatial distribution of emission lines; the extracted source spectrum, 1-D spectrum, is used for comparing to the radiative transfer simulation. The datacube products are collected from the Herschel Science Archive, processed with SPG v14.0.1 (PACS) and SPG v14.1.0 (SPIRE). The calibrations for PACS and SPIRE are version 72 and `spire_cal_14_2`, respectively.

The 1-D spectrum is extracted from the PACS and SPIRE data cubes with two different methods that best represent the nature of the source and instruments. The size of BHR71 is larger than a single spaxel of PACS and SPIRE, except for the SPIRE Long Wavelength Spectrometer Array (SLW). Therefore, neither a standard point source calibration nor an extended source calibration is suitable for extracting the entire observation into a single spectrum. For PACS, we aim to extract a 1-D spectrum that best matches the SPIRE spectrum. The 1-D spectrum is calculated

from all PACS spaxels (total 25 spaxels) weighted by their fraction of pixel area within a circular aperture centered at the central spaxel. The size of the aperture is chosen to be 31.8″, yielding a flux in a same area as the central 3x3 spaxels, to match the SPIRE spectrum. For the photometry, we measure the fluxes within the same aperture in three PACS bands (70 μm, 100 μm, and 160 μm) with the aperture correction described in the Data Analysis Guide (Section 4.21.2.4). The images observed in the Open Time Program led by J. Tobin are collected from the Herschel Science Archive without any further reduction. The SPIRE images are collected in the same fashion as the PACS images.

For SPIRE, we utilize the Semi-extended Corrector Tool (SECT) in Herschel Interactive Processing Environment (HIPE) v.14 in the spectral calibration. The purpose of SECT is mitigate the difference between the two modules (SSW and SLW) due to the beam size dependence on wavelength and the fact that the source is semi-resolved. The detailed procedures are illustrated in Makiwa et al. (2016b). Here we highlight the critical steps. SECT fits a source size for a given source model, which we choose to be a 2-D Gaussian, and scales the entire spectrum into a wavelength-independent Gaussian reference beam. There are two SECT processes in our calibration pipeline. The first one fits the source size with the default Gaussian reference beam (40″). The second one runs with the fitted source size without further optimization, and scales the spectrum into a Gaussian reference beam with the same size as the fitted source size. The photometry fluxes at three SPIRE bands (250 μm, 350 μm, and 500 μm) are calculated by performing aperture photometry on the extended source corrected images with beam correction, color correction and aperture correction. The aperture sizes are set to be the convolution of the fitted source size and the mean FWHM of the beam at each band (see Table 3.1).

3.2.2 Line Fitting

After the data reduction, we performed a comprehensive and robust line fitting process to the spectrum of each spaxel as well as the 1-D spectrum. To make the fitting process general, we aimed to fit every line that fell into the range of wavelength of the spectra for several molecular and atomic species. The line information was collected from the Leiden Atomic and Molecular Database (Schöier et al., 2005b) and the Cologne Database for Molecular Spectroscopy (CDMS; Müller et al. 2005) to

construct a comprehensive line list including CO, ^{13}CO, H_2O, OH ladders and atomic fine-structure emission lines, except for the [N II] line centroids, which were adopted from the measurement in the CDF archive (Figure 6 in Green et al. (2016c)). For each region where a line could be, we performed multiple stages of calculations, in which baselines were fitted with second-order polynomials and lines were fitted with single or double Gaussian profiles from a continuum-subtracted spectrum. The core fitting method is `mpfit`, Levenberg-Marquardt non-linear least squares minimization (Markwardt, 2009). The fitting process is described in the next paragraph.

At the wavelength of each possible line, the fitting routine first fits the baseline locally, then subtracts the fitted baseline from the spectrum, and finally fits the line with baseline-subtracted spectrum. This procedure is denoted as "the first fitting". Although the line profile is extracted by "the first fitting" , its noise estimation might be contaminated by nearby lines. A line-free spectrum derived from the subtraction of any significant line in "the first fitting" serves as the pure noise spectrum in the second fitting which is exactly the same as "the first fitting" except for the noise input. Accurate noise estimation around the line centroid can be retrieved by combining the result of second fit and the noise spectrum from the first fit. The third, final, fitting is performed with this estimated noise as the uncertainty of the spectrum to get the best fit line flux and uncertainty.

In the baseline fitting, we selected a region of ± 10 spectral resolution elements around the line centroid. Any wavelength that could possibly have a line is not considered as a valid data point for baseline fitting in order to get the proper baseline without being affected by nearby lines. Most of the emission lines are fitted with a single Gaussian profile to the baseline-subtracted spectrum. But sometimes multiple lines lie too close in wavelength so that a single Gaussian profile is insufficient to decouple them. Therefore, we perform a double Gaussian profile fitting for a few heavily blended regions. To reduce the degrees of freedom, the line centroids and widths are fixed to theoretical values and the corresponding spectral resolution. The line width was allowed to vary within $\pm 30\%$ of the spectral resolution for fitting of isolated lines in the SPIRE spectra but was fixed for PACS spectra. One step in the reduction of the SPIRE spectra is apodization, which smooths the sinc function recorded by the FTS into a Gaussian-like profile, and it may result in a larger line width if some minor features are included in the apodization process. Therefore, we give more flexibility on the line width of the fitting of the SPIRE spectra. The signal-

to-noise ratio (S/N) is calculated by simply dividing the integrated line strength by the product of the full width at half maximum (FWHM) and the noise level obtained from the residuals after removal of both lines and continuum times a constant, 1.064, appropriate for a Gaussian line. The line fitting results are summarized in Section 3.3.4. In the following analysis, we consider a line as a detection if it has S/N greater than 3. This criteria represents a false-positive rate of 0.3%, yielding about 10 false detections over the whole PACS/SPIRE spectra. Applying a higher S/N criteria will lose too many real detections. If only the lines with S/N greater than 5 are retained, the total number of detections falls from 645 to 376. Therefore, we further visually inspect the fitting results to avoid the false-positive detections.

In addition to the line fluxes, a line-free spectrum was produced by subtracting all the lines and smoothing the result. This spectrum was compared to photometric data and the agreement was excellent ($\sim$10%) for the photometric fluxes at 70 μm, 100 μm, 250 μm, and 500 μm and was close ($\sim$ 20%) for the fluxes at 160 μm and 350 μm. Together with data from other telescopes, we use the line-free spectrum to constrain the models of the SED (Figure 3.2). A flat spectrum was then obtained by removing the continuum. The 1-D continuum-removed spectrum of BHR71 shows abundant molecular lines and the variation of the noise across the PACS and SPIRE modules (Figure 3.3).

3.3 Results

In addition to the *Herschel* data, we obtained data from 2MASS, *Spitzer*-IRAC, *Spitzer*-IRS, and SEST. We describe these other data sets first, then the results of the *Herschel* observations.

3.3.1 2MASS and *Spitzer*-IRAC Images

We acquired the 2MASS J, H, and K bands and *Spitzer*-IRAC images from the archives. Figure 3.4 shows, on the left, the false-color image of BHR71 with J band in blue, H band in green, and K band in red; on the right, the false-color image of BHR71 is shown with IRAC 3.6 μm in blue, IRAC 4.5 μm in green, and IRAC 8.0 μm in red. There are two infrared sources identified by Bourke (2001), IRS1 and IRS2, marked with blue and magenta crosses. The coordinates of IRS1 and IRS2 are

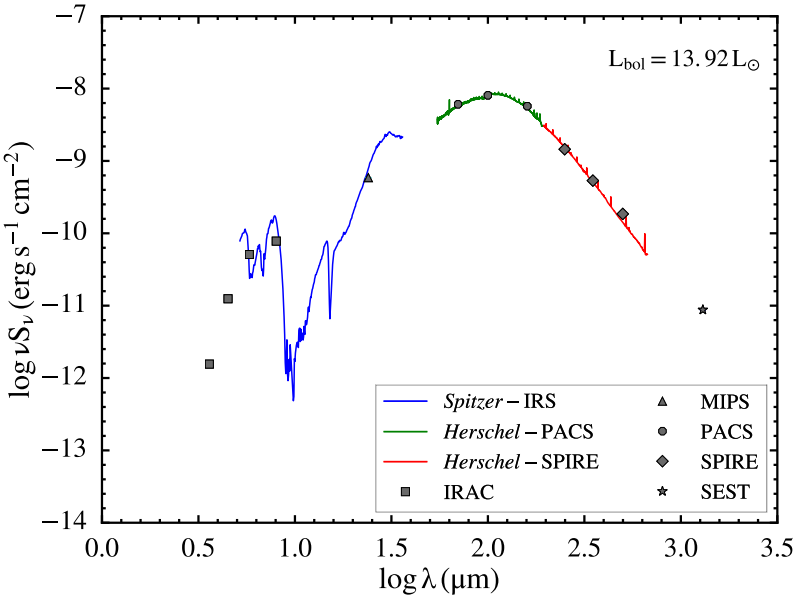

Figure 3.2: Spectral energy distribution (SED) of BHR71 including the *Spitzer*-IRS, *Herschel*-PACS/SPIRE and photometry measurements from archives. The observed bolometric luminosity is 13.92 $L_\odot$.

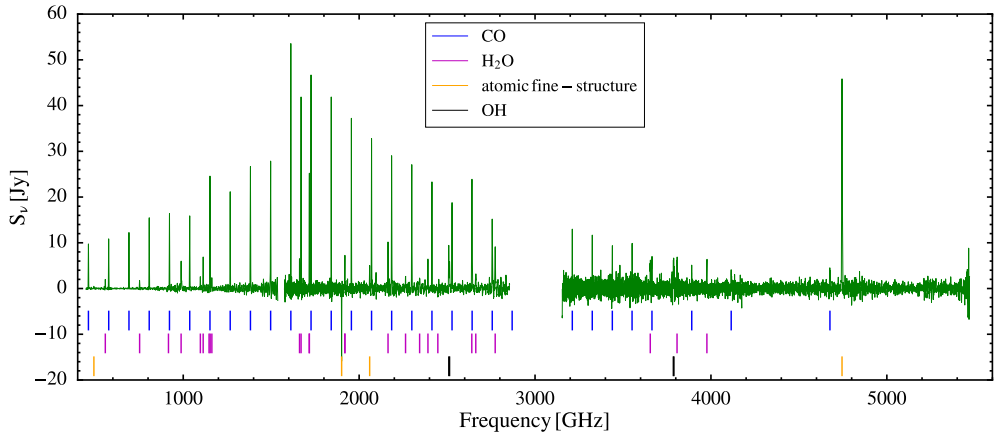

Figure 3.3: The flat spectra of BHR71 with PACS and SPIRE combined (green). The continuum is removed by the line fitting process. The CO rotational lines cluster at low frequencies peaking around $J = 16$ to 18. The [O I] 63 μm line is the strong line at the right side of the spectrum. The location of lines of CO, H_2O, atomic fine-structure lines, and OH are indicated by the bars at the bottom of the figure (see legend).

$12^h01^m36.81^s$ -$65^d08^m49.22^s$ and $12^h01^m34.09^s$ -$65^d08^m47.36^s$, respectively, measured from observations at 3 mm (Chen et al., 2008); positions at other wavelength, such as near-infrared, may differ because of extinction and scattering. The derived gas masses within about 7″ of the two sources are different by a factor of 50, $M_{\rm IRS1} = 2.12 \pm 0.41$ $M_\odot$ and $M_{\rm IRS2} = 0.05 \pm 0.02$ $M_\odot$ (Chen et al., 2008). Each infrared source has an associated outflow. However there is not sufficient evidence to establish the relationship between the two infrared sources. The bolometric luminosities of IRS1 and IRS2 are 13.5 $L_\odot$ and 0.5 $L_\odot$, respectively (Chen et al., 2008). In this study, the secondary source, IRS2, is not considered in detailed modeling, but it is discussed in Section 3.3.10.

B97 fitted the CO $J = 1 \rightarrow 0$ outflow observations with an edge-on biconical outflow cavity, and the *Spitzer*-IRAC image is roughly consistent with that picture. The center of IRS1 locates outside of the tip of the scattered light observed in the 2MASS image, while it locates within the tip of scattered light seen in the *Spitzer* image. Although Bourke et al. (1995a) deduced an inclination angle of 84° from the CO outflow, the fact that the center of IRS1 locates within the tip of scattered light in the *Spitzer* image hints that the inclination angle might not be so close to an edge-on view, which would make the center locate outside of the tip of the scattered light. We later conclude from the simulated images that the inclination angle should be close to 50° (see Section 3.4.4.2) The arc shape in IRAC 3.6 μm (blue) at the south of IRS1 shows that the outflow cavity is irradiated by the light from the center.

3.3.2 *Spitzer*-IRS Spectrum and Submillimeter Flux

The *Spitzer*-IRS spectrum was observed in high spectral resolution mode (R∼600) and extracted with the method described in Furlan et al. (2011). The flux at 1.3 mm is measured by Launhardt et al. (2010) from the observation of B97 with the Swedish-ESO Submillimeter Telescope (SEST). A total flux of 3.8 Jy is measured within a 9000 AU radius aperture (Chen et al., 2008).

3.3.3 The PACS and SPIRE 1D Spectra

The SED of BHR71 including *Herschel* PACS and SPIRE 1-D line-free spectra (green and red, respectively) is shown in Figure 3.2 along with the photometric data

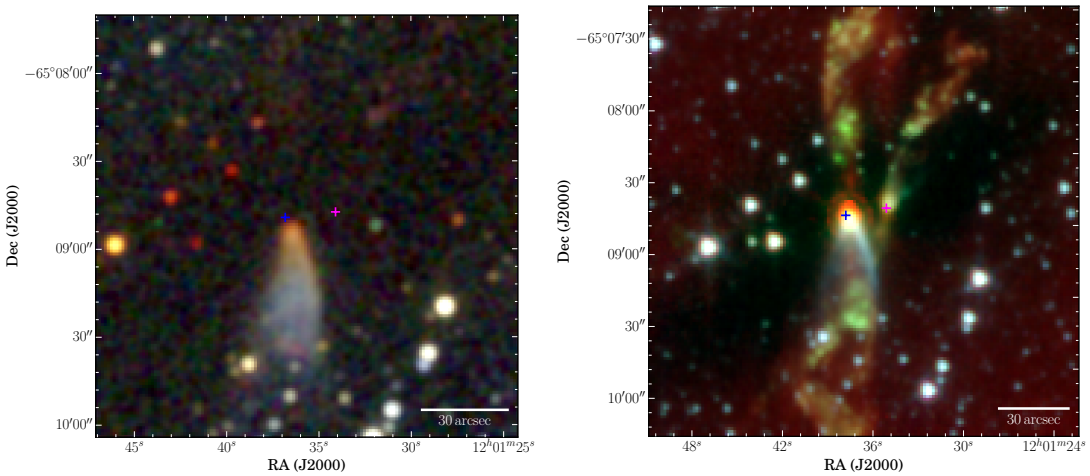

Figure 3.4: **Left:** The false-color image with 2MASS *J, H,* and *K* bands in blue, green, and red. The north lobe of the outflow is not seen in 2MASS image, while the south lobe shows a similar shape to the *Spitzer*-IRAC image on the right. This image is about 145″×145″, corresponding to 0.14 pc. The blue and magenta crosses label the location of IRS1 and IRS2. **Right:** The false-color image with *Spitzer*-IRAC 3.6 μm, 4.5 μm, and 8.0 μm in blue, green, and red. This image is 180″×180″, corresponding to 0.17 pc. The blue and magenta crosses are the continuum peaks measured in 3 mm continuum (Chen et al., 2008). The primary source, IRS1, is at the center of image (blue cross), while there is a secondary source, IRS2, at the right from the center (magenta cross) that has $\sim$ 2% of the mass of the primary source. The coordinates of IRS1 and IRS2 are $12^h01^m36.81^s$ -$65^d08^m49.22^s$ and $12^h01^m34.09^s$ -$65^d08^m47.36^s$, respectively.

obtained from the archive. The photometric fluxes observed by *Herschel* are calibrated as described in Section 3.2.1.

3.3.4 Line Fitting Results

We detect 61 lines in the 1-D PACS and SPIRE combined spectrum, 430 lines in the PACS-cube, and 215 lines in the SPIRE-cube. The line-fitting results for the 1-D spectrum are summarized in Table 3.2. The complete fitting results including all spaxels in PACS and SPIRE are available from the Herschel Science Archive[2].

[2] http://www.cosmos.esa.int/web/herschel/user-provided-data-products

Table 3.1: Photometric Fluxes

instrument/λ (μm)	flux (Jy)	uncertainty (Jy)	aperture (arcsec)
IRAC1 / 3.6	1.87×10^{-3}	6.18×10^{-4}	7.2
IRAC2 / 4.5	1.87×10^{-2}	3.67×10^{-3}	7.2
IRAC3 / 5.8	9.84×10^{-2}	6.81×10^{-3}	7.2
IRAC4 / 8.0	2.08×10^{-1}	1.15×10^{-2}	7.2
MIPS / 24	4.7	4.49×10^{-1}	20.4
PACS / 70	141.6	7.7	31.8
PACS / 100	269.2	10.6	31.8
PACS / 160	305.1	7.5	31.8
SPIRE / 250	121.0	12.9	24.1
SPIRE / 350	62.4	9.1	29.6
SPIRE / 500	30.9	6.6	39.8
SEST / 1300	3.8	0.57	90.0

Table 3.2: Line fitting, PACS+SPIRE 1D spectra

Transition	E_u (K)	Wave. (μm)	Flux[a] (10^{-18}W/m^2)	Transition	E_u (K)	Wave. (μm)	Flux[a] (10^{-18}W/m^2)
CO $J = 41 \rightarrow 40$	4737.13	64.11	134 [42.5]	CO $J = 18 \rightarrow 17$	944.97	144.79	652 [26.0]
CO $J = 36 \rightarrow 35$	3668.78	72.85	114 [33.0]	CO $J = 17 \rightarrow 16$	845.59	153.27	631 [14.1]
CO $J = 34 \rightarrow 33$	3279.15	77.05	93.2 [24.3]	CO $J = 16 \rightarrow 15$	751.72	162.82	667 [23.9]
CO $J = 32 \rightarrow 31$	2911.15	81.81	135 [26.6]	CO $J = 15 \rightarrow 14$	663.35	173.63	637 [15.5]
CO $J = 31 \rightarrow 30$	2735.28	84.41	209 [34.1]	CO $J = 14 \rightarrow 13$	580.49	186.00	622 [20.6]
CO $J = 30 \rightarrow 29$	2564.83	87.17	155 [29.3]	CO $J = 13 \rightarrow 12$	503.13	200.28	654 [33.1]
CO $J = 29 \rightarrow 28$	2399.82	90.16	165 [23.6]	CO $J = 12 \rightarrow 11$	431.29	216.92	612 [34.1]
CO $J = 28 \rightarrow 27$	2240.24	93.34	182 [23.0]	CO $J = 11 \rightarrow 10$	364.97	236.61	459 [19.9]
CO $J = 25 \rightarrow 24$	1794.23	104.47	423 [36.4]	CO $J = 10 \rightarrow 9$	304.16	260.25	467 [17.2]
CO $J = 24 \rightarrow 23$	1656.47	108.75	508 [43.9]	CO $J = 9 \rightarrow 8$	248.88	289.10	356 [14.3]
CO $J = 23 \rightarrow 22$	1524.19	113.46	489 [22.8]	CO $J = 8 \rightarrow 7$	199.11	325.24	365 [13.3]
CO $J = 22 \rightarrow 21$	1397.38	118.59	530 [36.1]	CO $J = 7 \rightarrow 6$	154.87	371.64	349 [8.47]
CO $J = 21 \rightarrow 20$	1276.05	124.19	595 [17.8]	CO $J = 6 \rightarrow 5$	116.16	433.54	279 [4.07]
CO $J = 20 \rightarrow 19$	1160.20	130.37	634 [33.7]	CO $J = 5 \rightarrow 4$	82.97	520.14	247 [5.94]
CO $J = 19 \rightarrow 18$	1049.84	137.22	662 [27.5]	CO $J = 4 \rightarrow 3$	55.32	650.23	220 [5.70]
^{13}CO $J = 9 \rightarrow 8$	237.93	302.42	43.9 [13.2]				
OH $^2\Pi^-_{1/2,\ 1/2} \rightarrow {}^2\Pi^+_{3/2,\ 3/2}$	181.9	79.12	128 [34.3]	OH $^2\Pi^-_{3/2,\ 5/2} \rightarrow {}^2\Pi^+_{3/2,\ 3/2}$	120.7	119.34	165 [25.7]
OH $^2\Pi^+_{1/2,\ 1/2} \rightarrow {}^2\Pi^-_{3/2,\ 3/2}$	181.7	79.18	128 [34.3]	OH $^2\Pi^+_{3/2,\ 5/2} \rightarrow {}^2\Pi^-_{3/2,\ 3/2}$	120.5	119.44	280 [25.7]
o-H_2O $3_{21} \rightarrow 2_{12}$	305.3	75.38	155 [26.5]	o-H_2O $5_{23} \rightarrow 4_{32}$	642.4	156.27	57.4 [17.1]
o-H_2O $4_{23} \rightarrow 3_{12}$	432.2	78.75	123 [36.7]	o-H_2O $3_{03} \rightarrow 2_{12}$	196.8	174.63	347[b] [16.3][b]
o-H_2O $6_{16} \rightarrow 5_{05}$	643.5	82.02	110 [28.2]	o-H_2O $2_{12} \rightarrow 1_{01}$	114.4	179.53	516 [14.6]
o-H_2O $2_{21} \rightarrow 1_{10}$	194.1	108.10	324 [44.7]	o-H_2O $2_{21} \rightarrow 2_{12}$	194.1	180.48	89.0 [14.0]
o-H_2O $7_{43} \rightarrow 7_{34}$	1339.9	112.5	97.7 [23.1]	o-H_2O $3_{21} \rightarrow 3_{12}$	305.3	257.82	54.0 [17.8]

o-H_2O $4_{14} \rightarrow 3_{03}$	323.5	113.54	427 [22.8]	o-H_2O $3_{12} \rightarrow 2_{21}$	249.4	259.99	148 [17.2]
o-H_2O $7_{25} \rightarrow 7_{16}$	1125.7	127.91	81.0 [24.0]	o-H_2O $3_{12} \rightarrow 3_{03}$	249.4	273.20	58.0 [15.2]
o-H_2O $4_{23} \rightarrow 4_{14}$	432.2	132.43	58.0 [18.4]	o-H_2O $1_{10} \rightarrow 1_{01}$	61	538.21	41.7 [5.90]
p-H_2O $4_{04} \rightarrow 3_{13}$	319.5	125.38	171 [19.0]	p-H_2O $1_{11} \rightarrow 0_{00}$	53.4	269.30	168 [15.9]
p-H_2O $3_{13} \rightarrow 2_{02}$	204.7	138.52	207 [23.1]	p-H_2O $2_{02} \rightarrow 1_{11}$	100.8	303.46	146 [13.2]
p-H_2O $3_{22} \rightarrow 3_{13}$	296.8	156.20	79.6 [17.1]	p-H_2O $2_{11} \rightarrow 2_{02}$	136.9	398.63	35.6 [5.95]
[O I] $^3P_1 \rightarrow {}^3P_2$	227.71	63.18	2009 [74.0]	[C II] $^2P_{3/2} \rightarrow {}^2P_{1/2}$	91.21	157.75	-227[c] [17.7]
[O I] $^3P_0 \rightarrow {}^3P_1$	326.58	145.54	202 [21.8]	[C I] $^3P_1 \rightarrow {}^3P_0$	23.62	609.15	13.2 [4.02]

[a]The uncertainty of the line flux is labeled in the bracket.

[b]The o-H_2O $3_{03} \rightarrow 2_{12}$ line may be contaminated by p-H_2O $5_{33} \rightarrow 6_{06}$ line, but the separation between two lines is too small to decouple their contribution.

[c]The absorption found at [C II] $^2P_{3/2} \rightarrow {}^2P_{1/2}$ is likely to be the artifact of the subtraction of the off-source position during the observation.

3.3.5 CO Rotational Diagram

There are 30 rotational transition lines detected in the 1-D spectrum, ranging from J=41→40 to J=4→3. Here we focus on the 1-D spectrum for the best constraint on the excitation temperatures for the whole object. The relative strengths of transitions of the same molecule probe the excitation environment of the molecule. By constructing a rotational diagram for CO, we can constrain the excitation temperature and the total number of CO molecules. We follow the procedures described by Green et al. (2013c) to construct the rotational diagrams.

A single rotational temperature does not fit the observed population distribution (Figure 3.5). Fitting the rotational diagram with multiple temperature components is necessary. We recover four temperature components, 43 K, 197 K, 397 K, and 1057 K. We let the break points between different temperature components be flexible during the χ^2 minimization. The ranges of the CO J-levels defined by the best-fitted break points are $J_{\rm up} = 4$ to $J_{\rm up} = 7$ (cold), $J_{\rm up} = 8$ to $J_{\rm up} = 15$ (cool), $J_{\rm up} = 16$ to $J_{\rm up} = 25$ (warm), and $J_{\rm up} = 26$ to $J_{\rm up} = 41$ (hot), where $J_{\rm up}$ is the rotational angular momentum quantum number of the upper level of transitions. The highest and second highest temperature components are consistent with the "warm" and "hot" temperature components found in Green et al. (2013c) with the PACS spectrum only. The need for the "cool" ($T_{\rm rot} \sim 200$ K) and "cold" ($T_{\rm rot} \sim 50$ K) components emerges from the SPIRE data.

3.3.6 Distribution of CO Emission

With the spaxel configuration of *Herschel*, the spatial distribution of the emission lines can be extracted from the spectra. Figure 3.6 shows a subset of the CO maps (blue contours) on top of continuum images (false color). The low-J CO ($J \leq 13$) lines are extended along the north-south direction of the outflow mapped by CO $J = 1 \rightarrow 0$ and H_2 (B97, Giannini et al. 2011; Gusdorf et al. 2011). The common characteristic of low-J CO lines is that the peak intensity is located at off-center positions. The CO $J = 13 \rightarrow 12$ line is actually undetected in the central spaxel, but detected in off-center positions, similar to the CO $J = 1 \rightarrow 0$ line wing distribution (B97).

In contrast, the high-J CO lines ($J_{\rm u} > 13$) are well-centered on the continuum, tracing the hot gas component near the central protostar. An extension toward north-east direction is found for high-J levels (e.g. last row in Figre 3.6). The reason for

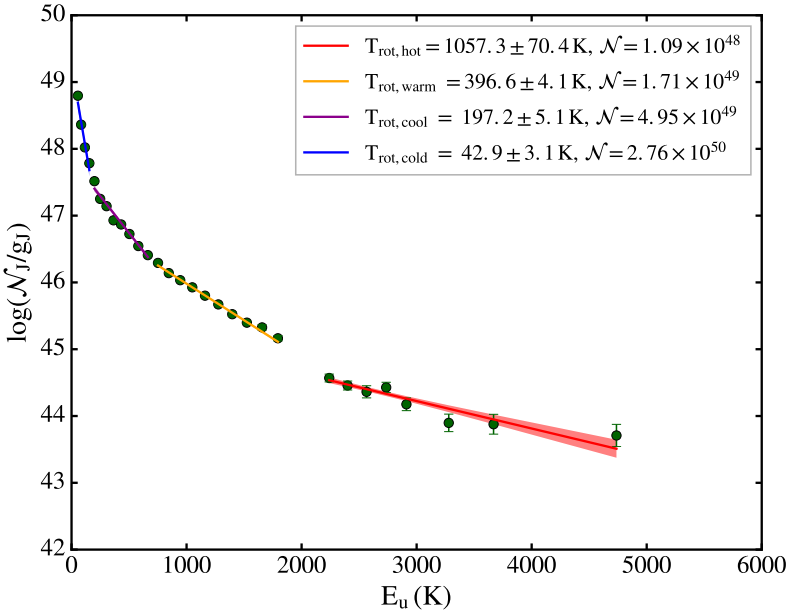

Figure 3.5: CO rotational diagram with a four-temperature fit. The $\mathcal{N}_J$ is the total number of CO molecules at J level, g_J is the multiplicity at J level, and E_u is the energy of the upper level of the corresponding transition. The best-fit is plotted as a solid line, while the uncertainty of the fit is shown in the corresponding shaded area.

such effect is inconclusive from the data presented here, but it may be due to the occurrence of spot shocks in the outflow cavity. Note that the difference between low-J and high-J distributions is partly caused by the switch from SPIRE to PACS at $J_{up} = 14$, because the PACS observations do not cover the extended outflow.

3.3.7 Distribution of OH Emission

The OH contours do not exhibit the bipolar morphology seen in the low-J CO contours (Figure 3.7). However, two lines that have multiple detections across the field of view show extension toward the north-east. Most of the spaxels have no detections of OH lines except for the doublet lines with the lowest upper state energy. These two lines also show extension toward north-east similar to the morphology found in high-J CO distributions, which may be due to the occurrence of spot shocks in the outflow cavity (Figure 3.7). The spot shocks are the J-type shocks that occur when the wind first impacts the envelope or outflow cavity (Mottram et al., 2015).

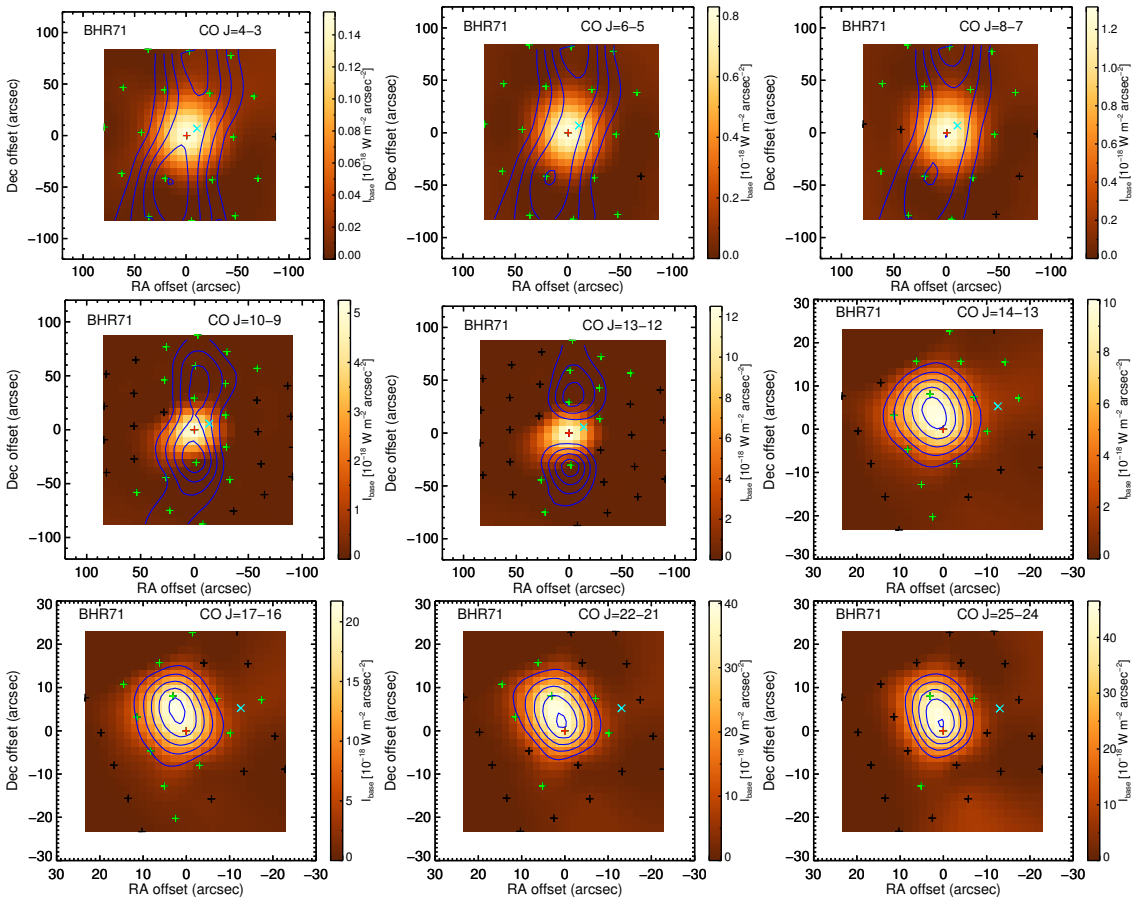

Figure 3.6: CO contours of different transitions with the local continuum in color. The blue contours are plotted at 20% intervals down to 20% of the maximum line strength. The black crosses are the configuration of spaxels, and green crosses indicate line detection. The red cross indicates the center of the field of view and the position of IRS1, while the cyan "X" indicates the position of IRS2. The contours of CO $J = 4 \rightarrow 3$ to CO $J = 13 \rightarrow 12$ are observed with a larger beam of SPIRE, while the contours of CO $J = 14 \rightarrow 13$ and the lines from higher upper energy levels are observed with a smaller beam of PACS. Therefore, these two groups have different spaxel configuration and field of view.

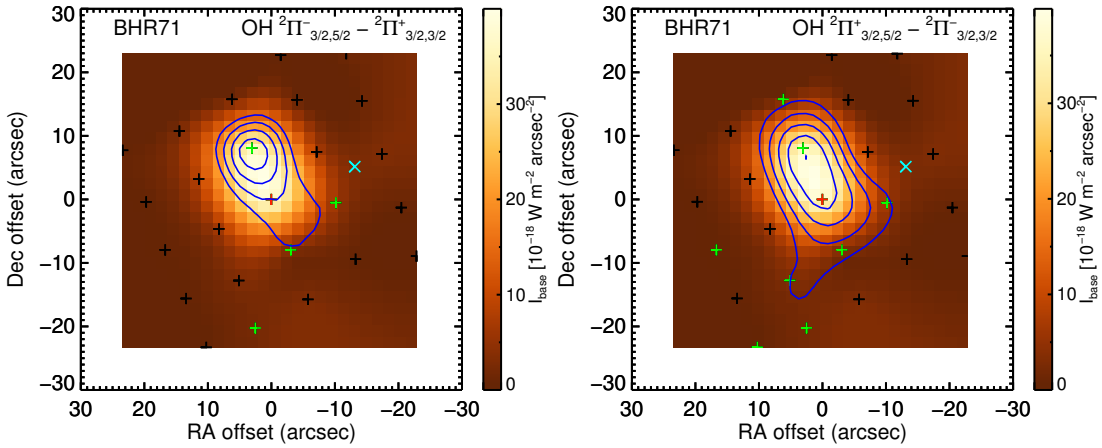

Figure 3.7: The contours of OH doublet lines at 119.23 μm (left) and 119.46 μm (right). The color code, contour levels, and symbols are the same as Figure 3.6

3.3.8 Distribution of Water Emission

3.3.8.1 Large Scale: SPIRE

Lines of both ortho-water (o-H_2O) and para-water (p-H_2O) were detected. The difference in the field of view between PACS and SPIRE modules makes the emission line distributions hard to compare directly. This section focuses on the large scale distribution, observed by SPIRE, while the small scale distribution, observed by PACS, is presented in the next section.

Figure 3.8 shows the detected water line distributions with an approximate $200'' \times 200''$ field of view and the spatial resolutions about $19''$ and $35''$ for SSW and SLW modules respectively. The roughly north-south distribution of water lines, which is along the outflow direction, is the common feature of lines detected in the SPIRE module. Two water lines, o-H_2O $1_{10} \rightarrow 1_{01}$ and p-H_2O $2_{11} \rightarrow 2_{02}$ have detections at the center of dust continuum with an emission distribution extended north-south. The other three lines are not detected at the center, but the emission distributes along the outflow direction with a similar size and morphology to the other two lines. This morphology is similar to the distribution seen in CO $J = 13 \rightarrow 12$ lines.

3.3.8.2 Small Scale: PACS

The spaxel distribution of PACS provides a smaller, $40'' \times 40''$, field of view with better spatial resolution of $9''$ to $18''$. Figure 3.9 shows the detected water emission line

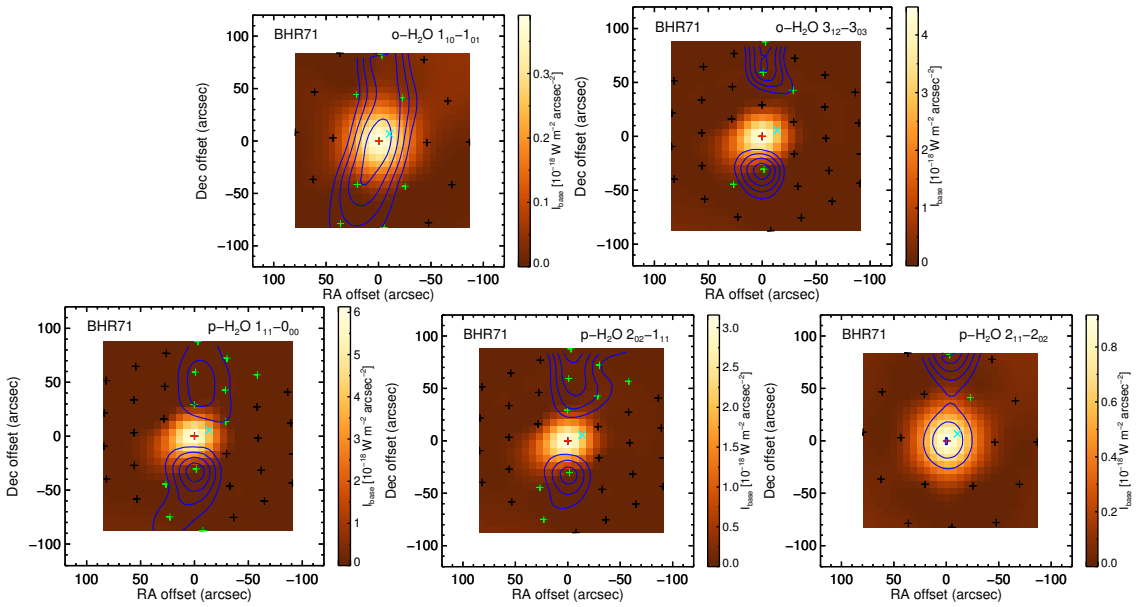

Figure 3.8: The water emission lines distribution on a large scale, observed by SPIRE. The color code, contour levels, and symbols are the same as Figure 3.6.

distributions observed by PACS. Unlike the characteristic north-south distribution seen in large scale SPIRE contours, the distributions are either centered or extended toward the east-west direction at small scales. Some lines are not detected at the central position.

The distributions of several water lines extend toward IRS2, marked in cyan "X". The o-H_2O $2_{21} - 2_{12}$ and o-H_2O $4_{23} - 4_{14}$ lines peak around IRS2 with only little or no emission detected at IRS1. Other emission lines, including o-H_2O $2_{12} - 1_{01}$, o-H_2O $2_{21} - 1_{10}$, o-H_2O $3_{03} - 2_{12}$, p-H_2O $3_{13} - 2_{02}$, and p-H_2O $4_{04} - 3_{13}$ show clear extension from the center toward IRS2, but peaking at IRS1. The correlation of the water emission with IRS2 indicates that IRS2 may contribute an outsized portion of the water emission given that its luminosity is only $\sim 5\%$ of the luminosity of IRS1.

3.3.9 Distribution of Atomic Fine-structure Transitions

The atomic fine-structure lines of [O I] trace shocked regions in the protostellar environment (Hollenbach, 1985b; Hollenbach & McKee, 1989), especially the low density environment ($n \lessapprox 10^5$ cm^{-3}), where O I is the dominant coolant. In the [O I] contours (Figure 3.10), the distribution of [O I] $^3P_1 \rightarrow {}^3P_2$ at 63 μm is fairly

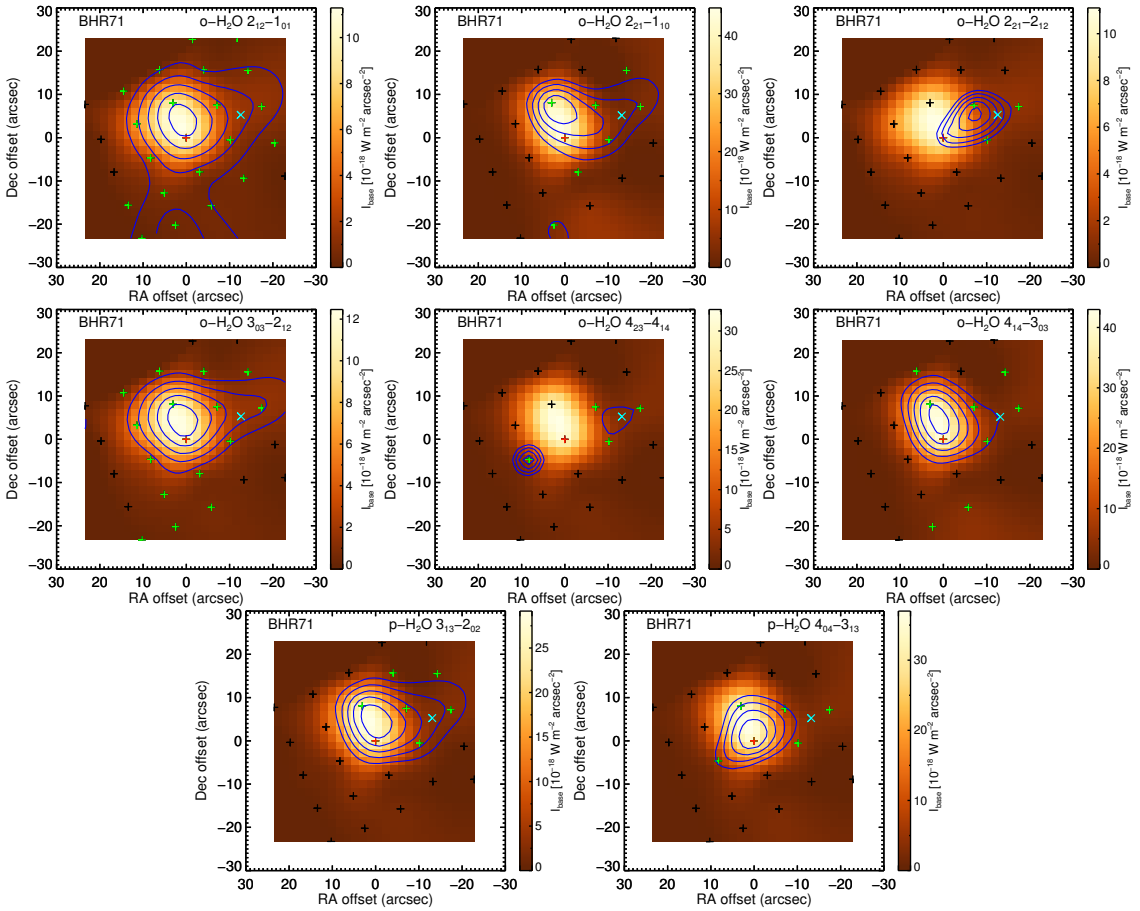

Figure 3.9: The water emission lines distribution, observed by PACS. The color code, contour levels, and symbols are the same as Figure 3.6.

symmetric, while the [O I] $^3P_0 \rightarrow {}^3P_1$ at 145 μm is only detected at the central spaxel. Figure 3.10 shows that [C I] $^3P_1 \rightarrow {}^3P_0$ emission lines are extended toward the north, while the continuum is well-centered. We observed [C II] $^2P_{3/2} \rightarrow {}^2P_{1/2}$ in absorption, likely the result of off-source emission. Due to regional widespread [C II] emission, the telescope nodding during the observations results in absorption when the off-source position has more [C II] emission than BHR71.

3.3.10 Relation between IRS1 and IRS2

IRS2, first observed with ISOCAM by Bourke (2001), is separated by $\sim$17″ ($\sim$ 3400 AU) in projection from IRS1 toward the west. Two sources can be eas-

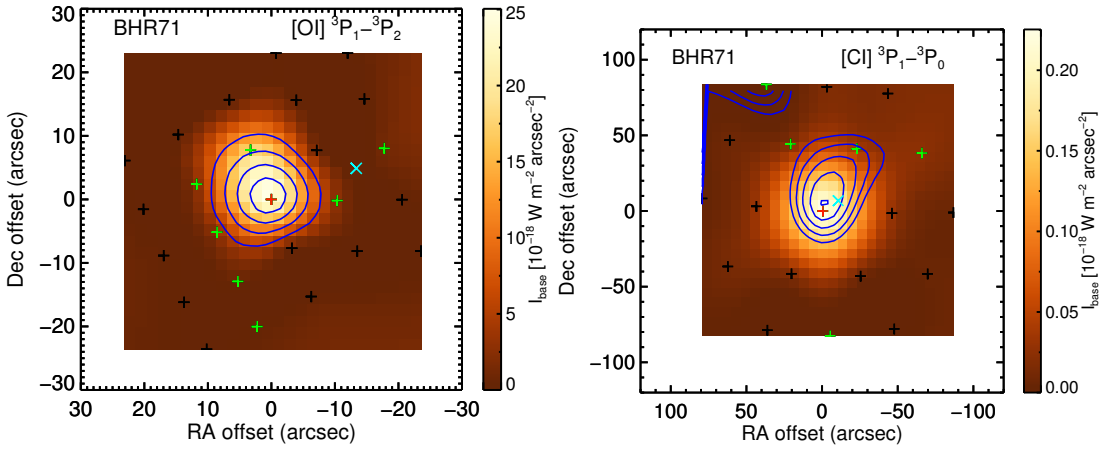

Figure 3.10: The [O I] $^3P_1 \rightarrow {}^3P_2$ emission line distribution is shown at the left, and the distribution of [C I] $^3P_1 \rightarrow {}^3P_0$ is shown at the right. The color code, contour levels, and symbols are the same as Figure 3.6.

ily seen in the *Spitzer*-IRAC image (Figure 3.4) with a bipolar outflow associated with each source. Observations of the CO $J = 3 \rightarrow 2$ line (Parise et al., 2006a) reveal the kinematics of the CO outflows of each source; the outflow driven by IRS1 has a PA of $\sim 165° - 170°$, while the outflow driven by IRS2 has a PA between $-35°$ and $-30°$. Mundy et al. (2000) summarized that two protostellar sources with their own independent envelope are likely to be separated by $\geq$6000 AU; and two sources are likely to share a common envelope if the separation is between 150-3000 AU. However, the projected separation of 3400 AU between IRS1 and IRS2 does not provide a clear indication of the relation between two sources. Note that the separation of 3400 AU is the minimum distance between two sources. Chen et al. (2008) found that the kinematics are dominated by IRS1 from their observation with ATCA. Therefore, it is still uncertain whether the two sources are formed by initial core fragmentation or rotational fragmentation during the core collapse.

Herschel-PACS has a spatial resolution of $\sim 9'' - 18''$, with which IRS2 may be resolved from IRS1; *Herschel*-SPIRE has a spatial resolution of $\sim 17'' - 40''$, barely separating the two sources at the shortest wavelength. Our *Herschel* observations show that emission from IRS1 dominates the continuum emission at all wavelengths. The continuum emission from IRS2 can be seen only in the PACS 70 μm image with a logarithmic stretch (Figure 3.11, top). The flux ratio of IRS1 to IRS2 is about 17 at 70 μm. Two circles (solid and dashed) show the regions used for extracting the

1-D spectrum at PACS wavelengths and SPIRE 500 μm. The peak of IRS2 is not included for the PACS spectrum and photometry, and the flux contributed by IRS2 is at most 6%. The spatial resolution at SPIRE wavelengths cannot separate IRS1 and IRS2. Assuming the same flux ratio measured from PACS 70 μm image, the flux contributed from IRS is $\sim$6%, similar to the assumption made in Chen et al. (2008). IRS2 alone would produce a dust temperature equal to that produced by IRS1 within a radius of 137 AU, or 0.″7, a very small fraction of the region we model. Without further constraints on the nature of IRS2, we focus on IRS1 in the following continuum simulations (see Section 3.4).

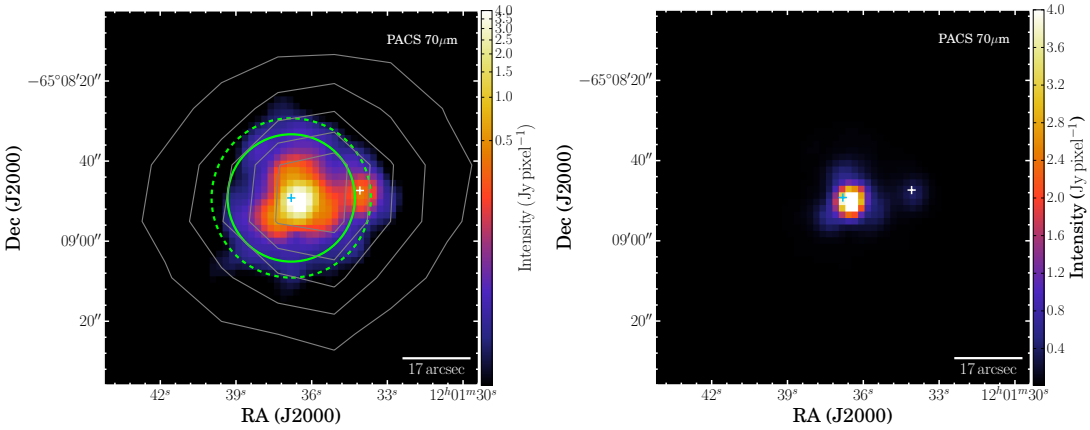

Figure 3.11: *Herschel* 70 μm image of BHR71 acquired from the Herschel Science Archive. The center of the image is at the center of BHR71 IRS1. The flux is plotted with the same maximum and minimum values in logarithm scale on the top and linear scale on the bottom. The blue and white crosses indicate the positions of IRS1 and IRS2 measured by Chen et al. (2008). The solid and dashed circles shown in the top figure indicate the region used for extracting 1-D PACS photometry and SPIRE 500 μm photometry, respectively. The grey contour shows the SPIRE 500 μm emission.

3.4 Modeling the Continuum Emission

A radiative transfer simulation can reveal the contribution and the structure of central protostar, disk, outflow, and envelope in detail. BHR71 is formed within an isolated Bok globule (Bourke et al., 1995a), making it a good candidate for a detailed dust radiative transfer simulation. With a very complete SED, ranging from

3.6 to 1300 μm and spatial information at some wavelengths, we can constrain a fairly complex and realistic model for the source structure. We use information from previous observations for the distance (200 pc). The integral over all wavelengths in Figure 3.2 yields an observed luminosity of 13.92 $L_\odot$. The actual luminosity is likely to be higher because not all the beams cover the entire source and because of inclination effects, so we constrain models to match the observed luminosity by simulating observations into the actual beam sizes. In optimizing the model, we use azimuthally averaged radial profiles of intensity at 160 μm, the ratio of emission at IRAC bands from the north and south sides, and the SED. How each of these constrains different model parameters is explained in the relevant sections.

The simulated flux densities into the observed apertures are compared to the observations in Table 3.1. For the *Spitzer* spectrum, we adopt the size of four pixels for each module of *Spitzer* (Equation 3.1), which is the averaged aperture size adopted in the reduction.

$$\begin{aligned} d_{\rm aper} &= 7.2'' && \text{for } 5\ \mu\text{m} < \lambda \leq 14\ \mu\text{m} \\ &= 20.4'' && \text{for } 14\ \mu\text{m} < \lambda \leq 40\ \mu\text{m} \end{aligned} \tag{3.1}$$

For the *Herschel* spectrum, we use a constant aperture size, 31.8″ for PACS wavelength, and use aperture sizes that increase with wavelength for the three SPIRE bands (see Table 3.1).

3.4.1 Dust Radiative Transfer Simulation

We use HYPERION, a publicly available three-dimensional radiative transfer calculation package (Robitaille, 2011), as our tool to compare the synthetic observations of different models to the observed spectra. The simulation uses a two-step procedure, calculating the dust temperature with the Monte Carlo method and ray-tracing photons from each cell. We set the convergence criteria of the Monte Carlo calculation with three parameters described in Robitaille (2011), p, Q and Δ, as 95, 2, and 1.02 in HYPERION. In other words, the convergence is achieved when 95% of the differences in specific energy absorption rate between two iterations are less than a factor of 2 and the differences of the 95th percentile of the value difference are less than a factor of 1.02. The simulation is able to produce reliable results with shorter computational time with this convergence setup. A model takes $\sim$ 20 minutes to run, using twenty

2.6 GHz processors. Each simulation is run with a million photons for determining dust temperature, imaging, and raytracing. We increase the number of photons for imaging to 50 million for the best fit model and the same model with the geometry suggested by B97 for better image quality (see Section 3.4.4.2).

An input density distribution (Section 3.4.2), assuming a gas-to-dust ratio of 100, serves as the input of the Monte Carlo dust radiative transfer calculation, together with the dust properties, which are taken from Table 1 Col. 5 in Ossenkopf & Henning (1994) and extended with anisotropic scattering (Section 2.1 in Young & Evans (2005)), hereafter referred to as OH5 dust.

3.4.2 Physical Model Setup

Envelope, disk, and outflow cavity are included in the dust density distribution. The three components are constructed separately but share some parameters. We include the outflow cavity in our structure to make the simulation consistent with the outflow activities observed around BHR71. As discussed later in Section 3.5.1, the outflow cavity is essential to achieving the best fit model for BHR71.

3.4.2.1 Envelope Model

We construct the envelope model based on the "inside-out" collapse model (Shu, 1977b) and its slowly rotating generalization. Before the cloud collapse, the cloud can be approximated as an isothermal sphere with $\rho(r) \propto r^{-2}$ (Equation 3.2).

$$\rho(r) = \frac{c_{\mathrm{s,\ eff}}^2}{2\pi G r^2} \tag{3.2}$$

where $c_{\mathrm{s,eff}}$ is the effective sound speed of the cloud, including the contribution of non-thermal velocity. After the cloud starts to collapse, the inner regions of the cloud are infalling, while the outer regions are still in a static phase because the collapse propagates outward at the sound speed of the cloud. Protostars embedded in envelopes are mostly considered to be in this stage. The conservation of angular momentum requires that the outermost material can fall to only the centrifugal radius instead of the center of the cloud. To take the effects of rotation into account, we use the slowly rotating collapse model (Terebey et al. (1984b); hereafter TSC model) to calculate the envelope density structure. The TSC model is specified by three input

parameters, the effective sound speed, the age ($t_{\rm col}$), and the initial rotation speed ($\Omega_\circ$). The age is the time since the collapse began and does not include the pre-collapse evolution. The relation between these three parameters and other properties are illustrated in Equation 3.3.

$$\begin{aligned}
\dot{M}_{\rm env} &= 0.975\frac{{c_{\rm s,eff}}^3}{G} \\
M_\star &= \dot{M}_{\rm env} t_{\rm col} \\
R_{\rm c} &= \frac{\Omega_\circ^2 G^3 M_\star^3}{16{c_{\rm s,eff}}^8} \\
R_{\rm inf} &= c_{\rm s,eff} t_{\rm col},
\end{aligned} \tag{3.3}$$

where $\dot{M}_{\rm env}$ is the mass infall rate of the envelope, $M_\star$ is the mass of the central star, $R_{\rm c}$ is the centrifugal radius of the envelope, and $R_{\rm inf}$ is the radius reached by the wave of infall.

It is necessary to include the static envelope beyond the infall radius in the envelope model for early stage protostars, because only the inner part of their envelopes are collapsing. The popular model grids of Robitaille et al. (2006b) do not include the static envelope and assume the asymptotic solution, which applies only to the inner part of the infalling, rotating envelope. Our envelope model setup has the full TSC model, which includes the transitional region between the infalling inner part and the static outer part (Dunham et al., 2010a). In contrast, the collapse-only model is calculated from equation 3.4 (Ulrich, 1976).

$$\begin{aligned}
\rho(r,\theta) = \frac{\dot{M}_{\rm env}}{4\pi(GM_\star R_{\rm c}^3)^{1/2}} \left(\frac{r}{R_{\rm c}}\right)^{-3/2} \left(1+\frac{\mu}{\mu_\circ}\right)^{-1/2} \\
\times \left(\frac{\mu}{\mu_\circ} + \frac{2\mu_\circ R_{\rm c}}{r}\right)^{-1}
\end{aligned} \tag{3.4}$$

where (r,θ) is defined in spherical coordinate, μ is cosθ (θ is the polar angle with respect to the rotational axis), $\mu_\circ$ is the cosine of the angle of a streamline of infalling particles as $r \rightarrow \infty$. We use the streamline equation to solve for the $\mu_\circ$ at each cell (Equation 3.5).

$$\mu_\circ^3 + \mu_\circ\left(\frac{r}{R_{\rm c}} - 1\right) - \mu\left(\frac{r}{R_{\rm c}}\right) = 0 \tag{3.5}$$

Figure 3.12 (left) compares the density profiles of the TSC model including the static outer envelope to an infall-only model. The infall-only model shows a sharp

density condensation toward the centrifugal radius and follows $\rho \propto r^{-1.5}$ relation everywhere beyond the centrifugal radius. This model has been widely used in the simulations of protostars (Robitaille et al., 2006b), etc. On the other hand, the full TSC model has a smoother density profile around the centrifugal radius and has more density within the centrifugal radius. In addition, the full TSC model does not follow a $r^{-1.5}$ relation at all radii between the centrifugal radius and infall radius, and it includes the static profile beyond the infall radius, $\rho \propto r^{-2}$. The effects of these differences on the SED and the radial intensity profile are substantial (Figure 3.12, right).

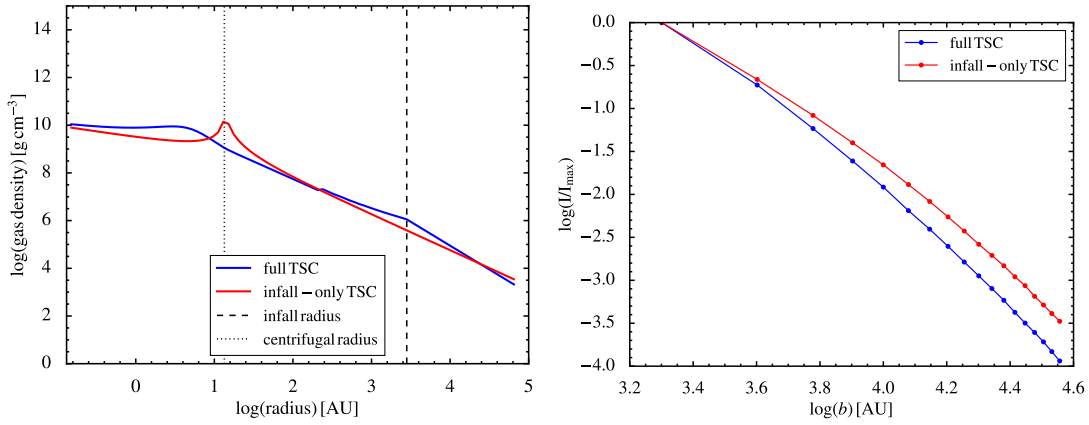

Figure 3.12: **Left:** The radial density profiles of the full TSC (blue) and infall-only TSC model (red). Both models are calculated with the parameters listed in Table 3.4, except for the angular speed. The parameters are adopted from Table 3.4. Both profiles are density profiles along the equatorial plane without disks, illustrating the effect of the full TSC model within the centrifugal radius. The centrifugal radius (black dotted lines) is 13 AU, and the infall radius (black dashed line) is 2800 AU. **Right:** The radial intensity profiles of the full TSC (blue) and infall-only TSC model (red).

The inner radius is set to the dust sublimation radius. There is a dust-free region at the very inner radius, where the dust is destroyed by the radiation from the central protostellar source. To get an idea about the effect of dust sublimation on the inner radius of the envelope, we calculate the sublimation radius with a simple dust model, blackbody dust, so that $\langle Q_{\rm abs} \rangle_\star = \langle Q_{\rm abs} \rangle_{T_{\rm d}} = 1$, where the star in the subscript means the absorption of protostellar radiation and the $T_{\rm d}$ in the subscript means the absorption of dust at the temperature of $T_{\rm d}$. Combining the equations, we can

calculate the dust sublimation radius, $d_{\rm sub}$, with Equation 3.8, where $T_{\rm sub}$ is the dust sublimation temperature.

$$\langle Q_{\rm abs}\rangle_\star \pi a^2 u_\star c = 4\pi a^2 \langle Q_{\rm abs}\rangle_{T_{\rm d}} \sigma T_{\rm d}^4 \tag{3.6}$$

where $u_\star$ is the energy density written in terms of the stellar flux ($F_\star$) or luminosity ($L_\star$) and distance:

$$u_\star = \frac{1}{c} F_\star = \frac{L_\star}{4\pi d^2 c} \tag{3.7}$$

$$\frac{d_{\rm sub}}{\rm AU} = 7.76 \times 10^4 \left(\frac{L_\star}{\rm L_\odot}\right)^{1/2} \left(\frac{T_{\rm sub}}{\rm K}\right)^{-2} \tag{3.8}$$

In the model setup, we set the dust sublimation temperature to 1600 K, similar to the value in Eisner et al. (2005), yielding $d_{\rm sub}$ = 0.11 AU for an initial guess with $L_\star$=13.92 $\rm L_\odot$. HYPERION calculates the radiative balance with each cell assuming local thermal equilibrium with the constraint of the dust sublimation temperature. We use the "slow" mode of dust sublimation in HYPERION, which means that HYPERION decreases the dust density if the dust temperature of a certain cell is found greater than the dust sublimation temperature until the resulting dust temperature is equal to the dust sublimation temperature (Robitaille, 2011).

3.4.2.2 The Disk Model

We add a flared accretion disk model (Shakura & Sunyaev, 2073; Robitaille et al., 2006b) (Equation 3.9) to the envelope model.

$$\rho(\varpi, z) = \rho_0 \left(1 - \sqrt{\frac{R_\star}{\varpi}}\right) \left(\frac{R_\star}{\varpi}\right)^\alpha \times \exp\left\{-\frac{1}{2}\left(\frac{z/h_{100}}{(\varpi/100\ \rm AU)^\beta}\right)^2\right\} \tag{3.9}$$

where ϖ and z in the equation are the variables in a cylindrical coordinate system, ρ_0 is the normalization constant for the given disk mass, h is the disk scale height, $\alpha = \beta$+1, where β is the flaring power. The disk scale height follows a simple power law with the flaring power β, where $h \propto \varpi^\beta$. The offset of the disk scale height profile is determined by h_{100} as the scale height at 100 AU. The disk inner radius is set to the dust sublimation radius, while the outer radius is set to the centrifugal radius calculated by the collapse model.

3.4.2.3 The Outflow Cavity Model

We include an outflow cavity described in cylindrical coordinates by $z = c_\circ \varpi^{1.5}$, based on the model in Robitaille et al. (2006b), where the constant $c_\circ$ is determined by the cavity opening angle ($\theta_{\rm cav}$) in Equation 3.10. We define the cavity opening angle as the angle of the edge of the cavity at 10000 AU with respect to the axis along the pole so that the full width opening angle is $2\theta_{\rm cav}$. Under this definition, the constant $c_\circ$ can be written as

$$c_\circ = \frac{1}{(10000\ {\rm AU})^{0.5}} \frac{\cos\theta_{\rm cav}}{\sin^{1.5}\theta_{\rm cav}} \tag{3.10}$$

The "cavity" is not empty; we fill it with dust from the protostellar wind. We modeled a variety of density distributions, including pure power laws and power laws modified to have a constant density region near the source. To conserve the total mass in each slice of the outflow, the density decreases as r^{-2}, because the area of each slice increases approximately as r^2. At the inner region of the outflow cavity, we expect a higher density region due to the shock into the ambient envelope, like the cavity shocks defined in Mottram et al. (2014a). To quantify the property of this inner region, we simplify its structure as a region with a higher constant density.

First, we estimate the approximate density of the constant density region at the inner region of the cavity as an initial guess. The idea of this estimation is to calculate the density at the innermost region of the cavity where the mass is distributed by outflows with a velocity of 300 km s^{-1} for a year. An outflow travels about 60 AU in one year with a velocity of 300 km s^{-1}, resulting in a volume of 1.8×10^{45} cm^3 with the cavity opening angle of 20°. For the mass loss rate in the outflow, we have 3.7×10^{-6} M$_\odot$ yr^{-1} derived from the momentum and the dynamical age of CO outflow measured by B97, assuming a wind speed of 300 km s^{-1}. This value is used as an initial guess as the inclination angle may change after the model optimization. Combining the total mass in the outflow within a one year travel time and the corresponding volume, we estimate the gas density of the constant density region as 4×10^{-18} g cm^{-3}. We then further adopt the gas-to-dust ratio of 100, resulting in a dust density of 4×10^{-20} g cm^{-3}, which is the initial guess of the density of the constant density region at the innermost part of outflow cavity.

We use a logarithmic grid on the r-axis, and a linear grid on the θ-axis and ϕ-axis. The logarithmic grid can give us enough resolution at the central region, where the

inner part of the outflow cavity and the disk have relative smaller structures, while the lower resolution in the outer envelope reduces the computing time. The cell size is limited to 100 AU in r-axis to ensure a sufficient resolution in the outer envelope. Since the density profile is azimuthally symmetric, the regular grid is good enough to sample the density structure well.

Besides the density profile, the central luminosity ($L_\star$) is a free parameter in the model. Because of the asymmetric structure the observed luminosity is not the same as the central luminosity. HYPERION takes two parameters, a stellar radius and a stellar temperature to specify the luminosity. We assume the radius of the protostar ($R_\star$) is 3 $R_\odot$ (Palla & Stahler, 1992). We use the Stefan-Boltzmann law to calculate the effective temperature ($T_\star$) from the luminosity of the protostar. Note that the actual luminosity is mostly due to accretion. The effective temperature is simply a way to parameterize the central luminosity.

$$L_{\rm cen} = 4\pi R_\star^2 \sigma T_\star^4 \tag{3.11}$$

3.4.3 Fixing Some Parameters

There are 13 parameters in the model (Table 3.3). We focus on constraining the best fit model here, but the effect of each parameter is explored in the Appendix.

With a computational time of ∼20 minutes per model, the time for a full grid over all 13 parameters would be prohibitive ($\sim 5^{13}$ models if 5 models for each parameter). We use the parameter studies described in the Appendix to guide our evaluation of the effect of parameter variations.

The search for the best fit model starts from fixing the parameters that have been derived from other observations to reduce the degrees of freedom and avoid degeneracies in simulations. The sound speed in the envelope ($c_{\rm s,eff}$) and the initial rotational speed ($\Omega_\circ$) can be derived from the kinematics of molecular emission lines. We fix the sound speed to avoid the degeneracy in the simulated SED between models with a smaller sound speed and a later age and models with a larger sound speed and an earlier age, discussed in Appendix B.1. We derive the effective sound speed from the linewidth measurement of NH_3, which has a full width at half maximum of 0.74 km s^{-1}, contributed by the thermal velocity dispersion with T=13 K derived by Bourke et al. (1995b), and 1-D turbulence velocity dispersion. Using the formulae in Equation 3.12, we derive a 1-D turbulent velocity dispersion of 0.34 km s^{-1} and an

Table 3.3: Model parameters

Envelope parameters	
$t_{\rm col}$	Age of the protostellar system after the start of collapse.
$c_{\rm s,eff}$[a]	Sound speed of the envelope including the turbulent velocity.
$\Omega_\circ$[a]	The initial angular speed of the cloud.
Disk parameters	
$M_{\rm disk}$[b]	Total mass of the disk.
β[a]	The flaring power of the disk.
h_{100}[a]	The disk scale height at 100 AU.
Outflow cavity parameters	
$\theta_{\rm cav}$[a]	The cavity opening angle defined in Section 3.4.2.3.
$\rho_{\rm cav,\circ}$	The dust density of the inner cavity.
$R_{\rm cav,\circ}$	The radius where the cavity density starts to decrease.
$\theta_{\rm incl.}$	The inclination angle of the protostar, 0° for face-on and 90° for edge-on view.
Other parameters	
$R_{\rm max}$[a]	Outer radius of the envelope as well as the outer radius of the model.
$T_\star$	The temperature of the central protostellar source assuming blackbody radiation.
$R_\star$[a]	The radius of the central protostellar source.

[a]These parameters are fixed in the search of the best fit model.

[b]The disk mass is set to be 25% of the total accreted mass.

effective sound speed of 0.37 km s^{-1}.

$$\sigma_{\rm NH_3} = \frac{\rm FWHM_{NH_3}}{\sqrt{8ln2}} = \left(\frac{kT}{m_{\rm NH_3}} + \sigma^2_{\rm NT}\right)^{1/2}$$
$$c^2_{\rm s,eff} = \left(\frac{kT}{\mu m_{\rm H}} + \sigma^2_{\rm NT}\right). \quad (3.12)$$

The observations of ^{13}CO (B97) show a deconvolved map size (FWHM) of 0.65×0.4 pc, with a geometric mean of 0.525 pc. We adopt an envelope outer radius of 0.315 pc, which gives the same area as a two-dimensional Gaussian with a FWHM of 0.525 pc. The resulting total gas mass of our best fit model is 19 M$_\odot$, while B97 derived a total molecular mass of ∼40 M$_\odot$ from ^{13}CO emission. An overestimated dust opacity by us or/and an underestimated abundance of ^{13}CO by B97 could explain the factor of two difference. Shirley et al. (2011) compared the dust opacity measured from infrared extinction and submillimeter continuum emission and found that the OH5 opacity at 850 μm can be overestimated by a factor of two. Therefore, the total envelope mass can be underestimated by a factor of two. B97 assumed a [^{12}CO/^{13}CO] ratio of 89, close to the value found in our Solar system. However, Langer & Penzias (1993) found an isotope ratio of 62±4 from four interstellar clouds. The value often used for local ISM is around 77 (Wilson & Rood, 1994). The lower isotope ratios would result in lower estimates for optical depth and lower masses inferred from ^{13}CO, effects that approach a factor of two. Some of the discrepancy in mass may also come from the extended structure, which is not included in our model but lies along the line of sight. Chen et al. (2008) also estimated the gas mass from 3 mm continuum observation, from which they derive 2.12 M$_\odot$ within 0.075×0.069 pc. If we scale down our total gas mass to the radius of a tophat beam that gives the same area, it would be 2.6 M$_\odot$, suggesting that our model setup sucessfully produces the observed envelope properties on small scales. The observations of N_2H^+ indicate a velocity gradient of 7.8 km s^{-1} pc^{-1} (Chen et al., 2008), corresponding to a rotational speed, $\Omega_\circ = 2.5 \times 10^{-13}$ s^{-1}, which we adopt.

Additionally, the disk mass is set to be a certain fraction of the total infallen mass, calculated from the products of mass infall rate and age (Equation 3.3). We assume that 25% of the total infallen mass forms the mass of the disk, about the maximum usually assumed for stable disks (Shu et al., 1990; Vorobyov, 2009). The other disk parameters are fixed, as we find that the disk is not very significant for the young

ages we find. Also, we fix the radius of the protostar as 3 $R_\odot$, suggested by Palla & Stahler (1992) and adjust the stellar temperature to change the luminosity to match the observations.

Lastly, we fix the outflow cavity opening angle as 20° based on the observation of B97. The geometry of the outflow cavity was modeled by B97, assuming a cavity opening angle of $15° \pm 5°$ to fit the CO $J = 1 \rightarrow 0$ distribution with a biconical flow model, resulting in an inclination angle of 84°. The cavity opening angle measured from the *Spitzer* image shows a similar value (Figure 3.4). Because of the degeneracy between the cavity opening angle and the cavity inclination angle (see Appendix B.3), we choose to fix the opening angle at its largest estimated value in simulations, leading to an upper limit to the inclination angle, defined so that 90° represents an edge-on view.

After fixing 8 out of 13 parameters in our model (see Table 3.4), we are left with the following parameters: $t_{\rm col}$, $\rho_{\rm cav,\circ}$, $R_{\rm cav,\circ}$, $\theta_{\rm incl.}$, and $T_\star$.

3.4.4 Best-Fit model

We start with initial guesses for the remaining free parameters based on the best fit model extracted from the grid of SEDs from Robitaille et al. (2006b). We then explore the parameter space around those values until a best fit model is found. Among all free parameters, we first constrain the remaining flexible envelope parameter, the age.

Figure 3.13 shows the radial density profile of our hybrid cavity profile at different polar angles, 0°, 22°, 45°, 67°, and 90°. The flat plateau at the smaller radii represents the constant density region at the innermost cavity followed by a power law decrease, while the flared disk contributes to the density excess at polar angle of 90° at radii shorter than centrifugal radius. The density jump seen at every line of sight except for the one with a polar angle of 90° occurs when the line of sight enters the envelope from the outflow cavity. The glitch around $\log(r) = 2.2$ is an artifact from the calculations of TSC model. We find no abrupt change in the simulated SEDs due to this glitch, while exploring the parameter space.

Figure 3.14 and Figure 3.17 show the best fitting SED and radial intensity profile. Table 3.4 lists the best fitting model parameters. Figure 3.15 shows the gas density profile and the dust temperature profile, with the quantities averaged over azimuth.

The overall fit to the radial profile and the SED is very good, but the exact

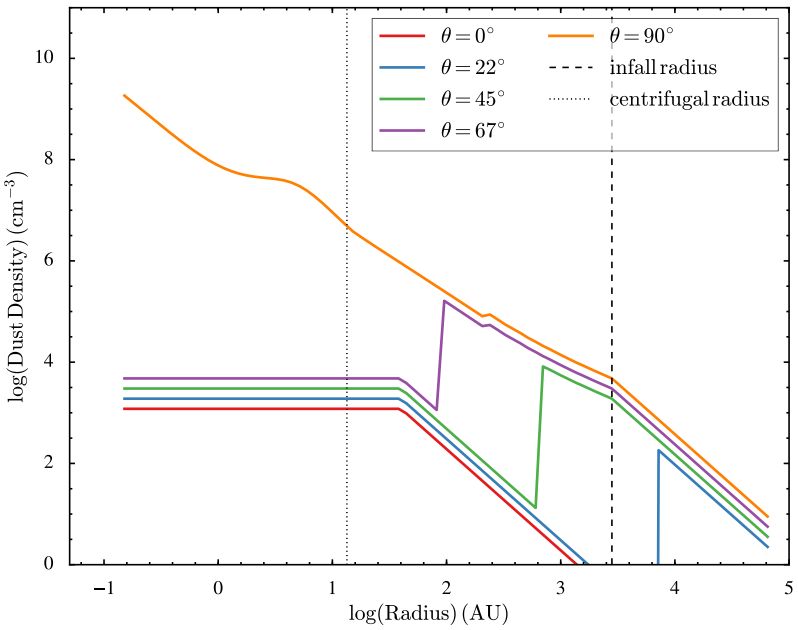

Figure 3.13: The radial dust density profile of the entire model setup at different polar angles (θ). The density profiles are offset by 0.2 dex between adjacent lines for a better visualization, while the dust profile at 90° (perpendicular to the outflow axis) is unchanged.

shape of the SED from 3-5 μm is not recovered with this model, suggesting that the emission from hot dust ($\sim$500 K) can reach the observer via other channels which are not included in our model. Also note that we overestimate the observations at the shortest wavelengths, possibly due to the lack of understanding of the structures near the center and the uncertainty in the dust model. The detailed SED in the 3-20 μm region includes many ice features, which are not included in our dust opacity model, such as the CO_2 ice feature at 15.2 μm. The 1.3 mm flux is underestimated in our best fit model possibly due to more extended emission (as seen in our 500 μm image in Figure 3.16), which is not included in our model. Although the observed fluxes around 100-500 μm are reasonably reproduced by our best fit model, the fitting may be improved with a better constraint on the initial rotational speed of the envelope. We assume the current rotational speed measured by Chen et al. (2008) is the initial rotational speed in our model. However, the rotational speed will constantly increase as the envelope collapses. So the value we use here should be the upper limit of the initial rotational speed of the envelope. As we discuss in Appendix B.1, if the

rotational speed is smaller, the fluxes around 100-500 μm will be increased slightly and produce a better fit.

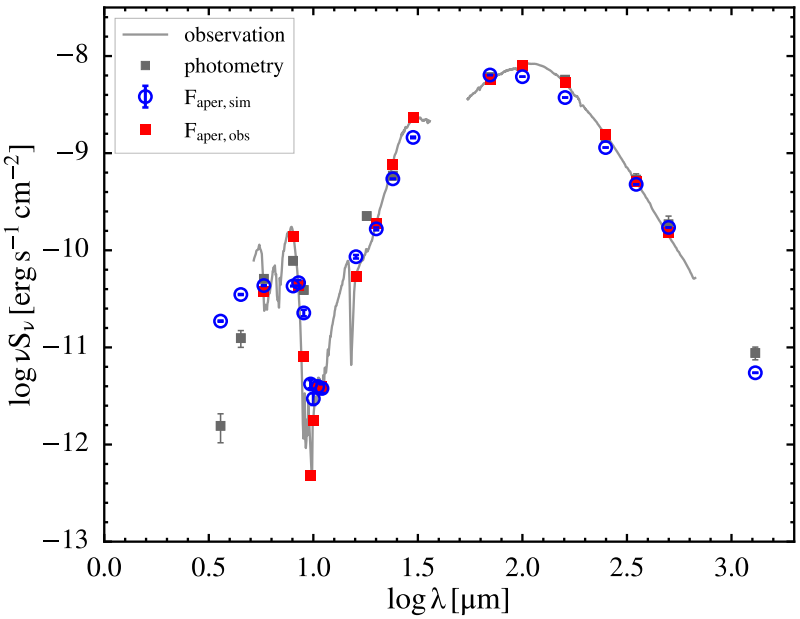

Figure 3.14: The best fit model compared with the observations. The filter-convolved and beam-convolved simulated fluxes are shown in blue circles, while the observational data processed with the same procedure are shown in red squares. The observations are shown in gray, while the photometric fluxes are shown in gray squares.

3.4.4.1 Constraining the age (submillimeter)

The age ($t_{\rm col}$) is determined by fitting the azimuthally-averaged radial intensity profile from the observation with simulations instead of fitting the SEDs. Shirley et al. (2002) demonstrated that the azimuthally-averaged radial intensity profile is diagnostic for the age of the envelope. As the infall radius increases over time, the structural changes in the envelope are manifested in changes in the radial profile. The fluxes in SED are the sum of the total flux within given apertures, which do not have the information regarding the radial profiles. Therefore, the radial intensity profile better traces the age of the envelope. In addition, the radial intensity profiles are normalized to their peak value so that the effect of the absolute flux calibration is insignificant. We find that the χ^2 values from fitting the radial intensity profiles are only sensitive to age, while the χ^2 values from fitting the SED shows more significant

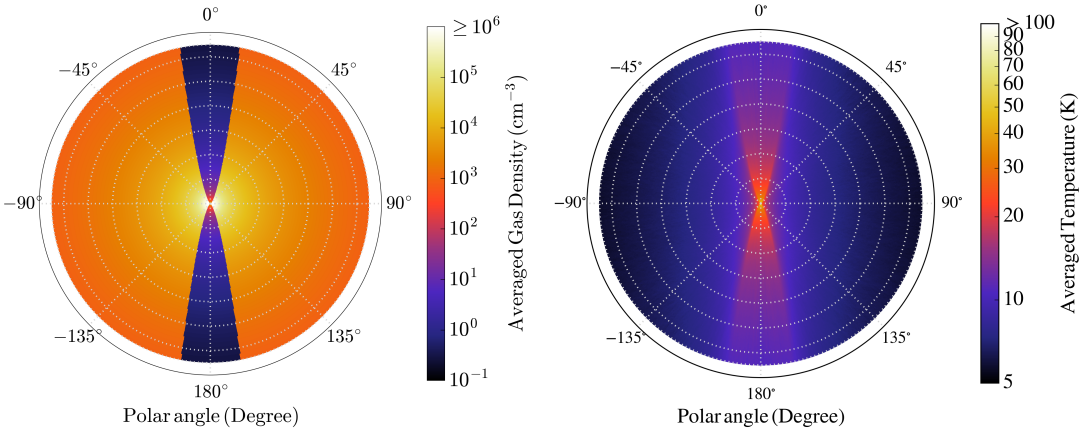

Figure 3.15: **Left:** The gas density profile in the best fit model. This figure shows the density averaged in azimuth for better illustration. The gas density profile is translated into dust density with gas-to-dust ratio of 100. **Right:** The temperature profile calculated from the Monte Carlo radiative transfer simulation. The temperature in the outflow cavity is about 20 K, while the temperature in the envelope is about 10 K. The spacing of the illustrative grids is 10000 AU.

correlations with other parameters. The χ^2 for the radial profile is evaluated by Equation 3.13.

$$\begin{aligned} \chi^2 &= \sum (I_{\rm sim} - I_{\rm obs})^2 \Big/ \sigma^2_{\rm comb} \\ \chi^2_{\rm reduced} &= \frac{\chi^2}{n-1} \\ \sigma^2_{\rm comb} &= \sigma^2_{\rm sim} + \sigma^2_{\rm obs} \end{aligned} \tag{3.13}$$

where $I_{\rm sim}$ and $I_{\rm obs}$ are the intensities from simulation and observation, respectively; $\sigma_{\rm sim}$ and $\sigma_{\rm obs}$ are the corresponding uncertainties to $I_{\rm sim}$ and $I_{\rm obs}$; and n is the total number of data points considered in χ^2 calculation.

The comparison of the radial intensity profiles with the observed profile is performed at 160 μm, near the SED peak. The key factor is to avoid any extended emission that does not belong to the collapsing envelope. We found the emission at longer wavelengths, such as 500 μm, is extended irregularly compared to shorter wavelength, such as 160 μm (Figure 3.16). The contour of 500 μm emission shows an irregular distribution beyond 100″ radius (Figure 3.16, right). Also the irregular emission coincides with the region of extinction seen in the optical image obtained

Table 3.4: Best-Fit Model parameters

Envelope parameters		
$t_{\rm col}$	36000 years	
$c_{\rm s,eff}$	0.37 km s^{-1} [a]	(fixed)
$\Omega_\circ$	2.5×10^{-13} s^{-1} [a]	(fixed)
Disk parameters		
$M_{\rm disk}$	0.0875 M$_\odot$ [b]	(fixed)
β	1.093	(fixed)
h_{100}	8.123 AU	(fixed)
Outflow cavity parameters		
$\theta_{\rm cav}$	20° [a]	(fixed)
$\rho_{\rm cav,\circ}$	3×10^{-20} g cm^{-3}	
$R_{\rm cav,\circ}$	40 AU	
Other parameters		
$R_{\rm max}$	0.315 pc[a]	(fixed)
$T_\star$	6950 K	
$R_\star$	3 R$_\odot$ [a]	(fixed)
$\theta_{\rm incl.}$	50°	

[a]These parameters are fixed in the search of the best fit model.

[b]The disk mass is set to be 25% of the total accreted mass.

from ESO archive (Corporon & Reipurth, 1997). The radial intensity profile extracted from 500 μm shows a flatter tail due to the extended emission at larger radii, which has a different characteristic from the profile at inner radii. Thus, we focus on the radial profile within 90″ (18000 AU) to minimize the effect of the extended emission. The model with an age ($t_{\rm col}$) of 36000 years has $\chi^2 = 1$, while the models with smaller ages have even smaller reduced χ^2, suggesting that the uncertainties are overestimated. We set a 1-σ upper limit of 44000 years to the age (Figure 3.17). The lower limit for the age is constrained by the outflow dynamical age, discussed in the next section.

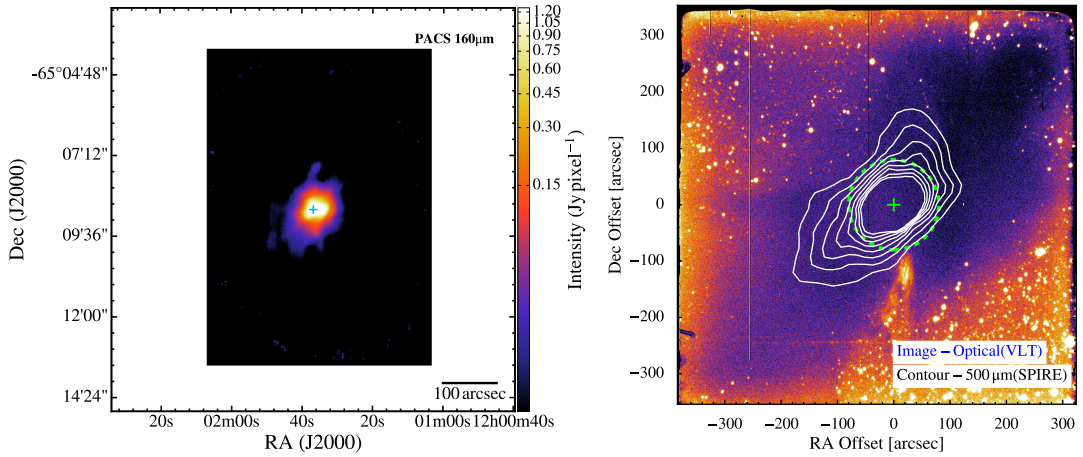

Figure 3.16: **Left:** The *Herschel* 160 μm image, plotted at the same scale as the image on the right. **Right:** The VLT-EFOSC2 image taken with Gunn r filter (#786), centering at 681.4 nm, with the contours from the *Herschel*-SPIRE 500 μm image. The increment between adjacent contours is 0.5σ with the lowest contour at 1σ above the background noise. The length of the image is about 11.8 arcmin. The green crosses indicate the location of BHR71, and the green dashed circle indicates the region (90″ radius) considered for radial intensity profile analysis.

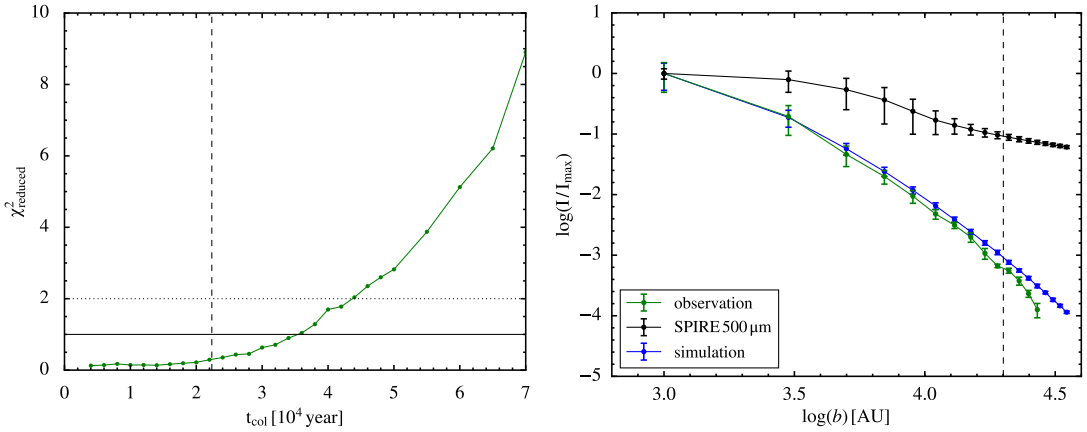

Figure 3.17: **Left:** The χ^2 distribution from the radial intensity profiles as a function of $t_{\rm col}$. The dashed vertical line indicates the dynamical age of the outflow, while the horizontal solid line represents $\chi^2 = 1$, and the horizontal dotted line represents $\chi^2 = 2$. **Right:** The azimuthal-averaged radial intensity profile at 160 μm of the best fit model shown in blue, corresponding to an age of 36000 years, while the radial intensity profile extracted from *Herschel*-PACS 160 μm image is shown in green and the profiles extracted from *Herschel*-SPIRE 500 μm image is shown in black. The dashed line indicates the maximum radius, 20000 AU, used for χ^2 analysis.

3.4.4.2 Constraining the inclination angle (near-infrared and mid-infrared)

The inclination angle ($\theta_{\rm incl.}$) primarily affects the emission below 50 μm. The *Spitzer*-IRAC images (Figure 3.4) show significant brightness differences between the north and south lobe of the outflow cavity, indicating a smaller inclination angle than found by B97. We use the flux ratios at the north and south part of the outflow cavity as a probe for the inclination angle. The flux of the IRAC 1 image is measured from a polygon aperture, which includes visually-identified extended features associated with outflow cavity but excludes point source contamination. The flux ratio from simulated images is measured from two box apertures at the south and north. Figure 3.18 shows the flux ratio of simulated images with various inclination angles compared with the ratio measured from the *Spitzer*-IRAC 1 image, 3.2. The flux ratio increases with decreasing inclination angle as we expected; however, the ratio begins to decline when the inclination angle is smaller than 50 degree, because the emission from the outflow cavity starts to appear in the opposite (north) lobe. Despite the fact that the maximum ratio from simulated images is still smaller than the ratio from IRAC 1 image, this comparison favors an inclination angle of 50 degrees.

B97 measured the dynamical age of the outflow of BHR71 to be about 10000 years, but the dynamical age is proportional to $1/\tan(\theta_{\rm incl.})$ (Dunham et al., 2014a), yielding a larger dynamical age with the smaller inclination indicated by the *Spitzer* images. However, if we assume that outflows are only launched after the beginning of the collapse, the dynamical age of the outflow should be the lower limit of the age of envelope. An inclination angle of 50 degree results in an outflow dynamical age of 24630 years, based on the visual extent and the characteristic velocity of the CO outflow (B97). Based on the lower limit from the outflow and inclination angle, and the upper limit from the radial profile, we choose the age of 36000 years, for which the reduced χ^2 from the radial profile reaches unity, as the most likely value.

Although an angle of 50 degree best reproduces the IRAC 1 image, this inclination conflicts with the close to edge-on view (84 degree) derived from the CO outflow by B97. Figure 3.19 compares the IRAC 1 image with simulated images with 50 degree and 84 degree inclinations. The morphology of the simulation with 50 degree inclination matches with IRAC 1 image. The contrast of brightness between two outflow lobes increases with smaller inclination angles until about 50°, where it best

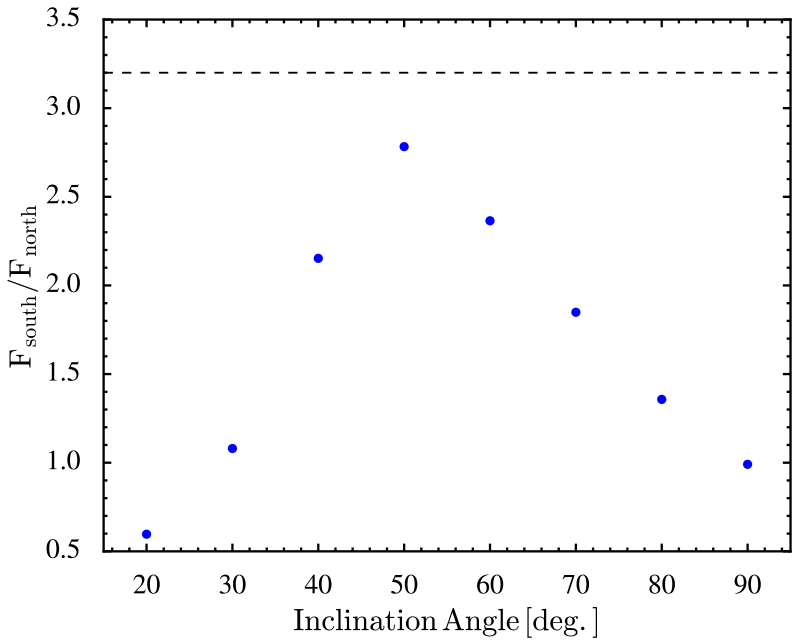

Figure 3.18: The flux ratio of the south and north lobes of the outflow cavity at given inclination angles, extracted from simulated images with a $100'' \times 100''$ box aperture toward the north and south directions. Only emission at 3.6 μm is considered in this figure. The dashed line represents the flux ratio measured from BHR71 *Spitzer*-IRAC 1 image as a reference.

matches the observed ratio. If we measure the outflow cavity opening angle as defined in Section 3.4.2.3, we will find the opening angles at 10000 AU from two models are similar (17 degree and 22 degree). Another possibility is that the extinction in the inner envelope is greater in the north than in the south, due to some deviation from symmetry. The resolution of the conflict between a smaller inclination angle needed to fit the IRAC data and an edge-on orientation based on the CO outflow awaits further observations to understand the kinematic structure of outflows and higher resolution studies of the envelope.

3.4.4.3 Constraining the central luminosity

The central luminosity source is ultimately constrained by the observed bolometric luminosity. However, the relation depends on the inclination angle. We optimize the luminosity source at two stages, one after determining the envelope parameters, and another one after fixing the inclination angle. In the first stage, we only tune

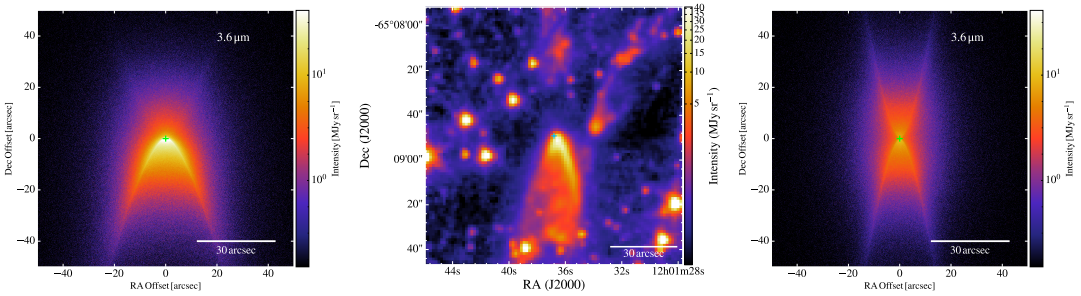

Figure 3.19: The simulated image at 3.6 μm of the best fit model in this study (left) and the best fit model with the geometry suggested by B97 (right), compared with the *Spitzer*-IRAC1 (3.6 μm) image shown in the middle. The three images are plotted at a similar spatial scale.

the central luminosity to match the peak of the SED at far-infrared wavelengths. The optimization of the central luminosity before fixing the inclination provides less confusion when constraining the viewing angle. A smaller inclination angle produces more emission at shorter wavelengths, which can increase the observed luminosity by as much as 60%. With the inclination angle optimized, we then fine tune the central luminosity to best agree with the observed bolometric luminosity, 13.92 $L_{\odot}$.

The best fit model requires a central luminosity, 18.8 $L_{\odot}$, which is $\sim$35% greater than the observed bolometric luminosity. The reason is that the asymmetric density structure, with an outflow cavity and flattened envelope, channels the radiation out the direction of the outflow. Also, the observations do not always include all the emission, especially at longer wavelengths. Thus, the intrinsic luminosity in the model is greater than the observed bolometric luminosity, 13.92 $L_{\odot}$ for our optimum inclination angle.

3.4.4.4 Calculating the χ^2 from SED fitting

We constrain other parameters by calculating a χ^2 value for the SED. To avoid overweighting the high fluxes around the peak of the SED, we calculate the χ^2 with the fractional difference instead of the absolute difference between the simulations and

observational data. The prescription of calculating the χ^2 is shown in Equation 3.14.

$$\begin{aligned}
\chi^2 &= \sum \left(\frac{F_{\rm sim} - F_{\rm obs}}{F_{\rm obs}} \right)^2 \Big/ \sigma^2_{\rm comb}, \quad F = \nu S_\nu \\
\chi^2_{\rm reduced} &= \frac{\chi^2}{n-1} \\
\sigma^2_{\rm comb} &= \left(\frac{F_{\rm sim}}{F_{\rm obs}} \right)^2 \left(\frac{\sigma^2_{\rm sim}}{F^2_{\rm sim}} + \frac{\sigma^2_{\rm obs}}{F^2_{\rm obs}} \right)
\end{aligned} \tag{3.14}$$

where n is the number of aperture-convolved fluxes and $F_{\rm sim}$ and $F_{\rm obs}$ are the aperture-convolved fluxes from the observation and simulation. The aperture-convolved fluxes are selected by their abilities to represent the features of the simulated SED. The fluxes at the following wavelengths, 3.6, 4.5, 8.5, 9, 9.7, 10, 10.5, 11, 16, 20, 24, 30, 70, 100, 160, 250, 350, 500, and 1300 μm, are selected and calculated by convolving with the photometric filters and beam of the instruments when the corresponding data are photometric, or averaging with the spectral resolution of the instruments when the corresponding data are spectroscopic.

3.4.4.5 Constraining the cavity density profile (mid-infrared)

The parameters left to be determined are $\rho_{\rm cav,\circ}$ and $R_{\rm cav,\circ}$. We find that pure power-law profiles for the cavity density fail to reproduce the observed emission at 20-40 μm (Figure 3.20), suggesting that more warm dust ($\sim$100 K) is needed. Our preferred cavity density profile consists of a constant density region at the inner radius and a region where the density declines as r^{-2} (see Section 3.4.2.3 and Figure 3.13). The motivation for this hybrid cavity profile arises from the discrepancy between simulations and observations at 20-40 μm from pure power-law profiles and the flux levels at both sides of the absorption feature at 10 μm. All profiles fail to reproduce the ice absorption features at wavelengths shorter than 10 μm and around 15 μm, because the ices causing those absorptions are not included in the dust model. A uniform density across the entire cavity might fit the observation; however, it would produce too much emission at 20-40 μm if we want to match the emission at near-infrared wavelengths. Also a constant density across the entire cavity is unphysical, considering that the mass flux has to be conserved while moving into a larger area. The underestimated flux at 20-40 μm suggests more warm dust, which usually exists in the inner region. Therefore, we introduce a constant density region in the inner

cavity to concentrate more dust toward the center compared to simple power law profiles (r^{-2} and $r^{-1.5}$). Figure 3.20 shows that this profile can successfully produce the observed emission at 20-40 μm. A grid search of these two parameters ($\rho_{\rm cav,\circ}$ and $R_{\rm cav,\circ}$) suggests the best fitted values of $3{\times}10^{-20}$ g cm^{-3} and 40 AU.

This wavelength region is quite diagnostic of the cavity density distribution. The origin of this constant density region is currently unclear. We can only speculate that it can be the result of a recent mass ejection or pseudo-disk due to magnetic field. Observations with high angular resolution, such as ALMA, can provide more information about this hybrid profile by mapping the continuum flux distribution with sub-arcsec resolution.

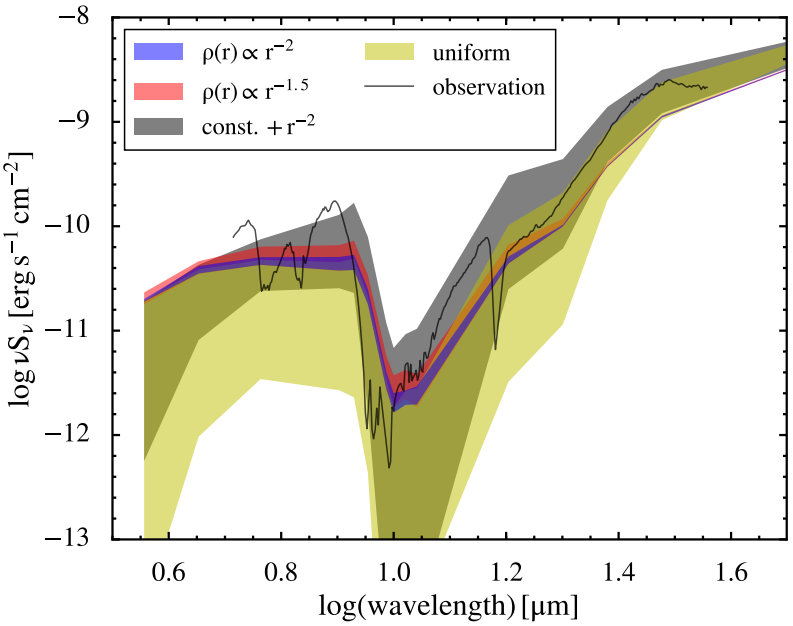

Figure 3.20: The simulated SEDs with cavity density profile of r^{-2} (blue), $r^{-1.5}$ (red), a constant region with a r^{-2} tail (black), and uniform density (yellow). The shaded area indicates the range of simulated SEDs with a same grid of density at the innermost cavity, ranging from 5×10^{-18} to 5×10^{-21} g cm^{-3} (four models with density increasing by a factor of 10). The olive green region is the overlap between the yellow and gray regions. The observed SED is shown in the black solid line.

3.5 Discussion

3.5.1 Comparison to Other Models

We compare the simulated SED of our best fit model to other possible models in Figure 3.21. Kristensen et al. (2012a) modeled the water emission with 1-D infalling envelope, suggesting an envelope with an infall radius of 3500 AU and a mass accretion rate of 3×10^{-5} $M_{\odot}$ yr^{-1}, translating into an age of $\sim 3.3 \times 10^4$ year with the model of Shu (1977b), very similar to our best-fit age. We adopt the values from Kristensen et al. (2012a) for age, sound speed, and the outer radius of the envelope, while adopting other parameters from our best fit model, without a disk or outflow cavity. We also test the geometry of the outflow cavity derived from the CO outflow map (B97), which suggests an inclination angle of 84° and an outflow cavity opening angle of 15°.

The two other models are shown in Figure 3.21 in magenta and green dashed lines. All three models show a good agreement at far-infrared to submillimeter wavelengths, indicating that similar properties of the envelope are found. The distinct difference at wavelengths below 50 μm between our best fit model and modified model of Kristensen et al. (2012a) shows that an outflow cavity is required to fit the whole SED. The lack of emission below 50 μm in the model with geometric parameters from B97 due to the large inclination angle further illustrates the disagreement between $\theta_{\rm incl}$ we derive and that derived from the distribution of CO emission lines.

3.5.2 Effect of Not Including the Full TSC Model

As we mentioned in Section 3.4.2.1, we adopt a full TSC envelope including a static outer envelope instead of an infall-only envelope. The simulated SEDs of two types of TSC models are shown in Figure 3.22. The infall-only TSC model produces too much mid-infrared emission and too little submillimeter emission, while the full TSC model fits fairly well. For young embedded protostars, the infall radius has to be smaller than the outer radius of the envelope. Therefore, the transitional region to the isothermal profile and the outer, static envelope are required to fully describe the envelope structure. The models in the widely used grid by Robitaille et al. (2006b) do not include these regions.

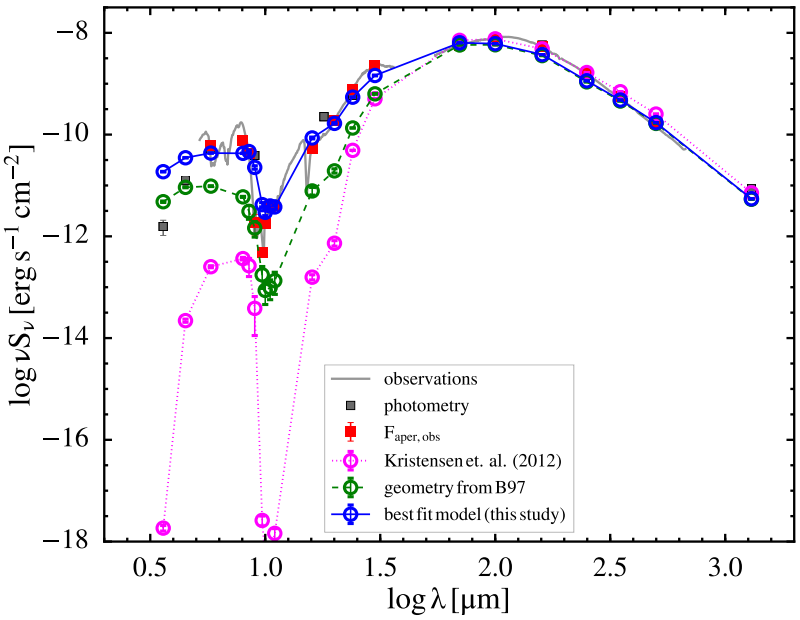

Figure 3.21: Simulated SEDs of our best fit model (solid blue), the model from Kristensen et al. (2012a) (dotted magenta), and the model with geometry from B97 (dashed green). The values of parameters of the best fit model are listed in Table 3.4. The observations including spectra and photometry are shown in gray. The simulated SEDs and observed spectra are both extracted with the aperture sizes used in the observations (open blue circles and red squares).

3.5.3 Mass Flows

The mass infall rate ($\dot{M}_{\rm inf}$) can be compared with the rate of accretion onto the central star ($\dot{M}_{\rm acc}$) and the mass loss rate in the wind ($\dot{M}_{\rm wind}$) under several assumptions.

The mass infall rate of our best fit model, $\dot{M}_{\rm env} = 1.2 \times 10^{-5}$ M$_\odot$ yr^{-1}, derived by Equation 3.3 agrees with that of Kristensen et al. (2012a) within a factor of 2.5. The rate of accretion onto the central star can be estimated by assuming that the central luminosity is dominated by the accretion process; therefore the accretion rate can be calculated with Equation 3.15, if the photospheric luminosity is ignored (Dunham et al., 2014c).

$$\dot{M}_{\rm acc} = \frac{L_{\rm cen} R_\star}{G M_\star f_{\rm acc}} \tag{3.15}$$

where $L_{\rm cen}$ is the central luminosity in the best fit model, $R_\star$ is the radius of the pro-

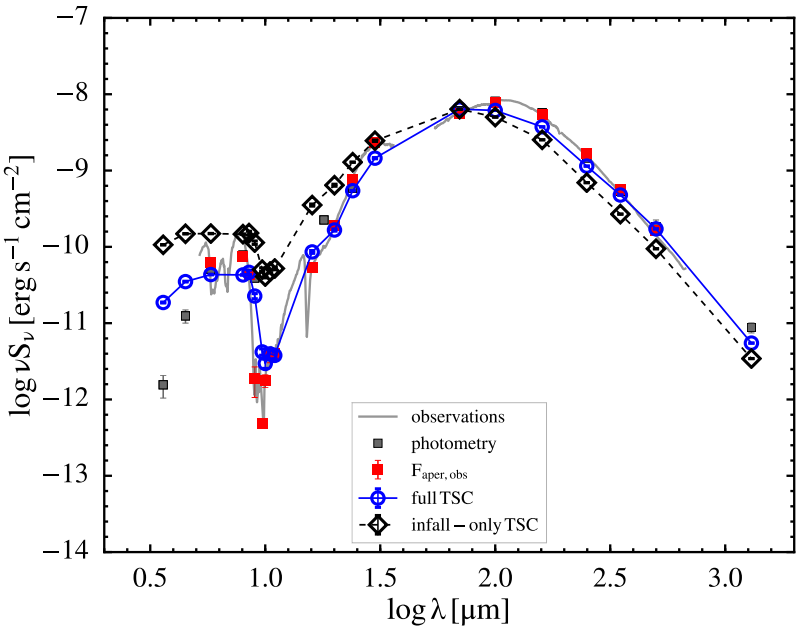

Figure 3.22: The simulated SEDs of the full TSC model (solid blue line/circles) and infall-only TSC model (dashed black line/diamonds). The observation and aperture-convolved spectrophotometry are shown in light gray and red squares for comparison.

tostar, G is the gravitational constant, $M_\star$ is the total mass that has fallen into the star, and $f_{\rm acc}$ is the radiative efficiency of accretion. The central luminosity (18.8 $L_\odot$) is more representative for the accretion process than the bolometric luminosity. Assuming 25% of the infallen mass remains in the disk, $M_\star = 0.32$ $M_\odot$ derived by $M_\star = 0.75\ \dot{M}_{\rm env}\ t_{\rm col}$. The simulation of spherical accretion shows $R_\star = 3$ $R_\odot$ according to the mass of the protostar in our model (Figure 1, Palla & Stahler (1992)). We take $f_{\rm acc} = 0.5$. Adopting the values described above, we derive the rate of accretion onto the central star, $\dot{M}_{\rm acc} = 1.1 \times 10^{-5}$ $M_\odot$ yr^{-1}, very close to the mass infall rate fitted by this study and only a factor of 2.5 lower than the rate fitted by Kristensen et al. (2012a). This agreement suggests that BHR71 at this time does not show any sign of episodic accretion, which has been inferred from studies of other sources (Dunham et al. 2014c and references therein).

The average mass loss rate in the wind is calculated by dividing the momentum of the molecular outflow by its dynamical age and the speed of the wind. We use the observations of the low-J CO outflow (B97), but we adopt the best fitted inclination angle from this study to calculate the momentum of the outflow and the dynamical

age of the outflow. An inclination angle of 50 degrees leads to a momentum of 15.4 $M_\odot$ km s^{-1} and a dynamical age of about 24600 years. These values imply a mass loss rate in the wind of 2.1×10^{-6} $M_\odot$ yr^{-1}, assuming a wind speed of 300 km s^{-1}. This is much lower than the values found by Nisini et al. (2015) of 4.2-53 $\times 10^{-6}$ $M_\odot$ yr^{-1}, mainly because of the smaller inclination angle in our best-fitting model. Our mass loss rate is about 20% of the rate of accretion onto the central star, similar to the factor of 0.1 that is usually assumed (Shu et al., 1994; Bontemps et al., 1996a; Pelletier & Pudritz, 1992; Wardle & Koenigl, 1993; Watson et al., 2016), while the wind mass loss rate of Nisini et al. (2015) was larger than the mass accretion rate. In a different sample of Class 0/I protostars analyzed by Bontemps et al. (1996a), the highest mass loss rate is $\sim 1.2 \times 10^{-7}$ $M_\odot$ yr^{-1}, only one third of the mass loss rate of BHR71. A high average mass loss rate suggests that BHR71 has not had much lower mass accretion rates in the past. Unlike many Class 0 objects, there is no evidence for episodic accretion or mass loss events.

If the [O I] emission measures the wind mass loss rate, we can use Equation 3.16 to obtain an alternative estimate of the mass loss rate in the wind (Hollenbach, 1985b).

$$\dot{M}_{\rm wind}(10^{-5}\ M_\odot\ {\rm yr}^{-1}) = 10 L_{63}(L_\odot) \tag{3.16}$$

where L_{63} is the luminosity of the 63 μm [O I] line. We derive a mass loss rate in the wind of 2.2×10^{-7} $M_\odot$ yr^{-1}, which is about one order of magnitude smaller than we estimated from the momentum of the outflow from CO.

The [O I] 63 μm line traces the the mass flux in the dissociative shocks; however, other physical processes may contribute to the observed [O I] line flux, such as photodissociation regions. So the mass loss rate derived from the [O I] 63 μm line flux should be an upper limit of the mass loss rate in the dissociative shocks. The ratio of the mass loss rate measured in [O I] to the mass accretion is 0.02, which is consistent with Nisini et al. (2015), where they find a ratio of 0.05. The main factors for the difference come from their assumption of stellar mass and radius. This ratio is also consistent with the ratio predicted by the theoretical MHD jet launching model, $\sim 0.05 - 0.5$ (Ferreira et al., 2006).

The difference between the mass loss rate derived from CO outflow momentum and [O I] 63 μm could be explained by the different time scales that the two tracers probe. The CO outflow momentum is measured from the entire outflow, therefore averaging the mass loss rate throughout the lifetime of the outflow, while the [O I] 63 μm probes

the mass flux in the outflow-induced shock regions, reflecting the instantaneous mass loss rate in the outflow. However, there is no indication of episodic accretion in this source and the current luminosity is quite high. In addition, other mechanisms can contribute to the [O I] line, so the weakness is especially puzzling. This discrepancy is wide-spread, casting doubt on the [O I] line as a wind tracer. With a different sample, Karska et al. (2013b) and Nisini et al. (2015) both find that the mass loss rates derived from CO outflow are up to two orders of magnitude higher than the mass loss rates indicated by [O I] line flux for embedded sources.

3.6 Conclusions

Combining *Herschel* PACS and SPIRE spectra, we find 61 lines in the 1-D spectrum and 645 lines in the full PACS and SPIRE 2-D datacube. Among those lines, we detect CO $J = 4 \rightarrow 3$ up to CO $J = 41 \rightarrow 40$ with only a few non-detected levels. The high-J CO lines are detected only at the center of BHR71, suggesting a shock origin within 2000 AU of the center. Our rotational diagram analysis shows four temperature components, 43 K, 197 K, 397 K, and 1057 K from 1.09×10^{48}, 1.71×10^{49}, 4.95×10^{49}, and 2.76×10^{50} CO molecules respectively, from the 1-D spectrum. The wide range of temperatures indicates a range of excitation environments.

The low-J and high-J CO lines differ in morphology. The low-J CO emission distributes in a bipolar direction along the outflow, while the high-J emission is compact, near the center of the source. The low-J CO emission lines are also found at the off-center positions. B97 finds a similar feature in CO $J = 1 \rightarrow 0$. The low energy water emission lines have a similar morphology to the low-J CO contours, while the high energy water lines are usually found to be off-center on the plane normal to the outflow, with a possible extension to IRS2. Atomic cooling lines are detected in [O I] $^3P_1 \rightarrow {}^3P_2$, [O I] $^3P_0 \rightarrow {}^3P_1$, and [C I] $^3P_1 \rightarrow {}^3P_0$. [C I] $^3P_1 \rightarrow {}^3P_0$ emission is found to be extended across the field of view with a local minimum on IRS1. [O I] $^3P_1 \rightarrow {}^3P_2$ emission is well centered with a slight extension toward the NE direction, while [O I] $^3P_1 \rightarrow {}^3P_0$ emission is only detected at the central spaxel.

We perform three dimensional dust radiative transfer simulations, study the effect of various parameters, and find the best fit model. The model consists of the rotating, collapsing envelope described by Terebey et al. (1984b), a flared disk, and an

outflow cavity. The envelope parameters can be constrained by the shape of the SED at submillimeter wavelengths, while the properties of the disk are not constrained because of the small mass of the disk. Our parameter studies (see Appendix) reveal the degeneracy of the SEDs caused by the trade-off between the sound speed and age. A model with a smaller sound speed and a later age can have a SED similar to a model with a larger sound speed and a earlier age. An accurate sound speed measurement is necessary to constrain the age of the envelope. The properties of the outflow cavity and the inclination heavily influence the mid-infrared SED. Our model shows that a constant density region at the apex of the cavity is required in order to fit the mid- and submillimeter SED simultaneously. The need for the constant density region in the model shows promise as a means of probing the structure in the inner region of the outflow cavity.

Several parameters are fixed prior to the model optimization based on existing observations, leaving five to fit. We first constrain the age of the envelope, then find the best inclination angle of the outflow cavity, and finally tune the density profile of the outflow cavity that best fits the SED. The azimuthally-averaged radial intensity profile is only sensitive to the age of the source, therefore better constraining the age, while the SEDs are affected by many other factors. A maximum age of 44000 yr is found by comparing the radial intensity profile at 160 μm with observations. The best fitting inclination angle is determined from the flux ratio seen in the *Spitzer*-IRAC 1 image. An inclination angle of 50 degree best reproduces the observed morphology; with this value, the minimum age from the CO outflow is 24630 yr. We choose an intermediate value of 36000 yr for the age. The smaller inclination angle required by the IRAC data conflicts with the angle derived from the CO outflow (B97). Further studies of the kinematic structure of the outflow may resolve this apparent discrepancy.

The best fit model has a higher central luminosity (18.8 $L_\odot$) than the observed bolometric luminosity because of the asymmetric structure, in which radiation escapes from the center more easily along the outflow direction. The mass accretion rate derived from the central luminosity in the model results in a mass accretion rate of 1.1×10^{-5} $M_\odot$ yr^{-1}, similar to the mass infall rate of the TSC envelope, 1.2×10^{-5} $M_\odot$ yr^{-1}, agreeing with the rate fitted by Kristensen et al. (2012a) within a factor of 2.5. Our best fit model can well constrain the evolution of the collapse envelope, and this method can be adopted to a larger sample with known sound

speeds to determine the evolutionary sequence of embedded protostars. The mass outflow rate in the wind ($\dot{M}_{\rm wind}$), 2.1×10^{-6} $M_\odot$ yr^{-1}, is about 20% of the mass accretion rate, close to the usual assumption of 10% of the accretion rate ($\dot{M}_{\rm acc}$) if calculated from the CO outflow and lower if calculated from [O I]. We suspect that the [O I] is not measuring the wind mass loss rate.

Chapter Four: Constraining the Infalling Envelope of Embedded Protostars: BHR71 and its Hot Corino

4.1 Introduction

Infall of gas and dust transforms dense cores into protostars. The collapse of protostellar envelopes begins when the the gravity exceeds the supports from thermal and non-thermal pressures due to turbulence and magnetic fields. Several theoretical models have proposed solutions for the evolution of the collapsing envelope with different assumptions and initial conditions (Gong & Ostriker, 2009; Offner & Chaban, 2017); however, their predictions need to pass the observational tests. A Larson-Penston similarity solution (Larson, 1969b; Penston, 1969) predicts a much larger linewidth compared to the observations of low-mass star-forming regions, whereas the "inside-out" collapse from a singular isothermal sphere (Shu, 1977b) matches the data (Zhou, 1992). Observations of rotation, magnetic fields, and outflows in star-forming regions suggest a more complex environment than the assumption adopted for these theoretical models. Based on the paradigm of Shu (1977b), the models considering rotation (Terebey et al., 1984b, hereafter TSC) and magnetic fields (Galli & Shu, 1993a,b) produce more realistic predictions. Modern numerical simulations start to produce the collapsing protostellar envelopes similar to the observed morphology (Zhao et al., 2018), but only a limited number of observation directly test the connection to observations (Yen et al., 2018).

The observations that probe the kinematics of infalling envelopes would constrain the model of infall. Molecular transitions that have high critical density are easily excited at the densest part of the protostellar envelopes, tracing the kinematic structure of the envelopes (Evans, 1999a). However, rotation and outflows produce comparable kinematic signatures on the line profiles of molecular emission, complicating the interpretation. Leung & Brown (1977) first proposed using optically-thick molecular emission to probe the infalling gas in the envelope. The opaque infalling gas in the foreground leads to a red-shifted absorption in the line profile (Zhou & Evans, 1994;

Choi et al., 1999). With single dish observations, outflows and foreground large-scale clouds may also contribute to the line profile due to the large beam, confusing the interpretation of the red-shifted absorption (Choi et al., 2004). Di Francesco et al. (2001) demonstrated that a smaller beam would observe the red-shifted absorption below the continuum, placing the infalling gas indisputably at the foreground of the central protostar. Moreover, a smaller beam greatly reduces the contamination from unrelated kinematics signatures, such as the broad emission from outflows. Thus, we would begin to observe the absorption of the compact continuum by the infalling opaque gas, which is an unambiguous signature of infall. Atacama Large Millimeter/submillimeter Array (ALMA) provides the best instrument for such observation. Pineda et al. (2012) reported the first detection with ALMA of the infall signature from the emission of methyl formate toward IRAS 16293 B, fitted with a two-layer infall model (Myers et al., 1996). Evans et al. (2015) demonstrated the first comprehensive modeling of the infall signatures detected toward B335 using the optically-thick transitions of simple molecules, including HCO^+ $J = 4 \rightarrow 3$, HCN $J = 4 \rightarrow 3$, and CS $J = 7 \rightarrow 6$. Constraining the underlying infall kinematics requires radiative transfer calculations using models of envelope structure along with the chemical abundance profile of the selected tracers. Analytic approximations of the chemical abundance can successfully reproduce the observations of simple molecules, such as CO (Jørgensen et al., 2005), and agree with the results of self-consistent chemo-dynamical model, where the chemistry is solved along with the dynamics (Lee et al., 2004). But for more complex molecules, such as CS, H_2CO, and CS, the chemo-dynamical model suggests substantially different abundance profile compared to the analytic approximations. However, a chemo-dynamical model is not always available and has a greater uncertainty for complex organic molecules (COMs), where only a few observations exist to constrain the model (Aikawa, 2013).

Heavier or more complex molecules, such as cyclic-C_3H_2 and SO, also trace the kinematics of protostellar envelopes, especially at the disk-forming region (Sakai et al., 2014). These molecules are more difficult to excite compared to HCO^+ and HCN. Sakai et al. (2014) show that the morphology of the position-velocity (PV) diagrams of cyclic-C_3H_2 and SO observed toward L1527 constrains a rotating infalling envelope conserving angular momentum. A pure rotation would show blue-shifted emission at one side of the central protostar and red-shifted emission at the other side. A rotating infalling envelope produces red-shifted emission from the infalling gas in the

foreground of the rotating disk, which contributes the dominant blue-shifted emission, and an opposite behavior occurs at the other side. This envelope model predicts a radius where infall stops, named the centrifugal barrier, suggesting the outer radius of the embedded disk. A rotating infalling envelope has been applied to interpret the observations of heavier or more complex molecules, such as CH_3OH and CH_2DOH for HH 212 (Lee et al., 2017), CS for IRAS 04365+2535 (Sakai et al., 2016) and L483 (Oya et al., 2017), cyclic-C_3H_2 for L1527 (Sakai et al., 2014), and OCS for IRAS 16293−2422 (Oya et al., 2016).

BHR 71 is a Bok globule associated with the Southern Coalsack at 200 pc (Seidensticker & Schmidt-Kaler, 1989b; Straizys et al., 1994), hosting two protostars, IRS1 and IRS2, separated by 17″ (Bourke, 2001). Tobin et al. (2019) detect opposite velocity gradients toward IRS1 and IRS2, suggesting that the binary system is likely formed via turbulent fragmentation. BHR 71 IRS1 dominates the luminosity of BHR 71 with $L = 13.5$ $L_\odot$ (Yang et al., 2018), whereas IRS2 only has 1.7 $L_\odot$ (Tobin et al., 2019). Because of the wide separation and low luminosity of IRS2, we focus on the IRS1 in this study. BHR 71 IRS1 (hereafter BHR 71 if not mention specifically) is a Class 0 protostar based on its bolometric temperature and the fraction of its emission in submillimeter wavelengths (Green et al., 2013c; Yang et al., 2018). Yang et al. (2017a, hereafter Y17) performed 3D radiative transfer calculations of a TSC envelope model modified to include outflow cavities and a disk to constrain the structure of BHR 71, using primarily the *Herschel* spectra along with archival *Spitzer* spectra and photometry. The best fitted TSC envelope suggests an age of 36000 years with an inclination angle of $-50°$. The age is defined as the time since the start of the collapse in the TSC model; and the inclination is defined as the angle between the rotation vector of the envelope and the plane of sky. A positive inclination angle indicates the rotation vector is in front of the plane of sky. High resolution ALMA ^{13}CO observations also indicate an inclination angle between 35°–63°. BHR 71 also shows prominent outflows in the north-south direction (Bourke et al., 1997), resulting in several active shocked regions (Giannini et al., 2011; Gusdorf et al., 2011, 2015).

We use ALMA data for this study. We describe the observation and reductions in Section 4.2, an overview of the results in Section 4.3, the infall signatures and a 3D radiative transfer modeling in Section 4.4, the serendipitous discovery of COMs Section 4.5, and finally we summarize our conclusion in Section 4.6.

4.2 Observations

The observations of BHR 71 were obtained in Project 2016.0.00391S (PI: Y.-L. Yang) on November 18 2016 by ALMA with 45 12-m antennas and the Band 7 receiver in the C40-4 configuration. The minimum and maximum baselines of the observation were 15.1 m and 918.9 m, respectively, resulting in a synthesized beam of $0\farcs39\times0\farcs27$. The water vapor during the observation was stable, varying between 0.64 mm and 0.72 mm. The calibration source was J0538−4405.

The ALMA Correlator was configured to have four spectral windows of 1920 channels. The local oscillator was tuned to observe HCN $J = 4 \rightarrow 3$ (354.505473 GHz), HCO^+ $J = 4 \rightarrow 3$ (356.734242 GHz), CS $J = 7 \rightarrow 6$ (342.882857 GHz), and $H^{13}CN$ $J = 4 \rightarrow 3$ (345.339756 GHz). Three windows have 234.38 MHz bandwidth ($\sim$200 km s^{-1}) and 0.122 MHz (0.1 km s^{-1}) resolution, while the $H^{13}CN$ $J = 4 \rightarrow 3$ window has 468.75 MHz ($\sim$400 km s^{-1}) and 0.244 MHz (0.2 km s^{-1}) resolution.

4.2.1 Data Reduction

The data were reduced by ALMA Pipeline version 38366. We further performed self-calibration with the Common Astronomy Software Applications (CASA) version 4.7.2, and the imaging was performed with CASA version 5.1.1. We identified a strong continuum source, 0.56 Jy beam^{-1}, with a signal-to-noise ratio (S/N) of 222, in the pipeline-reduced data, suggesting that the continuum of BHR 71 is sufficiently strong for self-calibration. Prior to the self-calibration, we selected the continuum channels and updated the continuum flag, assuming that the lowest flux in the spectra represents the continuum. We update this continuum flag again after extracting the 1D spectra for each spectral window by using the same criterion to select line-free channels from the 1D spectra, and re-run the entire calibration process. With a S/N of 222 for the continuum source. we further performed the self-calibration for both phase and amplitude. For the phase calibration, we gradually reduce the solution interval from `'inf'` to `'int'` to ensure the quality of the calibration solution. For amplitude calibration, we set the solution interval to infinity (e.g. one solution per scan). The S/N of the continuum source increases from 222 to 819 after the self-calibration.

The *uv*-visibility from interferometers is related to images by Fourier transforma-

tion. A typical procedure to extract images consists an imager and a deconvolver, so called the "clean" process. The imager first grids the *uv*-visibility and then perform fast Fourier transform to produce an image, which is the convolution of astronomical emission and the point spread function (PSF) of ALMA. Starting with the image provided by the imager, the deconvolver performs an iterative process consists selecting high S/N feature as the model, updating the model, convolving the model with the PSF, and subtract the convolved model from the image. The deconvolver performs this iterative process, so called the minor cycle, for many times. Then the imager performs an inverse fast Fourier transform to convert the model image back to the model *uv*-visibility, which is subtracted from the observed *uv*-visibility, producing the residual visibility. A fast Fourier transform converts the residual visibility to the residual image, where the stopping thresholds of the imaging process are evaluated. The procedures performed by the imager are called the major cycle, where many minor cycles can be done within a single major cycle.

We perform the imaging with CASA version 5.1.1 to use `tclean` task, which has better efficiency and flexibility. Using the "hogbom" method for deconvolution and the "briggs" weighting with a robust parameter of 0.5, the root-mean-sqaure (RMS) noise reaches 0.904 mJy beam^{-1} for the continuum. For the line emission, we use the "auto-multithresh" method for selecting the source emission for deconvolutions in the `tclean` process with a flux threshold of 30 mJy, which is three times of the RMS noise of the images. We configure the masking algorithm to only select structures greater than 30% of the beam (`minbeamfrac=0.3`) and confine the masking within the region where the primary beam efficiency is greater than 0.5 (`pbmask=0.5`) to to avoid selecting structures smaller than the synthesized beam or at low S/N regions. The continuum emission remains in the spectral cubes until the line emission is imaged to prevent the expected absorption features confusing the source selection of the "auto-multithresh" method. The RMS noise levels reach 13 mJy beam^{-1}, 14 mJy beam^{-1}, 12 mJy beam^{-1}, and 8 mJy beam^{-1} for the spectral windows centered on HCN $J = 4 \rightarrow 3$, HCO$^+$ $J = 4 \rightarrow 3$, CS $J = 7 \rightarrow 6$, and H^{13}CN $J = 4 \rightarrow 3$, respectively. Finally, we selected the line free regions by assuming no absorption existing in the spectra except for the regions around the four targeted lines (HCN, HCO$^+$, CS, and H^{13}CN). This continuum regions also update the continuum flag for the calibration, which is then run for the second time. Thus, the lowest flux should approximate the continuum emission, which is removed using the CASA `imcontsub`

task. The synthesized beam size is $0\farcs39\times0\farcs27$.

4.3 Results

4.3.1 Continuum

The ALMA observation reveals a compact continuum source marginally resolved by a beam of $0\farcs39\times0\farcs27$ with a position angle of $131\fdg25$ (Figure 4.1). Table 4.1 lists the properties of the continuum source fitted with a 2D Gaussian profile using the CASA `imfit` task. Beside the compact continuum source, Figure 4.1 shows extended emission surrounding the continuum source, which has intensities of 10–20 mJy beam^{-1}. This extended emission may probe the inner envelope; however, with a maximum recoverable scale of $\sim3''$, most of the extended emission may be resolved out.

Dust emission can relate to the dust mass using Equation 4.1 if the dust emission is optically thin. We first estimate the optical depth of dust emission using the model of BHR 71 from Y17 (hereafter the Y17 model). Within the deconvolved size of the continuum source, the Y17 model suggests a dust mass column density of 4.1×10^{-3} g cm^{-2}, resulting in an optical depth $\tau_\nu = \kappa_\nu N_{\rm dust} = 0.008$, where $\kappa_\nu = 1.863$ cm^2 per gram of dust covered with thin ice mantles at a gas density of 10^6 cm^{-3} (Ossenkopf & Henning, 1994, hereafter the OH5 dust). Therefore, the dust emission remains optically thin. However, we cannot rule out the existence of any compact optical thick structure not included in the Y17 model.

We can derive the mass of optically thin dust at the compact continuum source with the following equation

$$M_{\rm dust} = \frac{S_\nu d^2}{\kappa_{356\ \rm GHz} B_\nu(356\ \rm GHz, T_{\rm dust})}, \tag{4.1}$$

where S_ν is the continuum flux density, d is the distance to BHR 71, $\kappa_{356\ \rm GHz}$ is the dust opacity at 356 GHz, and $B_\nu(356\ \rm GHz, T_{\rm dust})$ is the Planck function at 356 GHz given a temperature of $T_{\rm dust}$. The assumption of a single dust temperature results in $\sim$10–50% uncertainty on the derived mass (Fig. A.1, Kauffmann et al., 2008). Thus, we use a mass-weighted temperature of 148 K (Equation 8, Kauffmann et al. 2008) as the dust temperature for Equation 4.1, assuming the density profile of an infalling envelope ($\rho(r) \propto r^{-1.5}$, Ulrich, 1976), the opacity of the OH5 dust ($\kappa_\nu \propto \nu^{1.8}$,

Table 4.1: The best-fitted continuum emission

Parameter	Value
R.A.	$12^h01^m36.^s4988 \pm 0.^s0001$
Dec.	$-65^d08^m49.^s3819 \pm 0.^s0007$
Convolved size	
Semi-major axis FWHM[a]	521.3±2.1 mas
Semi-minor axis FWHM	394.0±1.3 mas
Position angle	124°.91±0°.48
Deconvolved size	
Semi-major axis FWHM	349.5±3.6 mas
Semi-minor axis FWHM	278.9±2.7 mas
Position angle	113°.7±2°.0
Integrated flux	1.129 ±0.006 Jy
Peak flux	586.9 ±2.2 mJy beam^{-1}
Beam size	0.″39×0.″27 (PA=−48°.75)

[a]Full width at half maximum

Ossenkopf & Henning, 1994) and $T(r)$ =114 K at 70 au (0.″35) from the Y17 model. We derive the optically thin dust mass of $2.3 \times 10^{-2} \pm 1.2 \times 10^{-4}$ $M_\odot$, suggesting a gas mass of 2.3±0.01 $M_\odot$ with a gas-to-dust ratio of 100. From the Y17 model, the mass infall rate would be $\dot{M} = 0.975 c_s^3/G = 1.2 \times 10^{-5}$ $M_\odot$ yr^{-1}, using $c_s = 0.37$ km s^{-1}. The total infalling gas mass at the best-fitted age of 36000 years would be 0.43 $M_\odot$, which is 18% of the gas mass derived from the dust emission. As we later show in Section 4.4.2.5, our ALMA observations prefer a younger age of 15000 years, making the total infalling gas mass only 7.8% of the gas mass derived from the continuum. If we consider the optically thick dust emission, the discrepancy becomes even greater. Such discrepancy hints that the infall rate may have been higher in the past as some theoretical models suggest (Offner & Chaban, 2017).

4.3.2 Molecular Emission

4.3.2.1 Intensity Maps

The intensity maps of HCN, HCO^+, CS, and $H^{13}CN$ emission (Figure 4.2) illustrate the structure of outflows and the inner envelope within the central 12″, separated into the ranges of $-5 < v - v_{lsr} < 0$ km s^{-1} (blue-shifted) and $0 < v - v_{lsr} < 5$ km s^{-1} (red-shifted). The source velocity is -4.45 km s^{-1}, measured from the NH_3 spectra in Bourke et al. (1997). We apply the correction of primary beam to all maps shown in this study. While the emission peaks at the center of BHR 71 across a range of velocity ($|v - v_{source}| \lesssim 6$ km s^{-1}), the low velocity ($|v - v_{source}| \lesssim 3$ km s^{-1}) emission

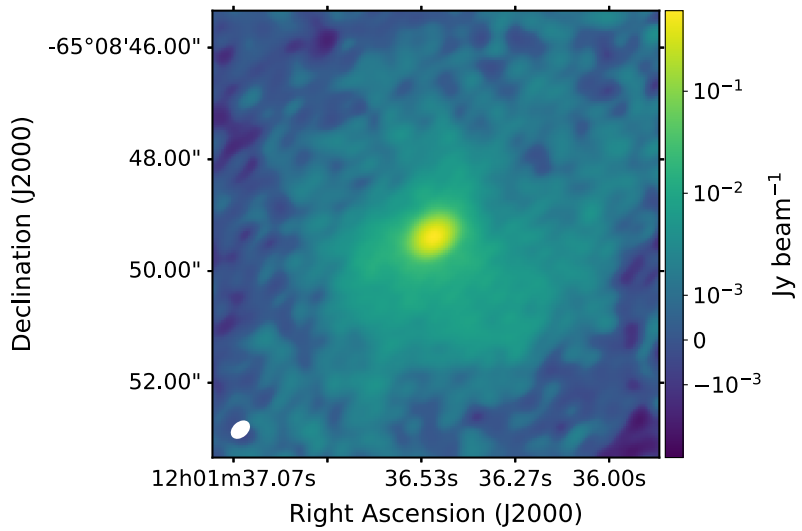

Figure 4.1: The continuum emission of BHR 71 at 356 GHz. Table 4.1 lists the properties of the continuum source.

also traces the morphology of outflows. Here we describe their morphology in the red-shifted and blue-shifted velocities in detail.

The brightness of the HCN $J = 4 \rightarrow 3$ line extends toward north at the blue-shifted velocities and toward south at the red-shifted velocities, while large scale ^{12}CO maps show red-shifted emission in the north and blue-shifted emission in the south (Bourke et al., 1997; Parise et al., 2006c). The HCN emission is concentrated into a few compact blobs with a size of $\sim 0\farcs5$ or less, which will be further discussed in Section 4.4.3.

At red-shifted velocities, the HCO$^+$ $J = 4 \rightarrow 3$ emission resembles the shape of a triangular outflow cavity, similar to the outflow traced by CO (Tobin et al., 2019). But, at blue-shifted velocities, the emission becomes more extended than the morphology at the red-shifted velocities, containing two filamentary structures at the west and south of BHR 71. A boxy blob with a size of $2'' \times 3''$ appears at $3''$ north of BHR 71 at both blue-shifted and red-shifted velocities.

The CS $J = 7 \rightarrow 6$ line also traces the morphology of outflow cavities. At blue-shifted velocities, the emission becomes more extended at the north and only traces the outflow cavity walls at the south; at red-shifted velocities, the emission shows a similar morphology but reflects through the east-west plane, tracing the outflow cavity walls at the north and extending toward south. The emission of HCO$^+$ and

CS trace a shape that is similar to that of the outflow cavities.

The $H^{13}CN$ $J = 4 \rightarrow 3$ emission has two peaks less than 0.″5 away from the center of BHR 71, one at the north and one at the south. The morphology of $H^{13}CN$ emission is similar at blue-shifted and red-shifted velocities. Overall, all four emission lines have morphologies more complex than a single peak, tracing structures along the outflow direction. Both CS and HCO^+ trace the outflow cavities, while HCN and $H^{13}CN$ appear as collections of compact blobs.

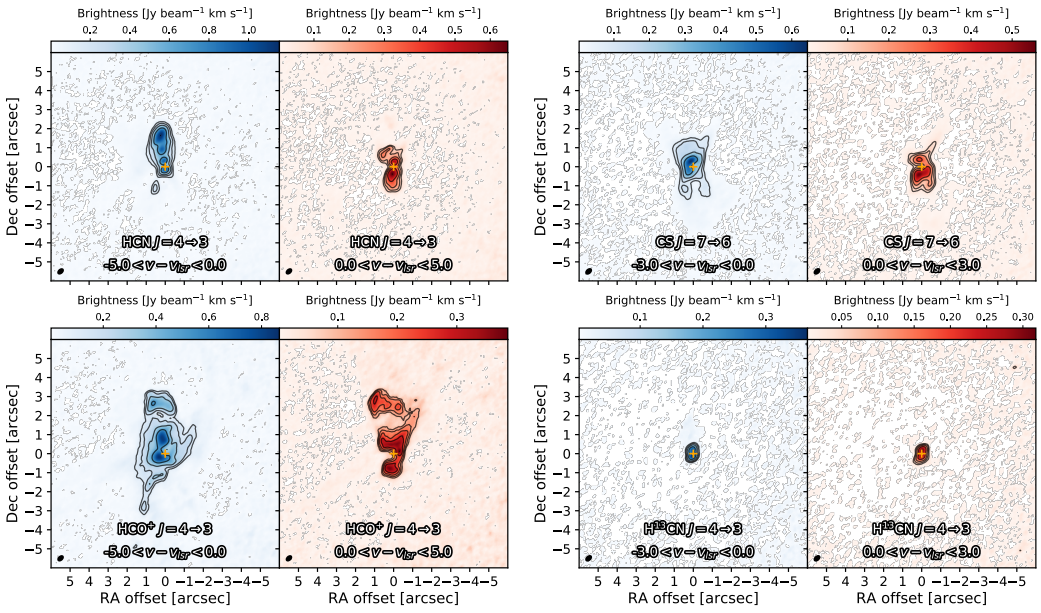

Figure 4.2: The moment 0 maps of the HCN $J = 4 \rightarrow 3$, HCO^+ $J = 4 \rightarrow 3$, CS $J = 7 \rightarrow 6$, and $H^{13}CN$ $J = 4 \rightarrow 3$ lines shown separately for blue-shifted and red-shifted velocities with respect to the source velocity. The orange plus signs indicate the position of the continuum source identified in Section 4.3.1. The maps only show the central 12″ of the entire observation as regions outside of this area contain no significant emission. The contours show five equally-separated levels in logarithmic scale from 2σ to their maximum values. There is very little emission at $|v - v_{\rm source}| > 3$ km s^{-1} for the CS $J = 7 \rightarrow 6$ and $H^{13}CN$ $J = 4 \rightarrow 3$ lines; therefore, we reduce the velocity range to better visualize the weak emission.

4.3.2.2 Velocity Maps

Figure 4.3 shows the first moments, intensity-weighted velocity, of all four lines. The HCN, CS, and $H^{13}CN$ lines show red-shifted emission at the south and blue-shifted emission at the north, suggesting an opposite kinematics of the large scale of

CO outflows (Bourke et al., 1997; Parise et al., 2006c). However, the high velocity emission appears in the north and south at red-shifted and blue-shifted velocities, respectively, consistent with the kinematics of the large-scale outflows (Figure 4.4).

The moment 1 map of the HCO^+ emission shows a complex structure. The red-shifted emission resides at the western side of BHR 71, while the blue-shifted emission surrounds the source. Toward the south, a red-to-blue velocity gradient appears to align with the filamentary structure found in the intensity map. At the northern blob identified in the intensity map (Figure 4.2), a strong velocity gradient from blue-shifted in the west to red-shifted in the east coincides with the blob, along with the weak red-shifted emission right next to the blue-shifted component of the blob.

4.3.2.3 Channal Maps

Figure 4.4 shows the channel maps of all four lines, providing a detailed view of the velocity structure of these lines. For the HCN $J = 4 \rightarrow 3$ line, we identify four compact blobs at low velocity, especially $-4 < v - v_{\rm source} < 2$ km s^{-1}. We further discuss the origin of these blobs in Section 4.4.3. The channel maps of the HCO^+ $J = 4 \rightarrow 3$ line show a similar morphology to the moment 0 map. The extended emission in the north disappears at low velocities, where more filamentary structure appears around the source. The CS $J = 7 \rightarrow 6$ line shows a single compact emission at most of the velocities except for the low velocities, where the emission exhibits an hour glass shape, resembling the shape of the outflow cavities. The hour glass shape appears in the low-velocity emission of HCN and HCO^+. The size of the flat bottom of the outflow cavity is $\sim$0.″6–1″, corresponding to 120–200 au. Since these are optically thick transitions, the radius is an upper limit. Lastly, the $H^{13}CN$ line has a single compact source at high velocity, consistent with the kinematics of the large-scale outflows, while two compact sources appear at low velocities with a separation of $\sim$0.″5 (100 au). As shown in the moment 1 map of the $H^{13}CN$ $J = 4 \rightarrow 3$ line (Figure 4.3), the northern and southern sources have brighter emission at blue-shifted and red-shifted velocities, respectively, which shows an opposite kinematics as the high-velocity emission.

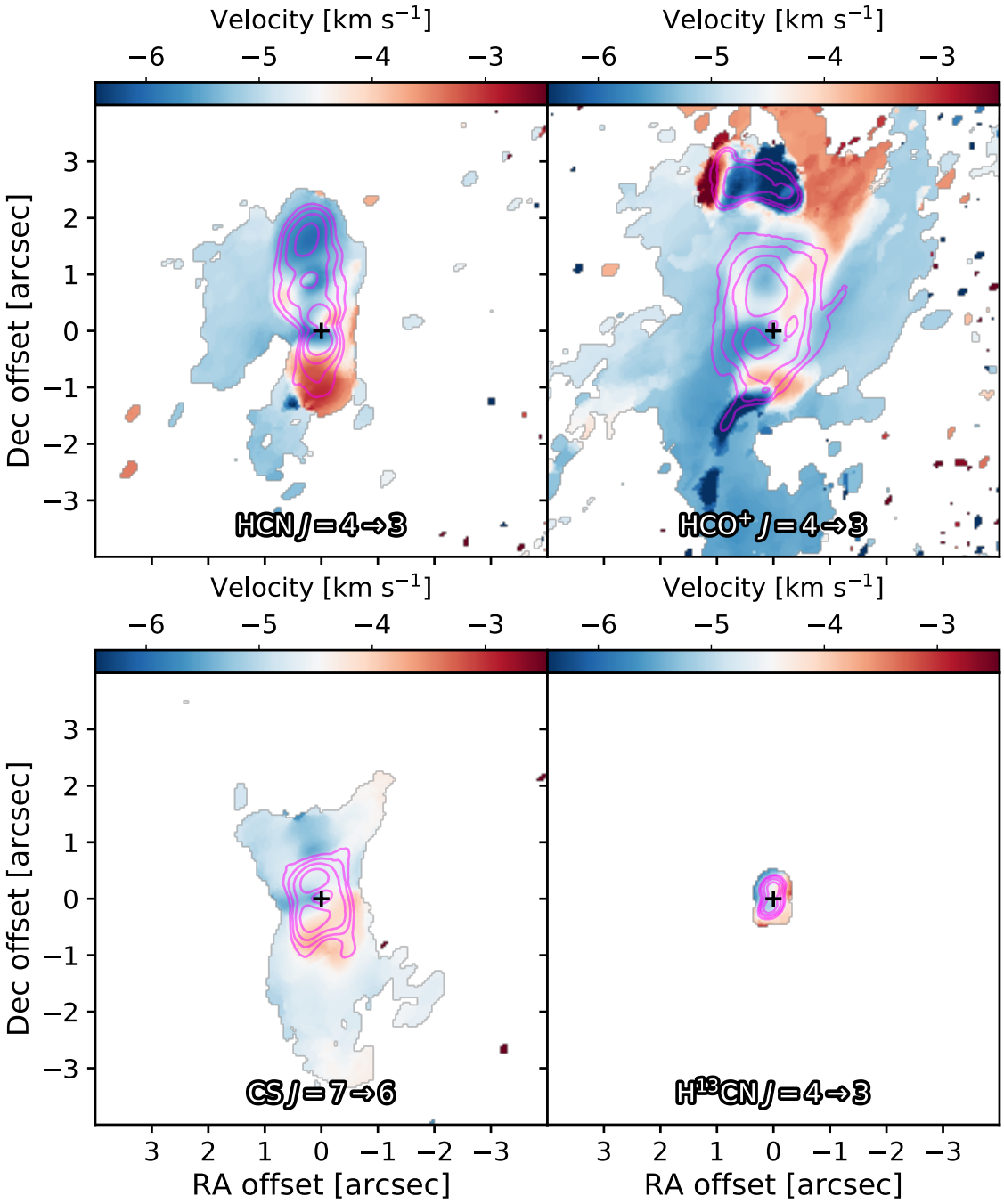

Figure 4.3: The moment 1 maps of the HCN $J = 4 \rightarrow 3$, HCO^+ $J = 4 \rightarrow 3$, CS $J = 7 \rightarrow 6$, and $H^{13}CN$ $J = 4 \rightarrow 3$ lines shown together with the moment 0 maps in magenta contours, which show five equally-separated levels in logarithmic scale from 2σ to their maximum values. Both moment 0 and 1 maps are calculated from $|v - v_{\rm source}| \leq 5$ km s^{-1}. The plus signs indicate the position of the continuum of BHR 71.

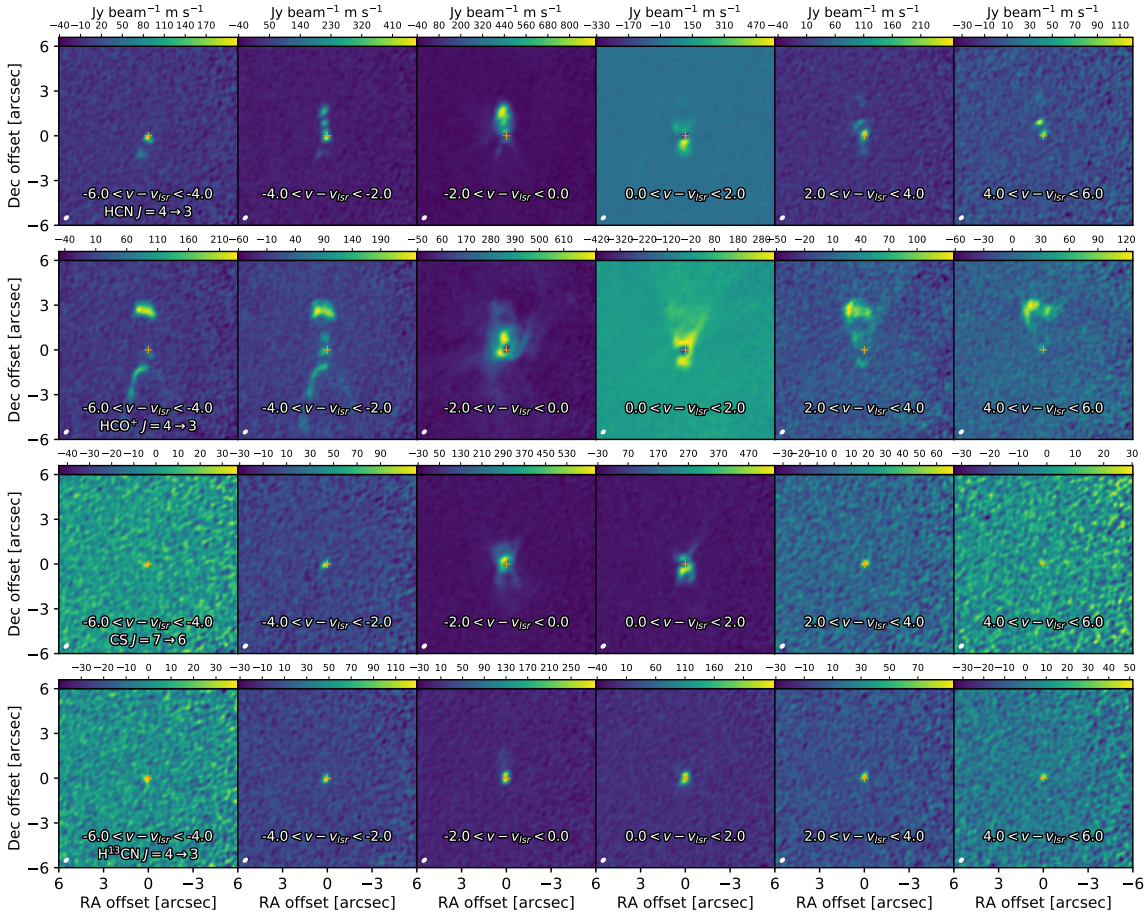

Figure 4.4: The channel maps of HCN $J = 4 \rightarrow 3$, HCO^+ $J = 4 \rightarrow 3$, CS $J = 7 \rightarrow 6$, and $H^{13}CN$ $J = 4 \rightarrow 3$ from the top to bottom rows. The subset images show the moment 0 map calculated with the velocity ranges shown in the images, and each image has its own scaling to show a complete structure at each channel.

4.4 Infall Kinematics

We use four molecular lines, HCN, HCO^+, CS, and $H^{13}CN$, to trace the infall kinematics in the envelope of BHR 71. The infall signature is best illustrated by the 1D line profiles. Here we first characterize the observed line profiles, then present a 3D radiative transfer model to constrain the underlying kinematics traced by these lines.

4.4.1 The Infall Signature

We extract the spectra of HCN, HCO^+, CS, and $H^{13}CN$ lines from the region of continuum emission ($0\farcs52 \times 0\farcs39$) to search for the red-shifted absorption against the continuum, indicative of the infalling gas in the foreground of the envelope (Leung & Brown, 1977; Zhou, 1992; Choi et al., 1999; Di Francesco et al., 2001; Evans et al., 2005, 2015). The line of sight toward the continuum source would have the deepest absorption as well as the least contamination from the outflows, therefore, the best position to search for the infall signature. We use the CASA `specflux` task to calculate the mean intensity, and fit the baseline for the second time. This baseline fitting fits a linear baseline individually to the line-free channels visually selected from each spectral window (Figure 4.22), which also update the line-free channels for calibration. The RMS temperatures are 0.56 K, 0.61 K, 0.60 K, and 0.41 K for the spectral windows centered on HCN $J = 4 \rightarrow 3$, HCO^+ $J = 4 \rightarrow 3$, CS $J = 7 \rightarrow 6$, and $H^{13}CN$ $J = 4 \rightarrow 3$ lines.

Figure 4.5 shows the line profiles of HCN, HCO^+, CS, and $H^{13}CN$ targeted for measuring the infall kinematics. All four lines show blue asymmetric double-peaked profiles with the HCO^+ $J = 4 \rightarrow 3$ line having the greatest asymmetry among these four, followed by CS $J = 7 \rightarrow 6$, HCN $J = 4 \rightarrow 3$, and $H^{13}CN$ $J = 4 \rightarrow 3$, which has almost an equal intensity for the double-peaked profile. Both the HCN $J = 4 \rightarrow 3$ and HCO^+ $J = 4 \rightarrow 3$ lines show red-shifted absorptions below the continuum. The absorption of the HCN $J = 4 \rightarrow 3$ line is narrower and has a greater red-shift than the one of the HCO^+ $J = 4 \rightarrow 3$ line. Within the absorption feature, if we take the mid-point of the velocities where the flux density is equal to the continuum as an estimate of the red-shift of the absorption feature, the absorptions in the HCN $J = 4 \rightarrow 3$ and HCO^+ $J = 4 \rightarrow 3$ lines center at 0.17 km s^{-1} and 0.14 km s^{-1}, respectively. The CS and $H^{13}CN$ lines also show absorptions at their line centers but not below the continuum flux. There is a small peak at the bottom of both HCO^+ and HCN lines, while the CS line shows a similar peak in the middle of its absorption feature. The HCN line profile also has several weak narrow absorption features, decreases of $\sim$ 6 K, which are not consistent with the hyperfine spliting of the HCN $J = 4 \rightarrow 3$ line; therefore, the nature of these absorption features remain unclear. The full widths at the half maximum of the line profiles excluding the absorption are 6.0 km s^{-1}, 3.1 km s^{-1}, 3.2 km s^{-1}, and 4.1 km s^{-1}, for the HCN $J = 4 \rightarrow 3$, HCO^+ $J = 4 \rightarrow 3$,

CS $J = 7 \rightarrow 6$, and $H^{13}CN$ $J = 4 \rightarrow 3$ lines, respectively, showing that the HCN line is significantly broader than the other lines. The profile of the HCO^+ line resembles the infall signature as first proposed by Leung & Brown (1977), Zhou (1992), and Di Francesco et al. (2001).

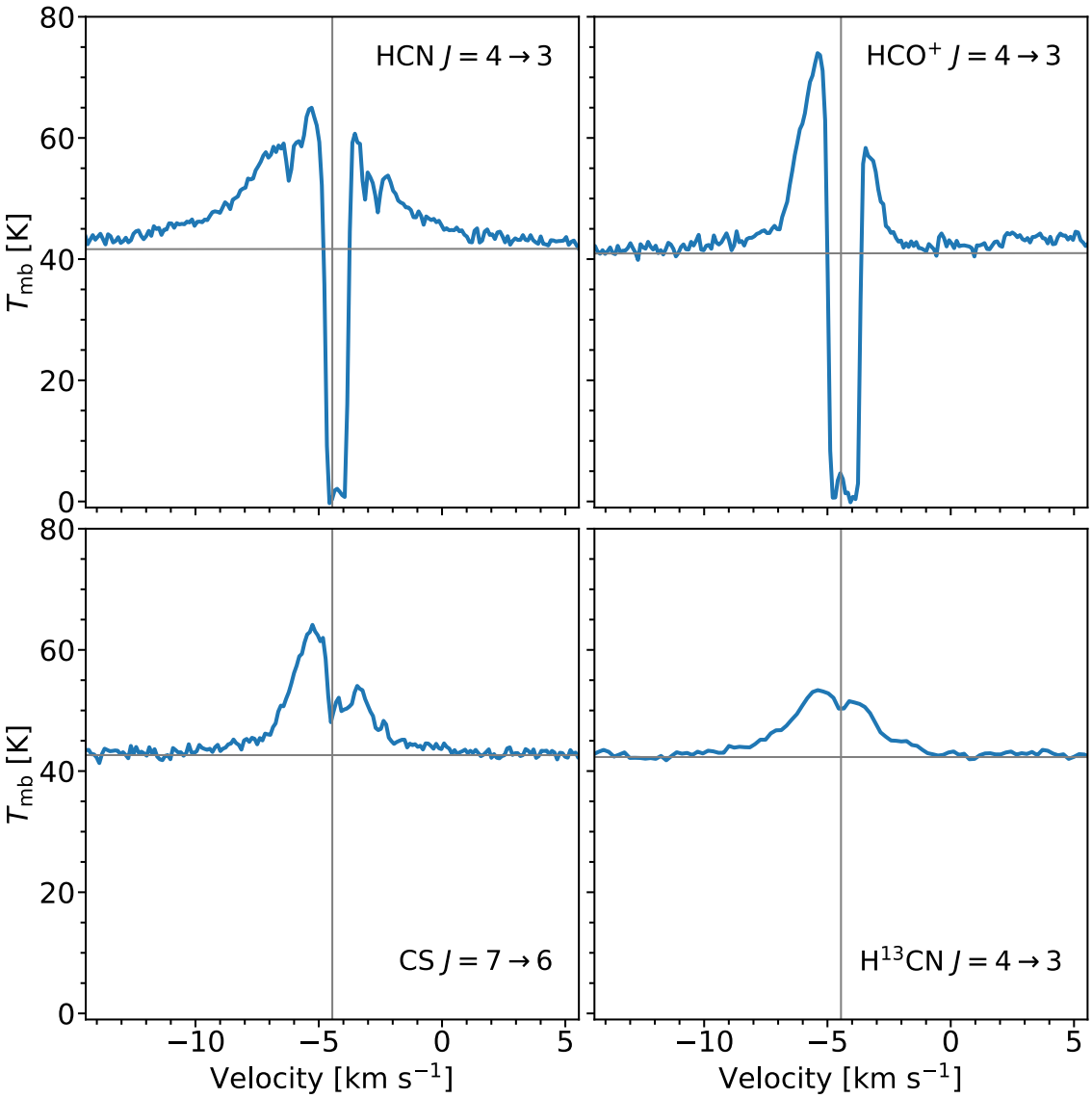

Figure 4.5: The spectra of HCN $J = 4 \rightarrow 3$, HCO^+ $J = 4 \rightarrow 3$, CS $J = 7 \rightarrow 6$, and $H^{13}CN$ $J = 4 \rightarrow 3$ tracing the infalling envelope. The source velocity is -4.45 km s^{-1} (Henning & Launhardt, 1998). The horizontal lines indicate the fitted continuum, while the vertical lines indicate the source velocity.

4.4.2 Modeling the Infall

We successfully detect the infall signatures from our ALMA observations (Section 4.4.1). The red-shifted absorption against the continuum provides strong evidence for the presence of infalling gas along the line of sight (LOS). The absorption allows us to probe the velocity field and thus the age and rotation of the infalling envelope. To constrain the underlying kinematics, we model the line profiles using non-LTE radiative transfer to properly consider the absorption due to the interaction between molecules and radiation. We start our model based on the 3D envelope model in Yang et al. (2017a) constrained by continuum, then focus on optimize the chemical abundance to reproduce the observations.

4.4.2.1 Updating the Continuum Model

The Y17 model of BHR 71 constrains an envelope based on the prescription of Terebey et al. (1984b, hereafter TSC) along with the geometry of outflow cavities in three dimensions. We discovered a numerical error in calculating the density around the centrifugal radius (13 au in the Y17 model), causing an underestimation of the density around the centrifugal radius. The updated radial density profile (Figure 4.6) has a clear density peak at the centrifugal radius similar to the analytical solution of the disk in Ulrich (1976) and Cassen & Moosman (1981). Dominated by the envelope, the radial brightness profile extracted from the synthetic image at 160 μm still agree with the *Herschel* observation, which determines the age of the TSC model (Yang et al., 2017a). The synthetic spectral energy distribution (SED) based on the younger envelope still agrees with the observation (Figure 4.7).

4.4.2.2 The 3D Radiative Transfer Model

We perform radiative transfer calculations to constrain the kinematics of the infalling envelope. Figure 4.8 illustrates the work flow for modeling the infall signature. The Y17 model constrains the parameters of the TSC envelope, which provides the gas density and velocity vector fields as functions of radius r and polar angle θ. We further extend the 2D profile of density and velocity to 3D, assuming an axisymmetry with respect to the ϕ-axis. Y17 constrain the 3D dust temperature $T_{\rm dust}$ with the far-infrared *Herschel* spectra and the archival data of BHR 71. We set

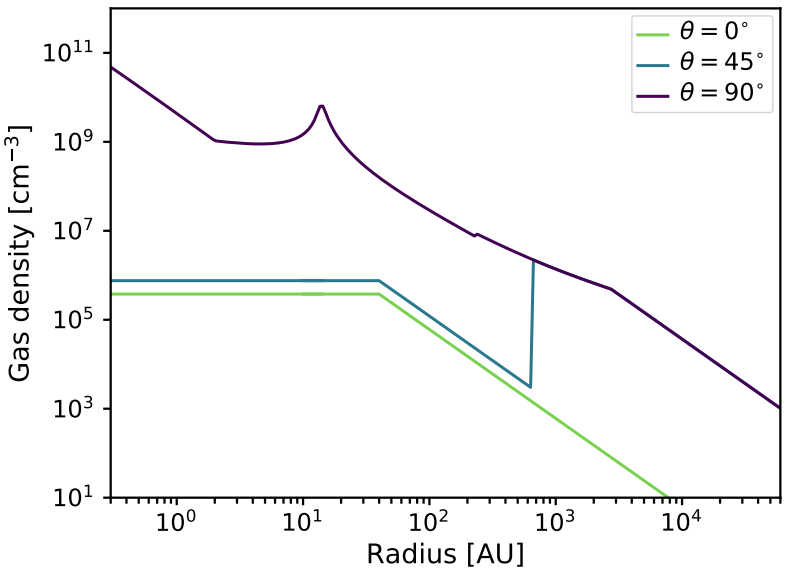

Figure 4.6: The radial density profiles of the updated continuum model of BHR 71. Each line illustrates the radial density profile along the rotation axis ($\theta = 0°$), 45°, and the midplane of the envelope ($\theta = 90°$). The profile along $\theta = 0°$ is offset by 50% for a better visualization.

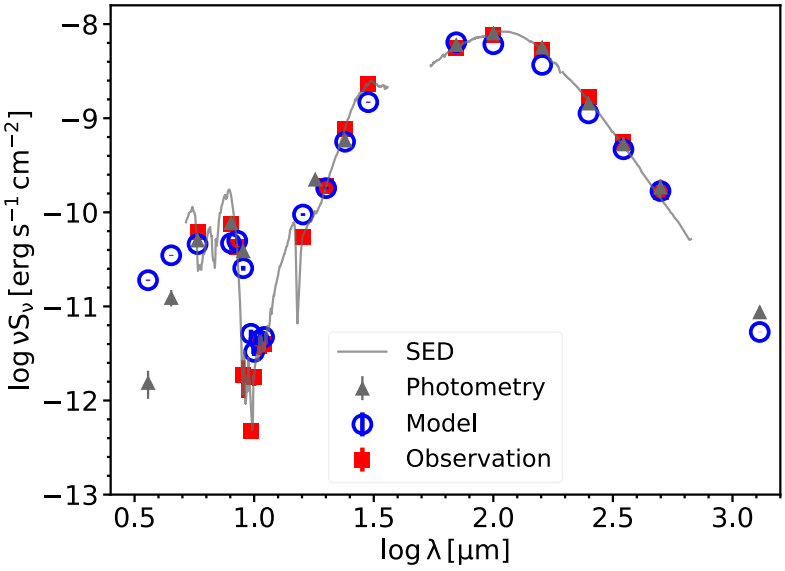

Figure 4.7: The SED of BHR 71 compared with the synthetic SED from our envelope model. The spectroscopy and photometry data of BHR 71 are shown in gray lines and triangles. The blue circles show the synthetic SED at representative wavelengths, while the red squares show the observations extracted with the same method.

the gas temperature equal to the dust temperature when $T_{\rm dust} > 10$ K. The temperatures of gas and dust are in equilibrium when the gas density is greater than 10^4–10^5 cm^{-3}(Young et al., 2004b), where the Y17 model suggests $\sim 10^4$ au for both the radius of $\rho_{\rm gas} = 10^4$ cm^{-3} and the radius of $T_{\rm dust} = 10$ K. Thus, we set the gas temperature to the dust temperature when $T_{\rm dust} > 10$ K, and then apply external heating correction when $T_{\rm dust} < 10$ K.

The Y17 model has the lowest temperature of $\sim$6 K without the external radiation field. To test the impact of the heating from the external radiation field, we introduce an external heating correction for the cells with temperatures lower than 10 K. The external heating is approximated by a linear correction temperature that increases as a function of radius so that the temperature at the edge of the envelope becomes 15 K, described as

$$\begin{aligned} T(r) &= T(r) + \Delta T_{\rm ext.}(r), \text{if } T(r) < 10 \text{ K}; \\ \Delta T_{\rm ext.}(r) &= \frac{(r - r_{10\,\rm K})}{(r_{\rm max} - r_{10\,\rm K})}(15 - T(r_{\rm max})), \end{aligned} \tag{4.2}$$

where $r_{\rm max}$ is the envelope outer radius of 0.315 pc, and $r_{10\,\rm K}$ is the radius where the temperature becomes less than 10 K. A typical $r_{10\,\rm K}$ is $\sim$10000 au, similar to the values derived from self-consistent radiative transfer calculations of dense cores (Young et al., 2004b). Figure 4.9 shows the radial temperature profile before and after applying the external heating. While the external heating correction has no significant impact on the synthetic line profile, we apply the external heating as described in Equation 4.2 to the model for consistency.

With all other parameters taken from the best-fitting dust model, the abundances of the molecules are the main free parameters in this study. In Section 4.4.2.4, we investigate the impact of different abundance profiles on the observed infall signature. Here we describe the procedures for calculating the synthetic line profiles. We employ the Line Modeling Engine (LIME; Brinch & Hogerheijde, 2010) to obtain the molecular level populations and then post-process the model with a customized ray-tracing code to include a central continuum source. LIME iteratively solves the equation of radiation transport assuming non-local thermodynamical equilibrium (non-LTE), and produces image cubes (2D spatial and 1D spectral data) for the specified molecular transition.

Gridding is critical to ensure a realistic representation of the input model. LIME

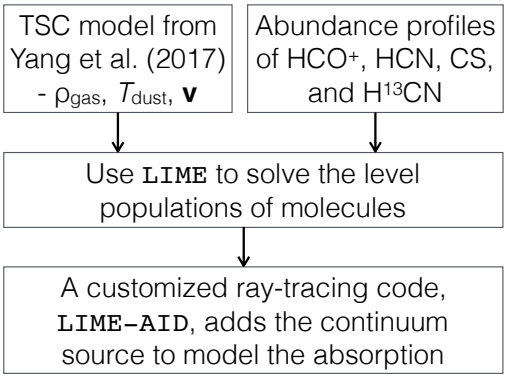

Figure 4.8: The workflow of modeling the infall profile. The $\rho, T_{\rm K}$, and $\boldsymbol{v}$ represent the gas density, kinetic temperature, and velocity vector, respectively.

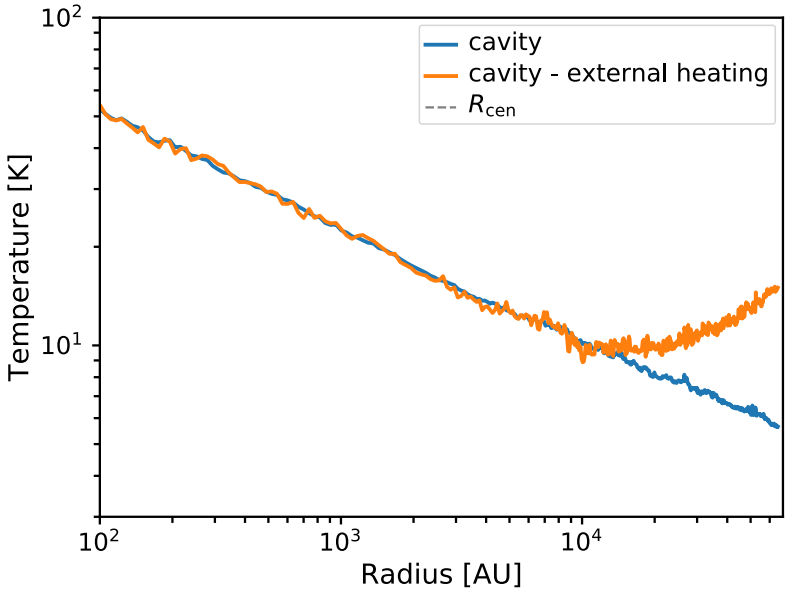

Figure 4.9: The radial temperature profiles of envelopes with cavities. The orange line shows the profile with the external heating, while the blue line shows the profile without the external heating.

automatically determines the gridding based on the temperature and density profiles. However, discontinuities, such as the cavities, in models often lead to unrealistic cell structure in the gridding. Thus, we run LIME with the density profile without the cavities to ensure a robust gridding. The temperature and abundance profiles, which are calculated with cavities, will include the effect of cavities in the resulting synthetic spectra. The synthetic continuum emission may be slightly overestimated, but negligible due to the low density in the cavities.

We set up the LIME model with 50000 grid points between the minimum and maximum radius of 1 au and 30000 au. While using more grid points will reduce the potential clustering, where the grid points show an unusual overdensity at a localized region, we find no difference in the synthetic line profiles calculated with 50000 grid points and 500000 grid points. We also set the maximum radius in LIME smaller to the maximum radius in the model, 64973 au, to better sample the high density regions. Extending the model to the full size of the envelope has negligible effect on the synthetic line profiles. LIME uses sink points at the surface of the model for imaging. Because we post-process the LIME output to add the central continuum source, the number of the sink points is irrelevant.

We need to add the central protostar in the ray-tracing process to simulate the observed continuum absorption, which is beyond the capability of LIME. Therefore, we developed a ray-tracing package, LIME-AID (LIME-Additional Intensity Decoder), with the flexibility to include continuum sources in our model, taking the level populations from LIME along with the temperature, density, velocity, and abundance to calculate updated LOS image cubes. The code itself is a derivative of the Cosmic Lyα Transfer code (COLT; Smith et al., 2015), with the Monte Carlo scattering procedures replaced by ray-tracing. The code also runs natively on unstructured data (Smith et al., 2017), i.e. the Voronoi tessellation of points, which is efficiently and robustly constructed with the Computational Geometry Algorithms Library (The CGAL Project, 2018).

In steady state conditions without scattering, the specific intensity I_ν obeys the radiative transfer equation:

$$\frac{\mathrm{d}I_\nu}{\mathrm{d}s} = j_\nu - k_\nu I_\nu \,, \tag{4.3}$$

where ds is the traversed distance along the LOS, j_ν denotes the volume emissivity (in $\mathrm{erg\,s^{-1}cm^{-3}Hz^{-1}}$), and k_ν denotes the absorption coefficient (in $\mathrm{cm^{-1}}$). Equation 4.3

may be solved for individual sightlines by integrating along the corresponding rays, starting (finishing) at the far (near) end of a sphere of radius $R_{\rm max}$, with zero intensity initial conditions. Assuming piecewise constant conditions within each Voronoi cell, the observed intensity is modified according to the solution in homogeneous media:

$$\Delta I_\nu = \left(\frac{j_\nu}{k_\nu} - I_{\nu,0}\right)\left(1 - e^{-\Delta\tau_\nu}\right) , \tag{4.4}$$

where $I_{\nu,0}$ denotes the intensity carried over from the previous cell and $\Delta\tau_\nu = k_\nu \Delta\ell$ is the optical depth accrued by traversing a LOS distance $\Delta\ell$ within the cell. We assume a Gaussian profile for line emission. To account for gas motion, we also need to Doppler-shift into the frame of the gas such that the coefficients j_ν and k_ν are effectively evaluated at the normalized frequency in the absolute frame: $\Delta u = (\Delta v + \boldsymbol{n}\cdot\boldsymbol{v}_i)/b_i$, where $\Delta v \equiv -c\Delta\nu/\nu_0$ with ν_0 the frequency at line center, $\boldsymbol{n}$ is a unit vector in the direction of the observer, $\boldsymbol{v}_i$ is the cell velocity, and $b_i \equiv (2k_{\rm B}T_i/m + v_{\rm turb}^2)^{1/2}$ is the line broadening parameter in the cell with $k_{\rm B}$ the Boltzmann constant, T_i the gas temperature, m the mass of the molecule, and $v_{\rm turb}$ the microturbulent velocity. Assuming thermal and turbulent broadening are dominant, under this prescription we evaluate the line coefficients as

$$j_{\nu,\rm gas} = j_{\nu,0} e^{-\Delta u^2} \quad \text{and} \quad k_{\nu,\rm gas} = k_{\nu,0} e^{-\Delta u^2} , \tag{4.5}$$

with the precomputed values at line center given by

$$j_{\nu,0} = \frac{hc}{4\pi}\frac{n_2 A_{21}}{\sqrt{\pi} b_i} \text{ and } k_{\nu,0} = \frac{hc}{4\pi}\frac{(n_1 B_{12} - n_2 B_{21})}{\sqrt{\pi} b_i} , \tag{4.6}$$

where the Einstein coefficients are related by the degeneracies of the two transition levels $g_1 B_{12} = g_2 B_{21}$ and $B_{21} = A_{21} c^2/(2h\nu_0^3)$. The emissivity and absorption coefficients for the dust are

$$j_{\nu,\rm dust} = k_{\nu,\rm dust} B_\nu(T_{\rm dust}) \quad \text{and} \quad k_{\nu,\rm dust} = \kappa \rho_{\rm dust} , \tag{4.7}$$

where B_ν denotes the Planck function for a given dust temperature, while κ and $\rho_{\rm dust}$ are the dust opacity per gram of dust and density, respectively. Finally, for this study when the ray intersects the LOS midplane we also add a continuum source, whose brightness follows a 2D Gaussian profile in the plane parallel to the image plane. The fitted continuum parameters from the ALMA observation (Table 4.1) determine the

Table 4.2: Basic data of the modeled transitions

Parameters	HCN $J = 4 \rightarrow 3$	HCO^+ $J = 4 \rightarrow 3$	CS $J = 7 \rightarrow 6$
Frequency [MHz]	354505.478	356734.288	342882.850
Einstein-A_{21} [s^{-1}]	2.05×10^{-3}	3.63×10^{-3}	8.40×10^{-4}
Dust opacity [cm^2 g^{-1}]	1.84	1.86	1.74
Microturbulent velocity [km s^{-1}]		0.34	

input 2D Gaussian profile. For completeness and concreteness, we list the basic data for the modeled transitions in Table 4.2.

To ensure convergence of the image cubes in space and frequency we employ an adaptive convergence scheme. Specifically, we specify a base image resolution and perform ray tracing at each of the pixel corner locations, saving each value. Then for each pixel we trace additional rays for the center and midpoints of the edges. We then compare the average pixel intensity based on the trapezoidal (linear) and Simpson's (quadratic) integration schemes, which use four and nine point stencils, respectively. This allows us to accurately estimate the error caused by a sparse point sampling. If the relative error is above a specified tolerance level, e.g. $|1-I_{\nu,\mathrm{trap}}/I_{\nu,\mathrm{Simp}}| > \varepsilon \sim 10^{-6}$ for any frequency, then we refine the pixel into four sub-pixels. Each of these are tested and adaptively refined until the convergence criterion is met for all frequencies, with the hierarchy of rays tracked maintained with a quadtree data structure, which is eventually aggregated from the bottom up for an efficient and robust determination of the area-averaged intensity for each pixel. We note that our radiative transfer calculations produce line profiles that are nearly indistinguishable from the results obtained by LIME, when we do not include a central continuum source. Now we can efficiently and realistically test various models for the abundance profile and viewing angles in a rapid post-processing fashion.

4.4.2.3 The Kinematics of Infalling Envelopes

We use the kinematics of the TSC envelope to be consistent with the density profile. Figure 4.10 illustrates the velocity in spherical coordinates along three different polar angles. The velocity vector is defined with respect to the origin of the model, the center of the envelope (i.e. negative indicates infall). Along the mid-plane of the envelope ($\theta = 90°$), the centrifugal force becomes significant at small radii compared to other LOS. Thus, the radial velocity decreases most slowly along the mid-plane

of the envelope and the azimuthal velocity increases most rapidly as the radius decreases. In the polar direction ($\theta = 0°$), gas infalls without the effect of rotation; therefore, the radial velocity increases the fastest as the radius decreases, while the polar and azimuthal velocities remain zero.

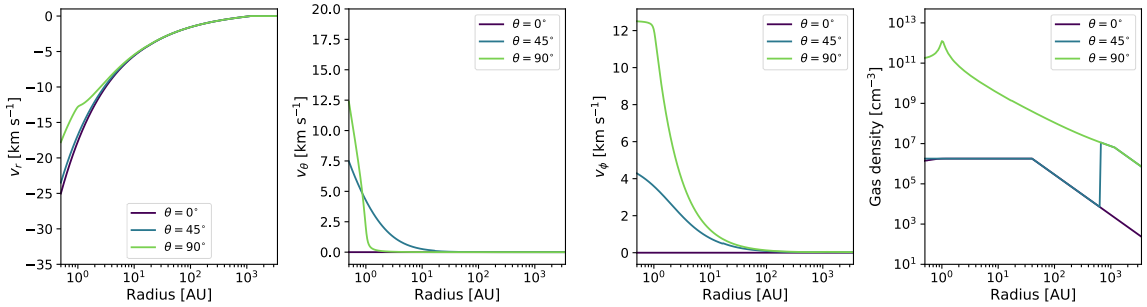

Figure 4.10: The radial, polar, and azimuthal velocity profiles as well as the gas density as a function of radius from the best-fitted TSC envelope (from top left to bottom right), which is the same model in Y17 with an age of 15000 years instead. The velocity profiles along three different polar angles are shown, where $\theta = 0°$ is pole-on and $\theta = 90°$ is edge-on. The negative velocity for v_r indicates that the gas is moving toward the center.

4.4.2.4 Constraining the Abundance Profile

The molecular abundance is a strong function of temperature and density in the protostellar envelope. Molecules start to freeze out onto the dust grains when the dust temperature falls below the condensation temperature for that particular species. Thus, while the molecule is mostly in the gas phase at the outer envelope due to photodissociation, it becomes increasingly frozen out as the radius decreases, where the density is higher (Lee et al., 2004). When the temperature is higher than the evaporation temperature of the molecules, the abundance increases again as the molecules are released from the ices. Jørgensen et al. (2004b) use a "drop function," a constant abundance along with a region of the depleted abundance, to simplify the freeze-out process for modeling the CO line profiles. Here we start with the simple drop function for the abundance profile to try to fit the observed infall profiles.

The drop function depends on the four parameters, the evaporation temperature ($T_{\rm evap}$), the depleted density ($n_{\rm depl}$), the undepleted abundance (X_0), and the depleted abundance ($X_{\rm depl}$). We test the feasibility of the drop function on the

HCO^+ $J = 4 \rightarrow 3$, whose profile is the most typical. The desorption temperature of CO determines the production of HCO^+; therefore, we set the evaporation temperature of HCO^+ to 30 K (Jørgensen et al., 2002b). Additionally, we add a destruction temperature of 100 K, where water becomes evaporated and destroys HCO^+ (Jørgensen et al., 2013), acting as an inner cutoff radius of the abundance profile. We explore the parameter space using 25 models with $10^{-9.5} \leq X_0 \leq 10^{-7}$, $10^{-12.5} \leq X_{\rm depl} \leq 10^{-9.5}$, and $10^{5.5} \leq n_{\rm depl}$ ($\rm cm^{-3}$) $\leq 10^8$, distributed evenly in logarithmic scale. Figure 4.12 show the spectra of all 25 synthetic line profiles compared with the observation. The models with the drop function result in too much emission at high velocities, while the peak velocities disagree with the observation. Evans et al. (2005) also found that a simple step function requires unlikely combinations of parameters to fit the observations of B335. Our experiment suggests that the simple analytic abundance profiles are insufficient for modeling the high SNR ALMA spectra.

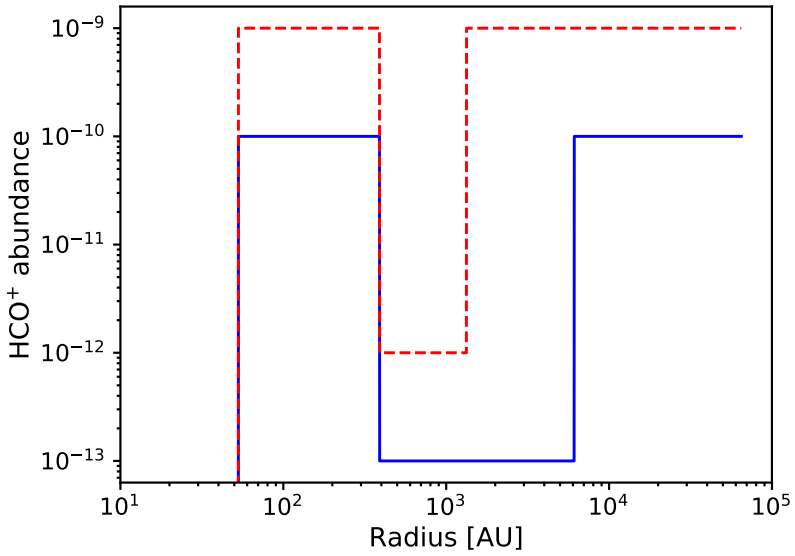

Figure 4.11: Two examples of the profiles of the abundances with the drop function. The blue solid and red dashed lines indicate the drop function with $n_{\rm depl} = 10^5\,\rm cm^{-3}$ and $10^6\,\rm cm^{-3}$, respectively. Both models have $T_{\rm evap} = 30$ K.

To overcome the limitation of the drop function abundance, we construct a parameterized abundance profile that resembles the features in the chemo-physical modeling (Lee et al., 2004). Such profile has the flexibility to reproduce not only the abun-

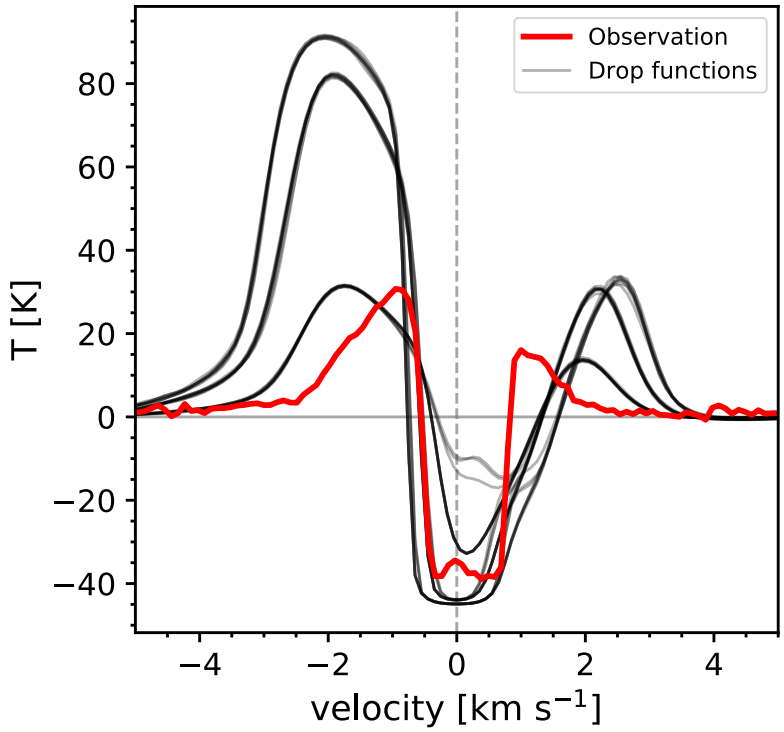

Figure 4.12: The observed HCO^+ $J = 4 \rightarrow 3$ line profile along with the spectra modeled with the drop function abundance.

dance of HCO^+ but also HCN, CS, and $H^{13}CN$. Here we use HCO^+ as an example to describe the effect of each parameter (Table 4.3). HCO^+ is a daughter molecule of CO and H_3^+, described as

$$CO + H_3^+ \rightarrow HCO^+ + H_2. \tag{4.8}$$

Thus, the abundance of CO dominates the abundance of HCO^+. Instead of a sudden drop in the abundance in the "drop function", we set the abundance proportional to r^{a_f} in the freeze-out zone until the molecule becomes evaporated at the inner high temperature region. The high CO abundance at the warm inner envelope enhances the production of HCO^+, and other carbon-bearing molecules. When the temperature becomes higher than 100 K, water, a major destroyer of HCO^+, sublimates, reducing the abundance of HCO^+. The gas-phase chemical equilibrium may also reduce the molecular abundance at high temperature. Toward the edge of the envelope, HCO^+ experiences more photoelectrons from the interaction of external radiation and CO, which destroy HCO^+ via the dissociative recombination. Thus, we introduce a

Table 4.3: The parameters of the abundance profile

Parameter	Description	HCO^+	HCN	CS	$H^{13}CN$
$X_{\rm out}$	The maximum abundance	5.0×10^{-9}	8.0×10^{-10}	1.0×10^{-10}	2.7×10^{-10}
$X_{\rm evap}$	The abundance of the evaporation zone	2.0×10^{-9}	1.0×10^{-8}	2.5×10^{-9}	3.3×10^{-9}
$r_{\rm max,i}$	The inner radius of the maximum abundance region	1000 au	1000 au	1000 au	1000 au
$r_{\rm max,o}$	The outer radius of the maximum abundance region	1500 au	1200 au	1500 au	1200 au
$r_{\rm evap,i}$	The inner radius of the evaporation zone	50 au	1 au	10 au	1 au
$r_{\rm evap,o}$	The outer radius of the evaporation zone	100 au	10 au	400 au	10 au
$a_{\rm f}$	The power-law index of the freeze-out zone	1.6	0.0	0.0	0.0
$a_{\rm p}$	The power-law index of the outer decreasing region dominated by photodissociation	−2.0	−2.0	−5.0	−10.0

decrease of the abundance at the outer radius as $r^{a_{\rm p}}$. Lastly, we set the abundance at the inner evaporation zone ($X_{\rm evap}$) lower than the outer region, which has the maximum abundance ($X_{\rm out}$). The abundance of HCO^+ would be less than the maximum abundance because the abundance of H_3^+ decreases at high densities even if CO becomes abundant inside its evaporation radius. $X_{\rm out}$ is not necessarily greater than $X_{\rm evap}$ for other molecules.

To constrain the abundance profile, we set the initial parameters with the insights of the chemical modeling in Young et al. (2004b). Then we manually search for the best-fitting abundance profile while exploring the effect of each parameter. For HCO^+, we use the evaporation temperature of CO (∼30 K) and H_2O (∼100 K) to determine the boundaries of the evaporation region. Thus, we set the initial evaporation region from 50–400 au.

The chemical evolution of CO also controls the abundance profiles of HCN and CS. When CO freezes onto dust grains, HCN and CS are also depleted. Once CO becomes evaporated, the gas-phase production of HCN and CS increases (Lee et al., 2004). For HCN, the gas-phase abundance eventually becomes unsustainable for chemical equilibrium so that its abundance decreases at higher temperature region (i.e. inner radius). Lee et al. (2004) find three peaks in the abundance profile of HCN in the protostellar stage, corresponding to the evaporations of CO, HCN, and CN, respectively. $H^{13}CN$ follows the abundance of HCN. CS has two peaks in its abundance profile. The first one occurs when CO is evaporated, while the second one occurs at

an inner radius where CS is evaporated, which has a higher evaporation temperature. The abundance of CS remains high at the inner radius, where most of the oxygen still freezes onto dust grains as atomic oxygen and water. Thus, sulfur atoms tend to stay in CS rather than SO, which would be preferred if oxygen abundance increases. At large radii, CS has a low abundance due to the destruction by UV photons.

Different chemistry dominates the abundances of HCO^+, HCN, and CS, resulting in a wide range of fitted abundance profile. We assume that the abundance of $H^{13}CN$ follows the abundance of HCN scaled by the $^{12}C/^{13}C$ ratio in HCN. In general, the peak emission at $|v|$ $\sim$1 km s^{-1} originates from the freeze-out zone, controlled by the maximum abundance ($X_{\rm out}$) and the freeze-out slope ($a_{\rm f}$). The properties of the evaporation zone, the evaporation abundance ($X_{\rm evap}$) and the size of the evaporation zone ($r_{\rm evap,i}$ and $r_{\rm evap,o}$), determine the emission in the line wing ($|v| \gtrsim 2$ km s^{-1}). The abundance outside of the maximum abundance zone typically contributes to the absorption at the source velocity.

4.4.2.5 The Best-fitting Model

Figure 4.13 shows the best-fitting infall profiles sampled with the same *uv*-coverage of our ALMA observation using the CASA tasks SIMOBSERVE and SIMANALYZE. We take the best-fitted parameters from Y17 as the initial guess of the model, and iterate the abundance profiles and ages to find the best-fitting model. The best-fitting abundance profiles of HCO^+, HCN, CS, and $H^{13}CN$ are shown in Figure 4.14 with the parameters listed in Table 4.3. We also summarize the effect of cavities and inclination in Appendix C.1.

The parametrized abundance profile provides a great flexibility to model the infall signature. However, the velocities where the line profile peak as well as the shape of the absorption feature remain invariable to the changes in the abundance profile. Compared to our observation, a TSC envelope with an age of 36000 years (Yang et al., 2017a) leads to the profiles peaking at higher velocities. Under our model, only a younger envelope model can shift the peaks toward lower velocity. The HCO^+ and HCN lines require an age of 20000 years, while the CS line only agrees with an even younger envelope with an age of 15000 years, which also reproduces the line profiles of HCO^+ and HCN. The envelope with a younger age still reproduces the radial brightness profile of BHR 71, because the χ^2 value essentially levels off below

36000 years (Yang et al., 2017a).

We iteratively test different abundance profiles for each molecule to find the best-fitting model. Our models well reproduce the line profiles of HCN $J = 4 \rightarrow 3$, HCO^+ $J = 4 \rightarrow 3$, and CS $J = 7 \rightarrow 6$ lines, but overestimate the absorption in the $H^{13}CN$ $J = 4 \rightarrow 3$ line. The HCO^+ abundance follows the typical expectation with a deep freeze-out zone and an evaporation zone at the inner 50–100 au. The line profiles of HCN and CS prefer the abundance profiles with higher abundance at the evaporation zone than the outer envelope and no freeze-out zone. For the models with freeze-out zones, the synthetic line profiles show a much weaker emission compared to the observations. The best-fitting HCN model has high abundance at the region as close as 1 au to the central protostar, driven by the broad peak at the blue-shifted velocity. We do not find any model under our setup that can reproduce the broad high velocity emission. Outflows would be a possible origin of the high velocity emission; however, the high velocity emission is mostly concentrated at the center (Figure 4.4) instead of following the morphology of the outflows. Thus, the high velocity emission suggests an unexpected structure at the inner envelope.

To model the profile of the $H^{13}CN$ $J = 4 \rightarrow 3$, we start with scaling the HCN abundance by 70, the isotope ratio of $^{12}C/^{13}C$ (Wilson & Rood, 1994). However, such abundance profile produces a very weak line profile inconsistent with the observation. Then we test different $^{12}C/^{13}C$ ratios and find the best fit for a ratio of 3 for the model best-fitting the observation, which has a ratio of 3 for $^{12}C/^{13}C$. While a $^{12}C/^{13}C$ ratio of 3 is highly unlikely, such a high ratio suggests that the $H^{13}CN$ $J = 4 \rightarrow 3$ line requires additional molecules on top of our model. Given the compact morphology of the $H^{13}CN$ emission (Figure 4.2), a highly concentrated structure at the center of BHR 71 may reproduce the observation. The model for another protostar, B335, also shows a similar discrepancy on the $H^{13}CN$ $J = 4 \rightarrow 3$ line (Evans et al., 2015). The possible underlying structure remains unknown, but future observations on the emission of complex organic molecules which concentrated at the central region may provide insights to this inconsistency. Besides the overall strength of the $H^{13}CN$ $J = 4 \rightarrow 3$ line, our model predicts a significant absorption, whereas the observation shows only a self-absorption of $\sim$5 K. Typically, increasing the exponent of the power-law for the outer photodissociation region reduces the absorption, but in the case of $H^{13}CN$, where we drastically decrease the abundance at the outer envelope (Figure 4.14), the absorption still largely disagrees with the ob-

servation. The best-fitting CS abundance has a large evaporation zone ranging from 10 au to 400 au. To match the observed absorption feature, we not only make the abundance decreases more rapidly at the photodissociation region but we also need to reduce the $X_{\rm out}$.

The absorption features seen in the HCO^+ and HCN lines have a small peak at the bottom, whereas our model produces a simple smooth absorption. Because this small peak appears on top of a deep absorption, the origin of this peak must be in front of the dense envelope. Such emission could arise from a foreground layer of gas that is dense enough to have the emission of HCO^+ and HCN, or the surface layer of the envelope heated by the interstellar radiation field.

4.4.2.6 Comparison to the Single-dish Observations

Figure 4.15 shows the synthetic spectrum of the HCO^+ $J = 3 \rightarrow 2$ line using the best-fitting model of HCO^+ compared with the archival APEX observation. While the synthetic emission has a strength comparable to the observation, the line profile is significantly different. The observation shows significant blue-asymmetry between the two peaks, whereas the model suggests an equal strength double-peaked profile. Given that our model is optimized for the ALMA observation, which is only sensitive to the structure smaller than $3''$, we do not optimize our model for the single disk observation. However, a comparable strength with a different line profile suggests that the temperature profile at few thousands au scale, best probed by the single dish observation, may be inconsistent with the TSC envelope. Observations that measure the chemical abundance of HCO^+, such as the observation of $H^{13}CO^+$, and probe the intermediate scales between the single dish data and our ALMA observation may revise our model to fit the data at both low and high resolutions.

4.4.2.7 Infall Kinematics from the Envelope to the Inner 100 au

While the infall signature toward the continuum source provides the least contaminated signature to constrain the underlying infall kinematics, the variations of infall signatures across the midplane of the envelope will show the effect of the underlying abundance profile and highlight any asymmetry across the envelope. Here we focus on the HCO^+ $J = 4 \rightarrow 3$ line best fitted by our model. For HCO^+ $J = 4 \rightarrow 3$, the blue asymmetric double-peaked profile only appears within the inner $0\farcs5$ region,

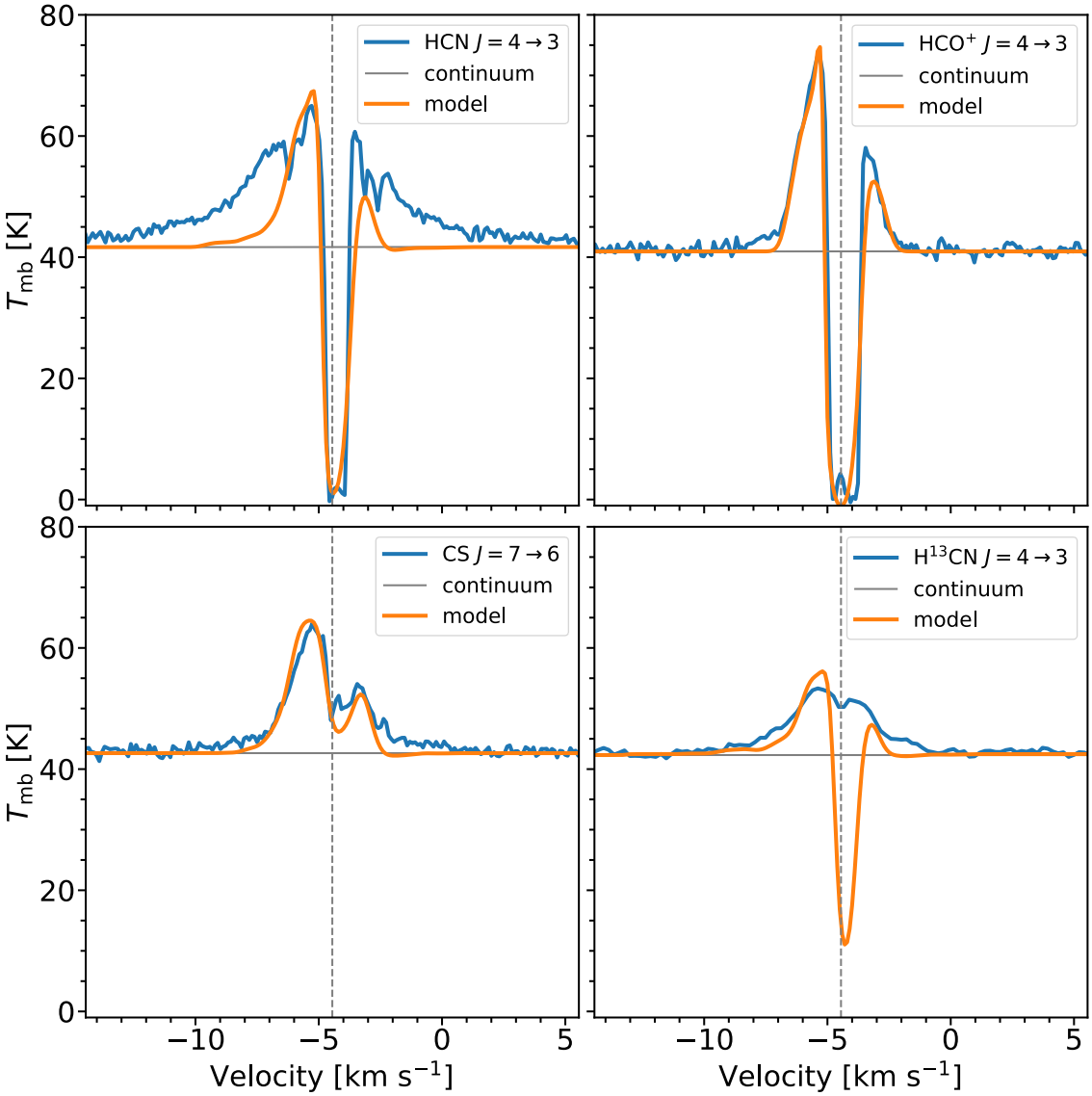

Figure 4.13: The synthetic spectra of HCN $J = 4 \rightarrow 3$, HCO$^+$ $J = 4 \rightarrow 3$, CS $J = 7 \rightarrow 6$, and H^{13}CN $J = 4 \rightarrow 3$ in orange along with the observed line profile in blue.

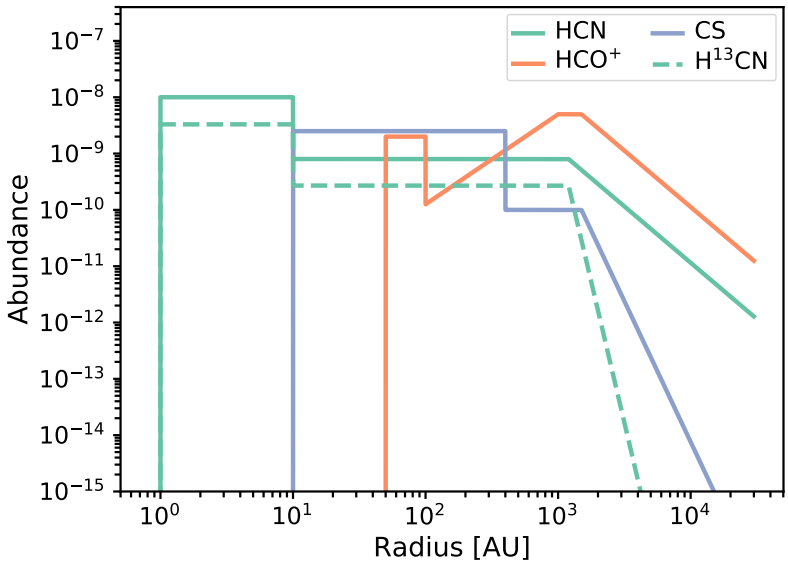

Figure 4.14: The best-fitted parametrized abundance profiles for HCN, HCO^+, CS, and $H^{13}CN$. The $H^{13}CN$ abundance is one third of the abundance of HCN.

whereas only a single blue peak exists beyond the inner 0.″5 region (Figure 4.16). The strength of the red peak increases from east to west, whereas we expect a decrease in red-shifted emission from east to west due to the rotation. Except for pointings toward the center and −0.″5, the model disagrees with the observation. The synthetic profile shows a higher intensity when the pointing is displaced by 0.″5 from the center due to the reduction of the optical depth. As we move further away from the center along the midplane, the decrease of molecular abundance starts to dominate the behavior of the synthetic profile, resulting in a gradual decrease in the overall intensity.

The comparison between our model and the observation highlights two issues. First, a rotating infalling envelope fails to reproduce the variation of the red-shifted peak across the inner 0.″5 region. The model predicts a significantly higher intensity of the red-shifted peak in the east (left), whereas the observation shows only a modest difference (magenta lines in Figure 4.16). A TSC envelope with twice the best-fitting rotation speed, 5×10^{-13} rad s^{-1}, leads to a greater asymmetry for the line profiles at one side of the midplane to another; for the line profile at the 0.″5 offset, the peak of the difference (magenta line) becomes ∼10 K. However, the observation shows a difference of ∼20 K, suggesting a much faster rotation at the inner 0.″5 region, whereas

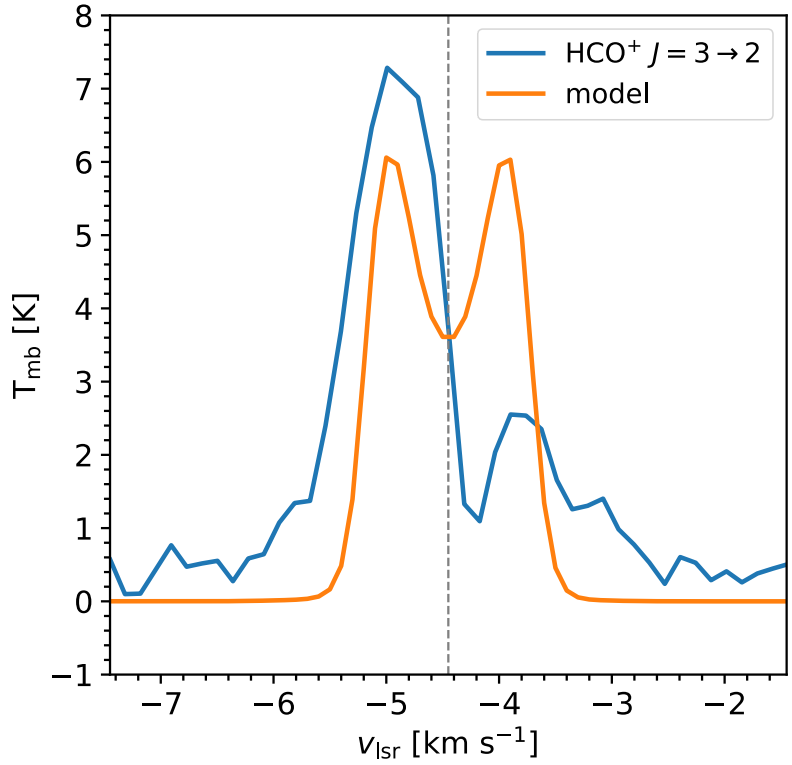

Figure 4.15: The synthetic HCO^+ $J = 3 \rightarrow 2$ line profile (orange) compared with the archival APEX observation (blue). The model is the same best-fitted model for the HCO^+ $J = 4 \rightarrow 3$ line extracted from a $23\farcs3$ circular aperture without any beam correction.

the TSC envelope predicts a sub-Keplerian rotation velocity within the disk inherited from the infalling gas close to the rotation axis, which has small angular momentum.

Secondly, the model fails to explain the disappearance of the red-shifted emission beyond the inner $0\farcs5$ region. Moreover, the synthetic infall signatures overestimate the intensity at off-center positions, suggesting a more complex abundance profile. The temperature gradient in the envelope governs the degree of asymmetry between the blue-shifted and red-shifted peaks, and also ensures the appearance of the red-shifted emission as long as the warm gas in the foreground of the infalling envelope falls within the LOS. If we increase the depletion in the freeze-out zone of the abundance profile to fit the red-shifted peaks, both the blue-shifted and red-shifted peaks would have the same sudden disappearance beyond the inner $0\farcs5$ region, which is not observed. The lack of red-shifted emission may also explain the significant blue-

asymmetry in the HCO^+ $J = 3 \rightarrow 2$ line observed by APEX, while our model predicts an equal strength double-peaked profile.

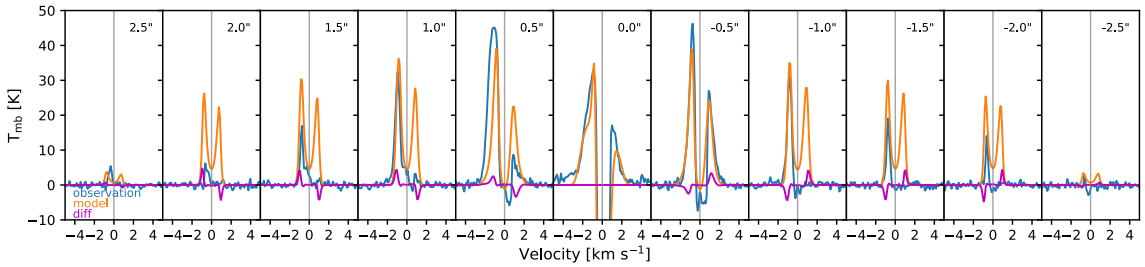

Figure 4.16: A grid of the HCO^+ $J = 4 \rightarrow 3$ line profiles extracted with $0\farcs5 \times 0\farcs5$ box regions. Those regions offset from the center ranging from $2\farcs5$ to -$2\farcs5$ in RA. The observation is shown in blue, while the model is shown in orange. The magenta lines show the difference in the synthetic spectra to the opposite side of the offset (i.e. the line for $0\farcs5$ is the difference of profiles toward $0\farcs5$ and $-0\farcs5$).

4.4.3 Peculiar Kinematics of HCN Blobs

The channel maps of the HCN $J = 4 \rightarrow 3$ emission reveal four compact blobs with their spectra peaking at 0.5–1.5 km s^{-1}, locating along the outflow direction. Table 4.4 lists the sizes of the blobs fitted with a 2D Gaussian profile. Three of them lie in the north (N1, N2, and N3), which is the red-shifted outflow lobe (Bourke et al., 1997; Parise et al., 2006c), and one of them locates in the south (S1), where the outflow is blue-shifted. Interestingly, if we focus on ± 2 km s^{-1} around the source velocity, the three northern blobs peak at the blue-shifted velocity, while the southern blob peaks at the red-shifted velocity, presenting a pattern opposite to that of the outflow defined by CO. At the velocities greater than 4 km s^{-1}, the HCN emission only appears in south at the blue-shifted velocity and in north at the red-shifted velocity, following the kinematics of the outflows. Two of the four blobs also appear in the CO observation with a similar resolution as that of HCN (priv. comm. with Michael Dunham) at the same velocity range (Figure 4.17). Figure 4.21 (top) shows the PV diagrams along the outflow direction at low velocities and across the entire velocity range of the spectrum, indicating triangular features peak at the blob positions most significantly at N2 and N3.

We propose two scenarios to explain the origin of those blobs, which have kinematics opposite to the outflows and small ($\sim$1 km s^{-1}) velocity shifts. The blobs

Table 4.4: Source fitting of the HCN blobs

Name	R.A.	Dec.	FWHMs [mas]	PA
N3	$12^h01^m36^s.54$	$-65^d08^m47^s.81$	819±32×588±20	$154^\circ.8\pm4^\circ.2$
N2	$12^h01^m36^s.52$	$-65^d08^m48^s.58$	656±12×495±8	$163^\circ.2\pm2^\circ.2$
N1	$12^h01^m36^s.52$	$-65^d08^m49^s.05$	567±21×489±16	$145^\circ.5\pm9^\circ.1$
S1	$12^h01^m36^s.50$	$-65^d08^m49^s.59$	515±8×388±5	$97^\circ.8\pm1^\circ.9$

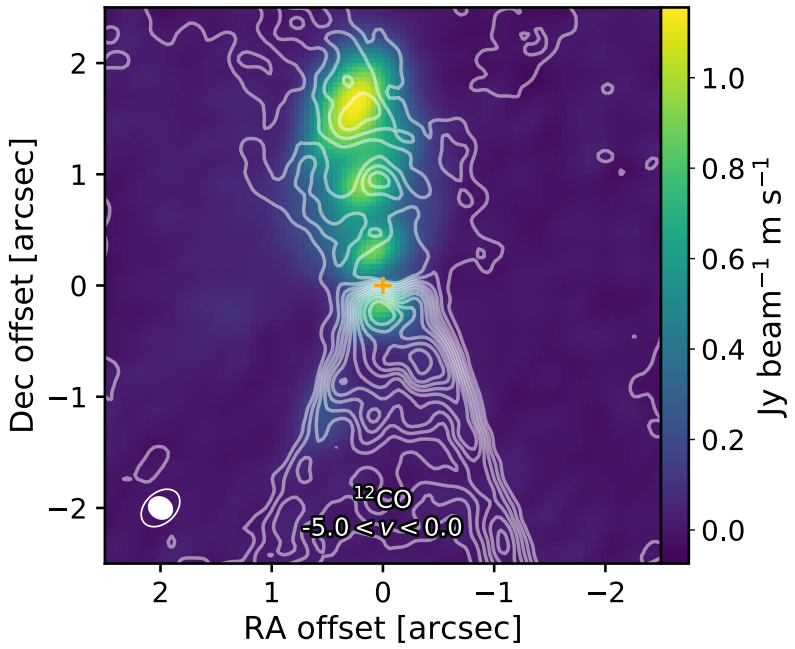

Figure 4.17: The moment 0 map of the HCN emission shown as an image with the moment 0 of the CO $J = 2 \rightarrow 1$ emission plotted as contours (M. Dunham, priv. comm.). Both moments are calculated from -5 to 0 km s^{-1}. Shown at the bottom left corner, the solid ellipse indicates the beam size of the CO observation, while the the greater ellipse outline indicates the beam size of the HCN observation.

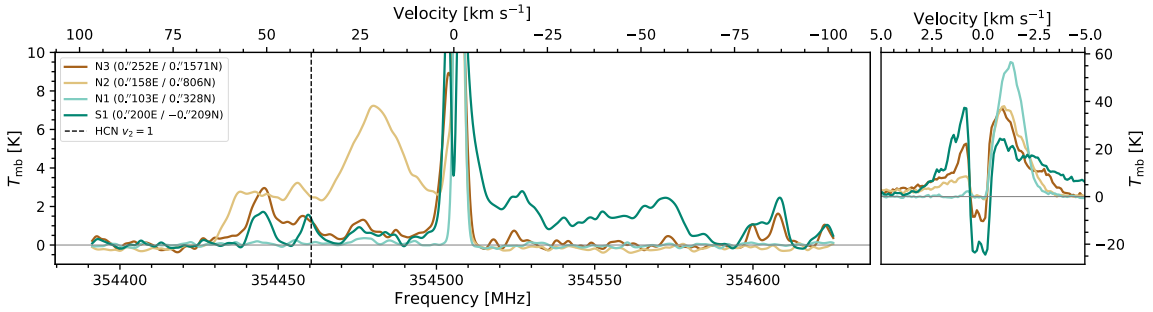

Figure 4.18: **Left:** The full spectra of the four HCN blobs extracted from the fitted 2D Gaussian sources (Table 4.4). **Right:** The spectra of the same four HCN blobs shown only around the line centroid of the HCN $J = 4 \rightarrow 3$ line.

may be part of the outflows. The front side of the red-shifted outflow can appear as blue-shifted emission if the outflow opening angle is large enough to have parts of the outflow in front of the plane of sky. With an outflow opening angle of 20° and an inclination angle of 50°, the projected location of the blobs is consistent with the region where the outflow extends in front of the plane of sky in high inclination, supporting this scenario (Figure 4.19). The outflow opening angle is defined as the angle between the rotation axis to the edge of the outflow cavity at 10000 au (Yang et al., 2017a). However, if shocks lead to the excitation of those HCN blobs, we expect to observe broad spectral feature from the shocked gas that is in blue-shifted at the northern blobs and red-shifted for the southern blob. Only N2 and S1 have broad features in their spectra, but the features appear at the opposite velocity as we expect.

The blue-shifted infalling gas behind the outflow cavity can also result in the small blue-shifted emission in the red-shifted outflow. The best-fitting model of the infall profile has similar velocities as the velocity offset of those blobs; however, the model also predicts more red-shifted emission (Figure C.3), which disagrees with the observation, and the model does not include the kinematics of the outflows. In this case, we expect to see broad spectral feature at the red-shifted velocity for the northern blobs, which is consistent with the spectra of N2. Future observations for probing the excitation mechanism of those blobs, such as SiO tracing the shocked gas, may reveal the nature of these blobs.

A compact feature also appears at high velocity. An offset compact emission peaks at ∼354480 MHz, if the source velocity of −4.45 km s^{-1}is assumed, in the spectrum

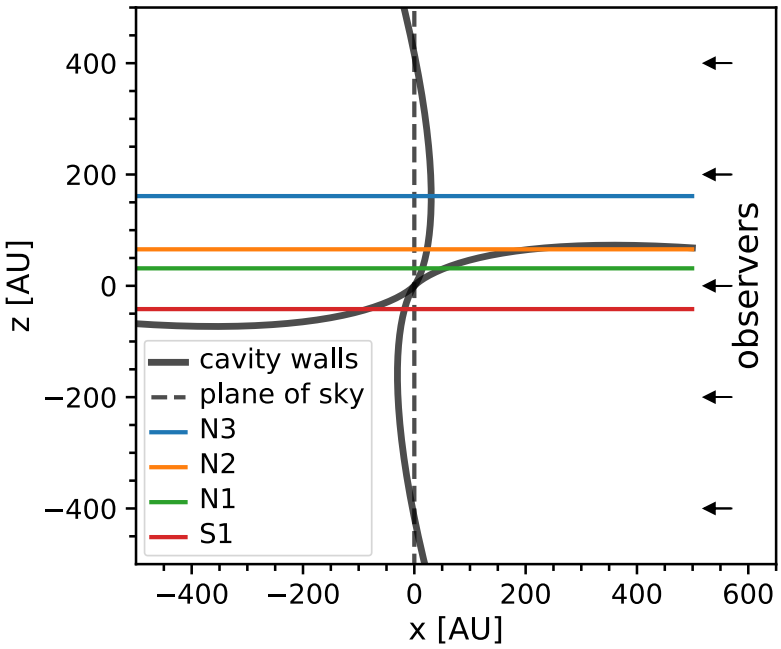

Figure 4.19: An illustration of outflow cavity (black thick solid line) and the plane of sky (black dashed line) along with the line of sights of the HCN blobs (colored lines), assuming an outflow opening angle of 20° and an inclination angle of 50°. An opposite kinematics would occur where the cavity walls appear at the opposite side to the majority of the outflow cavities with respect to the plane of sky (i.e. the northern red-shifted outflow has parts of its cavity wall in front of the plane of sky.).

centered on the HCN $J = 4 \rightarrow 3$ line, extending over a wide range of frequencies. Measured by the CASA `imfit` task, this compact high velocity emission peaks at $12^{\rm h}01^{\rm m}36\overset{\rm s}{.}53$ / $-65^{\rm d}08^{\rm m}48\overset{\rm s}{.}42$ with a size of $0\overset{\prime\prime}{.}54\times0\overset{\prime\prime}{.}47$. Figure 4.20 shows the spectrum of the high velocity compact emission. Only seen offset from the center, the broad line profile is unlikely to emitting from COMs. Shock-excited HCN $J = 4 \rightarrow 3$ $v = 0$ and $v_2 = 1$ lines may contribute to the broad features extending toward high redshift velocities and the velocity offset matches the kinematics of the outflows. Comparing to the HCN blobs defined at low blue-shifted velocities, this high red-shifted velocity compact feature peaks in between N2 and N3 and much closer to the N2 blob, suggesting that the same physical structure may contribute to the emission at both the low blueshift velocity and the high redshift velocity.

Across the entire velocity range, high velocity broad emission appears at both red-shifted and blue-shifted velocities, occurring at $+0.9''$ and $-0.4''$ to the contin-

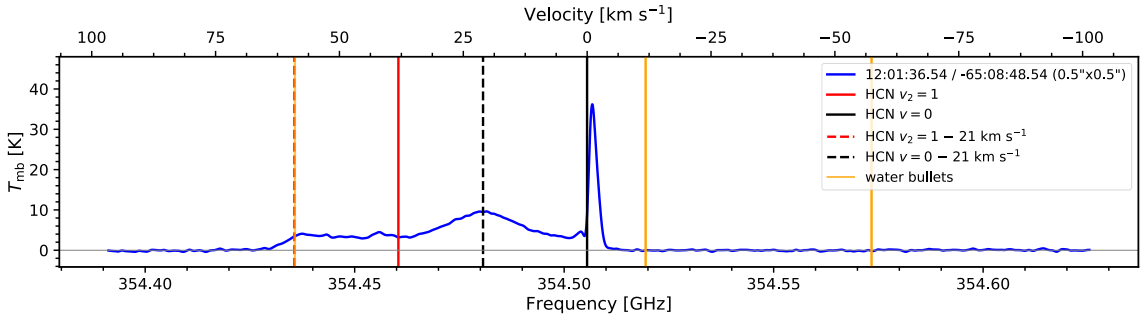

Figure 4.20: The spectrum of the high velocity compact feature in the spectral cube centered on the HCN $J = 4 \rightarrow 3$ line extracted from a $0\farcs5 \times 0\farcs5$ region. The black solid and dashed lines indicate the rest frequencies of the HCN $J = 4 \rightarrow 3$ $v = 0$ and $v_2 = 1$ lines, respectively, while the red solid and dashed lines show the same two transitions shifted by -21 km s^{-1} to match the broad peak at 21 km s^{-1}. The orange lines indicate the velocities of the water bullets identified by Kristensen et al. (2012a); Mottram et al. (2014a).

uum source (Figure 4.21, bottom). Kristensen et al. (2012a) identify high velocity "bullets," narrow offset features, from the water $1_{10} \rightarrow 1_{01}$ emission, where Mottram et al. (2014a) isolate the bullets at -57.4, -11.8, and 59.0 km s^{-1}. The spectrum has no clear signatures of bullets; however, the velocities of the broad features cover the water bullets at the red-shifted velocities, whereas no broad feature exists at the blue-shifted velocities to match the water bullets.

4.5 Complex Organic Molecules

The bandwidths of our observation ($\sim$200 km s^{-1} and $\sim$400 km s^{-1}) allows us to not only measure those infall indicators but also survey the emission of complex molecules at similar frequencies. As the infall drives the dynamical evolution of dense cores, the chemical state of the infalling gas evolves as the material experiences an increase in both density and temperature, which determines the available chemical reactions. Thus, the chemical complexity grows along with the evolution of the infalling envelope. Over the last decade, observations reveal a new class of protostars that exhibit rich spectra of complex organic molecules (COMs), so called the "hot corinos" (Ceccarelli, 2004; Ceccarelli et al., 2007). The leading formation theory of COMs suggests that the COMs are formed through reactions on the grain surface at

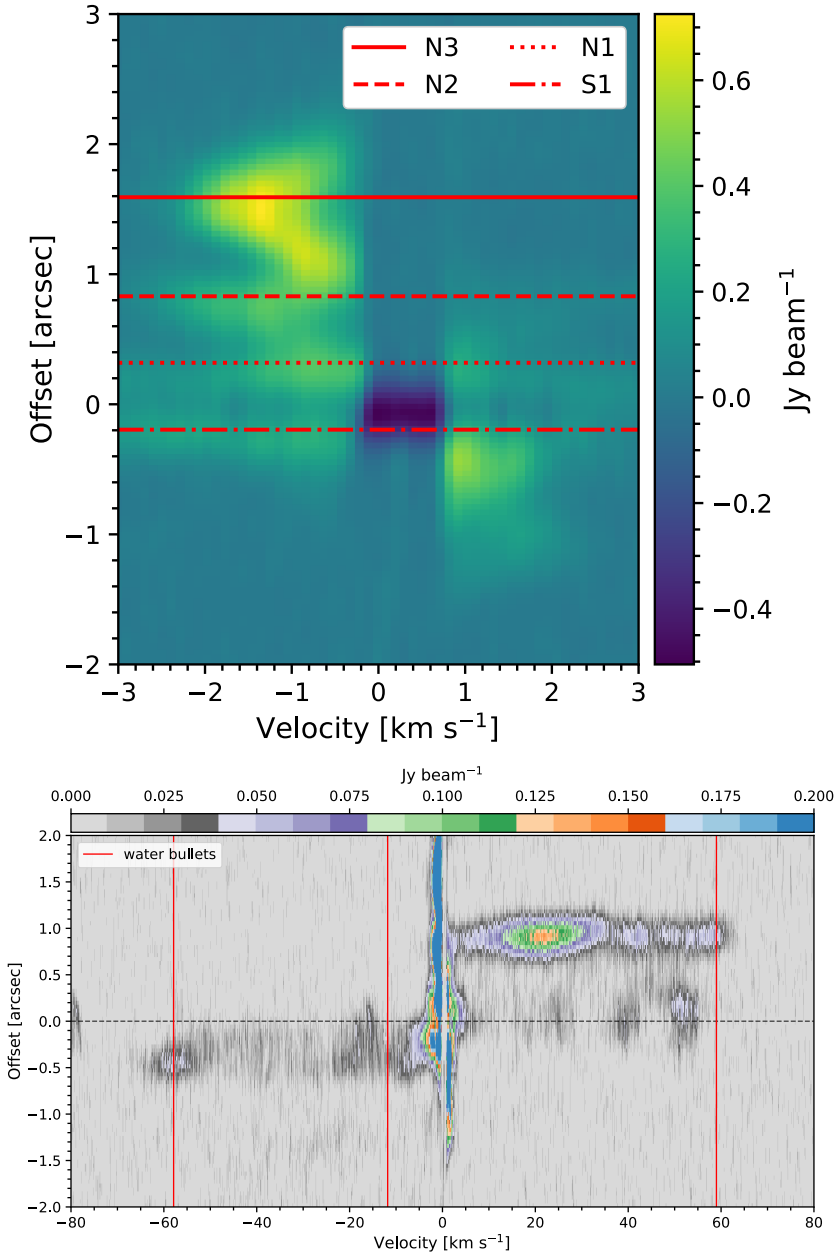

Figure 4.21: **Top:** The position-velocity diagram extracted along the HCN blobs. The horizontal lines indicate the locations of blobs. **Bottom:** The position-velocity diagram extracted from the same slice as the left figure shown in the full velocity range. The vertical lines indicate the velocities of the water bullets identified by Kristensen et al. (2012a) and Mottram et al. (2014a).

temperatures of 15–40 K (Garrod et al., 2008; Aikawa, 2013), suggesting a coupled evolution between dynamics and chemistry. While ALMA has been revolutionizing the characterization of the hot corinos (e.g. Jørgensen et al., 2016), there are only a few known hot corinos to constrain the interplay between infall and chemistry.

4.5.1 The Spectra of Complex Organic Molecules

We identified 62 features other than the four transitions that trace the infall (Figure 4.22). Table 4.5 shows the line fitting results using CLASS[1]. The line fitting starts with a fitting of a single gaussian profile. If a single gaussian profile fails to reproduce the spectral feature, we tried a double or triple gaussian profile to achieve a better fit. Also the line width may be fixed to 3.5 km s^{-1} to fit blended lines. Table 4.5 lists the adopted methods other than the default single gaussian profile. The window of the H^{13}CN $J = 4 \rightarrow 3$ line (Figure 4.22, bottom) contains more than half of the lines we found, making the identification of those molecules a challenging task.

The mean line width is 4.3±0.3 km s^{-1} with a median width of 3.5 km s^{-1}; however, the line width of some lines may be overestimated due to the blending with other lines. Table 4.5 also lists the source size fitted with 2D Gaussian profiles, using the CASA `imfit` task. Most of the emission comes from a small compact region centered at the continuum source, which has an averaged deconvolved size of $0\farcs50\pm0\farcs13\times0\farcs21\pm0\farcs09$ (100 au×42 au), while several lines show extensions in the north-south direction.

[1]http://www.iram.fr/IRAMFR/GILDAS

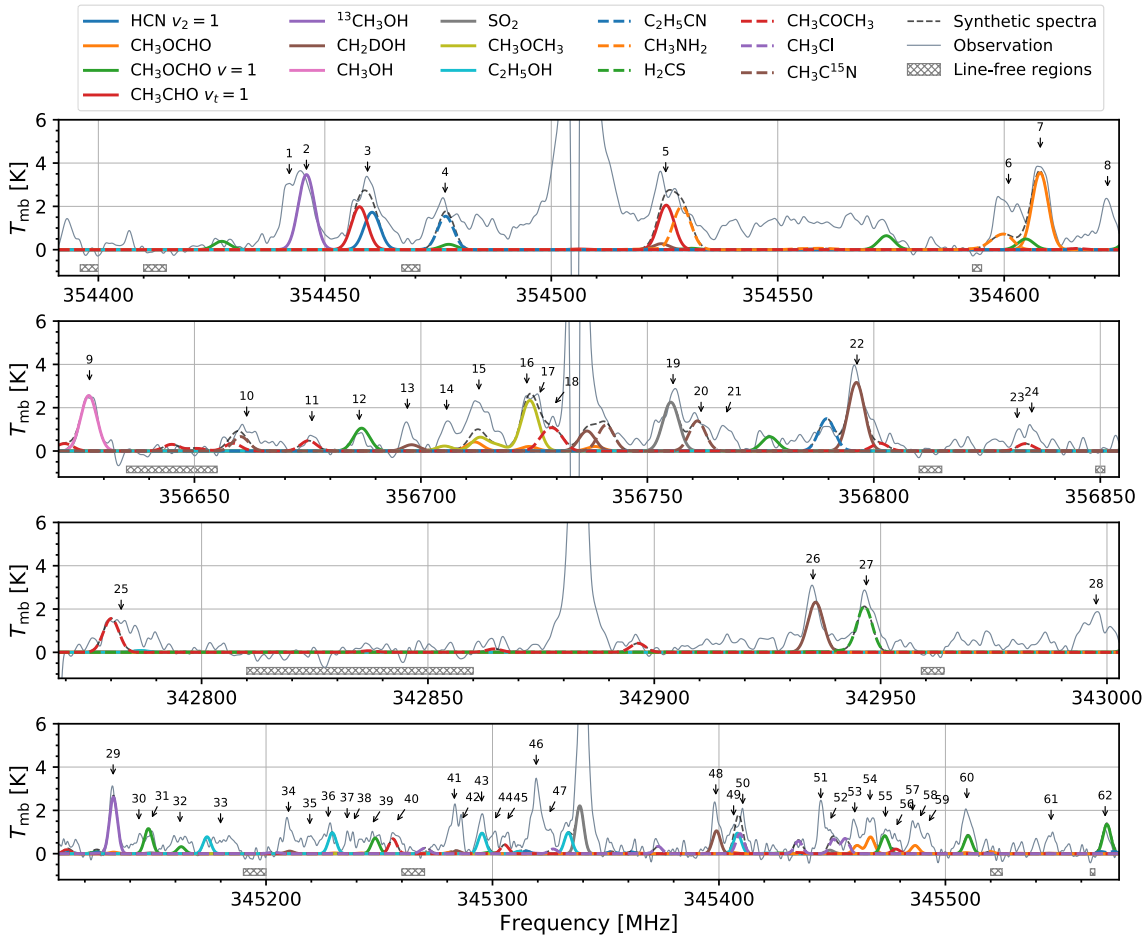

Figure 4.22: The 1D spectra of BHR 71 with identified emission lines labelled. The observed spectra are smoothed with an 1D Gaussian kernel which has a FWHM of 1 km $s^{-1}$to achieve a higher S/N on the weak emission. The numbers of the identified features are consistent with the line number shown in Table 4.5. The colored lines show the synthetic spectra of the identified species fitted by XCLASS (Table 4.3). Line 46 is identified as the emission of CH_3OD, which is not included in the database queried by XCLASS, hence not modeled. The horizontal bars beneath the spectra indicate the line-free regions selected for baseline fitting and calibration.

Table 4.5: Line Fitting

Line No.	Frequency [MHz]	Line Width [km s^{-1}]	Integrated Flux [K km s^{-1}]	Deconvolved FWHMs [arcsec]	PA [deg.]	Method[a]
			HCO$^+$ $J = 4 \rightarrow 3$			
1	354442.152 (0.068)	3.5 (n/a)	10.5 (0.3)	$0\farcs61 \pm 0\farcs06 \times 0\farcs19 \pm 0\farcs04$	$160\fdg76 \pm 4\fdg17$	DG/FW
2	354445.941 (0.066)	3.5 (n/a)	11.3 (0.3)	$0\farcs75 \pm 0\farcs06 \times 0\farcs17 \pm 0\farcs04$	$163\fdg93 \pm 2\fdg37$	DG/FW
3	354459.437 (0.060)	6.6 (0.1)	20.9 (0.3)	$0\farcs48 \pm 0\farcs07 \times 0\farcs15 \pm 0\farcs09$	$163\fdg4 \pm 8\fdg68$	
4	354476.565 (0.077)	7.7 (0.2)	16.3 (0.3)	$0\farcs55 \pm 0\farcs11 \times 0\farcs18 \pm 0\farcs13$	$164\fdg71 \pm 10\fdg74$	
5	354525.266 (0.133)	9.1 (0.4)	28.4 (0.9)	$0\farcs67 \pm 0\farcs07 \times 0\farcs27 \pm 0\farcs07$	$16\fdg21 \pm 6\fdg54$	
6	354600.954 (0.115)	5.9 (0.2)	15.1 (0.5)	$0\farcs45 \pm 0\farcs11 \times 0\farcs22 \pm 0\farcs12$	$159\fdg46 \pm 23\fdg35$	
7	354607.968 (0.020)	3.8 (0.0)	16.6 (0.2)	$0\farcs53 \pm 0\farcs06 \times 0\farcs21 \pm 0\farcs06$	$166\fdg72 \pm 7\fdg83$	
8	354622.820 (0.046)	3.3 (0.1)	8.0 (0.2)	$0\farcs55 \pm 0\farcs14 \times 0\farcs23 \pm 0\farcs19$	$176\fdg44 \pm 19\fdg62$	
			HCN $J = 4 \rightarrow 3$			
9	356626.832 (0.029)	3.6 (0.1)	10.1 (0.1)	$0\farcs63 \pm 0\farcs10 \times 0\farcs25 \pm 0\farcs06$	$152\fdg83 \pm 8\fdg26$	
10	356661.534 (0.120)	7.5 (0.3)	7.6 (0.2)	$0\farcs62 \pm 0\farcs28 \times 0\farcs18 \pm 0\farcs14$	$161\fdg76 \pm 40\fdg95$	
11	356675.940 (0.048)	2.6 (0.1)	2.1 (0.1)	$0\farcs54 \pm 0\farcs27 \times 0\farcs17 \pm 0\farcs02$[a]	$132\fdg84 \pm 3\fdg98$[a]	
12	356686.392 (0.077)	3.0 (0.2)	2.5 (0.1)	$0\farcs45 \pm 0\farcs19 \times 0\farcs25 \pm 0\farcs06$[a]	$111\fdg21 \pm 14\fdg71$[a]	
13	356697.008 (0.066)	2.3 (0.1)	3.2 (0.1)	$0\farcs50 \pm 0\farcs26 \times 0\farcs26 \pm 0\farcs19$	$8\fdg34 \pm 37\fdg52$	
14	356705.677 (0.052)	2.4 (0.1)	3.3 (0.1)	$0\farcs34 \pm 0\farcs21 \times 0\farcs28 \pm 0\farcs19$	$175\fdg46 \pm 85\fdg37$	DG
15	356712.809 (0.046)	6.1 (0.1)	14.2 (0.2)	$0\farcs39 \pm 0\farcs13 \times 0\farcs29 \pm 0\farcs14$	$164\fdg22 \pm 58\fdg56$	DG
16	356723.385 (0.122)	2.9 (0.1)	7.6 (0.1)	$0\farcs58 \pm 0\farcs14 \times 0\farcs46 \pm 0\farcs14$	$23\fdg16 \pm 62\fdg77$	TG
17	356726.062 (0.122)	2.0 (0.1)	4.4 (0.1)	$0\farcs51 \pm 0\farcs11 \times 0\farcs22 \pm 0\farcs17$	$5\fdg11 \pm 17\fdg43$	TG
18	356729.280 (0.122)	1.9 (0.1)	3.2 (0.1)	$0\farcs46 \pm 0\farcs14 \times 0\farcs31 \pm 0\farcs19$	$42\fdg73 \pm 135\fdg22$	TG
19	356755.672 (0.073)	6.0 (0.2)	15.7 (0.4)	$0\farcs92 \pm 0\farcs11 \times 0\farcs27 \pm 0\farcs08$	$16\fdg96 \pm 4\fdg35$	TG
20	356761.861 (0.143)	3.1 (0.2)	3.9 (0.4)	$0\farcs47 \pm 0\farcs12 \times 0\farcs34 \pm 0\farcs15$	$30\fdg08 \pm 84\fdg25$	TG
21	356767.248 (0.127)	3.5 (0.3)	4.4 (0.3)	$0\farcs68 \pm 0\farcs25 \times 0\farcs28 \pm 0\farcs13$	$171\fdg58 \pm 30\fdg66$	TG
22	356796.284 (0.080)	4.9 (0.2)	17.5 (0.6)	$0\farcs66 \pm 0\farcs08 \times 0\farcs21 \pm 0\farcs07$	$175\fdg06 \pm 5\fdg86$	
23	356831.654 (0.036)	1.6 (0.1)	1.5 (0.1)	$0\farcs37 \pm 0\farcs24 \times 0\farcs21 \pm 0\farcs07$[a]	$53\fdg03 \pm 22\fdg59$[a]	DG
24	356834.872 (0.047)	3.2 (0.1)	3.9 (0.1)	$0\farcs43 \pm 0\farcs34 \times 0\farcs06 \pm 0\farcs26$	$170\fdg54 \pm 31\fdg33$	DG
			CS $J = 7 \rightarrow 6$			
25	342782.231 (0.120)	9.4 (0.3)	13.3 (0.3)	$0\farcs39 \pm 0\farcs17 \times 0\farcs06 \pm 0\farcs09$	$135\fdg37 \pm 25\fdg55$	
26	342935.064 (0.123)	3.7 (0.4)	10.7 (0.7)	$0\farcs54 \pm 0\farcs11 \times 0\farcs20 \pm 0\farcs14$	$167\fdg08 \pm 13\fdg99$	
27	342946.841 (0.083)	4.5 (0.2)	11.8 (0.4)	$0\farcs79 \pm 0\farcs14 \times 0\farcs40 \pm 0\farcs10$	$173\fdg42 \pm 12\fdg93$	

Table 4.5 (continued)

Line No.	Frequency [MHz]	Line Width [km s^{-1}]	Integrated Flux [K km s^{-1}]	Deconvolved FWHMs [arcsec]	PA [deg.]	Method[a]
28	342997.608 (0.072)	6.8 (0.2)	11.3 (0.3)	$0\farcs28 \pm 0\farcs18 \times 0\farcs12 \pm 0\farcs09$	$142\fdg82 \pm 24\fdg05$	
				$H^{13}CN$ $J = 4 \rightarrow 3$		
29	345132.485 (0.067)	3.5 (0.1)	11.2 (0.4)	$0\farcs52 \pm 0\farcs06 \times 0\farcs26 \pm 0\farcs05$	$164\fdg94 \pm 10\fdg2$	
30	345143.859 (0.108)	3.5 (n/a)	3.5 (0.1)	$0\farcs47 \pm 0\farcs23 \times 0\farcs08 \pm 0\farcs11$	$145\fdg08 \pm 30\fdg91$	DG/FW
31	345149.137 (0.086)	3.5 (n/a)	4.0 (0.1)	$0\farcs65 \pm 0\farcs19 \times 0\farcs03 \pm 0\farcs13$	$154\fdg56 \pm 9\fdg46$	DG/FW
32	345162.016 (0.164)	8.7 (0.4)	7.7 (0.3)	$0\farcs31 \pm 0\farcs17 \times 0\farcs07 \pm 0\farcs27$	$16\fdg09 \pm 62\fdg29$	
33	345179.918 (0.313)	12.1 (0.6)	9.8 (0.4)	$0\farcs38 \pm 0\farcs08 \times 0\farcs26 \pm 0\farcs03$[a]	$160\fdg0 \pm 12\fdg82$[a]	
34	345209.918 (0.244)	5.4 (0.2)	7.5 (0.2)	$0\farcs46 \pm 0\farcs12 \times 0\farcs14 \pm 0\farcs09$	$166\fdg95 \pm 17\fdg18$	TG
35	345219.314 (0.244)	4.7 (0.2)	3.7 (0.2)	$0\farcs56 \pm 0\farcs12 \times 0\farcs30 \pm 0\farcs04$[a]	$10\fdg47 \pm 7\fdg2$[a]	TG
36	345227.487 (0.244)	5.1 (0.2)	5.8 (0.2)	$0\farcs51 \pm 0\farcs14 \times 0\farcs24 \pm 0\farcs10$	$142\fdg58 \pm 22\fdg79$	TG
37	345235.814 (0.244)	1.8 (0.2)	1.9 (0.2)	$0\farcs36 \pm 0\farcs22 \times 0\farcs27 \pm 0\farcs18$	$89\fdg92 \pm 86\fdg65$	DG
38	345238.350 (0.244)	1.6 (0.2)	1.6 (0.2)	$0\farcs55 \pm 0\farcs24 \times 0\farcs25 \pm 0\farcs18$	$125\fdg19 \pm 79\fdg34$	DG
39	345246.534 (0.227)	10.8 (0.7)	9.6 (0.5)	$0\farcs45 \pm 0\farcs19 \times 0\farcs37 \pm 0\farcs31$	$80\fdg18 \pm 84\fdg75$	
40	345257.273 (0.169)	5.5 (0.5)	5.4 (0.3)	$0\farcs78 \pm 0\farcs15 \times 0\farcs32 \pm 0\farcs03$[a]	$164\fdg72 \pm 4\fdg37$[a]	
41	345283.154 (0.081)	4.6 (0.2)	9.2 (0.3)	$0\farcs45 \pm 0\farcs09 \times 0\farcs24 \pm 0\farcs08$	$159\fdg98 \pm 20\fdg63$	DG
42	345286.337 (0.051)	1.1 (0.1)	1.2 (0.2)	$0\farcs58 \pm 0\farcs09 \times 0\farcs33 \pm 0\farcs03$[a]	$164\fdg57 \pm 6\fdg85$[a]	DG
43	345295.184 (0.032)	3.6 (0.1)	6.7 (0.1)	$0\farcs56 \pm 0\farcs11 \times 0\farcs14 \pm 0\farcs06$	$157\fdg86 \pm 8\fdg35$	DG
44	345300.725 (0.052)	2.9 (0.1)	3.2 (0.1)	$0\farcs54 \pm 0\farcs10 \times 0\farcs29 \pm 0\farcs03$[a]	$157\fdg73 \pm 6\fdg49$[a]	DG
45	345306.003 (0.325)	3.5 (n/a)	3.7 (0.4)	$0\farcs57 \pm 0\farcs21 \times 0\farcs24 \pm 0\farcs16$	$143\fdg29 \pm 33\fdg65$	FW
46	345319.304 (0.113)	3.5 (n/a)	12.8 (0.5)	$0\farcs52 \pm 0\farcs05 \times 0\farcs18 \pm 0\farcs06$	$168\fdg3 \pm 6\fdg29$	DG/FW
47	345324.737 (0.337)	3.5 (n/a)	4.8 (0.5)	$0\farcs44 \pm 0\farcs06 \times 0\farcs30 \pm 0\farcs03$[a]	$147\fdg78 \pm 9\fdg86$[a]	DG/FW
48	345398.605 (0.056)	3.6 (0.1)	8.0 (0.2)	$0\farcs48 \pm 0\farcs09 \times 0\farcs18 \pm 0\farcs08$	$156\fdg98 \pm 11\fdg65$	
49	345406.474 (0.000)	3.5 (n/a)	4.2 (0.2)	$0\farcs48 \pm 0\farcs07 \times 0\farcs34 \pm 0\farcs03$[a]	$158\fdg65 \pm 11\fdg42$[a]	DG/FW/FC
50	345410.505 (0.062)	3.5 (n/a)	6.1 (0.2)	$0\farcs39 \pm 0\farcs11 \times 0\farcs21 \pm 0\farcs14$	$165\fdg46 \pm 28\fdg93$	DG/FW
51	345444.943 (0.065)	2.1 (0.2)	4.2 (0.5)	$0\farcs51 \pm 0\farcs09 \times 0\farcs21 \pm 0\farcs10$	$172\fdg77 \pm 13\fdg21$	DG
52	345448.786 (0.405)	6.9 (0.6)	7.3 (0.8)	$0\farcs44 \pm 0\farcs17 \times 0\farcs27 \pm 0\farcs19$	$108\fdg81 \pm 67\fdg36$	DG
53	345459.960 (0.127)	5.1 (0.3)	6.8 (0.3)	$0\farcs43 \pm 0\farcs05 \times 0\farcs39 \pm 0\farcs05$[a]	$53\fdg47 \pm 54\fdg24$[a]	
54	345466.713 (0.147)	3.5 (n/a)	6.9 (0.3)	$0\farcs42 \pm 0\farcs10 \times 0\farcs25 \pm 0\farcs16$	$7\fdg53 \pm 29\fdg13$	FW
55	345473.520 (0.085)	3.5 (n/a)	4.0 (0.1)	$0\farcs30 \pm 0\farcs13 \times 0\farcs22 \pm 0\farcs11$	$18\fdg0 \pm 85\fdg98$	DG/FW
56	345477.958 (0.131)	3.5 (n/a)	2.6 (0.1)	$0\farcs50 \pm 0\farcs11 \times 0\farcs24 \pm 0\farcs02$[a]	$115\fdg56 \pm 4\fdg91$[a]	DG/FW

Table 4.5 (continued)

Line No.	Frequency [MHz]	Line Width [km s^{-1}]	Integrated Flux [K km s^{-1}]	Deconvolved FWHMs [arcsec]	PA [deg.]	Method[a]
57	345485.493 (0.422)	2.7 (0.7)	4.0 (1.2)	$0\farcs33 \pm 0\farcs10 \times 0\farcs11 \pm 0\farcs17$	$16\fdg0 \pm 35\fdg58$	TG
58	345488.343 (0.375)	2.2 (0.8)	2.6 (1.4)	$0\farcs43 \pm 0\farcs15 \times 0\farcs21 \pm 0\farcs16$	$17\fdg49 \pm 33\fdg47$	TG
59	345492.056 (0.344)	3.0 (0.6)	2.9 (0.6)	$0\farcs51 \pm 0\farcs10 \times 0\farcs41 \pm 0\farcs07$[a]	$52\fdg49 \pm 30\fdg88$[a]	TG
60	345509.462 (0.067)	4.9 (0.1)	10.0 (0.2)	$0\farcs29 \pm 0\farcs09 \times 0\farcs15 \pm 0\farcs09$	$1\fdg13 \pm 33\fdg02$	
61	345546.657 (0.062)	3.9 (0.1)	3.8 (0.1)	$0\farcs47 \pm 0\farcs21 \times 0\farcs05 \pm 0\farcs16$	$159\fdg85 \pm 33\fdg31$	
62	345570.537 (0.100)	3.3 (0.2)	3.9 (0.2)	$0\farcs48 \pm 0\farcs09 \times 0\farcs31 \pm 0\farcs04$[a]	$150\fdg65 \pm 11\fdg41$[a]	

[a]One (or both) of the fitted FWHM is smaller than the beam size. The fitted convolved sizes are shown instead. Such situation is typical for weak lines close to 3σ

The uncertainty of line width are shown inside the prentice when the line width remains flexible for the fitting.

4.5.2 Line Identification

We use SPLATALOGUE[2] to identify the species for those detected lines, and further test those identifications by modeling the spectra with XCLASS (Möller et al., 2017). A simple search for line identification in SPLATALOGUE with a given range of frequency would result in many identifications, where not all of them are applicable due to high upper energy, low Einstein-A value, or their rare abundance in the protostellar environment. The line identification is an iterative process. We started from the strong and less contaminated lines, and verified those identifications with the synthetic spectra. Before assigning the molecular species, we set up a few guidelines to secure the most likely identification inspired by Snyder et al. (2005).

- *Rest frequency*: The identified transition has to have its rest frequency measured in laboratory or calculated to have an uncertainty at least on the order of 1 part in 10 million, corresponding to $\sim$0.04 MHz for our data.
- *Frequency agreement*: To assign a robust identification from the selected possible transitions, the assigned transition needs to agree with the observed line within the half width at half maximum of the line.
- *Relative intensity*: After a transition is assigned, the relative strengths of all other transitions for the identified molecules need to match with the observation.

We start our line identification from the strongest lines with the least amount of contamination. For each line, we search for all possible transitions within a certain frequencies and a maximum upper energy of 1000 K. Then, we test each transition from the lowest upper energy with XCLASS using a fiducial model that has an excitation temperature of 100 K, a line width of 3.5 km s^{-1}, and an arbitrary column density. The synthetic spectra first confirm the frequency agreement between the transition and the observed line and secondly verify that the relative strengths all transitions of the selected molecule match the observation. Table 4.6 shows the result of the line identifications

[2]http://www.splatalogue.net/

Table 4.6: Line Identification

Line No.	Formula	Name	Frequency (MHz)	Transition[a]	Einstein-A[b]	E_u (K)
9	CH_3OH	Methanol	356626.667(0.016)	[J, K]= [23, 4]→[22, 5]	8.041(-5)	727.83
29	$^{13}CH_3OH$	Methanol	345132.599(0.05)	[4, 0, 4]→[3, 1, 3]	8.239(-5)	35.76
2	$^{13}CH_3OH$	Methanol	354445.95(0.05)	[4, 1, 3]→[3, 0, 3]	1.274(-4)	43.71
13	CH_2DOH	Methanol	356697.9372(0.0099)	[9, 2, 8]→[9, 0, 9]	3.536(-6)	131.85
22	CH_2DOH	Methanol	356796.1421(0.0034)	[8, 6, 3]→[7, 6, 2]	6.277(-5)	234.12
22	CH_2DOH	Methanol	356796.1421(0.0034)	[8, 6, 2]→[7, 6, 1]	6.277(-5)	234.12
48	CH_2DOH	Methanol	345398.9037(0.0112)	[16, 2, 14]→[15, 3, 13]	4.275(-5)	310.21
26	CH_2DOH	Methanol	342935.6452(0.0118)	[17, 2, 16]→[17, 1, 17]	1.227(-4)	342.83
46	CH_3OD[b]	Methanol	345319.587(0.359)	[J, K, parity]=[8, 2, −]→[8, 1, +]	8.1 ($\mu^2\Sigma S$)	100.14
54	CH_3OCHO	Methyl formate	345465.3445(0.0023)	[16, 13, 4]→[16, 12, 5], Sym=E	2.513(-5)	192.32
7	CH_3OCHO	Methyl formate	354608.0913(0.003)	[33, 0, 33]→[32, 1, 32]	1.097(-4)	293.10
7	CH_3OCHO	Methyl formate	354608.0919(0.003)	[33, 1, 33]→[32, 1, 32]	6.792(-4)	293.10
7	CH_3OCHO	Methyl formate	354608.0923(0.003)	[33, 0, 33]→[32, 0, 32]	6.792(-4)	293.10
7	CH_3OCHO	Methyl formate	354608.0928(0.003)	[33, 1, 33]→[32, 0, 32]	1.097(-4)	293.10
53	CH_3OCHO	Methyl formate	345461.011(0.1)	[28, 13, 15]→[27, 13, 14], Sym=E	4.94(-4)	351.85
58	CH_3OCHO	Methyl formate	345486.602(0.1)	[28, 13, 16]→[27, 13, 15], Sym=E	4.941(-4)	351.85
15	CH_3OCHO	Methyl formate	356711.841(0.1)	[29, 17, 12]→[28, 17, 11]	4.561(-4)	448.21
15	CH_3OCHO	Methyl formate	356711.841(0.1)	[29, 17, 13]→[28, 17, 11]	4.561(-4)	448.21
32	CH_3OCHO $v = 1$	Methyl formate	345162.544(0.1)	[11, 8, 3]→[10, 7, 3], Sym=E	7.091(-5)	269.30
31	CH_3OCHO $v = 1$	Methyl formate	345148.04(0.1)	[28, 6, 23]→[27, 6, 22], Sym=A	5.947(-4)	451.66
12	CH_3OCHO $v = 1$	Methyl formate	356686.906(0.1)	[29, 6, 24]→[28, 6, 23]	6.584(-4)	468.78
55	CH_3OCHO $v = 1$	Methyl formate	345473.217(0.1)	[28, 9, 19]→[27, 9, 18], Sym=E	5.626(-4)	480.66
60	CH_3OCHO $v = 1$	Methyl formate	345510.004(0.1)	[28, 9, 20]→[27, 9, 19], Sym=A	5.635(-4)	480.51
61	CH_3OCHO $v = 1$	Methyl formate	345571.314(0.1)	[27, 5, 22]→[26, 5, 21], Sym=E	6.055(-4)	480.80
39	CH_3OCHO $v = 1$	Methyl formate	345248.21(0.1)	[28, 10, 19]→[27, 10, 18], Sym=E	5.481(-4)	492.90
5	CH_3CHO $v_t = 1$	Acetaldehyde	354522.7114(0.1995)	[6, 6, 1]→[7, 5, 3]	3.184(-6)	304.34
3	CH_3CHO $v_t = 1$	Acetaldehyde	354457.6646(0.0409)	[18, 2, 16]→[17, 2, 15]	1.585(-3)	374.97
25	CH_3COCH_3	Acetone	342780.0361(0.0357)	[17, 17, 0]→[16, 16, 1]	1.85(-3)	47.05
25	CH_3COCH_3	Acetone	342780.0345(0.0357)	[17, 17, 1]→[16, 16, 0]	1.85(-3)	147.05
40	CH_3COCH_3	Acetone	345256.0368(0.0368)	[18, 15, 4]→[17, 14, 3]	1.287(-3)	150.83
45	CH_3COCH_3	Acetone	345305.3651(0.0367)	[18, 15, 3]→[17, 14, 4]	1.288(-3)	150.83

Table 4.6 (continued)

Line No.	Formula	Name	Frequency (MHz)	Transition[a]	Einstein-A[b]	E_u (K)
11	CH_3COCH_3	Acetone	356675.1969(0.0814)	[19, 13, 6]→[18, 12, 7]	6.123(-4)	157.74
10	CH_3COCH_3	Acetone	356658.4123(0.0187)	[27, 10, 17]→[26, 11, 16], Sym=EA	1.215(-3)	274.98
10	CH_3COCH_3	Acetone	356658.4780(0.0187)	[27, 11, 17]→[26, 10, 16], Sym=EA	1.215(-3)	274.98
10	CH_3COCH_3	Acetone	356658.5351(0.0184)	[27, 10, 17]→[26, 11, 16], Sym=AE	1.215(-3)	274.98
10	CH_3COCH_3	Acetone	356658.6016(0.0184)	[27, 11, 17]→[26, 10, 16], Sym=AE	1.215(-3)	274.98
18	CH_3COCH_3	Acetone	356729.9828(0.0153)	[27, 10, 17]→[26, 11, 16], Sym=EE	1.215(-3)	275.00
14	CH_3OCH_3	Dimethyl ether	356705.204(0.004)	[8, 4, 4]→[7, 3, 5], Sym=AE	9.249(-5)	55.27
15	CH_3OCH_3	Dimethyl ether	356712.951(0.002)	[8, 4, 5]→[7, 3, 5], Sym=EE	6.255(-5)	55.27
16	CH_3OCH_3	Dimethyl ether	356724.457(0.003)	[8, 4, 4]→[7, 3, 5], Sym=AA	2.095(-4)	55.27
16	CH_3OCH_3	Dimethyl ether	356724.864(0.003)	[8, 4, 5]→[7, 3, 5], Sym=AE	1.17(-4)	55.27
33	C_2H_5OH	gauche-Ethanol	345173.9493(0.0112)	[J, K_a, K_c, v_t]=[7, 7, 1(0), 0]→[6, 6, 1(0), 1][c]	2.515(-4)	139.90
36	C_2H_5OH	gauche-Ethanol	345229.238(0.05)	[J, K_a, K_c, v_t]=[21, 1, 21, 0]→[20, 1, 20, 0]	3.728(-4)	241.55
43	C_2H_5OH	gauche-Ethanol	345295.3553(0.0022)	[J, K_a, K_c, v_t]=[21, 1, 21, 1]→[20, 1, 20, 1]	3.731(-4)	246.22
49/50	C_2H_5OH	gauche-Ethanol	345408.1651(0.0022)	[J, K_a, K_c, v_t]=[21, 0, 21, 1]→[20, 0, 20, 1]	3.743(-4)	246.21
19	SO_2	Sulfur dioxide	356755.1899(0.0014)	[10, 4, 6]→[10, 3, 7]	3.281(-4)	89.83
27	H_2CS	Thioformaldehyde	342946.4239(0.0500)	[10, 0, 10]→[9, 0, 9]	6.08(-4)	90.59
3	HCN $v_2 = 1$	Hydrogen cyanide	354460.4346(0.0007)	J=4→3	1.869(-3)	1066.90
20	$CH_3C^{15}N$	Methyl cyanide	356761.0470(0.002)	[J, K]=[20, 1]→[19, 1]	3.962(-3)	186.97
4	CH_3CH_2CN	Ethyl cyanide	354476.6596(0.0015)	[40, 3, 38]→[39, 3, 37]	3.767(-3)	361.47
			Tentative identifications			
5	CH_3NH_2	Methylamine	354528.4832(0.0057)	[Sym, J, K]=[B_2, 8, 2]→[B_1, 7, 2]	2.156(-5)	92.76
6	CH_3NH_2	Methylamine	354600.5152(29.979)	[Sym, J, K]=[B_2, 8, 5]→[B_1, 7, 5]	1.399(-5)	174.05
6	CH_3NH_2	Methylamine	354600.5152(29.979)	[Sym, J, K]=[B_1, 8, 5]→[B_2, 7, 5]	1.399(-5)	174.05
6	CH_3NH_2	Methylamine	354600.5152(29.979)	[Sym, J, K]=[B_1, 8, 6]→[B_2, 7, 6]	1.016(-5)	216.84
6	CH_3NH_2	Methylamine	354600.5152(29.979)	[Sym, J, K]=[B_2, 8, 6]→[B_1, 7, 6]	1.016(-5)	216.84
49/50	CH_3Cl	Methyl chloride	345408.9874(0.0023)	[J, K, F]=[13, 3, 12.5]→[12, 3, 11.5]	7.764(-4)	183.47

[a]The typical quantum numbers are listed as [J, K_a, K_c] unless specified.

[b]The number in the prentice indicates the power of ten (e.g. 8.041(-5) represents 8.041×10^{-5}).

[c]Anderson et al. (1988).

[d]Two degenerate transitions occur for K_c=1 → 1 and 0 → 0.

After all identifications were confirmed with the synthetic spectra, we used XLCASS to fit the excitation temperature and column density for those identified species. With only limited transitions covered in our observation, the fitting with XCLASS provides a more rigorous identification and estimates of the excitation temperature and column density instead of an precise model of the identified molecules. To reduce the degeneracy as our observation only covers a few transitions for each species, we fix the excitation temperature to 100 K, and allow the column density to vary over two orders of magnitude around the best-fitted value. We assume a source size of $0\farcs5$ at the center and a line width of 3.5 km s^{-1} for all species. All of the identified species are modeled with XCLASS except CH_3OD, identified with the calculation in Anderson et al. (1988) and is not included in the database of XCLASS. The fitting successfully reproduces the observed spectra, except for the spectra of CH_3NH_2, which predicts an undetected emission line at 345520 MHz. The stronger lines of CH_3NH_2 are weighted more highly in the fitting routine, resulting in a smaller χ^2 despite the prediction of an unseen line. Thus, we decrease the temperature of CH_3NH_2 to 70 K to reduce the emission at 345520 MHz, and categorize CH_3NH_2 as a tentative identification (Section 4.5.4). Figure 4.22 shows the corrected synthetic spectra compared with the observation, and Table 4.3 summarizes the properties of each identified species along with its abundance relative to the total molecular gas column density, derived from the updated continuum model with an aperture of the deconvolved continuum size ($0\farcs35\times0\farcs28$).

4.5.3 Identified COMs

O-bearing molecules

Methanol (CH_3OH): We identified several emission lines of methanol and its isotopologues, including CH_3OH, $^{13}CH_3OH$, CH_2DOH, and CH_3OD. Line 27 is consistent with the emission of CH_3OD measured by Anderson et al. (1988), which is not included in SPLATALOGUE, thus not shown in Figure 4.22. The detection of CH_3OD toward IRAS 16293−2422 supports this identification at protostellar environment (Parise et al., 2002). If we exclude Line 2 and Line 46, which either is blended with an unidentified line or has its line width fixed during the line fitting, the mean width of methanol and its isotopologues is 3.7±0.2 km s^{-1}.

Table 4.7: Identified COMs and other species

Species	Formula	No. of lines	Column density	Abundance to $\mathcal{N}_{H_2}$
Hydrogen cyanide	HCN $v_2 = 1$	1	3.6×10^{17}	2.1×10^{-6}
Methyl formate	CH_3OCHO $v = 0$	4	8.0×10^{15}	4.7×10^{-8}
Methyl formate ($v_t = 1$)	CH_3OCHO $v_t = 1$	7	7.1×10^{16}	4.2×10^{-7}
Acetaldehyde	CH_3CHO $v_{15} = 1$	2	1.3×10^{16}	7.6×10^{-8}
Methanol	CH_3OH $v_t = 0$	1	1.8×10^{18}	1.1×10^{-5}
Methanol	CH_2DOH $v_t = 0$	3	5.5×10^{16}	3.2×10^{-7}
Methanol	$^{13}CH_3OH$ $v_t = 0$	2	9.9×10^{15}	5.8×10^{-8}
Methanol	CH_3OD	1	...	...
Sulfur dioxide	SO_2 $v = 0$	1	1.5×10^{15}	8.8×10^{-9}
Dimethyl ether	CH_3OCH_3 $v = 0$	3	1.0×10^{16}	5.9×10^{-8}
gauche-Ethanol	C_2H_5OH $v = 0$	5	6.4×10^{15}	3.8×10^{-8}
Ethyl Cyanide	C_2H_5CN $v = 0$	2	2.3×10^{15}	1.3×10^{-8}
Thioformaldehyde	H_2CS $v = 0$	1	7.7×10^{14}	4.5×10^{-9}
Acetone	CH_3COCH_3 $v = 0$	5	4.9×10^{15}	2.9×10^{-8}
Methyl cyanide	$CH_3C^{15}N$	2	5.1×10^{13}	3.0×10^{-10}
Tentative identification				
Methylamine[a]	CH_3NH_2 $v = 0$	2	3.4×10^{16}	1.3×10^{-7}
Methyl chloride	$CH_3{}^{35}Cl$	1	1.4×10^{14}	6.2×10^{-10}

[a]The excitation temperature of methylamine is lowered from 104 K to 70 K to match the observation.
The gas column density within a 0.5″ radius beam is 1.7×10^{23} cm^{-2}.

Figure 4.23 shows the morphology of methanol and its isotopologues. Excluding the offset emission at Line 2 (see Section 4.4.3), all isotopologues of methanol (4 of 7 methanol emission, Line 9, 29, 22, and 46) extends in the north-south direction. The other three lines peak at the north of the continuum source with extended emission toward south, except for Line 13.

Methyl formate (CH_3OCHO): We identify methyl formate in both the ground state and its first torsional excited state. The model reproduces the emission of the strongest ground state methyl formate (Line 7), but underestimates the emission of Line 15, 53, 54, and 57. The emission of the vibrationally excited methyl formate matches Line 12, 31, 39, 55, 60, and 62. A more detailed model dedicated to methyl formate may better constrain its properties.

Figure 4.24 shows the morphology of methyl formate in both ground state and the vibrational excited state. One of the ground state transitions (Line 7) peaks both north and south of the continuum source, while another ground state transition (Line 15) peaks at the center with extended emission toward north. The rest of the methyl formate transitions (10 of 12) have a compact emission peaked at the center.

Acetaldehyde (CH_3CHO): The torsionally excited acetaldehyde contributes to Line 3 and 5; however, both lines have complex line profiles due to blending. Together

with the emission of HCN $v_2 = 1$, the model of acetaldehyde reproduces the width of Line 3. But for Line 5, the combined profile of acetaldehyde and methylamine, which is a tentative identification, underestimates the emission at lower frequency. Line 3 appears as a compact source centered on the continuum source, while Line 5 has more extended emission toward south with a peak at the center (Figure 4.25).

Acetone (CH_3COCH_3): Line 25 provides the strongest constraint on the properties of acetone, which also matches Line 11, 18, 40, and 45. The emission of acetone also appears at Line 10, 23 and 24, but the predicted strengths are much weaker than the observation. Acetone emits from a compact region with a size of the continuum at the center (Figure 4.25).

Dimethyl ether (CH_3OCH_3): The emission of dimethyl ether matches Line 16, which also contributes to a small fraction of Line 14 and 15. All transitions of dimethyl ether peak at the center with an irregular overall morphology (Figure 4.25).

Ethanol (C_2H_5OH): We identify gauche-ethanol from our observation. Gauche-ethanol is a conformer of ethanol, where the hydrogen of the OH group points toward hydrogens of the methyl group. The gauche form dominates in the gas phase because of its twofold degeneracy (Scheiner & Seybold, 2009). Moreover, the transitions of gauche-ethanol has lower upper energies, compared to ∼1000 K for trans-ethanol. Our model of gauche-ethanol matches Line 33, 36, 43, 49/50, as well as the red wing of the $H^{13}CN$ $J = 4 \rightarrow 3$ line. Line 49 and 50 heavily blend with each other, and the peak frequency of gauche-ethanol lies between the two identified peaks. The identified gauche-ethanol emission shows a compact feature peaked at the center (Figure 4.26).

N-bearing molecules

Hydrogen cyanide (HCN $v_2 = 1$): Together with the torsional excited acetaldehyde, the emission of hydrogen cyanide from a vibrational excited state ($v_2 = 1$) successfully reproduces Line 3, which is significantly broader than other lines.

Methyl cyanide ($CH_3C^{15}N$): Our model of the isotopologue of methyl cyanide, $CH_3C^{15}N$, matches Line 20 and the blue wing of the HCO^+ $J = 4 \rightarrow 3$ line. The extended emission of $CH_3C^{15}N$ peaks at the south of the continuum source (Figure 4.27). While the low isotope ratio of $^{15}N/^{14}N$ in the solar system, ∼440 (Caselli & Ceccarelli, 2012), questions the identification of $CH_3C^{15}N$; that isotopologue has been detected toward IRAS 16293−2422 (Calcutt et al., 2018). Our observations do not cover the frequencies of CH_3CN to investigate the ratio of $^{15}N/^{14}N$.

Ethyl cyanide (CH_3CH_2CN): The emission of ethyl cyanide contributes to Line 4 as

well as the unlabelled feature at the lower frequency end of Line 22. At Line 4, the emission of ethyl cyanide appears to be compact around the center (Figure 4.27).

S-bearing molecules

Sulfur dioxide (SO_2): Line 19 agrees with the emission of sulfur dioxide, which blends with $CH_3C^{15}N$ in its blue wing. The emission of SO_2 extends over a $1''\times1''$ region, more than other identified complex molecules, peaking at both north and south sides of the continuum source (Figure 4.27).

Thioformaldehyde (H_2CS): The emission of thioformaldehyde agrees with Line 27. The emission of H_2CS has a morphology similar to that of SO_2, which is more extended than other molecules (Figure 4.27).

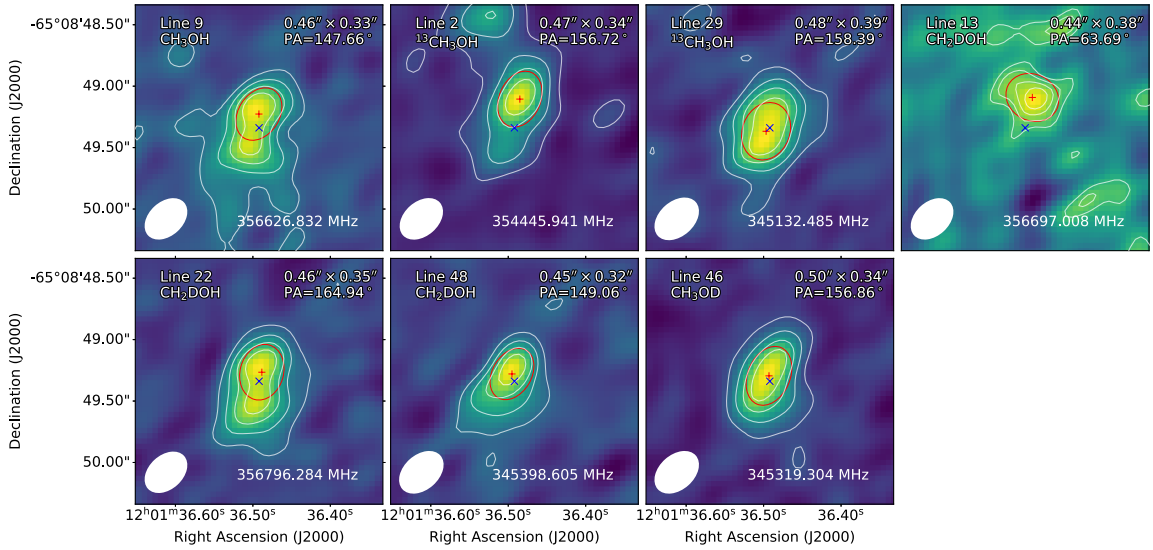

Figure 4.23: The moment 0 maps of methanol and its isotopologues ($^{13}CH_3OH$, CH_2DOH, and CH_3OD), calculated with a line width of 3.5 km s^{-1}. The white contours show the emission from the maximum to 3σ level. The red contour indicates the fitted size of the half power beam width (HPBW). The red cross shows the center of the fitted profile, while the blue "×" indicates the peak of the continuum emission.

4.5.4 Tentative Identifications

Methylamine (CH_3NH_2): The emission of methylamine agrees with the blue wing of Line 5 and contributes to Line 6. The fitting result from XCLASS has an excitation temperature of 104 K to match both Line 5 and 6, but it overestimates the line at ∼345520 MHz, which the observation shows no significant emission line. Thus, we

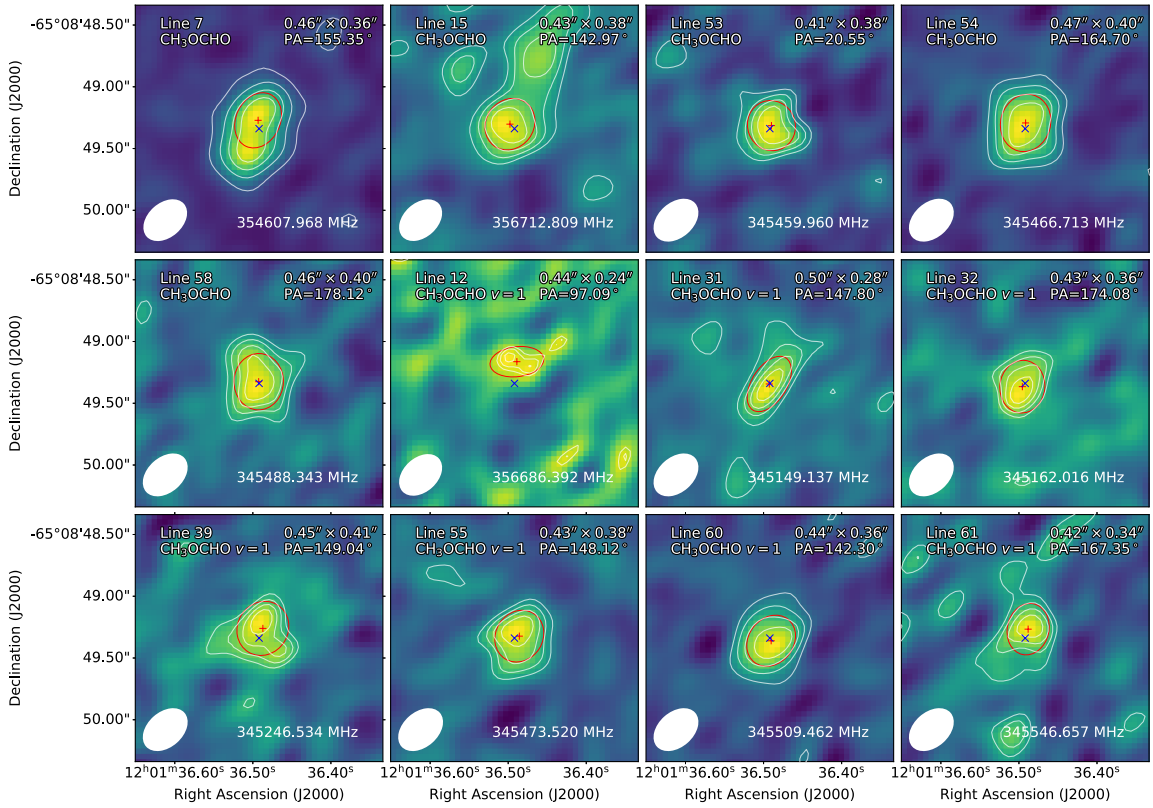

Figure 4.24: The same moment 0 maps as Figure 4.23 but for methyl formate.

decrease the temperature to 70 K so that the emission at ∼345520 MHz is consistent with the observation, whereas this model underestimates Line 6. Methylamine is rarely detected toward protostellar sources. Sgr B2 and Orion show the emission of methylamine from single dish observations (Fourikis et al., 1974; Kaifu et al., 1974); however, recent searches of methylamine with more sensitive interferometers find only upper limits (Ligterink et al., 2015, 2018). Thus, we categorize methylamine as a tentative identification before future observations unambiguously confirm this identification.

Methyl Chloride (CH_3Cl): Gauche-ethanol alone cannot fully describe the strength of the blended Line 49 and 50 (hereafter Line 49/50). The emission of methyl chloride matches the missing line at Line 49/50, but it also contributes to ∼345435 MHz, which is consistent with the data, and Line 52 and 53. While the predicted emission at Line 52 and 53 matches the data within the uncertainty, no clear observed feature can unambiguously confirm the identification of methyl chloride.

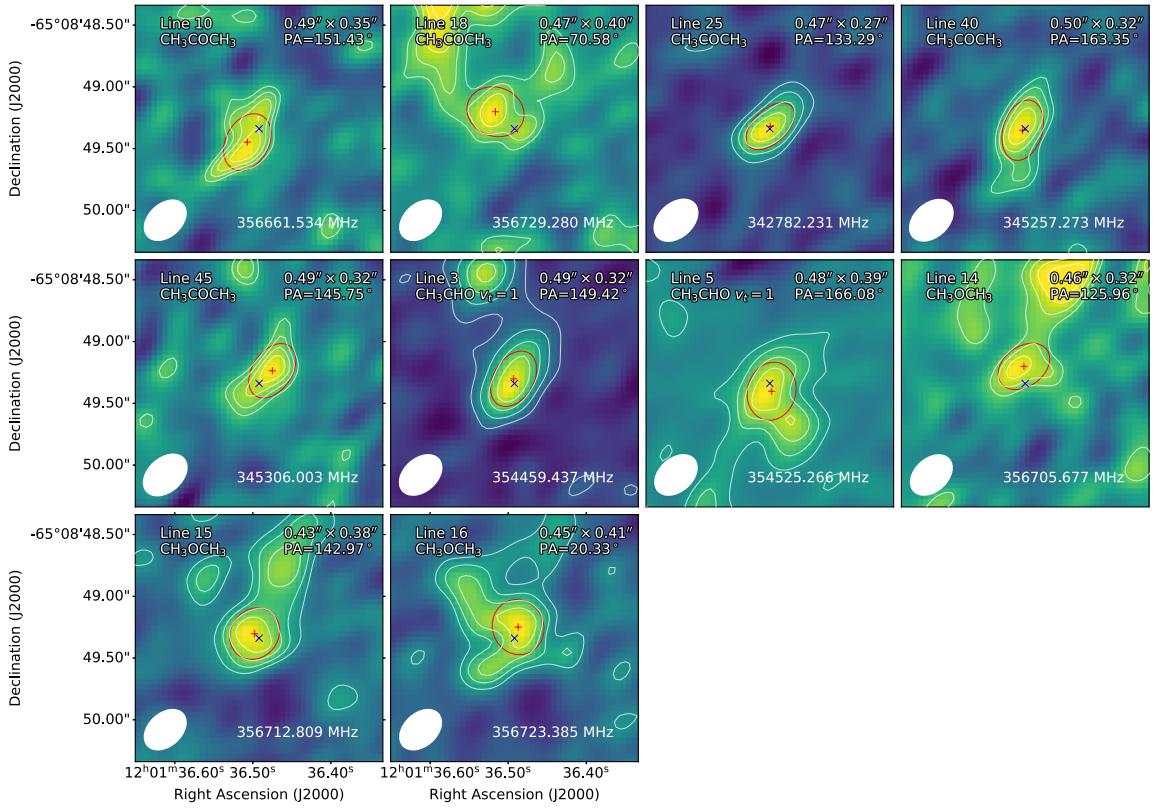

Figure 4.25: The same moment 0 maps as Figure 4.23 but for acetone, acetaldehyde, and dimethyl ether.

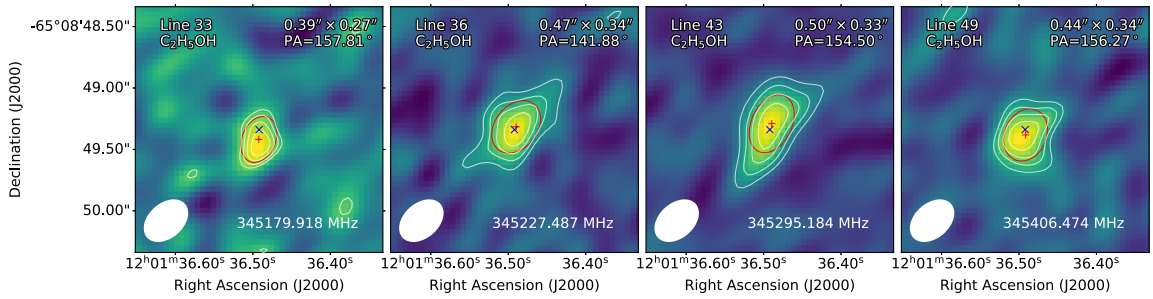

Figure 4.26: The same moment 0 maps as Figure 4.23 but for gauche-ethanol.

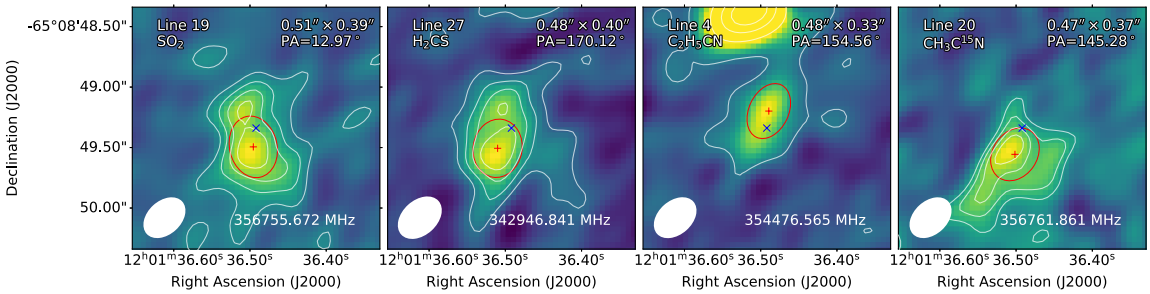

Figure 4.27: The same moment 0 maps as Figure 4.23 but for sulfur-bearing molecules, SO_2 and H_2CS, and complex cyanides, $CH_3C^{15}N$ and C_2H_5CN.

4.5.5 The Kinematics Traced by COMs

Figure 4.28 shows the moment 1 maps of a selection of unblended COM emission, suggesting a velocity gradient in the west-east direction from blue-shifted to red-shifted, consistent with the velocity gradient of seen in the emission of $C^{18}O$ (Tobin et al., 2019). Two of the COM emission lines, $^{13}CH_3OH$ at 354608.0 MHz and CH_3OCHO at 345132.5 MHz, show the most clear velocity gradient, allowing further analyses with PV diagrams. We further analyze this velocity gradient with position-velocity (PV) diagrams (Figure 4.29).

PV diagrams provide another view of the velocity structure of the infalling envelope in addition to the LOS velocity field toward the center, which we discussed extensively in Section 4.4.2. The morphology of PV diagrams best represent the velocity field with the emission of optically thin transitions that is free of absorption. Thus, we focus on the emission of complex organic molecules for PV diagrams analyses, assuming that the emission of COMs is optically thin due to their low column density. We construct the PV diagrams along a slice perpendicular to the outflow direction (north to south, Bourke et al., 1997; Parise et al., 2006c) to minimize the contamination from the outflows.

We test the PV diagrams against a pure Keplerian rotation model and a rotating infalling envelope that conserves angular momentum (Ohashi et al., 1997; Sakai et al., 2014). A pure Keplerian rotating disk would result in blue-shifted velocities only at the east and red-shifted velocities only at the west, whereas we see both red-shifted and blue-shifted velocities at both sides of the source along the direction perpendicular to the outflows (Figure 4.29). Sakai et al. (2014) apply the rotating infalling envelope model that simply follows the conservation of angular momentum as gas infalls Ohashi

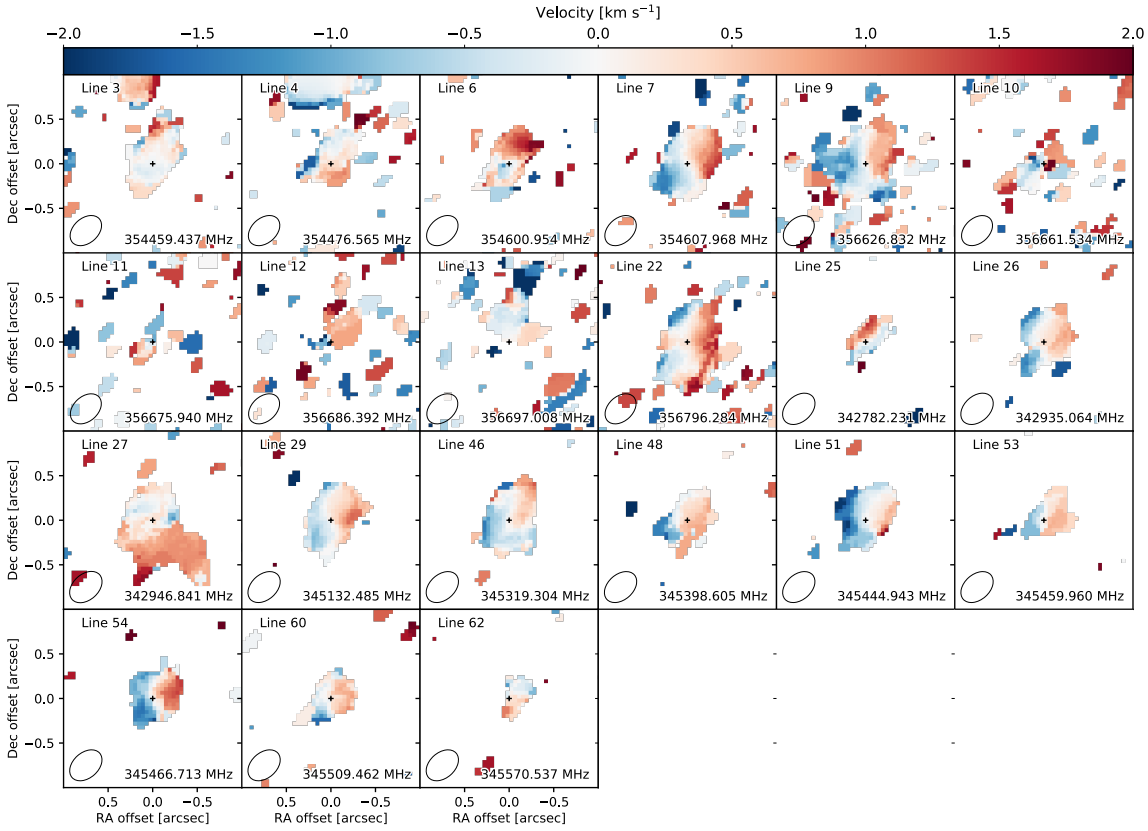

Figure 4.28: The moment 1 maps of the unblended COM emission, calculated with a 4 km s^{-1} window centered at the source velocity.

et al. (1997) to constrain the kinematics at ∼100 au. The kinematics become pure rotation when all of its energy converted into the rotation at the inner radius. At large radii, infall dominates the gas kinematics which also has small rotation. Thus, the red-shifted emission from the foreground infalling envelope at the blue-shifted side of the inner rotating disk results in both blue-shifted and red-shifted emission appearing in the PV diagrams at both sides of the source.

The rotating infalling envelope model can be described analytically. We briefly introduce the model here. We can write the velocity in r and θ components as

$$v_{\rm r} = \sqrt{\frac{2GM}{r} - \left(\frac{j}{r}\right)^2} \text{ and } v_\theta = \frac{j}{r}, \tag{4.9}$$

considering only the gravitational force and the conservation of angular momentum, where M is the mass of the central protostar, $j = L/m$ is the specific angular momentum, and r is the radius to the center. The velocity structure of the rotating collapsing

envelope can then be described as a function of the impact parameter (b) and the distance to the center of the source along the LOS (y), such as $v(b, y) = v_\theta \frac{b}{r} - v_\mathrm{r} \frac{y}{r}$. The maximum LOS velocity occurs when observed at the offset where gas is purely rotating, which can be described as

$$v_{\mathrm{max,LOS}} = \sqrt{\frac{2GM}{r}}. \tag{4.10}$$

Sakai et al. (2014) describe this radius as "the centrifugal barrier" where material cannot fall further inward, which can be described as

$$r_{\mathrm{cb}} = \frac{j^2}{2GM}. \tag{4.11}$$

We compare the observed PV diagrams with the maximum and minimum velocities, the boundaries on the PV diagrams, of the rotating collapsing envelope model, determined by L/m and M (Equation 4.9). We further fix the mass to the infallen mass ($\dot{M}t_{\mathrm{age}}$) from our best-fitting TSC model, 0.18 $\mathrm{M}_\odot$. The specific angular momentum determines the size of the emission at given velocity, where a higher specific angular momentum results in a narrower region along the axis of the offset on the PV diagrams. A typical boundary of this model shows both red-shifted and blue-shifted emission at both sides of the source and reaches the highest velocity at the centrifugal radius when the kinematics become pure rotation (Figure 4.29, black lines). The PV diagrams of $^{13}CH_3OH$ and CH_3OCHO show a different morphology. However, COMs only become gas-phase at the inner 100 au region so that the rotating infalling envelope needs to be truncated at ∼100 au. Furthermore, the highest velocity in the observation is ∼2.5 km s^{-1}, while the model predicts 4.8 km s^{-1}. To reduce the highest velocity in the model, we add an inner radius for the envelope. The observation of an outbursting protostar, V883 Ori, also shows a cutoff of brightness at the inner region for methanol, suggesting that the increasing optical depth of the continuum obscures the emission of methanol (Lee et al., 2019). Finally, we found the model with L/m =1.0×10^{20} cm^2 s^{-1} with an inner and outer radii of 50 au and 60 au, respectively, matches the observation (Figure 4.29). This model also suggests a centrifugal barrier of 14 au, hinting the outer radius of a disk that remains undetected. However, constraining the kinematics at the inner ∼100 au region requires a higher resolution observation to confirm the morphology seen in the PV diagrams of our observation.

Lee et al. (2017) observed a similar morphology in the PV diagram of the methanol emission toward HH 212. Along with the bar-like component, they also observed the differential component at high velocity interpreted as the Keplerian rotation. A ring-like structure along with thin layers on the disk atmosphere extended toward the inner radius fits the methanol PV diagram. The ring component results in the bar-like morphology in the PV diagram, similar to our PV analysis of BHR 71. The methanol in the disk atmosphere follows the Keplerian rotation of the disk, resulting in the high velocity component, which we do not observe in our data. The differential component of HH 212 is much weaker than the bar-like component, suggesting that the differential component may exist for BHR 71, but too weak for our observation to detect.

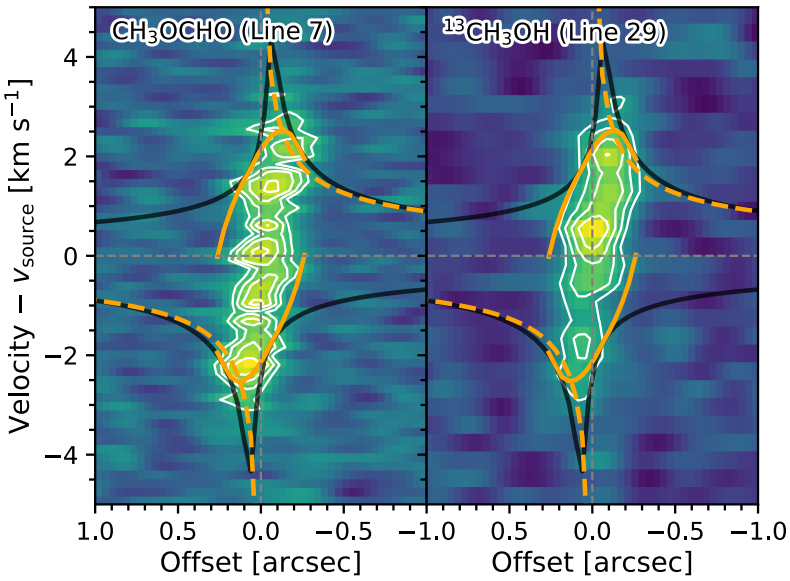

Figure 4.29: The PV diagrams of the emission of ^{13}C-methanol and methyl formate. The PV slice is perpendicular to the outflows. The orange lines indicate the maximum and minimum velocity of the best-consistent rotating infalling envelope model, while the black lines indicate the same model without the truncation at the inner and outer radius. The dashed lines illustrate the Keplerian rotation calculated with the same central mass in the rotating infalling envelop model.

4.5.6 The Chemistry in BHR 71 and the Deuteration Fractionation

Embedded protostars that show a rich abundance of complex organic molecules are named "hot corinos" for their chemical similarity with the chemically rich larger hot cores around more massive protostars (Ceccarelli, 2004). Our identification of complex organic molecules and their compact morphology at $< 1''$ region, suggesting that BHR 71 is a hot corino. Besides the COMs, ALMA ACA observations detect the emission of carbon-chain molecules (Ł. Tychoniec in prep., priv. comm.), suggesting that BHR 71 may have different degrees of complex chemistry at different spatial scales.

The deuterium fractionation of methanol is 1.0×10^{-2} measured from the ratio of CH_2DOH and CH_3OH, assuming an excitation temperature of 100 K. Deuterated species are enhanced at low temperature. At the pre-stellar phase, deuterium fractionation is generally greater than 0.1 (Ceccarelli et al., 2014, and the references therein), where the D-fraction in N_2H^+ can be as large as 0.7 (Pagani et al., 2007). At the late embedded protostellar phase, molecules show even higher deuteration fractionations with double and triple deuteration (see Figure 5 in Ceccarelli et al. 2014). The ratio of CH_2DOH to CH_3OH is $\sim$0.4–0.6 from single dish surveys (Parise et al., 2006c), much greater than the D/H ratio in methanol for BHR 71. Thus, methanol in BHR 71 may have gone through extensive chemical evolution as the gas experiences an increasing temperature due to the infall so that the high D/H ratio inherited from the chemical evolution at the prestellar stage has been diluted. A complete understanding of the chemical status of BHR 71 requires more complete line surveys with ALMA focusing each individual molecule.

4.6 Conclusion

Using a $0\farcs3$ beam of ALMA, we successfully observe red-shifted absorption against the continuum toward BHR 71 from the spectra of the HCO^+ $J = 4 \rightarrow 3$ and HCN $J = 4 \rightarrow 3$ lines, which is a direct signature of infall. We also observe red-shifted self-absorptions from the spectra of CS $J = 7 \rightarrow 6$ and $H^{13}CN$ $J = 4 \rightarrow 3$ lines.

To constrain the underlying infall kinematics, we test the infalling envelope model previously constrained by continuum by simulating the synthetic line profiles with

3D radiative transfer and comparing with the ALMA observations. The best-fitting model suggests an age of 15000 years instead of 36000 years, previously fitted with continuum observations, with the same mass infall rate of 1.2×10^{-5} $M_\odot$ yr^{-1}. We iterate the parameterized chemical abundance profiles to find the best-fitting models that reproduce the observations.

While the synthetic spectra qualitatively reproduce the observations of HCO^+ $J = 4 \rightarrow 3$, HCN $J = 4 \rightarrow 3$, CS $J = 7 \rightarrow 6$ lines, and $H^{13}CN$ $J = 4 \rightarrow 3$ lines, the best-fitting models cannot emulate all the features in the observations. Our model underestimates the red-shifted emission at the HCO^+ $J = 4 \rightarrow 3$ and HCN $J = 4 \rightarrow 3$ lines, and fails to reproduce the broad high velocity emission seen in the HCN $J = 4 \rightarrow 3$ line. The best-fitting model for the $H^{13}CN$ $J = 4 \rightarrow 3$ line requires a $^{12}C/^{13}C$ ratio of 3, which is highly unlikely, and shows an absorption against the continuum that is not observed.

We serendipitously detect the emission of SO_2, H_2CS as well as 12 species of COMs emitting from the central $\sim$100 au region, suggesting that BHR 71 has a hot corino. The synthetic spectra of COMs calculated with XCLASS reproduce the observation, confirming our identifications and providing estimations of the excitation temperatures and column density of the detected COMs.

The emission of $^{13}CH_3OH$ and CH_3OCHO shows a bar-shape morphology from their PV diagrams, probing the kinematics at the inner $\sim$100 au region. A truncated rotating infalling envelope that conserves angular momentum reproduces the extent of the morphology in the PV diagrams, which has an inner and outer radius of 50 au and 60 au, respectively, as well as a central mass of 0.18 $M_\odot$ and a specific angular momentum of 1.0×10^{20} cm^2 s^{-1}.

Chapter Five: Summary and Future Work

This dissertation focuses on understanding the assembly of protostars, starting from a large sample and proceeding to detailed models of an embedded protostar. The following paragraphs summarize this dissertation, and describe the possible future work.

5.1 Far-infrared Signatures of Outflows

I presented a well-calibrated far-infrared (50 μm to 670 μm) spectroscopy survey of 26 embedded protostars observed by the *Herschel Space Observatory*, along with the fitting results of more than 200 lines per pixel to characterize the far-infrared spectra of embedded protostars. The survey contains the data of the CO in Protostars *Herschel* Open Time Program (COPS, PI: J. Green) together with the data from the Dust, Ices, and Gas In Time *Herschel* Key Program (DIGIT, PI: N. Evans) and the FU Orionis Objects Surveyed with Herschel Open Time Program (FOOSH, PI: J. Green). I developed a method to properly reduce the 1D spectra of embedded protostars from the multiple pixels of PACS and SPIRE instruments. Most of the embedded protostars in the survey are marginally resolved by PACS and SPIRE so that neither a point source correction nor an extended source correction produces the correct spectrum. I used a customized reduction method to address this issue by modeling a finite source size for extracting the spectrum. Then an automatic line-fitting routine fits the atomic and molecular emission with a pre-defined line list. The entire reduced dataset is released to Herschel Science Archive, also known as the CDF archive, containing both spectroscopic and photometric data of 26 embedded protostars. The legacy value of the CDF archive will be very long-term, and provide key inputs as we look toward future far-IR missions with an eye toward protostellar studies.

With this dataset, I analyzed the origin of molecular emission and its morphology. From the detections of the CO rotational transitions from $J_{\rm up}$=4 to 48, the distribution of the CO excitation temperatures across the entire sample has two distinct populations at $\sim$100 K and 356 K. I interpret these temperature peaks as correspond-

ing to the entrained molecular gas (100 K) and shocked gas along the outflow cavities (350 K). This interpretation is supported by additional velocity-resolved observations of a handful of CO lines that indicate velocity components consistent with this picture (Kristensen et al., 2017c). Such agreement indicates the possibility of characterizing the gas components even without velocity information, a potential advantage for any future missions utilizing low resolution spectroscopy in far-infrared wavelengths. A ladder of CO rotational transitions at far-infrared wavelengths can distinguish the components in the outflows without resolving the emission lines.

I compared the strengths of the far-infrared emission lines from this dataset using a parameter referred to as Spearman's rank correlation coefficient, searching for non-obvious correlations between different lines. Unfortunately, the largest observed correlations were attributable to instrumental effects rather than astrophysical processes. Therefore, interpretations are limited to the lines observed within the same module of instruments. The correlations of CO emission shows a smooth distribution as a function of $J_{\rm up}$-levels, suggesting that the two outflow components, the entrained gas and the shocked gas, excite CO emission across a wide range of J-levels. The ^{13}CO emission has a better correlation to [C I] $^3P_2 \rightarrow ^3P_1$ than ^{12}CO, because both ^{13}CO and [C I] are associated with the UV-heated outflow cavity wall. The water emission also correlates with CO and OH. In particular, the correlation between water and CO elevates at the range of $J_{\rm up}$=10 to 15 for the CO emission, suggesting that water and CO may coexist in the outflow (Mottram et al., 2014b; Kristensen et al., 2017c) consistent with the prediction of the irradiated shock model in Karska et al. (2018).

The outflow morphology, traced by the CO emission, becomes less extended as the $J_{\rm up}$-level increases. I converted the 2D morphology to an 1D profile using the flux ratios of outer pixels to the central pixel as a function of the azimuthal angle, allowing a systematic morphological analysis across the $J_{\rm up}$-level of CO emission. At low-J, the CO emission traces the bipolar outflows, while at high-J the CO emission becomes more centrally peaked. The morphological variation suggests that the most recently shocked gas locates closer to the central protostar along the outflow cavities than that of the entrained gas.

5.2 The Anatomy of BHR 71

After a survey of embedded protostars at far-infrared wavelengths, I selected BHR 71 IRS1 from the *Herschel* survey for understanding interplays of different star formation processes. I present a 3D modeling of BHR 71 IRS1 constrained by observations. The 3D model aims to unveil the density, temperature, and kinematic structures of BHR 71 IRS1. I also discover a rich spectrum of complex organic molecules at the inner 100 au of BHR 71 IRS1, revealing the hot corino nature of BHR 71 IRS1.

5.2.1 Structures and Kinematics

Observations of protostars contain information about each component of the protostellar environment, separated in spatial and spectral axes. Characterizing the components of a protostellar system requires a 3D model constrained by observations. I constructed a 3D radiative transfer pipeline for both continuum and molecular line emission to produce synthetic observations to compare to observations. The continuum radiative transfer pipeline utilizes a publicly available package, HYPERION, to calculate the continuum emission of protostellar envelopes with a slowly rotating infalling envelope model, which has a bipolar outflow cavity. I also added a flared disk inside the centrifugal radius of the envelope.

I developed a roadmap for finding the best-fitting model constrained by continuum emission with *Spitzer* and *Herschel* observations. The roadmap starts with fixing several parameters constrained by observations, leaving five parameters for optimization. Then, the azimuthally-averaged radial brightness profile at 160 μm constrains the age. The *Spitzer*-IRAC1 image at 3.6 μm constrains the inclination of the envelope by comparing the flux ratio between the two outflow lobes. Finally, I ran several grids of models to optimize the rest of parameters.

The envelope dominates the emission at far-infrared wavelengths (50 μm to mm), while the outflow cavity determines the emission at mid-infrared wavelengths (5 μm to 50 μm). The density profile inside the outflow cavity was poorly constrained before this work and is crucial for fitting the emission at 20 μm to 40 μm. A constant density at the apex of the outflow cavity followed by a power-law decrease inside the cavity best fits the observation. The best-fitting model suggests an age upper limit of 36000

years for the envelope, while the outflow dynamical age of 24600 years sets the lower limit of the age of the envelope. The age is defined as the time since the collapse began. The best-fitting inclination angle is 50° instead of 84° from previous studies of CO outflows.

The best-fitting model suggests a mass infall rate of 1.2×10^{-5} $M_\odot$ yr^{-1}, while the mass accretion rate onto the protostar is 1.1×10^{-5} $M_\odot$ yr^{-1}, derived from the central luminosity of 18.8 $L_\odot$ assuming that the accretion dominates the central luminosity. The model shows no sign of episodic accretion, where the mass infall rate and the mass accretion differ by orders of magnitudes; however, any episodic accretion in the past is not ruled out. I also revise the mass loss rate measured from CO observations in the literature with the updated inclination angle. The revised mass loss rate is 2.1×10^{-6} $M_\odot$ yr^{-1}, whereas the mass loss rate derived from [O I] 63 μm emission is 2.2×10^{-7} $M_\odot$ yr^{-1}. The ratio of the mass infall rate and the mass loss rate derived from CO agrees with the canonical ratio of ~ 0.1. The order of magnitudes difference between the mass loss rates derived from CO and [O I] 63 μm emission suggests that [O I] 63 μm may not trace the entire mass loss in the outflows. Additionally, the [O I] 63 μm emission traces the gas currently shocked, whereas the CO emission traces the entrained gas averaged over a larger timescale.

I further modeled the molecular lines observed by ALMA to constrain the underlying infall kinematics of the envelope of BHR 71 IRS1. I present high resolution ($0\farcs3$) ALMA observations of HCO^+ $J = 4 \rightarrow 3$, HCN $J = 4 \rightarrow 3$, CS $J = 7 \rightarrow 6$, and $H^{13}CN$ $J = 4 \rightarrow 3$ lines toward the compact continuum source, which has a deconvolved size of 70 au×56 au. Both the HCO^+ $J = 4 \rightarrow 3$ and HCN $J = 4 \rightarrow 3$ lines show redshifted absorption below the continuum, indicative of the infalling cold dense gas in front of the compact continuum source. Such signature is an unambiguous detection of infall.

Constraining the underlying infall kinematics probed by molecular lines requires line radiative transfer calculations. I construct a 3D line radiative transfer pipeline using the publicly-available package, LIME, and a customized ray-tracing package, LIME-AID. For any given molecule, LIME calculates the level populations, which will be post-processed by LIME-AID to add the continuum source at the center, modeled as a 2D gaussian source according to the ALMA observation. The line modeling starts with the best-fitting model for the continuum emission. Then, I use a parametrized abundance profile for each molecule to resemble the variations in the abundance

profiles based on chemical models (Lee et al., 2004). An iterative process of changing the abundance profile and occasionally changing the envelope model results in the best-fitting models for all four molecules.

The best-ftting model suggests that the infall signatures probe the kinematics at 100–1000 au scale. The models match the line profile of HCO^+ $J = 4 \rightarrow 3$, HCN $J = 4 \rightarrow 3$, CS $J = 7 \rightarrow 6$, and $H^{13}CN$ $J = 4 \rightarrow 3$ with a few discrepancies. All the models have the same density, temperature, and velocity structures updated from the model for the continuum. The CS $J = 7 \rightarrow 6$ line profile requires a younger age of 15000 years for the infalling envelope to have the two peaks in the line profile move to a lower velocity, which none of the variation in the abundance profile can achieve. The younger age is consistent with the upper limit set by the continuum modeling and agrees with the outflow dynamical age within the uncertainty. Thus, the infall signatures from molecular lines suggest a younger envelope, 15000 years since the collapse began, for BHR 71 IRS1. The mass infall rate remains as 1.2×10^{-5} $M_\odot$ yr^{-1}, because the effective sound speed is the only parameter of the infall rate in the Shu-like envelope model.

In addition to the four lines targeted for probing the infall signature, the ALMA observation also shows emission of several other molecules, which is summarized in Section 5.2.2. In particular, the emission of methanol and methyl formate shows a bar-shape morphology on their position-velocity diagrams along the slice across the midplane of the envelope, which is assumed to be perpendicular to the outflow, tracing the kinematics at the inner 100 au of BHR 71 IRS1. The morphology disagrees with a Keplerian rotation, but is consistent with a ring of a infalling rotating envelope that conserves angular momentum. With the central mass fixed to the total infallen mass predicted by the best-fitting envelope model, 0.18 $M_\odot$, an infalling rotating ring matches the observation with a specific angular momentum of 1.0×10^{20} cm^2 s^{-1}. The inferred centrifugal barrier, where the infall stops, is 14 au, supporting the non-detection of a rotation-supported disk at the resolution of 70 au.

I demonstrated an approach to probe infall kinematics from envelopes to disk-forming regions with both simple and complex organic molecules. Using 3D radiative transfer, I constrained the density and temperature structures of an embedded protostar, BHR 71, and further derived the underlying infall kinematics based on two different models of infalling envelopes at the envelope (100 au–1000 au) and disk-forming region ($\lesssim$100 au). The HCO^+ $J = 4 \rightarrow 3$ line is the most robust tracer of

infall at the envelope scale, while methanol and methyl formate trace the kinematics at the inner 100 au.

5.2.2 Complex Chemistry

I identify 12 species of complex organic molecules (COMs) from the ALMA observation. The emission of COMs has a compact morphology with a averaged deconvolved size of $0\farcs50\pm0\farcs13$ $\times0\farcs21\pm0\farcs09$ (100 au$\times$42 au), where the best-fitting model of BHR 71 IRS1 has a temperature of $\sim$100 K. Therefore, BHR 71 IRS1 has a hot corino because of the presence of COMs at warm temperature region centered on the protostar.

The spectrum toward the continuum source shows the emission of several O-bearing molecules, whereas only a few N-bearing and S-bearing molecules are detected. The O-bearing COMs have six atoms for methanol (CH_3OH) to ten atoms for acetone (CH_3COCH_3), suggesting an extensive formation of COMs in the past. Most of the COMs consist of a methyl group (CH_3-) and another functional group, including aldehyde ($-$CHO), alcohol ($-$OH), ether ($-$O$-$), ketone ($-$CO$-$), ester ($-$OCO), while two COMs are based on the ethyl group, gauche-ethanol (C_2H_5OH) and ethyl cyanide (CH_3CH_2CN). The S-bearing molecules, SO_2 and H_2CS, are less complex than the O-bearing and N-bearing molecules.

Moreover, the spectrum shows the emission of isotopologues of methanol, such as CH_2DOH, CH_3OD, and $^{13}CH_3OH$. The estimated D/H ratio in methanol is 0.1. Compared to the typical D/H ratios measured from H_2CO (0.01–0.1), NH_3 (0.1–0.4), and N_2H^+ (0.1–0.7), a D/H ratio of 0.1 suggests that the methanol has not been further processed after its formation while frozen onto dust grains, and the observed methanol is likely recently sublimated when entering the warm inner 100 au region.

5.3 Possible Future Work

This dissertation has characterized the properties of embedded protostars and the detailed models of the density and velocity structures. Possible future works will focus on constructing a comprehensive picture of protostellar infall via the following directions.

1. Directly measure the infall kinematics from envelopes to disks.

   In Chapter 4, I derive the infall kinematics from the observations of HCO^+ $J = 4 \rightarrow 3$, HCN $J = 4 \rightarrow 3$, and CS $J = 7 \rightarrow 6$ lines, using an "inside-out" collapse model. However, numerical simulations suggest that other type of infall, such as an "outside-in" collapse also occur during the evolution of dense cores. Only few direct observation of infall exists to constrain the radial variation of infall, distinguishing between the "inside-out" and "outside-in" collapse. Future observations targeting multiple transitions of the molecules that trace infall may directly measure the infall kinematics at different radii, constructing the radial profile of infall. At different rotational transitions, the absorption arises from the infalling gas at different temperature, corresponding to different radius as the envelope is centrally heated. Thus, measurements of the redshifted absorption will empirically measure the infall velocity as a function of radius to constrain the model of infall.

   In the inner envelope, rotation starts to dominate the kinematics and may stop the infall. Where the infall stops, a disk begins to form. A radial profile of infall that extends to the disk-forming region will be critical to probe the effect of rotation and other processes, such as magnetic fields, on the infall, and investigate the dynamical process that results in the formation of disks. At the disk-forming region, where the simple molecules that trace infall are likely to be destroyed, COMs become a unambiguous tracer of kinematics. Future high resolution observations of COMs using ALMA that spatially resolve their emission will probe the kinematics all the way to the disk, tracing the kinematics that deviate from free-fall due to the effect of rotation and magnetic fields. Together with the radial infall profile measured from multiple transitions of optically thick lines, the emission of COMs completes the direct measurement of infall to the region where infall stops, allowing us to test the evolution of infall.

2. Constrain the chemical abundance for a more realistic model of kinematics from molecular emission.

   The chemical abundance of the molecules that trace the infall is the main uncertainty in constraining the underlying kinematics. Freeze-out, evaporation, and chemical reactions can change the abundance by a few orders of magnitude.

Therefore, an accurate representation of chemical abundance will substantially improve the precision of the measured infall kinematics. On the modeling side, the dynamical evolution of infalling envelopes need to include the chemical networks to fully simulate the coupled evolution of dynamics and chemistry. Solving chemistry for each time step of dynamical simulation may be infeasible due to the computational cost. I will start with post-processing the evolutionary history of trace particles to calculate the chemistry from simulations, which will compare with observations. Future collaborations with theorists will focus on gradually integrating chemistry into dynamical simulations and producing synthetic observations to test against actual observations. On the observation side, mapping the optically thin transitions of the molecules that trace infall will measure the column density of each species, constraining the chemical abundance.

3. Apply the successful prototype model of infall on a large sample of protostars which have a range of mass, luminosities, and environments.

   I plan to use the radiative transfer modeling tools that I have developed to construct a unified picture of infall that will be tested against observations toward a large sample of protostars. I will start with expanding the sample to include more isolated embedded protostars because of their simple environment. I will test if all the embedded protostars would have their age since the collapse begins constrained with molecular lines lower than that with continuum by a factor of 2.5 as we found toward BHR 71. Further observations will focus on the impact of environments and mass to characterize the physical processes that drive the infall. Forming in clustered environments, protostars may have different evolution timescales due to the feedback from nearby star formation activities compared to the isolated embedded protostars. Also protostars that form as single source and the ones form in multiple within a single dense core may experience different evolutionary track, resulting in different paths of infall.

   On the mass side, whether star formation proceeds similarly for both low- and high-mass protostars remain unclear. Several numerical simulations can apply to both low- and high-mass protostars. Future observations for the protostars along the mass spectrum will test those simulations via synthetic observations, identifying the effects of different physical processes.

Appendices

Appendix A: CO in Protostars (COPS): *Herschel*-SPIRE Spectroscopy of Embedded Protostars

A.1 List of OBSID of photometry

Table A.1 lists the OBSIDs used for calculating the PACS and SPIRE photometry in this study.

Table A.1: OBSID of Photometry

Source	PACS	SPIRE
IRAS 03245+3002	1342227103, 1342227104	1342190327, 1342190326
L1455 IRS3	1342227103, 1342227104	1342190327, 1342190326
IRAS 03301+3111	1342227103, 1342227104	1342190327, 1342190326
B1-a	1342227103, 1342227104	1342190327, 1342190326
B1-c	1342267246, 1342267247	1342190327, 1342190326
L1551 IRS5	1342202251	1342202250, 1342202251
TMR 1	1342228175, 1342228174	1342202252, 1342202253
TMC 1A	1342202252	1342202252, 1342202253
TMC 1	1342202252	1342202252, 1342202253
HH 46	...	...
Ced110 IRS4	1342223480, 1342224782, 1342224783	1342213179, 1342213178
BHR 71	1342224922, 1342224925, 1342224924, 1342224923	1342226633
DK Cha	1342212709, 1342212708, 1342213180	1342213180, 1342213181
IRAS 15398–3359	1342226705	1342213182, 1342213183
GSS 30 IRS1	1342227148, 1342227149, 1342205093, 1342205094	1342203074, 1342205093, 1342205094
VLA 1623−243	1342205093, 1342205094	1342203074, 1342205093, 1342205094
WL 12	1342238817, 1342238816	1342205093, 1342205094
RNO 91	1342263844, 1342263845	1342263844, 1342263845
L483	1342228397, 1342228398, 1342228395, 1342228396	1342229186
RCrA IRS5A	1342267429, 1342267427, 1342267428, 1342267430, 1342242076 1342241402, 1342241519, 1342241403, 1342242555, 1342242077 1342241314, 1342241520, 1342241313, 1342242554	1342206677, 1342206678, 1342216002
RCrA IRS7B/C	1342184510, 1342184511	1342206677, 1342206678, 1342216002
L723 MM	1342231917, 1342231918	1342229605
B335	1342196030, 1342196031	1342192685
L1157	1342224778, 1342224779, 1342189845	1342189844, 1342189843
L1014	1342225450, 1342225449	1342219974, 1342220631

We exclude HH 100 from the calibration with photometry, because the observation of HH 100 is heavily contaminated by a nearby source, RCrA IRS7B.

A.2 The 1D SPIRE spectra for the COPS-SPIRE sources

Figure A.1 shows the continuum-subtracted SPIRE 1-D spectra for the COPS sources. Three versions of spectra are available online, the files named by `[object]_spire_corrected` contain the SPIRE 1-D spectra used in this study, `flat_spectrum` in the file name indicates the continuum-subtracted spectra, `residual_spectrum` in the file name indicates the residual spectra after subtracting emission lines and continuum.

A.3 Classification of the 1D Profiles for Morphology

We classified the 1D smooth profile into three classes, bipolar, single, and irregular, depending on whether they have the double peaks, single peak, and flat profile, respectively. The irregular profile can be a result of complex source structure or the absence of outflows. The sources that have a bipolar feature identified in the 1D profile all exhibit outflows in the velocity-resolved observations. However, not all outflows observed in the velocity-resolved observations are identified from the 1D profiles due to the weak emission of the outflows or the complexity of the source. Thus, we further classified the 1D profiles into three types: (1) bipolar outflows (or single outflow) are identified in the 1D profile, which is also confirmed with the velocity-resolved observations; (2) no bipolar feature seen in the 1D profile, and the velocity-resolved observations show little CO emission in the high velocity wings; (3) outflows are seen from the velocity-resolved observations, whereas few off-center detection is found in our SPIRE data due to insufficient sensitivity; (4) the 1D profile is irregular, while the irregularity is consistent with the velocity-resolved observations, mostly due to the presence of multiple sources or broad outflows. Table A.2 lists the class and type for the 1D profile of each source. We found that spatially extended CO emission observed with SPIRE always has an outflow-related origin based on its morphology.

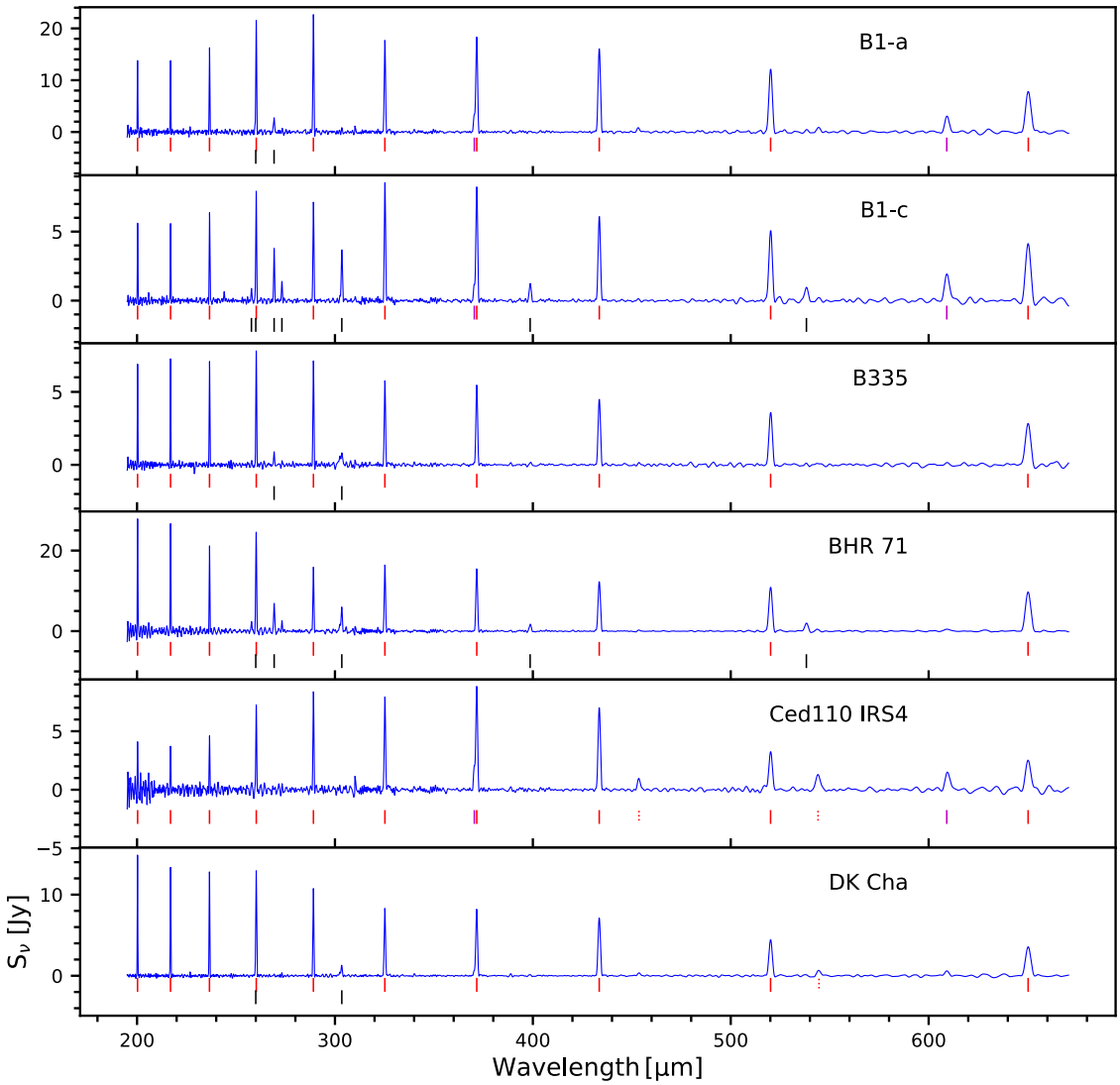

Figure A.1: The continuum-free SPIRE 1D spectra for the COPS sources. The vertical bars indicate the significant detections on emission lines. The red solid bars represent the CO emission, while the red dotted bars represent the ^{13}CO emission. The water lines are shown in black solid bars, while the OH lines are shown in black dotted bars. The orange bars indicate the emission of HCO^+, while the [C I] lines are shown in magenta bars. Note that the figure of RCrA IRS7B/C shows the spectrum of RCrA IRS7C due to the blending between of two sources.

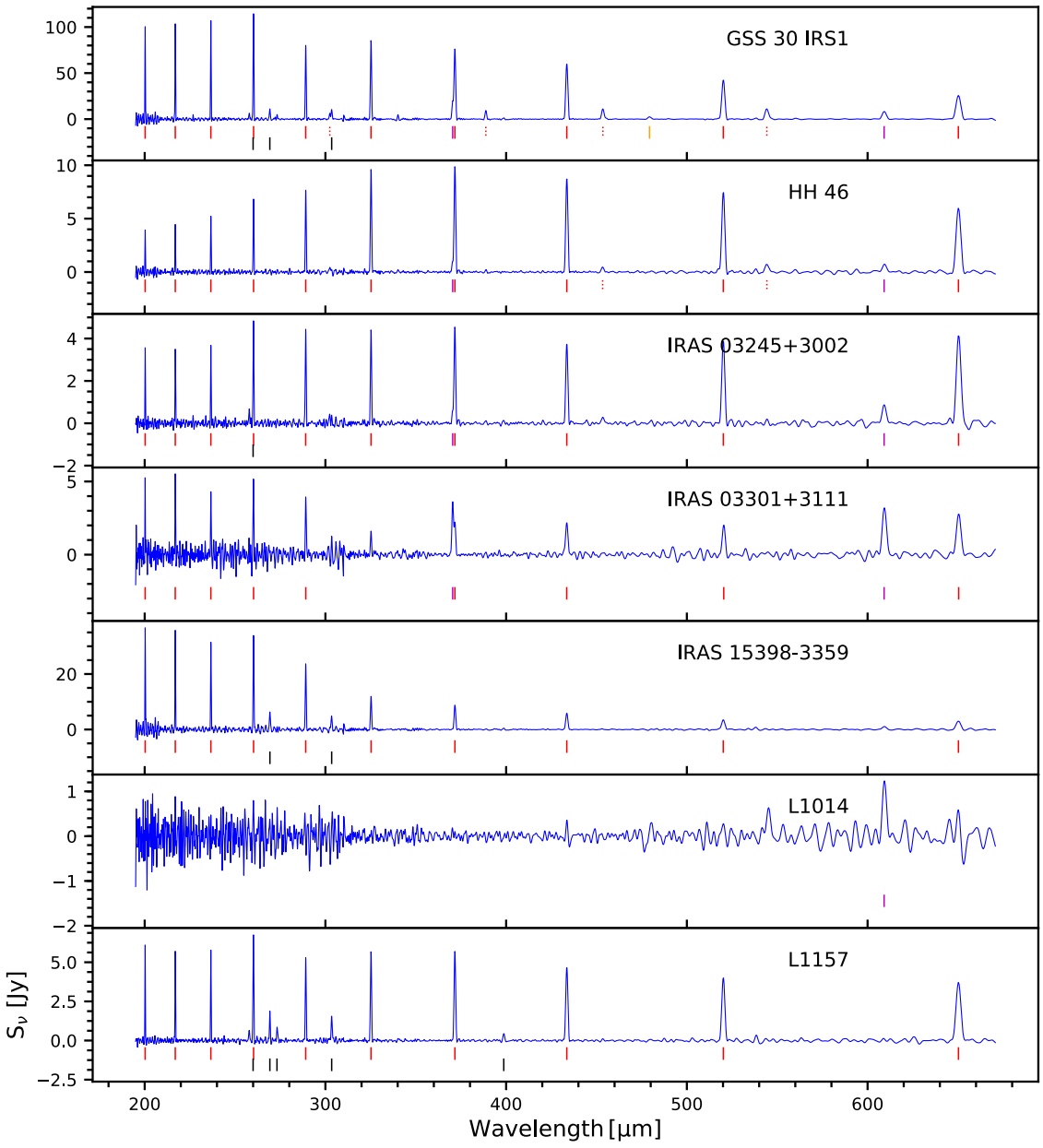
GSS 30 IRS1
HH 46
IRAS 03245+3002
IRAS 03301+3111
IRAS 15398-3359
L1014
L1157
S_ν [Jy]
Wavelength [μm]

Figure A.1

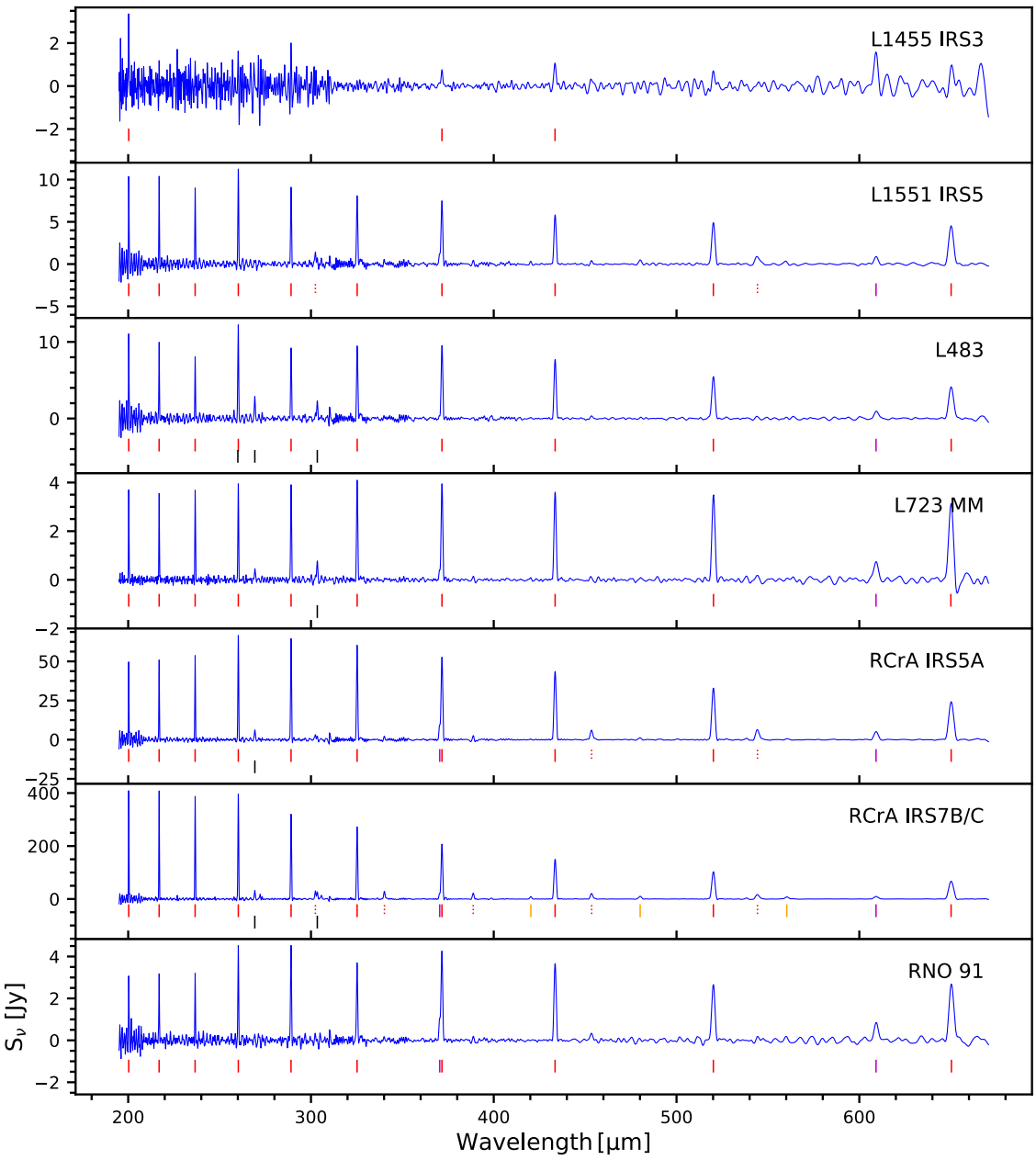
L1455 IRS3
L1551 IRS5
L483
L723 MM
RCrA IRS5A
RCrA IRS7B/C
RNO 91
S_ν [Jy]
Wavelength [μm]

Figure A.1

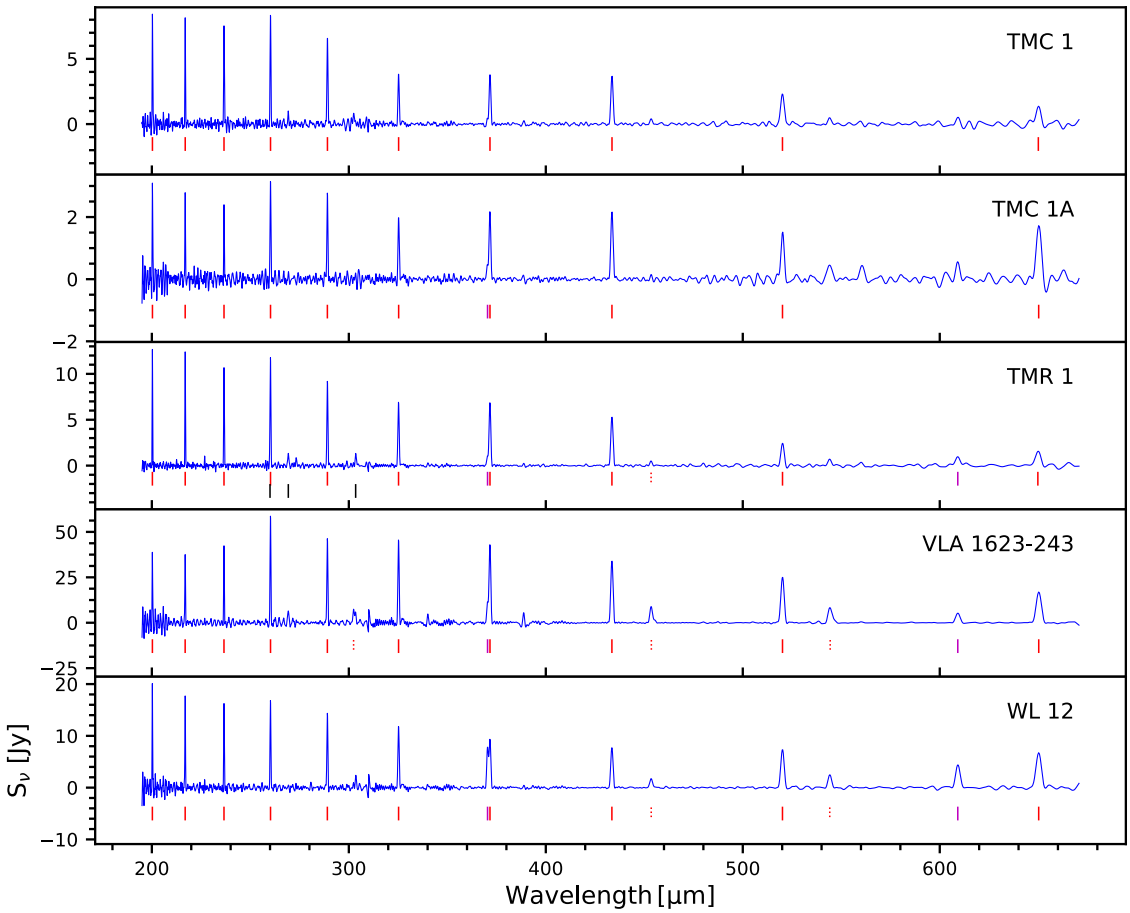

Figure A.1

A.4 Effect of Sensitivity on the Variation of Bipolarity

In Section 2.4.6.3, we use the peak-to-valley difference to quantify the strength of bipolarity and found a decrease of the difference suggesting the bipolarity diminishing at higher-J CO lines. However, the cause of the decrease of the peak-to-valley difference can be either the bipolar feature diminishing toward the higher J-levels or simply lower sensitivities at the higher J-levels. Thus, we investigate the effect of sensitivity by artificially decreasing the fluxes seen in CO $J = 4 \rightarrow 3$ (CO $J = 9 \rightarrow 8$) for the SLW (SSW) module and calculate the peak-to-valley differences. These two lines have the strongest strength at outer spaxels in each module. We use B1-c as

Table A.2: Summary of the morphology of CO emission

Source	1D profile	Presence of outflow	Ref.	Type[a]
IRAS 03245+3002	Ir	B/R	Chou et al. (2016)	4
L1455 IRS3	ND	N	Kang et al. (in prep.)	2
IRAS 03301+3111	ND	N	Kang et al. (in prep.)	2
B1-a	Si	B	Kang et al. (in prep.)	1
B1-c	Bi	B/R	Storm et al. (2014)	1
L1551 IRS5	Bi	B/R	Wu et al. (2009)	1
TMR 1	ND	B	Kang et al. (in prep.)	3
TMC 1A	ND	B	Yıldız et al. (2015)	3
TMC 1	ND	B/R	Yıldız et al. (2015)	3
HH 46	Si	R	Yıldız et al. (2015)	1
Ced110 IRS4	Ir	N	Yıldız et al. (2015)	2
BHR 71	Bi	B/R	Parise et al. (2006b)	1
DK Cha	Ir	N	Yıldız et al. (2015)	2
IRAS 15398–3359	ND	B/R	Yıldız et al. (2015)	3
GSS 30 IRS1	Si	B	Yıldız et al. (2015)	1
VLA 1623−243	Ir	B/R	Santangelo et al. (2015)	4
WL 12	Ir	B/R	Bontemps et al. (1996b)	3
RNO 91	Ir	N	Yıldız et al. (2015)	2
L483	Bi	B/R	Dunham et al. (2014a)	1
RCrA IRS5A	Si	N	Peterson et al. (2011)	... [b]
L723 MM	Ir	B/R	Bontemps et al. (1996b)	3
B335	Bi	B/R	Stutz et al. (2008)	1
L1157	Bi	B/R	Tafalla et al. (2015)	1
L1014	ND	B/R	Bourke et al. (2005)	3

The notation for the classification of 1D smooth profile: Bi: bipolar lobes; Si: single lobe; Ir: irregular profile; ND: not enough detection for constructing the 1D profile. The presence of outflow is labelled by B, R, and N for blue, red, and no outflow, respectively.
[a]Please see Appendix A.3 for the discussion of the types.
[b]No clear outflow detection for RCrA IRS5 in other studies; therefore, it is unclear whether the SIPRE morphology tracing outflows.

an example. Figure A.2 shows two sets of 1D smoothed profiles applied with various SNR reductions for the SLW and SSW modules, respectively. Ideally, if all signals remain significant after the SNR reduction is applied, the 1D profile should be the same, therefore the same peak-to-valley difference. It is only when the signal becomes non-detectable (i.e. SNR < 4), then the 1D profile and the peak-to-valley difference change correspondingly.

When the SNR reduction is small ($-\Delta$SNR=2 or 4), the low-SNR detections are reduced to the noise level, while the high-SNR detections remain significant but weaker. Therefore, the valley of the 1D profile becomes lower, resulting in a higher peak-to-valley difference (Figure A.2). As the SNR reduction becomes larger, we start to see the peak-to-valley difference decrease (Figure A.2, right). When most of the original detections become non-detections, the 1D profile is dominated by a few high-SNR detections preferentially found in the bipolar feature. Thus, a further

SNR reduction simply decreases the height of the peak in the 1D profile, reducing the derived peak-to-valley difference. In summary, the most robust analysis with the peak-to-valley difference should be restricted to the sources with significant detections at the outer spaxels over the J-levels ($J_{\rm up}$=4–13).

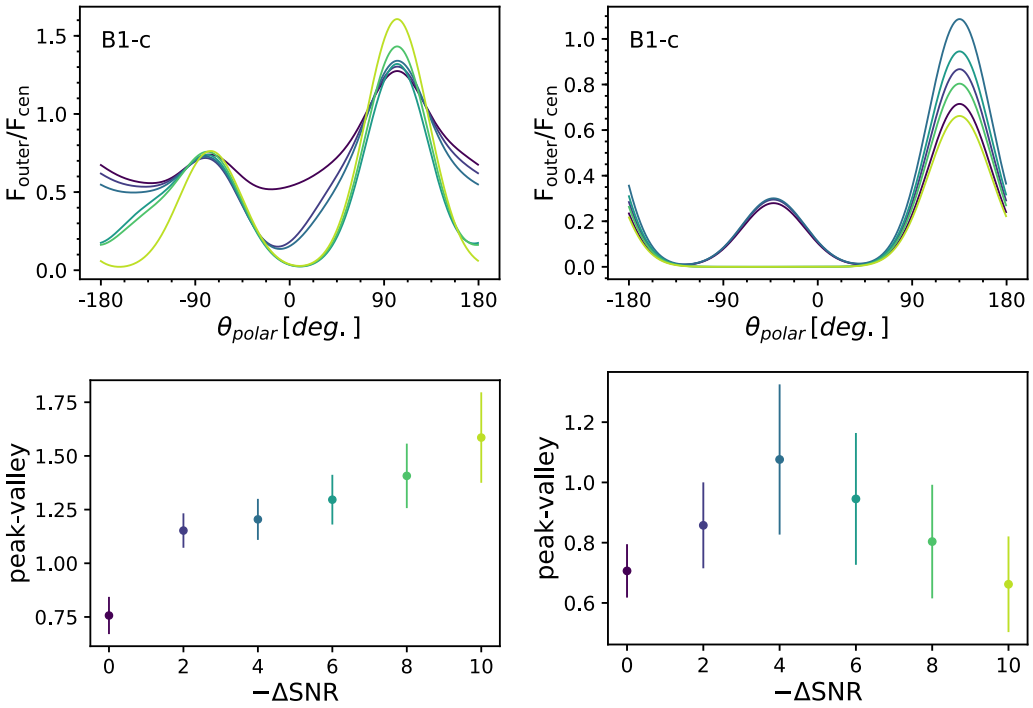

Figure A.2: **Top:** The 1D smoothed profiles of CO $J = 4 \rightarrow 3$ (left) and CO $J = 9 \rightarrow 8$ (right) with SNR reductions applied. The applied SNR reduction is indicated by the color of points in the figures shown in the bottom. **Bottom:** The peak-to-valley differences derived from the profiles with different SNR reductions applied.

A.5 Archival Photometry for COPS sources

Table A.3 shows part of a table that contains all PACS and SPIRE photometry derived in this study as well as the photometry collected from literatures. The entire table is available as machine readable table online.

Table A.3: Reference for photometry

Wavelength	Flux	Reference	Wavelength	Flux	Reference
		B1-a			
1.2	8.90(−3)	C03	1.7	3.80(−4)	C03
2.2	1.40(−3)	C03	3.6	1.64(−2)±9.00(−4)	c2d-DR4
4.5	4.93(−2)±2.50(−3)	c2d-DR4	5.8	8.45(−2)±4.00(−3)	c2d-DR4
8.0	1.15(−1)±5.00(−3)	c2d-DR4	12.0	2.50(−1)	IRAS2
24.0	1.69±1.60(−1)	c2d-DR4	25.0	1.39±1.40(−1)	IRAS2
70.0	6.45±6.10(−1)	c2d-DR4	100.0	7.54±3.64	CDF-v2
160.0	1.18(1)±4.45	CDF-v2	250.0	2.40(1)±7.95	CDF-v2
350.0	2.02(1)±7.20	CDF-v2	500.0	1.50(1)±6.41	CDF-v2
850.0	3.69	DF08			

The numbers in the prentices indicate the exponent of the power of ten. The uncertainties of fluxes are only shown if published in literatures. The entire table is available online as a machine readable table.

Appendix B: The Effect of the Parameters in the Continuum Model

The appendix contains studies of how the various parameters affect the predicted observables. These were used to constrain our exploration of parameter space, and we present them here as a guide to other modelers.

B.1 Envelope Parameters

The properties of the envelope are mainly determined by the TSC model along with the inner and outer radius of the envelope, which are fixed as the dust sublimation radius ($\sim$ 0.1 AU with a dust sublimation temperature of 1600 K) and 0.315 pc for these parameter studies. The three parameters of the TSC model are sound speed, age since the collapse began, and the initial rotational speed. The TSC model provides an evolutionary model of a collapsing envelope. Figure B.1 shows the evolutionary sequence from $t_{\rm col} = 5 \times 10^3$ years to 7.5×10^4 years with four different sound speeds: 0.27 km s^{-1}, 0.37 km s^{-1}, 0.47 km s^{-1}, and 0.57 km s^{-1}. The dust density profiles of these models are calculated with the setup described in Section 3.4.2 and the parameters in Table 3.4 except for the two varying parameters.

As the age increases, the broad peak in the far-infrared becomes wider and moves toward shorter wavelengths. This behavior reflects the fact that envelope mass decreases over time due to the accretion, resulting in a higher dust temperature peaking at a shorter wavelength and less extinction at mid-infrared wavelengths. For a given age, the contrast between mid-infrared and submillimeter wavelength increases with the sound speed. A higher sound speed provides more pressure support to prevent the gas from collapsing; therefore the initial density and the total mass of the envelope is greater with a higher sound speed, providing more extinction at shorter wavelengths and increasing the contrast (Equation 3.2). The bolometric temperature ($T_{\rm bol}$) of each model is shown in the corresponding panel derived with the method in Chen et al. (1995b). $T_{\rm bol}$ increases with the age, a pattern that is consistent with the protostar classification using bolometric temperature (Dunham et al., 2014c). Note

that beyond a certain age, the shape of the SED remains almost the same with only subtle changes at mid-infrared wavelengths.

The sound speed and age are degenerate to first order because the infall radius is just the product of the two. Figure B.1 shows the degeneracy of these two parameters: a model with higher sound speed and an earlier age can have a similar SED to a model with smaller sound speed and a later age. For example, the SED in the bottom right panel is similar to the SED in the fourth from the left of the third row. However, envelopes with higher sound speeds start with more mass, which is reflected best by the emission at the longest wavelengths (e.g., 1.3 mm). Figure B.2 shows the effect of sound speed and age. The long wavelength emission is more affected by sound speed than by age.

The azimuthally-averaged radial intensity profile at 160 μm is quite diagnostic of age (see Section 3.4.4.1 for definition). Figure B.3 shows the effect of age on the radial profiles, indicating that a later age results in a flatter profile. The emission at smaller radii increases with the age, while the shape of the radial profiles at larger radii remains the same. As the infall radius moves out, a larger fraction of the envelope has a flatter density profile, resulting in a flatter intensity profile. Because we use the **normalized** radial intensity profiles, the profiles are only sensitive to the structural change of the envelope, not the overall mass. Figure B.4 shows the age grid of radial intensity profiles with two different inclination angles, 53° and 61°. Both grids behave in the same way with the age of the envelope, suggesting that the effect of the inclination angle is insignificant for comparing radial intensity profiles measured at long wavelengths.

The third parameter of the TSC model is the initial rotational speed, $\Omega_\circ$. The initial rotational speed determines the centrifugal radius (R_c) and thus the disk radius. A larger $\Omega_\circ$ leads to a density profile more flattened toward the equator. Figure B.5 shows simulated SEDs with the initial rotational speed of 5×10^{-13}, 10^{-13}, and 5×10^{-14} s^{-1}, an age of 7.5×10^4 years, and other parameters from Table 3.4. The corresponding centrifugal radii are 4.7 AU, 19 AU, and 470 AU. A larger $\Omega_\circ$ results in more emission in the mid-infrared and less emission in the submillimeter. A larger centrifugal radius leads to the increase of material at smaller radii due to a more flattened inner envelope; therefore, the mid-infrared excess comes from the increase of hot material. The 1.3 mm emission, which is dominated by the total dust mass, is lower in the model with a large rotational speed due to a lower total dust mass in the

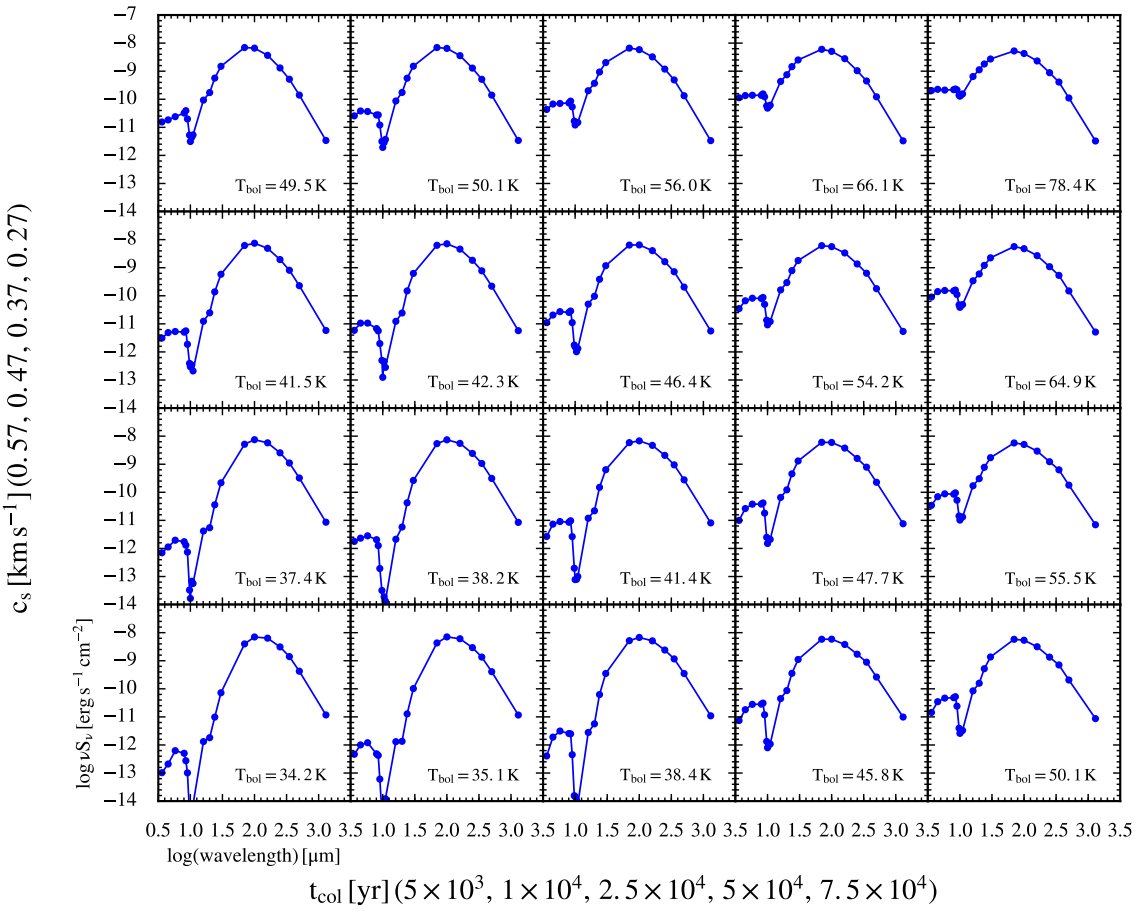

Figure B.1: The simulated SEDs of the evolution sequence of model with three different sound speeds (0.27 km s^{-1}, 0.37 km s^{-1}, 0.47 km s^{-1}, and 0.57 km s^{-1}). From top to down, each row shows a evolution sequence for given sound speed of 0.27 km s^{-1}, 0.37 km s^{-1}, 0.47 km s^{-1}, and 0.57 km s^{-1}. From left to right, each column shows a snapshot of the evolution sequence for three different sound speed. The age of the model increases from 5×10^3 years to 7.5×10^4 years. The blue dot/line shows the SED with aperture-extracted photometry from simulated spectra. Other parameters are adopted from Table 3.4.

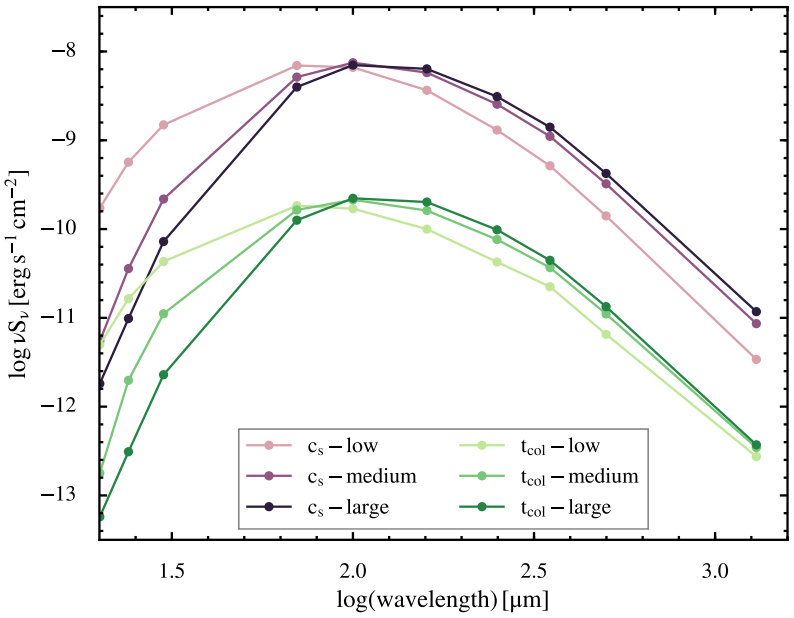

Figure B.2: The simulated SEDs selected from Figure B.1 (the first and the last two SEDs in the first column and the first, third and fifth SEDs from the left of the last row). The SEDs with different $t_{\rm col}$ are shown in purple and the SEDs with different sound speed are shown in green, while the series of $t_{\rm col}$ is offset by -1.5 dex.

envelope. Equation B.1, adopted from Eq. 4.43 of Hartmann (2009) can illustrate this effect.

$$\rho(r,\theta) = \frac{\dot{M}_{\rm env}}{4\pi(GMr^3)^{1/2}} \left(1 + \frac{\cos\,\theta}{\cos\,\theta_\circ}\right)^{-1/2} \left(\frac{\cos\,\theta}{\cos\,\theta_\circ} + \frac{2\cos^2\,\theta_\circ}{r/R_{\rm c}}\right)^{-1} \tag{B.1}$$

where $\dot{M}_{\rm env}$ is the mass infall rate in the envelope, M is the total mass, $\theta_\circ$ is the angle between the orbital plane of mass particles and the rotation axis of the system, and $R_{\rm c}$ is the centrifugal radius, which is proportional to $\Omega_\circ^2$. This equation represents the density for material at a given position in its collapsing trajectory, defined by θ and $\theta_\circ$. Changing the rotational speed ($\Omega_\circ$) only, all variables in Equation B.1 remain the same except for $R_{\rm c}$, which is proportional to $\Omega_\circ^2$. Therefore, a larger rotational speed results in a greater $R_{\rm c}$, making the second term in the last factor in Equation B.1 larger; since that factor is in the denominator, a higher rotational speed leads to a lower density, leading to a lower 1.3 mm emission. The influence from the flattened envelope and the disk is minimal unless the resulting centrifugal radius is larger than about 100 AU.

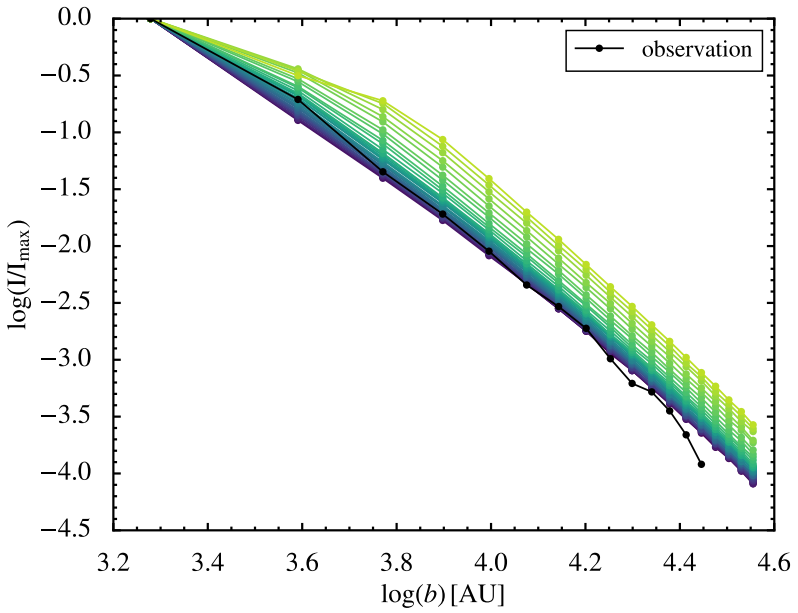

Figure B.3: The simulated radial intensity profiles at 160 μm are shown in sequential colors, where a lighter color corresponds to a later age. The radial intensity profile extracted from *Herschel* 160 μm image is shown in black. The models include 34 ages, spaced by 2000 years, extending from 4000 to 50000 years, and then spaced by 5000 years, extending from 55000 to 100000 years.

The effects of the envelope parameters are summarized as follows:

- $t_{\rm col}$: This controls the total amount of dust in the envelope, therefore the total amount of emission at submillimeter wavelengths. A later age results in a less massive envelope and an SED peaking at a shorter wavelength and a flatter radial profile. For example, in the last row of Figure B.1, the leftmost SED peaks around 10^2 μm, while the rightmost SED peaks around $10^{1.75}$ μm. And the flux level at shorter wavelengths is higher at large $t_{\rm col}$ (rightmost).

- $c_{\rm s,eff}$: This also controls the total amount of dust in the envelope. Although its effect on the SED is similar to the effect of age, it can affect the detailed shape of the broad far-infrared peak in the SED.

- $\Omega_{\rm o}$: The effect of the initial rotational speed is minimal for a very young stellar object, $t_{\rm col} \sim 10^4$ years with modest rotation rates, but it can be important for more evolved objects (Figure B.5).

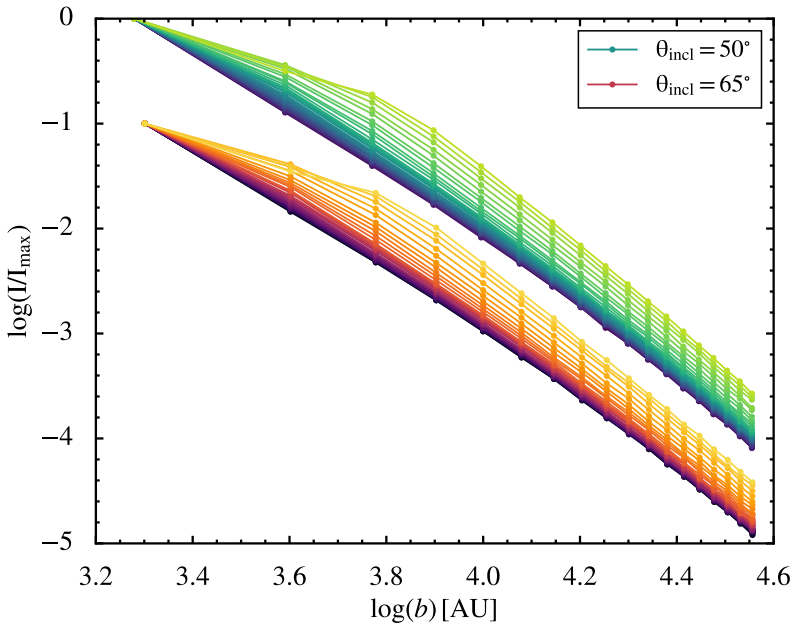

Figure B.4: Two groups of simulated radial intensity profiles with the same range of age but different inclination angles, 50° (green sequence) and 65° (red sequence). The grid with $\theta_{\rm incl} = 65°$ is shifted by -1.

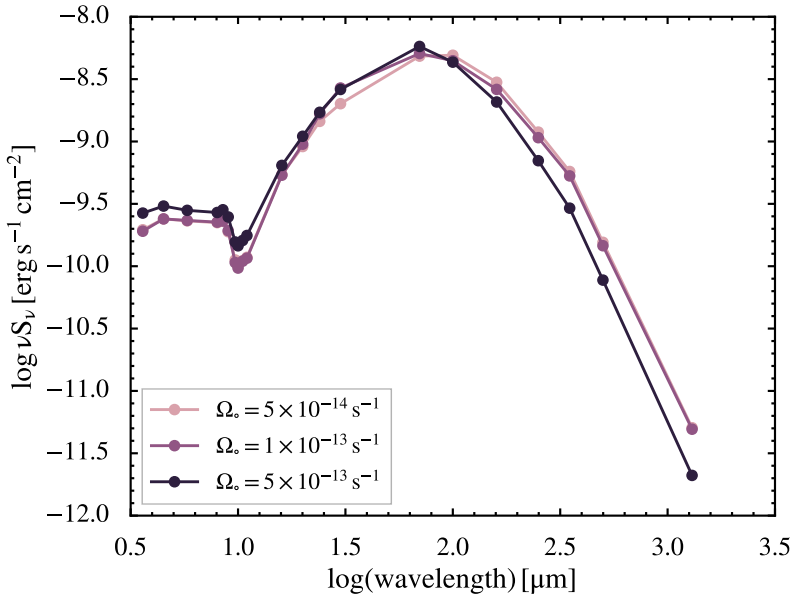

Figure B.5: The simulated SEDs of TSC model with the initial rotational speed of 5×10^{-13}, 10^{-13}, and 5×10^{-14} s^{-1} with an age of $7.5{\times}10^4$ years. Other parameters are adopted from Table 3.4.

B.2 Disk Parameters

The formation of the disk is a consequence of conservation of angular momentum. With a small but not negligible initial rotational speed, the centrifugal barrier becomes comparable to the gravitational force as material moves toward the center. However, the angular momentum cannot be conserved strictly; otherwise stars would spin too fast to remain stable. Outflows and magnetic fields are the major channels for reducing the angular momentum from the system (Li et al., 2014). Observationally, disks associated with protostars are widely observed in both late stages and early stages (Fedele et al., 2013b; Yen et al., 2015). Here we demonstrate the effect of the disk around the embedded protostars on their SEDs. Figure B.6 shows the effect of the disk at two ages, early and late. In both stages, early and late, the SED with a disk shows more emission at wavelengths shorter than 8 μm and slightly more absorption at the 10 μm silicate feature. Although the presence of disks does affect the SED, we find the SED at the early stage is not sensitive to the disk parameters due to the small size of the disk at the early stage ($R_{\rm disk} = 0.2$ AU). For objects as young as BHR71, the effects of the disk parameters on the SED are minimal. For consistency, we still include the disk in our model setup, but its properties are unconstrained by the observations. To emphasize the effects of the disk parameters on the SED, we show the models that have a disk radius $\sim$ 120 AU ($t_{\rm col} = 7.5 \times 10^4$ years and the rest of the parameters adopted from Table 3.4) in the following discussion.

Figure B.7 (top) shows the simulated SEDs with disk masses of 0.025 $M_\odot$, 0.075 $M_\odot$, and 0.25 $M_\odot$. The effect of the disk mass on the observed SED is primarily at near-infrared ($\lambda < 8$ μm) wavelengths because it is close to the central protostar, resulting in a higher temperature. A more massive disk leads to a small increase of emission at mid-infrared wavelengths. Note that these models have an inclination angle of 53°.

Figure B.7 (middle) shows the effect on the simulated SEDs of different disk flaring power-laws, β, of 1.0, 1.2, 1.4, 1.6, and 1.8. The disk flaring power, β, is translated into α, where $\alpha = \beta + 1$, when calculating the disk density profile with Equation 3.9 (also see Section 3.4.2.2). A larger β results in a more flared disk, therefore the surface area exposed to the starlight increases but with a lower density. Different disk flaring powers change the emission at mid-infrared wavelengths. The emission below 10 μm decreases as the flaring power increases, and the emission between 10 μm to 20 μm increases slightly, while the rest of SED remains the same, indicating that the

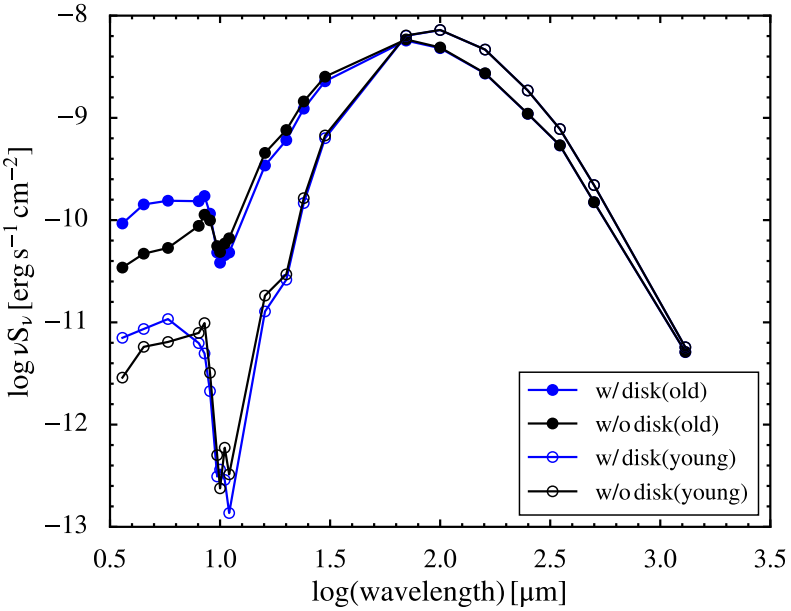

Figure B.6: The simulated SEDs with and without the presence of disk for early age and late age, 10^4 and 7.5×10^4 years respectively (open and filled circles), while other parameters are adopted from Table 3.4. The models with disk are shown in blue, while the models without disk are shown in black.

disk is less efficient for reproducing the radiation from the center with a more diffuse dust distribution.

Figure B.7 (bottom) shows the effect on the simulated SEDs of the disk scale height, h_{100}, of 6 AU, 8 AU, 10 AU, 12 AU, and 14 AU. Note that h_{100} is defined as the scale height at 100 AU. A larger scale height results in more emission at near-infrared wavelengths, and slightly less emission at mid-infrared wavelengths. Because of the increase of the disk thickness, the irradiated area at the disk inner radius is larger, resulting in more dust with a higher temperature, which increases the emission in the near-infrared. While more radiation is collected by the dust at the disk inner radius, less radiation can be received by the dust at a larger radius, leading to a slight decrease of the emission at mid-infrared wavelengths.

The effect of disk parameters can be summarized as follows:

- $M_{\rm disk}$: Increasing the disk mass increases the emission at near-infrared wavelengths, which can be seen from the SEDs below 10 μm in the top panel of Figure B.7.

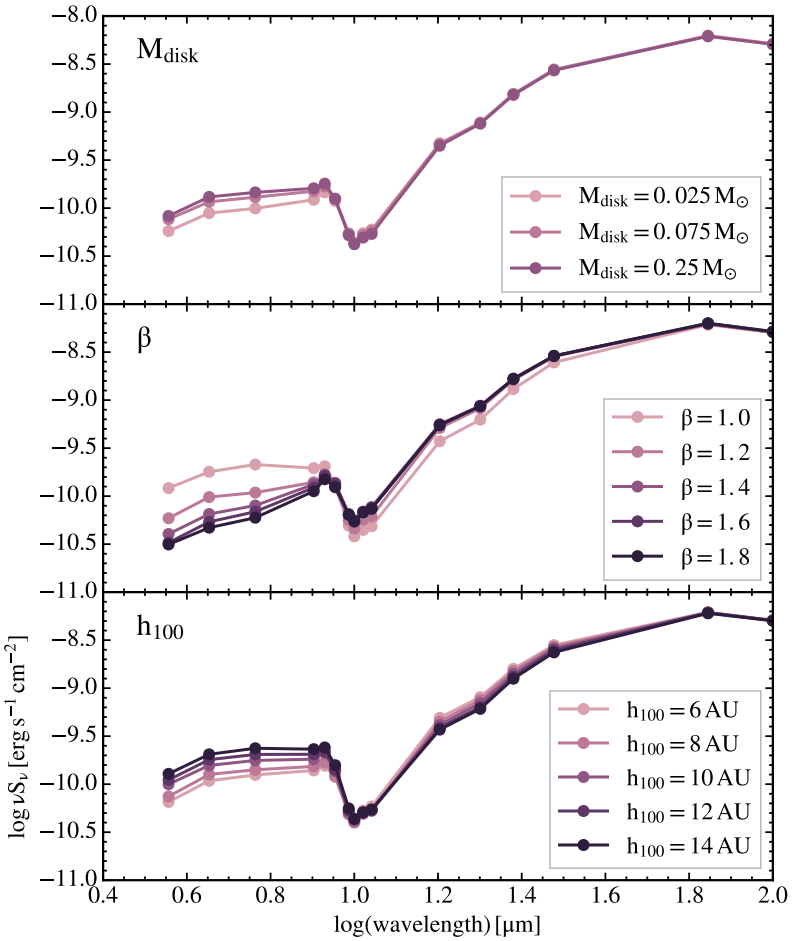

Figure B.7: **Top**: The simulated SEDs with disk mass of 0.025 $M_\odot$, 0.075 $M_\odot$, and 0.25 $M_\odot$(light to dark colors). **Middle**: The simulated SEDs with disk flaring power of 1.0, 1.2, 1.4, 1.6, and 1.8 (light to dark colors). **Bottom**: The simulated SEDs with disk scale height at 100 AU of 6 AU, 8 AU, 10 AU, 12 AU, and 14 AU (light to dark colors). All other parameters are adopted from Table 3.4, except for a larger age of 75000 years. The disk parameters change the SED at mid-infrared wavelength, while the rest of the SED remains the same (not shown here).

- β: Increasing the flaring power decreases the emission at near-infrared wavelength, and slightly increases the emission at mid-infrared wavelengths (the middle panel of Figure B.7).

- h_{100}: Increasing the disk scale height increases the emission at near-infrared wavelengths, and decreases the emission at mid-infrared wavelengths (the bottom panel of Figure B.7).

B.3 Outflow Cavity Parameters

The existence of the outflow cavity allows the radiation to escape from the center in bipolar directions. We use a power-law profile with a power of -1.5 for the shape of the outflow cavity (Section 3.4.2.3). Therefore the only parameter that scales the shape of outflow cavity is the cavity opening angle. Observing a 3-D object is a projection onto a plane so that the net effect of both cavity opening angle and inclination is to change the projected area of the outflow cavity, resulting in variations in mid-infrared emission.

We have tested several simple cavity density profiles of a uniform density, $\rho(\mathrm{r}) \propto \mathrm{r}^{-2}$, $\rho(\mathrm{r}) \propto \mathrm{r}^{-1.5}$, and a hybrid profile with a uniform density out to some radius, followed by a power law decrease (Figure B.8). The hybrid profile can be described with three parameters, the outer radius of the constant density region ($R_{\mathrm{cav},\circ}$), the dust density in the constant region ($\rho_{\mathrm{cav},\circ}$), and the cavity opening angle (θ_{cav}). The simulated SEDs with the simple power-law cavity profiles (r^{-2} and $r^{-1.5}$) show only minimal changes. We find that the ratio of the flux at 8 μm to the flux at 16 μm is most diagnostic for characterizing the effect of cavity profiles. For the SEDs with a lower density at the center ($\rho_{\mathrm{cav},\circ} = 10^{-21}$ g cm^{-3}), the flux ratio is approximately the same, while the ratio for the SEDs with a higher density at the center ($\rho_{\mathrm{cav},\circ} = 10^{-18}$ g cm^{-3}) is larger. This feature is seen for the power law cavity profile with r^{-2}, but not in the profile with $r^{-1.5}$. On the other hand, the hybrid profile can produce more emission at 10 μm to 20 μm, while having a similar emission at shorter wavelengths.

The major effects of the outflow cavity parameters are at mid-infrared wavelengths, while submillimeter emission is unaffected; therefore we plot the SED out to only 100 μm in the figures discussing the outflow cavity parameters. Figure B.9 shows a grid of SEDs with three inclinations (80°, 40°, and 30°) and five cavity opening an-

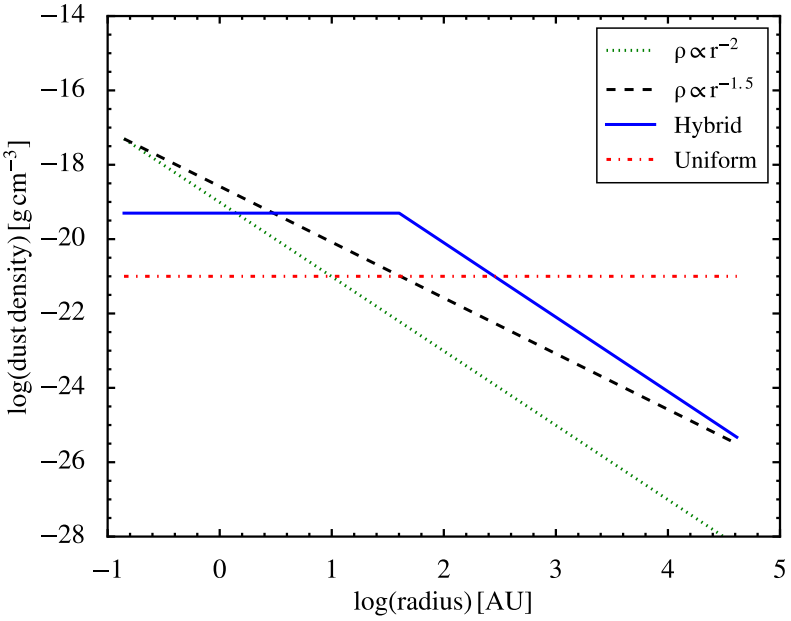

Figure B.8: The radial density profiles with prescriptions of two power laws (r^{-2} and $r^{-1.5}$) shown in black dahsed and green dotted lines, uniform density shown in red dot-dashed line, and the hybrid profile, which consists of a constant density region at the center followed by a power law decrease, shown in blue solid line.

gles (10°, 15°, 20°, 25°, and 30°). The definition of inclination follows the convention in HYPERION, where 0° means face-on and 90° means edge-on. For a certain opening angle, decreasing the inclination angle reduces the contrast between the mid-infrared and submillimeter emission and the depth of the silicate absorption feature. At a given inclination, the amount of emission in IRAC bands (3.6 μm, 4.5 μm, 5.8 μm, and 8.0 μm) increases with opening angles, because the low density region is larger in a wider cavity and more emission escapes from the center with less attenuation. Note that the SED at wavelengths from 20 μm to 40 μm is sensitive to the cavity opening angle, especially when the inclination angle is small (left two panels in Figure B.9).

The images at IRAC bands are direct probes of the inclination angle of the outflow cavity. Whitney et al. (2003) used two dimensional radiative transfer simulations to show that the contrast between two lobes of an outflow cavity is greater with a smaller inclination. The same effect is also found in our simulated images. We compare the flux ratio of the south and north lobe from simulations at various inclinations (Figure 3.18). The flux ratio is a maximum at intermediate inclination angles.

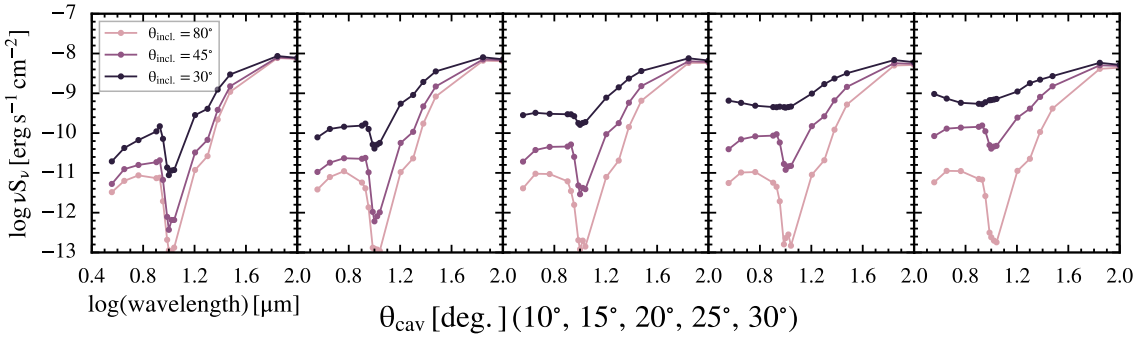

Figure B.9: The simulated SEDs with the grid of cavity opening angle and the inclination angle parameters. The purple dot/line shows the SED with aperture-extracted photometry from simulated spectra with the inclination angle of 80°, 40°, and 30° shown in different transparency. The cavity opening angles are 10°, 15°, 20°, 25°, and 30° from left to right. Other parameters are adopted from Table 3.4.

Figure B.10 shows the simulated SEDs with a grid of the size of the constant density region in the cavity, $R_{\rm cav,\circ}$, and the density of the constant density region, $\rho_{\rm cav,\circ}$. The models with $\rho_{\rm cav,\circ}$ of 5×10^{-20}, 1×10^{-19}, 5×10^{-19}, and 1×10^{-18} g cm^{-3} are shown in lines with different transparency, and the models with $R_{\rm cav,\circ}$ of 20 AU, 40 AU, and 60 AU are shown from left to right. Both $\rho_{\rm cav,\circ}$ and $R_{\rm cav,\circ}$ change the emission from 5-40 μm, a region where none of other parameters discussed so far have a significant effect. These two parameters together define the total mass at the constant density region, which affects the emission at 5-40 μm. It is shown that a higher $\rho_{\rm cav,\circ}$ increases the overall flux at 5-40 μm, while $R_{\rm cav,\circ}$ has the same effect but is less significant. Note that the fluxes at 3.6 μm and 4.5 μm are not affected by these two parameters.

The effects of outflow cavity parameters can be summarized as follows:

- $\theta_{\rm cav}$: Increasing the cavity opening angle increases the emission at wavelengths from 5 μm to 40 μm. However, the inclination angle must be considered at the same time. Increasing the inclination angle decreases the emission at wavelengths from 5 μm to 40 μm.

- $\rho_{\rm cav,\circ}$: It changes the absolute level of the SED at wavelengths from 5 μm to 40 μm. A larger $\rho_{\rm cav,\circ}$ leads to a higher flux level at mid-infrared wavelengths.

- $R_{\rm cav,\circ}$: It also changes the absolute level of the SED at wavelengths from 5 μm

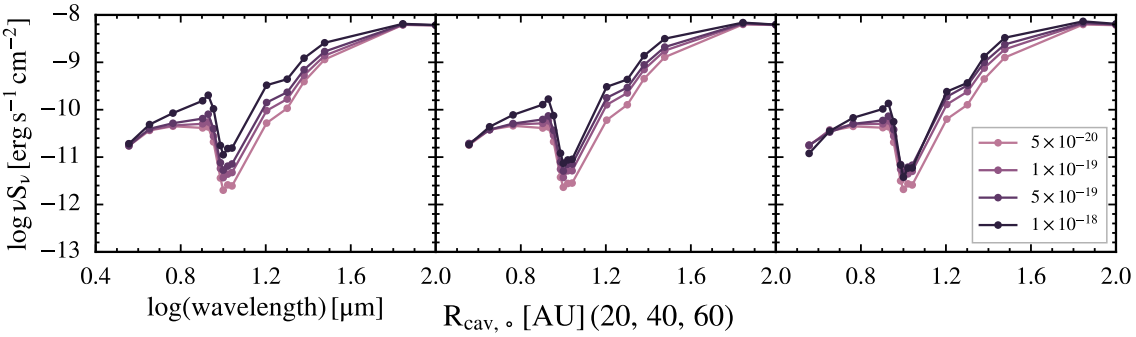

Figure B.10: The simulated SEDs with the grid of the dust density in the inner cavity and the extent of the inner cavity region parameters. The purple dot/line shows the SED with aperture-extracted photometry from simulated spectra with the innermost constant density of 5×10^{-20}, 1×10^{-19}, 5×10^{-19}, and 1×10^{-18} g cm^{-3} shown in different transparency. The size of the innermost constant density region increases from the left to right, 20 AU, 40 AU, and 60 AU. Other parameters are adopted from Table 3.4.

to 40 μm, but it is less effective than modifying $\rho_{\rm cav,\circ}$.

B.4 Other parameters

Model parameters in this category are less constrained by the observations in this study. Figure B.11 shows the effect of the envelope outer radius. Increasing the size of the envelope adds extinction, resulting in less emission at mid-infrared wavelengths. On the other hand, the emission at submillimeter wavelengths increases with the envelope outer radius, probing the total mass in the envelope. Note that the simulated spectra shown in Figure B.11 are from the full model, rather than values within apertures to better emphasize the effect of the envelope outer radius. If the apertures are smaller than the source size the effect of increasing the outer radius on the SED is much less noticeable.

The other two parameters, $T_\star$ and $R_\star$, are coupled in determining the central luminosity assuming a pure blackbody spectrum (Equation 3.11). The protostar radius also enters the disk density profile (Equation 3.9). Since the central protostar is highly embedded within the envelope, there is no direct measurement of its physical properties. In our model, these two parameters are degenerate except that the luminosity, which is calculated from $T_\star$ and $R_\star$, is required to make the luminosity

from the simulated observations fit the observed luminosity. Figure B.12 shows the simulated SEDs with protostar temperatures of 6450 K, 6950 K, and 7450 K, while the luminosity is fixed. The protostar radius is calculated accordingly. We find that the simulated SEDs show a subtle increase at wavelengths below 10 μm as we decrease the stellar temperature and a slight increase at wavelengths between 20 μm to 40 μm, suggesting that a small fraction of emission at near-infrared may be scattered light from the central luminosity source; therefore a lower stellar temperature leads to more stellar emission at near-infrared wavelength, resulting in a slight increase of emission at near-infrared wavelengths of the simulated SEDs.

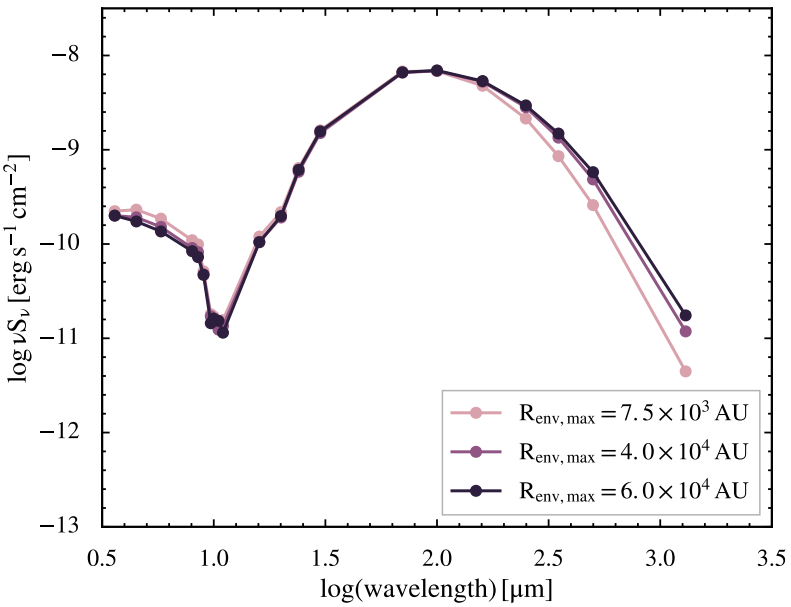

Figure B.11: The simulated SEDs with outer envelope radius of 7.5×10^3 AU, 1×10^4 AU, and 2.5×10^4 AU. The blue dot/line shows the SED with the extracted photometry from the simulated spectra *without* a specific aperture. Other parameters are adopted from Table 3.4.

The effect of other parameters can be summarized as follows:

- $R_{\rm max}$: Increasing the outer radius of the envelope decreases the emission at wavelengths from 5 μm to 15 μm and increases the total emission at the longest wavelengths.

- $T_\star$: Increasing the temperature of the star slightly decreases the emission at wavelengths below 10 μm, when the emission at 20 μm to 40 μm shows a slight

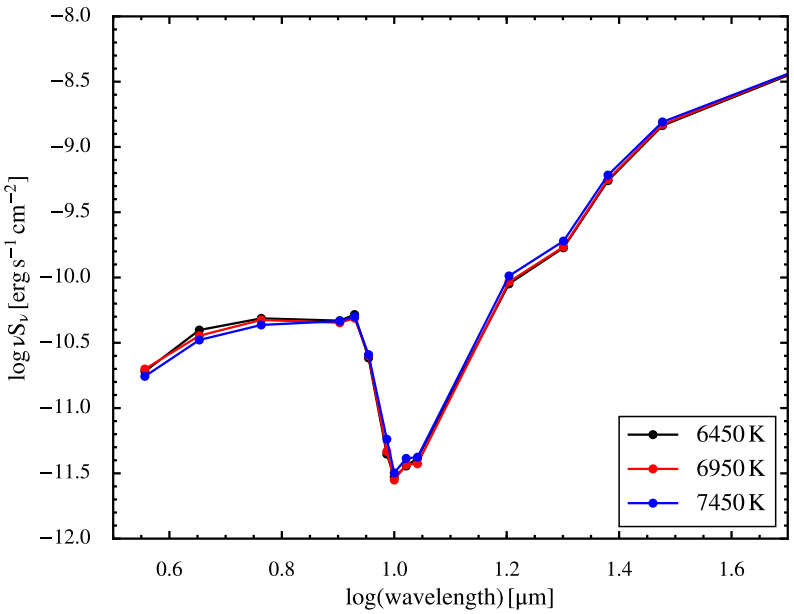

Figure B.12: The simulated SEDs with the central star temperature of 6450 K, 6950 K, and 7450 K, while the central luminosity remains the same, 18.8 $L_{\odot}$. The protostar radius is calculated accordingly to satisfy the same central luminosity. The simulated SEDs show no difference beyond 50 μm.

increase.

Appendix C: Constraining the Infalling Envelope of Embedded Protostars: BHR71 and its Hot Corino

C.1 Effects of Cavities and the Inclination of the Envelope

BHR 71 drives outflows in the north-south direction, which carve out cavities within the envelope. Traditional 1D or 2D radiative transfer calculations fail to fully test the effect of the cavity on the infall profile due to the lack of geometric dimensions. With LIME and LIME-AID, we investigate the effect of the outflow cavities and inclination angles on the infall profile.

Figure C.1 illustrates the effect of cavities on the infall profile. The model with cavities has more intensity at low velocity (from -2 to 2 km s^{-1}), while the high velocity emission remains the same. Although the LOS at an inclination angle of 50° passes through the cavity when $r \lesssim 1000$ au, where the abundance becomes zero, the finite size of the telescope beam still includes parts of the outflow cavity wall at small radii. Thus, with cavity, the overall intensity increases because of the higher temperature near the cavity walls.

The inclination angle is another critical parameter for the synthetic infall profile. Here we only consider the geometric effect of the inclination angle as the model does not include the outflowing gas. In the pure envelope case, the inclination angle has a negligible effect on the infall profile. For the TSC envelope with cavities, the infall profile strongly depends on the inclination angle (Figure C.2). The inclination angle is defined as the rotation axis pointed toward observers as 0°, and pointed toward north (up) as 90°. The line profiles are extracted with the size of the observed continuum source, $0\farcs52 \times 0\farcs39$. Along the LOS close to the outflow axis, the infall profile becomes narrower due to the zero abundance in the outflow cavity, which eliminates the emission at high velocity. Along the pole-on view, the absorption disappears as the molecular abundance becomes zero in the cavities, and the emission

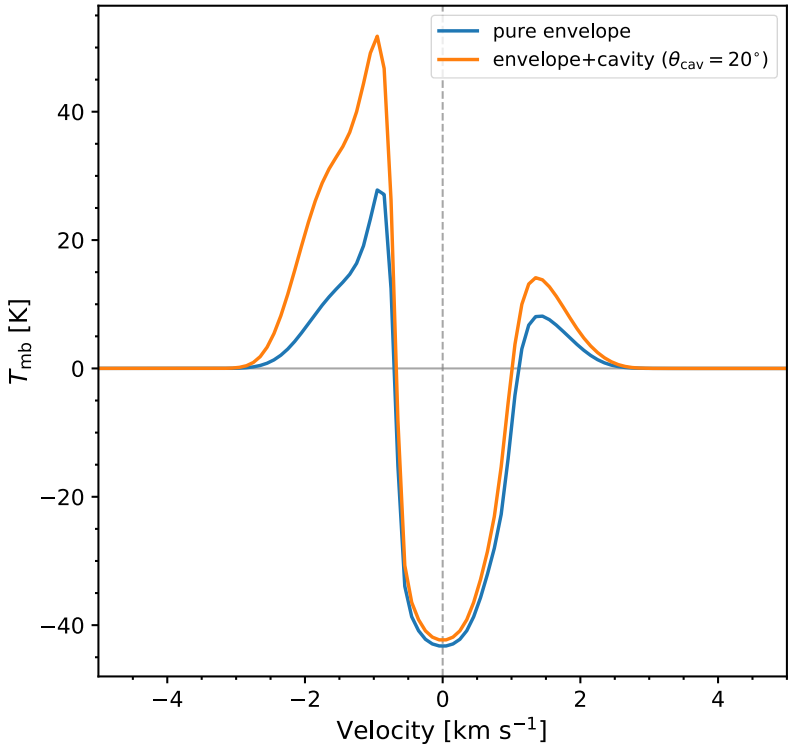

Figure C.1: The synthetic HCO^+ $J = 4 \rightarrow 3$ line profiles calculated with the envelopes with and without the outflow cavities.

from the inner edge of the envelope dominates the line profile. The inner radius of the evaporation zone is 50 au, which is 0.″25 at 200 pc.

As the inclination increases, the infall profile becomes dominated by the envelope, which consists of low-velocity warm gas and high-velocity hot gas. Thus, the intensity increases as more warm and hot gas enters the LOS, and the high velocity emission increases from the hot gas in the evaporation zone. At high inclination, the second absorption feature appears at 2.5 km s^{-1} as the molecules in the evaporation zone become optically thick to the continuum source.

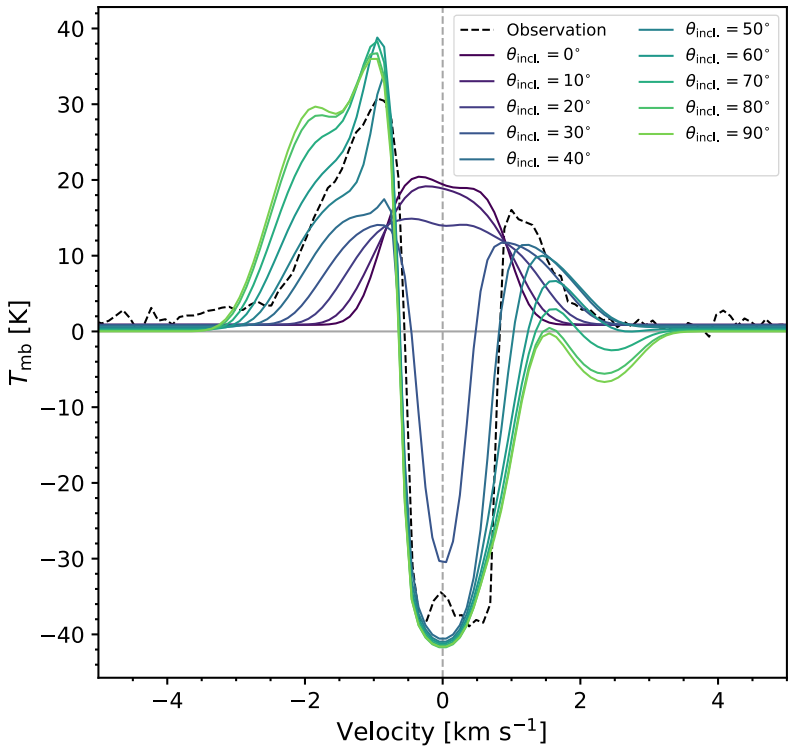

Figure C.2: The synthetic infall profiles of the HCO^+ $J = 4 \rightarrow 3$ line with inclination angles ranging from 0° to 90°. The model has a bipolar outflow with an opening angle of 20°.

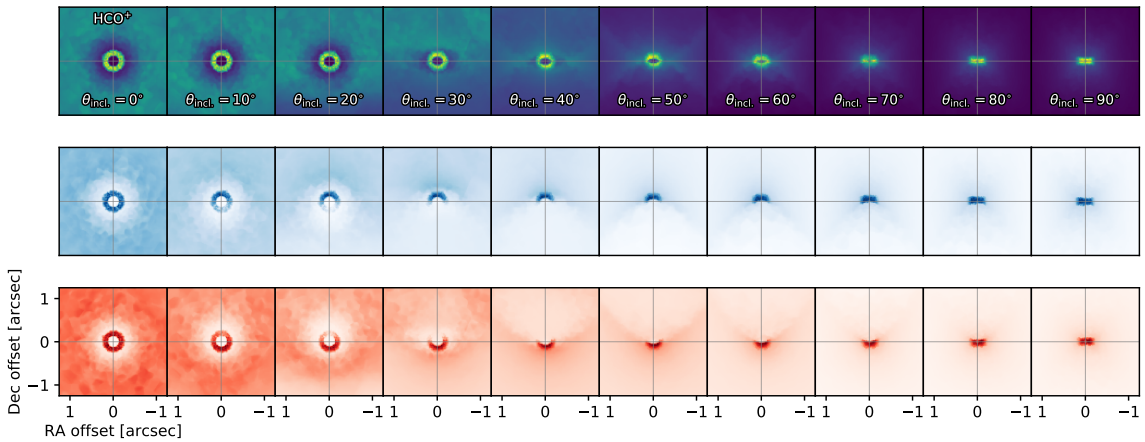

Figure C.3: The intensity maps of the best-fitting HCO^+ model viewed from different inclination angles. This model is ray-traced without the central continuum source to highlight the effects of cavities and inclinations. The inclination angle is defined as the rotation axis pointed toward observers as 0°, and pointed toward north (up) as 90°. Under this definition, the inclination of BHR 71 is −50°, corresponding to $\theta_{\rm incl.} = 50°$ but flipped upside down.

Bibliography

Adams, F. C., Lada, C. J., & Shu, F. H. 1987, ApJ, 312, 788

Aikawa, Y. 2013, Chemical Reviews, 113, 8961

Anderson, T., Crownover, R. L., Herbst, E., & De Lucia, F. C. 1988, The Astrophysical Journal Supplement Series, 67, 135

André, P., Di Francesco, J., Ward-Thompson, D., et al. 2014, in Protostars and Planets VI, ed. H. Beuther, R. S. Klessen, C. P. Dullemond, & T. Henning, 27

Andre, P., Ward-Thompson, D., & Barsony, M. 1993a, ApJ, 406, 122

—. 1993b, ApJ, 406, 122

—. 2000, Protostars and Planets IV, 59

André, P., Men'shchikov, A., Bontemps, S., et al. 2010, A&A, 518, L102

Apai, D., Tóth, L. V., Henning, T., et al. 2005, A&A, 433, L33

Arce, H. G., & Goodman, A. A. 2001, ApJ, 554, 132

Arce, H. G., Mardones, D., Corder, S. A., et al. 2013, ApJ, 774, 39

Arce, H. G., Shepherd, D., Gueth, F., et al. 2007, in Protostars and Planets V, ed. B. Reipurth, D. Jewitt, & K. Keil, 245

Audard, M., Ábrahám, P., Dunham, M. M., et al. 2014, Protostars and Planets VI, 387

Bate, M. R. 2009, MNRAS, 392, 1363

Belikov, A. N., Kharchenko, N. V., Piskunov, A. E., Schilbach, E., & Scholz, R.-D. 2002, A&A, 387, 117

Bell, K. R., & Lin, D. N. C. 1994, ApJ, 427, 987

Benz, A. O., Bruderer, S., van Dishoeck, E. F., et al. 2016, A&A, 590, A105

Bertout, C., Robichon, N., & Arenou, F. 1999, A&A, 352, 574

Bonnor, W. B. 1956, MNRAS, 116, 351

Bontemps, S., Andre, P., Terebey, S., & Cabrit, S. 1996a, A&A, 311, 858

—. 1996b, A&A, 311, 858

Bourke, T. L. 2001, ApJ, 554, L91

Bourke, T. L., Crapsi, A., Myers, P. C., et al. 2005, ApJ, 633, L129

Bourke, T. L., Hyland, A. R., & Robinson, G. 1995a, MNRAS, 276, 1052

Bourke, T. L., Hyland, A. R., Robinson, G., James, S. D., & Wright, C. M. 1995b, MNRAS, 276, 1067

Bourke, T. L., Garay, G., Lehtinen, K. K., et al. 1997, ApJ, 476, 781

Brandt, J. C., Stecher, T. P., Crawford, D. L., & Maran, S. P. 1971, ApJ, 163, L99

Brinch, C., Crapsi, A., Hogerheijde, M. R., & Jørgensen, J. K. 2007, A&A, 461, 1037

Brinch, C., & Hogerheijde, M. R. 2010, A&A, 523, A25

Calcutt, H., Jørgensen, J. K., Müller, H. S. P., et al. 2018, A&A, 616, A90

Carney, M. T., Yıldız, U. A., Mottram, J. C., et al. 2016, A&A, 586, A44

Caselli, P., & Ceccarelli, C. 2012, Astronomy and Astrophysics Review, 20, 56

Casey, B. W., Mathieu, R. D., Vaz, L. P. R., Andersen, J., & Suntzeff, N. B. 1998, AJ, 115, 1617

Cassen, P., & Moosman, A. 1981, Icarus, 48, 353

Ceccarelli, C. 2004, in Astronomical Society of the Pacific Conference Series, Vol. 323, Star Formation in the Interstellar Medium: In Honor of David Hollenbach, ed. D. Johnstone, F. C. Adams, D. N. C. Lin, D. A. Neufeeld, & E. C. Ostriker, 195

Ceccarelli, C., Caselli, P., Bockelée-Morvan, D., et al. 2014, in Protostars and Planets VI, ed. H. Beuther, R. S. Klessen, C. P. Dullemond, & T. Henning, 859

Ceccarelli, C., Caselli, P., Herbst, E., Tielens, A., & Caux, E. 2007, Protostars and Planets V, 47

Ceccarelli, C., Caux, E., Loinard, L., et al. 1999, A&A, 342, L21

Černis, K. 1993, Baltic Astronomy, 2, 214

Černis, K., & Straižys, V. 2003, Baltic Astronomy, 12, 301

Chen, H., Myers, P. C., Ladd, E. F., & Wood, D. O. S. 1995a, ApJ, 445, 377

—. 1995b, ApJ, 445, 377

Chen, X., Launhardt, R., Bourke, T. L., Henning, T., & Barnes, P. J. 2008, ApJ, 683, 862

Chiang, H.-F., Reipurth, B., & Hillenbrand, L. 2015, AJ, 149, 108

Choi, M., Kamazaki, T., Tatematsu, K., & Panis, J.-F. 2004, ApJ, 617, 1157

Choi, M., Panis, J.-F., & Evans, Neal J., I. 1999, The Astrophysical Journal Supplement Series, 122, 519

Chou, H.-G., Yen, H.-W., Koch, P. M., & Guilloteau, S. 2016, ApJ, 823, 151

Corporon, P., & Reipurth, B. 1997, in IAU Symposium, Vol. 182, Herbig-Haro Flows and the Birth of Stars, ed. B. Reipurth & C. Bertout, 85

Corradi, W. J. B., Franco, G. A. P., & Knude, J. 1997, A&A, 326, 1215

Dame, T. M., & Thaddeus, P. 1985, ApJ, 297, 751

de Geus, E. J., Bronfman, L., & Thaddeus, P. 1990, A&A, 231, 137

de Zeeuw, P. T., Hoogerwerf, R., de Bruijne, J. H. J., Brown, A. G. A., & Blaauw, A. 1999, AJ, 117, 354

Di Francesco, J., Myers, P. C., Wilner, D. J., Ohashi, N., & Mardones, D. 2001, ApJ, 562, 770

Dionatos, O., & Güdel, M. 2017, A&A, 597, A64

Dionatos, O., Jørgensen, J. K., Green, J. D., et al. 2013, A&A, 558, A88

Drabek, E., Hatchell, J., Friberg, P., et al. 2012, MNRAS, 426, 23

Dunham, M. M., Arce, H. G., Mardones, D., et al. 2014a, ApJ, 783, 29

Dunham, M. M., Evans, Neal J., I., Terebey, S., Dullemond, C. P., & Young, C. H. 2010a, ApJ, 710, 470

Dunham, M. M., Evans, N. J., Terebey, S., Dullemond, C. P., & Young, C. H. 2010b, ApJ, 710, 470

Dunham, M. M., Evans, II, N. J., Bourke, T. L., et al. 2006, ApJ, 651, 945

Dunham, M. M., Arce, H. G., Allen, L. E., et al. 2013, AJ, 145, 94

Dunham, M. M., Stutz, A. M., Allen, L. E., et al. 2014b, Protostars and Planets VI, 195

Dunham, M. M., Stutz, A. M., Allen, L. E., et al. 2014c, in Protostars and Planets VI, ed. H. Beuther, R. S. Klessen, C. P. Dullemond, & T. Henning, 195

Dunham, M. M., Allen, L. E., Evans, II, N. J., et al. 2015, ApJS, 220, 11

Ebert, R. 1955, Zeitschrift fur Astrophysik, 37, 217

Eggen, O. J. 1980, ApJ, 238, 919

Eisner, J. A., Hillenbrand, L. A., White, R. J., Akeson, R. L., & Sargent, A. I. 2005, ApJ, 623, 952

Enoch, M. L., Young, K. E., Glenn, J., et al. 2006, ApJ, 638, 293

Evans, Neal J., I. 1999a, Annual Review of Astronomy and Astrophysics, 37, 311

Evans, Neal J., I., Di Francesco, J., Lee, J.-E., et al. 2015, ApJ, 814, 22

Evans, Neal J., I., Lee, J.-E., Rawlings, J. M. C., & Choi, M. 2005, ApJ, 626, 919

Evans, Neal J., I., Dunham, M. M., Jørgensen, J. K., et al. 2009a, The Astrophysical Journal Supplement Series, 181, 321

Evans, N. J., Dunham, M. M., Jørgensen, J. K., et al. 2009b, ApJS, 181, 321

Evans, II, N. J. 1999b, ARA&A, 37, 311

Fedele, D., Bruderer, S., van Dishoeck, E. F., et al. 2013a, A&A, 559, A77

—. 2013b, A&A, 559, A77

Ferreira, J., Dougados, C., & Cabrit, S. 2006, A&A, 453, 785

Fischer, W. J., Megeath, S. T., Stutz, A. M., et al. 2013, Astronomische Nachrichten, 334, 53

Fischer, W. J., Megeath, S. T., Furlan, E., et al. 2017, ApJ, 840, 69

Flower, D. R., & Pineau Des Forêts, G. 2010, MNRAS, 406, 1745

Fourikis, N., Takagi, K., & Morimoto, M. 1974, ApJ, 191, L139

Furlan, E., McClure, M., Calvet, N., et al. 2008, ApJS, 176, 184

Furlan, E., Luhman, K. L., Espaillat, C., et al. 2011, The Astrophysical Journal Supplement Series, 195, 3

Galli, D., & Shu, F. H. 1993a, ApJ, 417, 220

—. 1993b, ApJ, 417, 243

Garrod, R. T., Widicus Weaver, S. L., & Herbst, E. 2008, ApJ, 682, 283

Giannini, T., Nisini, B., & Lorenzetti, D. 2001, ApJ, 555, 40

Giannini, T., Nisini, B., Neufeld, D., et al. 2011, ApJ, 738, 80

Giannini, T., Lorenzetti, D., Tommasi, E., et al. 1999, A&A, 346, 617

Goicoechea, J. R., Cernicharo, J., Karska, A., et al. 2012, A&A, 548, A77

Goldsmith, P. F., & Langer, W. D. 1999, ApJ, 517, 209

Goldsmith, P. F., Snell, R. L., Hemeon-Heyer, M., & Langer, W. D. 1984, ApJ, 286, 599

Gong, H., & Ostriker, E. C. 2009, ApJ, 699, 230

Green, J. D., Evans, II, N. J., Jørgensen, J. K., et al. 2013a, ApJ, 770, 123

Green, J. D., Evans, II, N. J., Kóspál, Á., et al. 2013b, ApJ, 772, 117

Green, J. D., Evans, Neal J., I., Jørgensen, J. K., et al. 2013c, ApJ, 770, 123

Green, J. D., Yang, Y.-L., Evans, II, N. J., et al. 2016a, AJ, 151, 75

Green, J. D., Jones, O. C., Keller, L. D., et al. 2016b, ApJ, 832, 4

Green, J. D., Yang, Y.-L., Evans, Neal J., I., et al. 2016c, AJ, 151, 75

Greene, T. P., Wilking, B. A., Andre, P., Young, E. T., & Lada, C. J. 1994, ApJ, 434, 614

Griffin, M. J., Abergel, A., Abreu, A., et al. 2010, A&A, 518, L3+

Gusdorf, A., Giannini, T., Flower, D. R., et al. 2011, A&A, 532, A53

Gusdorf, A., Riquelme, D., Anderl, S., et al. 2015, A&A, 575, A98

Haisch, Jr., K. E., Greene, T. P., Barsony, M., & Stahler, S. W. 2004, AJ, 127, 1747

Harsono, D., Jørgensen, J. K., van Dishoeck, E. F., et al. 2014, A&A, 562, A77

Hartmann, L. 2009, Accretion Processes in Star Formation: Second Edition

Heiderman, A., & Evans, Neal J., I. 2015, ApJ, 806, 231

Henning, T., & Launhardt, R. 1998, A&A, 338, 223

Herbig, G. H. 1977, ApJ, 217, 693

Herczeg, G. J., Karska, A., Bruderer, S., et al. 2012, A&A, 540, A84

Hirota, T., Honma, M., Imai, H., et al. 2011, PASJ, 63, 1

Hollenbach, D. 1985a, Icarus, 61, 36

—. 1985b, Icarus, 61, 36

Hollenbach, D., & McKee, C. F. 1989, ApJ, 342, 306

Isobe, T., & Feigelson, E. D. 1990, in BAAS, Vol. 22, Bulletin of the American Astronomical Society, 917–918

Isobe, T., Feigelson, E. D., & Nelson, P. I. 1986, ApJ, 306, 490

Je, H., Lee, J.-E., Lee, S., Green, J. D., & Evans, Neal J., I. 2015, The Astrophysical Journal Supplement Series, 217, 6

Jiménez-Donaire, M. J., Meeus, G., Karska, A., et al. 2017, A&A, 605, A62

Jørgensen, J. K., Schöier, F. L., & van Dishoeck, E. F. 2002a, A&A, 389, 908

—. 2002b, A&A, 389, 908

—. 2004a, A&A, 416, 603

—. 2004b, A&A, 416, 603

—. 2005, A&A, 435, 177

Jørgensen, J. K., van Dishoeck, E. F., Visser, R., et al. 2009, A&A, 507, 861

Jørgensen, J. K., Bourke, T. L., Myers, P. C., et al. 2007, ApJ, 659, 479

Jørgensen, J. K., Visser, R., Sakai, N., et al. 2013, ApJ, 779, L22

Jørgensen, J. K., van der Wiel, M. H. D., Coutens, A., et al. 2016, A&A, 595, A117

Kaifu, N., Morimoto, M., Nagane, K., et al. 1974, ApJ, 191, L135

Karska, A., Herczeg, G. J., van Dishoeck, E. F., et al. 2013a, A&A, 552, A141

—. 2013b, A&A, 552, A141

Karska, A., Kristensen, L. E., van Dishoeck, E. F., et al. 2014a, A&A, 572, A9

—. 2014b, A&A, 572, A9

Karska, A., Kaufman, M. J., Kristensen, L. E., et al. 2018, The Astrophysical Journal Supplement Series, 235, 30

Kauffmann, J., Bertoldi, F., Bourke, T. L., Evans, N. J., I., & Lee, C. W. 2008, A&A, 487, 993

Kaufman, M. J., & Neufeld, D. A. 1996, ApJ, 456, 611

Kenyon, S. J., Dobrzycka, D., & Hartmann, L. 1994, AJ, 108, 1872

Kirk, J. M., Ward-Thompson, D., Palmeirim, P., et al. 2013, MNRAS, 432, 1424

Knude, J., & Hog, E. 1998a, A&A, 338, 897

—. 1998b, A&A, 338, 897

Körtgen, B., & Banerjee, R. 2015, MNRAS, 451, 3340

Kristensen, L. E., Gusdorf, A., Mottram, J. C., et al. 2017a, A&A, 601, L4

Kristensen, L. E., van Dishoeck, E. F., Benz, A. O., et al. 2013, A&A, 557, A23

Kristensen, L. E., Visser, R., van Dishoeck, E. F., et al. 2010, A&A, 521, L30

Kristensen, L. E., van Dishoeck, E. F., Bergin, E. A., et al. 2012a, A&A, 542, A8

—. 2012b, A&A, 542, A8

Kristensen, L. E., van Dishoeck, E. F., Mottram, J. C., et al. 2017b, A&A, 605, A93

—. 2017c, A&A, 605, A93

Lada, C. J. 1987, in IAU Symposium, Vol. 115, Star Forming Regions, ed. M. Peimbert & J. Jugaku, 1

Langer, W. D., & Penzias, A. A. 1993, ApJ, 408, 539

Larson, R. B. 1969a, MNRAS, 145, 271

—. 1969b, MNRAS, 145, 271

Launhardt, R., Nutter, D., Ward-Thompson, D., et al. 2010, The Astrophysical Journal Supplement Series, 188, 139

Lavalley, M. P., Isobe, T., & Feigelson, E. D. 1992, in BAAS, Vol. 24, Bulletin of the American Astronomical Society, 839–840

Lee, C.-F., Hirano, N., Zhang, Q., et al. 2015a, ApJ, 805, 186

Lee, C.-F., Li, Z.-Y., Ho, P. T. P., et al. 2017, ApJ, 843, 27

Lee, J., Lee, J.-E., Lee, S., et al. 2013, The Astrophysical Journal Supplement Series, 209, 4

Lee, J.-E., Bergin, E. A., & Evans, Neal J., I. 2004, ApJ, 617, 360

Lee, J.-E., Lee, J., Lee, S., Evans, II, N. J., & Green, J. D. 2014, ApJS, 214, 21

Lee, J.-E., Lee, S., Baek, G., et al. 2019, Nature Astronomy, 3, 314

Lee, S., Lee, J.-E., & Bergin, E. A. 2015b, The Astrophysical Journal Supplement Series, 217, 30

Leung, C. M., & Brown, R. L. 1977, ApJ, 214, L73

Li, Z. Y., Banerjee, R., Pudritz, R. E., et al. 2014, in Protostars and Planets VI, ed. H. Beuther, R. S. Klessen, C. P. Dullemond, & T. Henning, 173

Li, Z.-Y., & Nakamura, F. 2006, ApJ, 640, L187

Ligterink, N. F. W., Tenenbaum, E. D., & van Dishoeck, E. F. 2015, A&A, 576, A35

Ligterink, N. F. W., Calcutt, H., Coutens, A., et al. 2018, A&A, 619, A28

Lindberg, J. E., Jørgensen, J. K., Green, J. D., et al. 2014, A&A, 565, A29

Lindberg, J. E., Jorgensen, J. K., & Herschel DIGIT Team. 2011, in IAU Symposium, Vol. 280, IAU Symposium, 235P

Lorenzetti, D., Tommasi, E., Giannini, T., et al. 1999, A&A, 346, 604

Lorenzetti, D., Giannini, T., Nisini, B., et al. 2000, A&A, 357, 1035

Luhman, K. L. 2008, Chamaeleon, ed. B. Reipurth, 169

Maheswar, G., Manoj, P., & Bhatt, H. C. 2004, MNRAS, 355, 1272

Makiwa, G., Naylor, D. A., Ferlet, M., et al. 2013, Appl. Opt., 52, 3864

Makiwa, G., Naylor, D. A., van der Wiel, M. H. D., et al. 2016a, MNRAS, 458, 2150

—. 2016b, MNRAS, 458, 2150

Manoj, P., Watson, D. M., Neufeld, D. A., et al. 2013, ApJ, 763, 83

Manoj, P., Green, J. D., Megeath, S. T., et al. 2016, ApJ, 831, 69

Markwardt, C. B. 2009, in Astronomical Society of the Pacific Conference Series, Vol. 411, Astronomical Data Analysis Software and Systems XVIII, ed. D. A. Bohlender, D. Durand, & P. Dowler, 251

Matuszak, M., Karska, A., Kristensen, L. E., et al. 2015, A&A, 578, A20

Meeus, G., Salyk, C., Bruderer, S., et al. 2013, A&A, 559, A84

Möller, T., Endres, C., & Schilke, P. 2017, A&A, 598, A7

Mottram, J. C., Kristensen, L. E., van Dishoeck, E. F., et al. 2014a, A&A, 572, A21

—. 2014b, A&A, 572, A21

—. 2015, A&A, 574, C3

Mottram, J. C., van Dishoeck, E. F., Kristensen, L. E., et al. 2017, A&A, 600, A99

Müller, H. S. P., Schlöder, F., Stutzki, J., & Winnewisser, G. 2005, Journal of Molecular Structure, 742, 215

Mundy, L. G., Looney, L. W., & Welch, W. J. 2000, in Protostars and Planets IV, ed. V. Mannings, A. P. Boss, & S. S. Russell, 355

Myers, P. C., & Ladd, E. F. 1993, ApJ, 413, L47

Myers, P. C., Mardones, D., Tafalla, M., Williams, J. P., & Wilner, D. J. 1996, ApJ, 465, L133

Neufeld, D. A. 2012, ApJ, 749, 125

Neuhäuser, R., & Forbrich, J. 2008, The Corona Australis Star Forming Region (Handbook of Star Forming Regions, Volume II, ed. Bo Reipurth), 735

Nisini, B., Antoniucci, S., Giannini, T., & Lorenzetti, D. 2005, A&A, 429, 543

Nisini, B., Giannini, T., & Lorenzetti, D. 2002, ApJ, 574, 246

Nisini, B., Benedettini, M., Codella, C., et al. 2010, A&A, 518, L120

Nisini, B., Santangelo, G., Antoniucci, S., et al. 2013, A&A, 549, A16

Nisini, B., Santangelo, G., Giannini, T., et al. 2015, ApJ, 801, 121

Nyman, L. Å. 2008, The Southern Coalsack, ed. B. Reipurth, Vol. 5, 222

Offner, S. S. R., & Chaban, J. 2017, ApJ, 847, 104

Offner, S. S. R., Clark, P. C., Hennebelle, P., et al. 2014, in Protostars and Planets VI, ed. H. Beuther, R. S. Klessen, C. P. Dullemond, & T. Henning, 53

Offner, S. S. R., Klein, R. I., McKee, C. F., & Krumholz, M. R. 2009, ApJ, 703, 131

Offner, S. S. R., Robitaille, T. P., Hansen, C. E., McKee, C. F., & Klein, R. I. 2012, ApJ, 753, 98

Ohashi, N., Hayashi, M., Ho, P. T. P., & Momose, M. 1997, ApJ, 475, 211

Olofsson, J., Augereau, J.-C., van Dishoeck, E. F., et al. 2009, A&A, 507, 327

Ortiz-León, G. N., Loinard, L., Kounkel, M. A., et al. 2017, ApJ, 834, 141

Ossenkopf, V., & Henning, T. 1994, A&A, 291, 943

Ott, S. 2010, in Astronomical Society of the Pacific Conference Series, Vol. 434, Astronomical Data Analysis Software and Systems XIX, ed. Y. Mizumoto, K.-I. Morita, & M. Ohishi, 139

Oya, Y., Sakai, N., López-Sepulcre, A., et al. 2016, ApJ, 824, 88

Oya, Y., Sakai, N., Watanabe, Y., et al. 2017, ApJ, 837, 174

Padoan, P., & Nordlund, Å. 2011, ApJ, 730, 40

Pagani, L., Bacmann, A., Cabrit, S., & Vastel, C. 2007, A&A, 467, 179

Palla, F., & Stahler, S. W. 1992, ApJ, 392, 667

Parise, B., Belloche, A., Leurini, S., et al. 2006a, A&A, 454, L79

—. 2006b, A&A, 454, L79

Parise, B., Ceccarelli, C., Tielens, A. G. G. M., et al. 2006c, A&A, 453, 949

—. 2002, A&A, 393, L49

Pelletier, G., & Pudritz, R. E. 1992, ApJ, 394, 117

Penston, M. V. 1969, MNRAS, 144, 425

Peterson, D. E., Caratti o Garatti, A., Bourke, T. L., et al. 2011, ApJS, 194, 43

Pilbratt, G. L., Riedinger, J. R., Passvogel, T., et al. 2010, A&A, 518, L1

Pineda, J. E., Maury, A. J., Fuller, G. A., et al. 2012, A&A, 544, L7

Poglitsch, A., Waelkens, C., Geis, N., et al. 2010, A&A, 518, L2

Rebull, L. M., Padgett, D. L., McCabe, C.-E., et al. 2010, ApJS, 186, 259

Rebull, L. M., Stauffer, J. R., Cody, A. M., et al. 2015, AJ, 150, doi:10.1088/0004-6256/150/6/175

Reynolds, R. J. 1976, ApJ, 203, 151

Robitaille, T. P. 2011, A&A, 536, A79

Robitaille, T. P., Whitney, B. A., Indebetouw, R., Wood, K., & Denzmore, P. 2006a, ApJS, 167, 256

—. 2006b, The Astrophysical Journal Supplement Series, 167, 256

Sakai, N., Sakai, T., Hirota, T., et al. 2014, Nature, 507, 78

Sakai, N., Oya, Y., López-Sepulcre, A., et al. 2016, ApJ, 820, L34

San José-García, I., Mottram, J. C., Kristensen, L. E., et al. 2013, A&A, 553, A125

Santangelo, G., Murillo, N. M., Nisini, B., et al. 2015, A&A, 581, A91

Santangelo, G., Nisini, B., Giannini, T., et al. 2012a, A&A, 538, A45

—. 2012b, A&A, 538, A45

Santangelo, G., Nisini, B., Codella, C., et al. 2014, A&A, 568, A125

Scheiner, S., & Seybold, P. G. 2009, Structural Chemistry, 20, 43. https://doi.org/10.1007/s11224-008-9395-7

Schöier, F. L., van der Tak, F. F. S., van Dishoeck, E. F., & Black, J. H. 2005a, A&A, 432, 369

—. 2005b, A&A, 432, 369

Segura-Cox, D. M., Looney, L. W., Tobin, J. J., et al. 2018, ApJ, 866, 161

Seidensticker, K. J., & Schmidt-Kaler, T. 1989a, A&A, 225, 192

—. 1989b, A&A, 225, 192

Shakura, N. I., & Sunyaev, R. A. 2073, A&A, 500, 33

Shirley, Y. L. 2015, Publications of the Astronomical Society of the Pacific, 127, 299

Shirley, Y. L., Evans, Neal J., I., & Rawlings, J. M. C. 2002, ApJ, 575, 337

Shirley, Y. L., Huard, T. L., Pontoppidan, K. M., et al. 2011, ApJ, 728, 143

Shu, F., Najita, J., Ostriker, E., et al. 1994, ApJ, 429, 781

Shu, F. H. 1977a, ApJ, 214, 488

—. 1977b, ApJ, 214, 488

Shu, F. H., Tremaine, S., Adams, F. C., & Ruden, S. P. 1990, ApJ, 358, 495

Smith, A., Becerra, F., Bromm, V., & Hernquist, L. 2017, MNRAS, 472, 205

Smith, A., Safranek-Shrader, C., Bromm, V., & Milosavljević, M. 2015, MNRAS, 449, 4336

Snyder, L. E., Lovas, F. J., Hollis, J. M., et al. 2005, ApJ, 619, 914

Stetson, P. B. 1987, PASP, 99, 191

Storm, S., Mundy, L. G., Fernández-López, M., et al. 2014, ApJ, 794, 165

Straižys, V., Černis, K., Kazlauskas, A., & Meistas, E. 1992, Baltic Astronomy, 1, 149

Straizys, V., Claria, J. J., Piatti, A. E., & Kazlauskas, A. 1994, Baltic Astronomy, 3, 199

Stutz, A. M., Rubin, M., Werner, M. W., et al. 2008, ApJ, 687, 389

Swinyard, B. M., Polehampton, E. T., Hopwood, R., et al. 2014, MNRAS, 440, 3658

Tafalla, M., Bachiller, R., Lefloch, B., et al. 2015, A&A, 573, L2

Terebey, S., Shu, F. H., & Cassen, P. 1984a, ApJ, 286, 529

—. 1984b, ApJ, 286, 529

The CGAL Project. 2018, CGAL User and Reference Manual, 4.12 edn. (CGAL Editorial Board). `https://doc.cgal.org/4.12/Manual/packages.html`

Tobin, J. J., Looney, L. W., Li, Z.-Y., et al. 2016, ApJ, 818, 73

Tobin, J. J., Bourke, T. L., Mader, S., et al. 2019, ApJ, 870, 81

Ulrich, R. K. 1976, ApJ, 210, 377

Urban, A., Martel, H., & Evans, II, N. J. 2010, ApJ, 710, 1343

van der Wiel, M. H. D., Naylor, D. A., Kamp, I., et al. 2014, MNRAS, 444, 3911

van Dishoeck, E. F., Kristensen, L. E., Benz, A. O., et al. 2011, PASP, 123, 138

van Kempen, T. A., van Dishoeck, E. F., Salter, D. M., et al. 2009a, A&A, 498, 167

—. 2009b, A&A, 498, 167

van Kempen, T. A., van Dishoeck, E. F., Güsten, R., et al. 2009c, A&A, 507, 1425

van Kempen, T. A., Green, J. D., Evans, N. J., et al. 2010, A&A, 518, L128

van Kempen et al. 2010, A&A, 518, L128

Vasta, M., Codella, C., Lorenzani, A., et al. 2012a, A&A, 537, A98

—. 2012b, A&A, 537, A98

Visser, R., Kristensen, L. E., Bruderer, S., et al. 2012a, A&A, 537, A55

—. 2012b, A&A, 537, A55

Vorobyov, E. I. 2009, ApJ, 692, 1609

Wampfler, S. F., Bruderer, S., Kristensen, L. E., et al. 2011, A&A, 531, L16

Wampfler, S. F., Bruderer, S., Karska, A., et al. 2013, A&A, 552, A56

Wang, P., Li, Z.-Y., Abel, T., & Nakamura, F. 2010, ApJ, 709, 27

Ward-Thompson, D., André, P., Crutcher, R., et al. 2007, Protostars and Planets V, 33

Wardle, M., & Koenigl, A. 1993, ApJ, 410, 218

Watson, D. M., Calvet, N. P., Fischer, W. J., et al. 2016, ApJ, 828, 52

Whitney, B. A., Wood, K., Bjorkman, J. E., & Cohen, M. 2003, ApJ, 598, 1079

Whittet, D. C. B., Prusti, T., Franco, G. A. P., et al. 1997, A&A, 327, 1194

Wilson, T. L., & Rood, R. 1994, Annual Review of Astronomy and Astrophysics, 32, 191

Wu, P.-F., Takakuwa, S., & Lim, J. 2009, ApJ, 698, 184

Wu, R., Polehampton, E. T., Etxaluze, M., et al. 2013, A&A, 556, A116

Yang, Y.-L., Evans, Neal J., I., Green, J. D., Dunham, M. M., & Jørgensen, J. K. 2017a, ApJ, 835, 259

Yang, Y.-L., Evans, II, N. J., Green, J. D., Dunham, M. M., & Jørgensen, J. K. 2017b, ApJ, 835, 259

Yang, Y.-L., Green, J. D., Evans, Neal J., I., et al. 2018, ApJ, 860, 174

Yen, H.-W., Koch, P. M., Takakuwa, S., et al. 2015, ApJ, 799, 193

Yen, H.-W., Zhao, B., Koch, P. M., et al. 2018, A&A, 615, A58

Yıldız, U. A., Kristensen, L. E., van Dishoeck, E. F., et al. 2012, A&A, 542, A86

—. 2013, A&A, 556, A89

—. 2015, A&A, 576, A109

Young, C. H., & Evans, Neal J., I. 2005, ApJ, 627, 293

Young, C. H., Jørgensen, J. K., Shirley, Y. L., et al. 2004a, ApJS, 154, 396

Young, K. E., Lee, J.-E., Evans, Neal J., I., Goldsmith, P. F., & Doty, S. D. 2004b, ApJ, 614, 252

Zhao, B., Caselli, P., Li, Z.-Y., & Krasnopolsky, R. 2018, MNRAS, 473, 4868

Zhou, S. 1992, ApJ, 394, 204

Zhou, S., & Evans, N. J., I. 1994, in Astronomical Society of the Pacific Conference Series, Vol. 65, Clouds, Cores, and Low Mass Stars, ed. D. P. Clemens & R. Barvainis, 183

VITA

Yao-Lun Yang (楊燿綸) was born in New Taipei City, Taiwan. He has been keen on science since his childhood. He attended the Chien Kuo Senior High school in Taipei. Then he attend the National Taiwan University (NTU) majored in physics, where he discovered his interest in astronomy after attending a star party hosted by the astronomy club in the university. He was awarded the Summer Student Fellowship at the Institute of Astronomy and Astrophysics at Academia Sinica (ASIAA) to start his astronomy research under the supervision of Dr. Ciska Kemper on the diffuse molecular gas in the Large Magellanic Cloud. After receiving Bachelor of Science from NTU, he served as a second lieutenant at the Army of Taiwan.

In 2013, he enrolled the Ph.D. program in the Department of Astronomy of the University of Texas at Austin, supervised by Prof. Neal J. Evans and Dr. Joel D. Green. During his candidacy, he worked on understanding the star-forming process at extremely young protostars using *Herschel* and ALMA observations as well as radiative transfer calculations. He was awarded observing time from Acatama Large Millimeter/submillimeter Array (ALMA) and Stratospheric Observatory for Infrared Astronomy (*SOFIA*) for his research along with a research funding of $97 000. He has been to Mauna Kea, Hawaii and Fort Davis, Texas for observing at the Infrared Telescope Facility (IRTF) and the Harlan J. Smith Telescope at McDonald Observatory. He obtained his Master of Arts in 2015, and was awarded the Best Thesis Award for his master thesis. In the summer of 2016, he was awarded an internship at Space Telescope Science Institute (STScI) under the supervision of Dr. Joel Green. He was awarded the Fred T. Goetting, Jr. Memorial Endowed Presidential Fellowship from the Department of Astronomy as well as the University Graduate Continuing Fellowship twice. Beside his research, he earned the Concentration in Teaching and Mentoring. Furthermore, he was part of the organizing committee for the Astronomy on Tap ATX, a monthly public outreach event, for three years.

Upon obtaining his Doctoral degree, he will be a JSPS postdoctoral fellow at RIKEN (Wako, Japan) working with Dr. Nami Sakai, and then become a Cosmic Origin postdoctoral fellow at University of Virginia (Charlottesville, VA, USA) and Chalmers University of Technology (Gothenburg, Sweden) working with Prof. Jonathan Tan.

Address: yaolunyang.astro@gmail.com

This dissertation was typeset with LaTeX by the author.